Developments Towards Low Loss Suspensions for Laser Interferometric Gravitational Wave Detectors

Sharon Melanie Twyford, B.Sc., M.Sc.,

Department of Physics and Astronomy.
University of Glasgow.

Presented as a thesis for the degree of Ph.D..
Department of Physics and Astronomy,
University of Glasgow, University Avenue, G12 8QQ.

September 23, 1998

ProQuest LLC.
789 East Eisenhower Parkway
P.O. Box 1346
Ann Arbor, MI 48106 – 1346

'....Are waves that beat on heavens shore.'

William Blake, 'Auguries of Innocence' (c. 1803) l. 71

Contents

List of Figures

List of Tables

Acknowledgements

I would first of all like to thank my supervisor Jim Hough for all of the help, advice and encouragement he has given me during the period of researching for and the writing of this thesis. I would equally like to thank Norna Robertson for all of the help and encouragement that she has given to me throughout my time as a research student. My thanks also go to Sheila Rowan whose support and advice (and sense of humour!) during my time in the laboratory and since have been very much appreciated. Thanks too go to Alison Forbes (née McLaren) for the short time we spent working together.

I wish to give a special thanks to Alastair Grant whose help and friendship throughout the course of writing my thesis has been gratefully received. I would also like to thank Ray Hutchins for his technical help and friendship over the last four years.

A big thank you goes to my fellow office-mates Morag Casey and Calum Torrie, for putting up with me over the last years and whose friendly banter I will sadly miss!

I am grateful for the support of all of the other members of the gravitational waves group, namely Gavin Newton, Harry Ward, Dave Robertson, Ken Strain, Mike Plissi, Ken Skeldon, Stuart Killbourn, Paul McNamara, David Clubley, David Palmer, Stephen McIntosh and Matt Husman. I would also like to acknowledge the encouragement given to me by the members of the other gravitational wave groups involved in the GEO 600 project. I would like to thank Colin Craig, Allan Latta and Angus McKellar for the technical support provided. I would also like to thank the workshop staff for all of their assistance. In addition my thanks go to Kaz Piechowiak of the Department of Electronics and Electrical Engineering for polishing the initial test pieces of fused quartz.

I am grateful for the support given to me by Professor R.P. Ferrier and Professor D.H.

Saxon during my time as a research student in this department. I was in receipt of financial support from P.P.A.R.C. during the period of this work.

Personal thanks go to Ants, whose support and razor-sharp wit have been a constant throughout my period as a research student. I want to thank Susan, Lorna and Loraine, Louise and Abby, and Chris and Neil for their friendship and just being there. Finally, I owe special thanks to my family; Chris, Lorraine and especially to mum for all of the love and patience she has shown me, especially over recent years.

Preface

This thesis is an account of the work conducted during the period October 1994 through to October 1997 towards the development of low loss suspensions for use in the GEO 600 laser interferometric gravitational wave detector.

Chapter 1 contains a brief introduction to the nature of gravitational radiation and the astrophysical processes that are predicted to produce such waves of a strength detectable on Earth. The two main detection schemes are discussed with emphasis on laser interferometric detectors. The noise sources which are expected to limit the sensitivity of such detectors are also reviewed, with the importance stressed of the need to reduce the effects of thermal noise in the suspensions of the test masses. The material presented in this chapter is derived from published literature.

An introduction to the theory of thermal noise is given in Chapter 2. The fluctuation-dissipation theorem (which relates the thermally induced displacement of the test masses to the mechanical loss of the system) is introduced. A discussion follows of the various forms of external and internal loss mechanisms which may be present in a system and which can lead to an increase in the level of thermal noise if care is not taken. A method of determining the level of mechanical loss associated with a given vibrational mode of the system is described. The various modes of a test mass suspension are discussed. The required levels for the loss factors associated with each of these modes for GEO 600 are given. The theory presented in this chapter is derived from published literature. The GEO 600 thermal noise specification is obtained from the GEO 600 design proposal [1].

In Chapter 3 the measurement of the loss factor of samples of carbon steel wire is discussed. It is concluded that a wire material of lower intrinsic loss is required if the

thermal noise specification of GEO 600 is to be met. Experiments to test the suitability of fibres pulled from commercially available ('standard grade') fused quartz are reported. In addition, the unexpectedly high level of gas damping observed in these experiments is discussed. The work described in this chapter was carried out with the assistance of Prof. J. Hough and Dr. S. Rowan. The RF furnace was developed by Mr. R. Hutchins formerly of the Dept. of Electronics and Electrical Engineering, University of Glasgow.

Recoil damping is a form of loss that can seriously limit the loss factor measured for a given mode of a test mass suspension. Chapter 4 contains a report of experiments conducted to determine the level of recoil damping present in the structure used to measure the loss associated with the longitudinal pendulum mode of our test pendulums. Having ascertained this, we took steps to improve the system, and an improved value for the level of recoil damping is given. The experiments were conducted with A. McLaren at the suggestion of Prof. J. Hough.

A discussion of experiments conducted to characterise the loss factor associated with the pendulum mode of pendulums suspended from carbon steel wires is presented in Chapter 5. The level of loss expected in the suspension due to an excess loss mechanism known as 'stick-slip' damping is derived and found to be consistent with that observed experimentally. An investigation into the source of an additional loss mechanism which was observed is reported and consideration given to such sources of loss as eddy current and hysteresis damping.

In Chapter 6 experiments conducted on small mass pendulums suspended from fused quartz fibres are reported. An unexpected loss mechanism was observed and was found to result from electrostatic charging of the pendulum mass. A model was devised that was consistent with the level of damping observed. Further experiments were conducted once the effect of charging had been effectively eliminated and it was found that the level of loss measured was still above that expected. Sources of loss such as a load dependence in the loss factor associated with the material of the suspension fibres and a loss introduced by the method of attaching the fibres to the point of attachment were considered. The excess loss was reduced significantly by clamping the fibres to the point of suspension and pendulum mode loss factors of the order required for use in GEO 600 were subsequently observed.

In Chapter 7 a number of techniques are discussed that can be employed to attach the fused quartz suspension fibres to fused quartz test masses. The bond strength and ease of forming each of the bonds are compared. Experiments conducted to measure the magnitude of the loss factor associated with four internal modes are reported for the various bonding techniques. The loss associated with each bond is then scaled to predict the level of loss for a GEO 600 sized test mass. The decision on which bonding method will be employed in GEO 600 is presented. The indium bonded mass used in these measurements was made by H. Rohner of JILA, Colorado. Hydroxide catalysis bonding has been developed by D.-H. Gwo of Stanford University. Both the experimental and modelling work reported in Chapters 5 to 7 were carried out with the assistance of Prof. J. Hough and Dr. S. Rowan.

In Chapter 8 the conclusions drawn from the work presented in this thesis are given.

Appendix A contains the derivation of an equation which can be employed to predict the loss factor associated with the level of external gas damping present in the system. This derivation followed from discussions with Dr. N.A. Robertson.

Appendix B contains a number of sections. Firstly there is a derivation of the level of recoil loss exhibited by the experimental test structure as a function of its mechanical properties. Following this is a discussion of an inverted pendulum accelerometer and its calibration. Finally a proof showing the phase relationship between the shadow sensed motion of the pendulum and the force applied to the support structure is given. The derivation of the recoil limit was carried out with advice from Prof. J. Hough.

In Appendix C there is a derivation of the expected levels of eddy current and hysteresis damping present in our pendulum suspended in a magnetic field gradient from carbon steel wires. The derivation of the limit due to eddy current damping was carried out following a suggestion from Prof. J. Hough, whilst that of hysteresis damping followed discussions with Mr. A. Grant.

Contained in Appendix D is a derivation of an expression for the rms motion induced in a pendulum due to seismic excitation of the point of suspension of the pendulum. The derivation was carried out with the assistance of Prof. J. Hough.

Appedix E contains a description of the revised mirror sizes for GEO 600 and the consequences in terms of the achievable levels of thermal noise associated with them. This summary is the work of the author based on the latest information available.

Summary

Developments Towards Low Loss Suspensions for Laser Interferometric Gravitational Wave Detectors

Einstein, in his General Theory of Relativity, predicted that fluctuations in gravitational effects propagate as waves at the speed of light through space-time. Currently there has only been indirect evidence for the existence of these elusive *gravitational waves.* Scientists working on a number of large-scale research projects around the world are concentrating their efforts on detecting gravitational waves directly. Not only will their detection provide a test of some of the predictions of Einstein's theory but also much information about the astrophysical processes and sources that produce them.

Gravitational waves are quadrupole in nature and produce a tidal strain in space. However their interaction with matter is very weak, making them difficult to detect. Gravitational waves emitted by violent astrophysical events are predicted to produce strains at the Earth of the order of $\sim 10^{-21}$ to $\sim 10^{-22}$ at frequencies accessible to ground-based detectors (i.e. a few tens of Hz to a few kHz). All detection schemes involve trying to sense these strains in space. One such detection scheme is based on the laser interferometer.

Researchers at the University of Glasgow are working with collaborators from Germany on a project called GEO 600. GEO 600 is an interferometer with arms of 600 m in which light from a Nd:YAG laser is reflected between mirrors suspended as pendulums in a vacuum system. Scientists from the Max-Planck-Institut für Quantenoptik at Hannover and Garching, the University of Cardiff and the Albert Einstein Institut at Potsdam also

work on this project, together with collaborators from the Laser-Zentrum, Hannover.

The design criteria of the GEO 600 detector defines that the thermal noise associated with internal modes of the fused silica test masses will limit the low frequency sensitivity of the detector. Taking a value of the intrinsic loss factor of $\phi_{internal}(\omega) = 2 \times 10^{-7}$ for fused silica, we can show that the thermal noise due to this loss results in a motion of one test mass of $\tilde{x}_{internal}(\omega) = 7 \times 10^{-20}\,\mathrm{m}/\sqrt{\mathrm{Hz}}$ at 50 Hz. The loss factors associated with the modes of the suspension, including the presence of any additional external loss mechanisms, can increase this minimum level of thermal noise and consequently decrease the detector sensitivity. In order to prevent the achievable level of thermal noise being degraded by contributions from these other sources of thermal noise a design specification is set. Our aim is to achieve a level of thermal noise displacement of no greater than $\tilde{x}_{pend}(\omega) = 2 \times 10^{-20}\,\mathrm{m}/\sqrt{\mathrm{Hz}}$ at 50 Hz at each test mass from the source of thermal noise associated with the 1 Hz pendulum mode. This corresponds to an acceptable loss factor of $\phi_{pend_{total}}(\omega) = 3.7 \times 10^{-8}$ at 50 Hz for a GEO 600 sized test mass.

The work contained in this thesis covers various methods of reducing the levels of loss in the test mass suspensions and thereby minimising the impact of thermal noise on the overall detector sensitivity. Suitable techniques have been developed towards the final design of a test mass suspension for GEO 600.

To achieve a low level of loss factor associated with the pendulum mode requires a suspension wire or fibre material which is itself of low intrinsic loss. The projected material loss at 50 Hz for samples of carbon steel wire is $\sim$40$\times$ higher than that set by the GEO 600 thermal noise specification. Fused quartz is known to be a material of low loss and so tests were performed on samples of ribbon fibres.

Measurements on fused quartz ribbons, corrected for thermoelastic damping, yielded values for the intrinsic loss factor of fused quartz of $\phi_{mat_{intrinsic}}(\omega) = (0.5 - 1) \times 10^{-6}$ in the frequency range 6 Hz to 160 Hz. This is potentially a factor of 10 better than the maximum acceptable material loss factor for the suspension fibres as set by the GEO 600 design specification. It was found that the internal loss mechanism exhibited by 'standard grade' fused quartz appeared to be consistent with that of structural damping. These measurements were especially interesting because they were made over a frequency range that lies partially within the detection band of GEO 600.

The loss factor associated with the pendulum mode of various masses suspended from two fused quartz fibres was measured. When the fibres were attached to the points of suspension by mechanical clamps, the level of loss factor observed was found to be equal to that determined by known losses of the system (i.e. the sum of the losses associated with the material of the suspension fibres and a contribution due to recoil damping – which results from the pendulum being suspended from a lossy support structure). All excess loss mechanisms were therefore eliminated.

An all-welded suspension was also constructed. The loss factor was again found to be set by the known losses in the system. By subtracting the recoil loss from the measured loss, we could use the value of the remaining loss to predict the loss factor achievable by a full sized GEO 600 suspension. This was calculated to be $\phi_{pend_{total}}(\omega) \sim 8.5 \times 10^{-9}$ at 50 Hz, which is lower (and therefore better) than the GEO 600 design specification. When attached with care to the point of suspension, fibres pulled from 'standard grade' fused quartz will be ideal for use in the test mass suspensions of GEO 600.

By considering various factors, a decision was made to use a four fibre suspension in GEO 600. In order to avoid increasing the level of thermal noise associated with the internal modes of the test masses, a low loss method of attaching the fibres to the test masses had to be found. The methods tested were welding, indium bonding and hydroxide catalysis bonding. The relative strengths and the ease of formation of each type of attachment were taken into account. The effects of the different types of bonding on the measured loss factors associated with four internal modes were measured. When the measurements (made on 500 g masses) were scaled to that expected for a full size GEO 600 suspension, the results suggested that hydroxide catalysis bonding could be used without introducing significant excess loss. Thus, taking all of the factors into consideration, it has been concluded that hydroxide catalysis bonding will be used to attach the fused quartz fibres to the synthetic fused silica test masses in GEO 600.

Chapter 1

The Nature, Possible Sources and Methods of Detection of Gravitational Waves

1.1 Introduction

In his General Theory of Relativity, Einstein [2] proposed that gravitational effects propagate with finite velocity i.e. the gravitational field does not alter instantaneously at an arbitrary distance from the source which is changing the field. In fact, the solutions to the linearised Einstein Field Equations show that the effect of gravity propagates as a *wave* with a velocity equal to that of light.

At present there is only indirect evidence for the existence of gravitational waves. This has come from radio observations of the binary pulsar PSR 1913 + 16 by Hulse and Taylor [3]. Data obtained from PSR 1913 + 16 has allowed a number of relativistic effects to be observed. By far the most interesting effect for those working in the field of gravitational wave detection, however, is one that can only be explained should the binary pulsar be emitting gravitational waves at a rate predicted by Einstein's theory.

It has been observed that the orbital period of the binary pulsar is decreasing. From the observed orbit Taylor [4] calculated the rate at which orbital energy should be lost

via gravitational radiation (as predicted by General Relativity). From the rate of loss he then calculated the associated rate of orbital inspiral. The calculated rate and observed rate agree within the accuracy of the experiment. Hulse and Taylor were awarded the Nobel Prize for Physics in 1993 in recognition of their work on the binary pulsar.

Direct detection of gravitational waves remains one of the most challenging fields of experimental physics this century. Scientists working on a number of large scale projects around the world are currently aiming at this goal. Once gravitational waves have been detected there will still be much to be learnt about their nature. Study of gravitational radiation data will allow some of the predictions of General Relativity to be tested, including measurements of the speed of propagation and polarisation of the waves, and from these the rest mass and spin of the graviton can be deduced. In addition, the study of gravitational waves will provide an opportunity to learn about the astrophysics of the events producing them – they will provide astronomers with another 'window' on the universe.

This chapter contains a brief discussion of the nature of gravitational waves, possible sources of production and methods of detection.

1.2 The Nature of Gravitational Waves

To help our understanding of these waves we can draw a number of analogies between electromagnetic theory and gravitation. For example, electromagnetic waves are produced by the acceleration of charge, whereas gravitational waves are produced by the acceleration of mass.

In electromagnetic theory there can be no monopole radiation (or, put another way, no time variation of the total electric charge). This is because there can be no change in the total charge in an isolated system. In electromagnetic theory the dominant contribution to the radiated field comes from the time variation of the electric dipole moment. Consider now the gravitational case; conservation of energy (and therefore total mass) is equivalent to conservation of charge in electromagnetism. From this we know that there can be no monopole term for gravitational radiation. Einstein's 'Equivalence Prin-

ciple' states that gravitational and inertial masses are the same. This, considered with the fact that the rate of change of the gravitational dipole moments must be constant due to the laws of conservation of linear and angular momentum, precludes the possibility of gravitational dipole radiation. Thus we are led to conclude that the lowest order of gravitational radiation must be quadrupole in nature. This means that only non-axisymmetric accelerations of mass distributions will produce gravitational waves.

Gravity is the weakest of the four fundamental forces of nature. Trying to produce a source of detectable gravitational radiation in the laboratory is quite impractical. Gravitational waves are so weak that we must search for those waves produced by astronomical scale masses (of high density), moving with large accelerations to have any chance of detecting them. It is for this reason that all gravitational wave detectors will be used to search for waves of an astronomical nature.

Before describing two of the main methods employed in the detection of gravitational waves we must first understand what makes them observable. The effect of a gravitational wave is to produce a tidal strain in space. This can be understood by considering the effect a passing gravitational wave would have on a circular ring of free test particles. One period of the disturbance produced by a gravitational wave of a particular polarisation is shown in figure 1.1 where the wave is propagating in the direction normal to the plane defined by the particles. As can be seen, the ring is effectively stretched along one axis and compressed in the orthogonal axis during one half of a wave cycle and vice versa in the second half. The amplitude of the gravitational wave is equivalent to the strain, h, in space that it produces where h is defined as

$$h = \frac{2\delta L}{L} \tag{1.1}$$

with L and δL as shown in figure 1.1. In general a gravitational wave is a superposition of two linearly independent polarisations. The first, h_+, is shown in figure 1.1. The second occurs when the maximum displacement induced in the ring of test particles is rotated through 45° from that shown in figure 1.1. This polarisation is denoted $h_\times$.

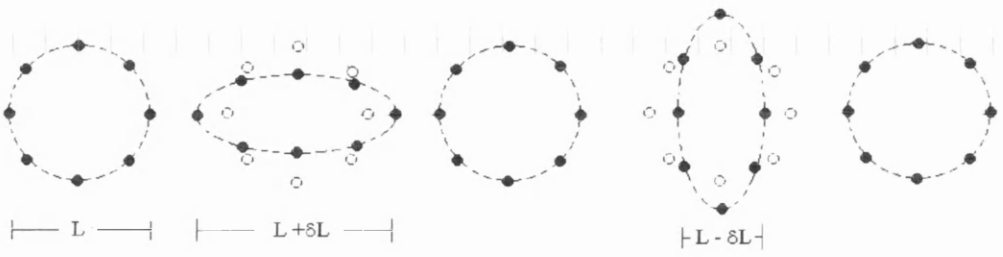

Figure 1.1: *Illustration of the effect of a gravitational wave on a ring of test particles.*

1.3 Sources of Gravitational Waves

This section contains a summary of the various sources that are expected to emit gravitational waves in the frequency range suitable for detection by ground based gravitational wave detectors. This frequency band typically ranges between a few tens of Hz (possibly a few Hz) and a few kHz.

1.3.1 Burst Sources

Burst sources emit a few cycles of gravitational radiation at a characteristic frequency or frequencies. They are typically associated with cataclysmic events in the Universe. Two such sources are considered below.

Supernovae

Supernovae, which are catastrophic stellar explosions, are among the most spectacular events to occur in the Universe. Supernovae are classified as either Type I or Type II. A Type I supernova is believed to occur in a binary system of low mass stars. Bonazzola and Marck [5] describe the two forms that a Type I supernova may take. The first can be described by the following: consider a binary system consisting of a white dwarf and a large, diffuse star. The supernova results from the detonation of the white dwarf on reaching the Chandrasekhar mass limit (where $M_{Ch} = 1.4M_{\odot} \approx 3 \times 10^{30}\,\mathrm{kg}$) [1], due to accretion from its companion. This scenario is not expected to generate a signifi-

[1] $M_{\odot}$ represents 1 solar mass

cant amount of gravitational radiation. The second scenario is more likely to produce detectable gravitational waves. If the two white dwarfs in a binary system are close together and the total mass exceeds the Chandrasekhar mass, the white dwarfs will merge. The smaller white dwarf is destroyed and forms a thick accretion disc around the more massive white dwarf. The larger white dwarf is now highly deformed due to its increased mass and angular momentum. If its mass exceeds M_{Ch}, it will collapse non-axisymmetrically with a strong emission of gravitational waves.

A Type II supernovae occurs when all of the core of a high mass star (greater than eight solar masses) has been converted to iron. The nuclear reactions in the core stop and the core starts to cool. Because the mass of the core is greater than the Chandrasekhar limit, electron degeneracy pressure can no longer support it. The stellar core suddenly collapses into a neutron star or, if the initial stellar mass is large enough, a black hole. If the collapse is non-axisymmetric a strong burst of gravitational radiation will result.

The physics of the supernovae event is complicated, thus making it difficult to estimate the strength of the gravitational wave emitted. Following the predictions of a typical rate of collapse and degree of asymmetry, Schutz [6] approximates the strain amplitude, h, that might be expected from a supernova as

$$h \approx 5 \times 10^{-22} \left(\frac{E}{10^{-3}\mathrm{M}_{\odot}\mathrm{c}^2}\right)^{\frac{1}{2}} \left(\frac{1\,\mathrm{ms}}{\tau}\right)^{\frac{1}{2}} \left(\frac{1\,\mathrm{kHz}}{f}\right) \left(\frac{15\,\mathrm{Mpc}}{r}\right) \tag{1.2}$$

where E is the total energy carried by the wave predominantly at a frequency, f, over a time scale, τ, and where r is the distance of the detector from the source.

Equation 1.2 shows that for a burst of gravitational waves of energy $10^{-3}\mathrm{M}_{\odot}\mathrm{c}^2$ ($\sim 1\%$ of the energy available [6]), emitted over a timescale of 1 ms at 1 kHz and at the distance of the Virgo cluster, a wave of amplitude $h \approx 5 \times 10^{-22}$ would reach the detector.

Coalescing Compact Binaries

Binary systems are among the most common astronomical systems and consist of two stars orbiting around their common centre of mass. Compact binary systems are a type

of binary system where the density of each of the two stars is very high (e.g. neutron star–neutron star, neutron star–black hole, black hole–black hole binaries). Compact binary systems, at a stage in their evolution close to coalescence, appear to be a promising burst source of gravitational radiation. An example of a compact binary system has already been discussed in the case of PSR 1913+16. As was previously explained, the compact binary system emits gravitational wave energy causing the orbit to decay. The two stars gradually approach each other, and the emitted radiation slowly increases in frequency. The frequency of the radiation, at twice the orbital frequency of the system, is too low for detection using ground-based techniques until the orbit has decayed so that the components are within a few stellar radii of one another. At this point the frequency of the radiation increases to one within the detection band of terrestrial detectors. In the final few seconds before the two stars coalesce, the compact binary system will emit a strong burst of gravitational radiation. The resulting quasi-sinusoidal waveform, rapidly sweeping up in amplitude and frequency, is known as a 'chirp'.

The expected signal strength for two coalescing neutron stars at a distance, r, and of mass parameter, $\mathcal{M}$, is [7]

$$h \approx 1 \times 10^{-23} \left(\frac{100\,\mathrm{Mpc}}{r}\right) \left(\frac{\mathcal{M}}{M_\odot}\right)^{\frac{5}{3}} \left(\frac{f}{200\,\mathrm{Hz}}\right)^{\frac{2}{3}} \tag{1.3}$$

where $\mathcal{M}^{\frac{5}{3}} = \mu M^{\frac{2}{3}}$, M is the total mass, $M_1 + M_2$ and μ is the reduced mass equal to $\frac{M_1 M_2}{M_1 + M_2}$.

The timescale, τ, over which the frequency changes is

$$\tau = \frac{f}{\dot{f}} \approx \left(\frac{200\,\mathrm{Hz}}{f}\right)^{\frac{8}{3}} \left(\frac{M_\odot}{\mathcal{M}}\right)^{\frac{5}{3}}. \tag{1.4}$$

Schutz [7] noted that the product of h and τ is independent of mass. If h, f and τ are measured (by a network of three detectors) and their values substituted into the product of equation 1.3 and equation 1.4, a value for r can be determined. A measure of the difference in burst arrival time at each detector can also be obtained. This will give additional information about the direction of the source. A method for determining Hubble's constant, H_0, is available if, in addition to measuring r, it is also possible to

obtain a value of the recessional velocity of the source from the optical redshift [6].

The major uncertainty about coalescing binary systems is the prediction of their event rate. An estimate of the number of these sources can be made by considering both the number of observed pulsars existing in binary systems and the estimated pulsar birth rate. This gives a coalescence event rate of 3 per year out to 300 Mpc [8]. A fraction of the total number of binary systems will contain black holes instead of neutron stars. The radiation amplitude of a black hole-neutron star coalescence would be larger than the neutron star-neutron star coalescence considered above, thus increasing the chance of detecting the event.

If detection of gravitational waves from coalescing binaries was made in conjunction with observations from γ-ray telescopes, it would be possible to establish whether γ-ray bursts were generated by such systems.

1.3.2 Continuous Sources

Continuous signals are emitted by stably rotating systems. As a result the gravitational wave signal is quasi-monochromatic. A continuous signal (if emitted in the detection band of a ground-based detector) can be located by a single detector if the output of the detector is Fourier transformed into the frequency domain (i.e. is effectively searched with a series of parallel filters) over long observation times. The achievable detector sensitivity increases as the square root of the observing time (assuming that the noise present is random). Once the frequency of the source is known the detector sensitivity can be further improved by narrow banding the data processing around the observed frequency (and, if the detector is an interferometer, making the interferometer resonant at the observed frequency – this technique, known as 'signal recycling', is discussed further in section 1.6). The signal frequency is Doppler shifted in a characteristic way due to the detector (positioned on the Earth) accelerating through space. This complication needs to be taken into account in the detection algorithm.

Ordinary binary systems, and compact binary systems at a stage in their evolution long before coalescence, produce continuous gravitational wave signals. The frequency of these signals is however too low to be observed by ground-based detectors. Much more

likely sources of detectable continuous gravitational waves are discussed below.

Pulsars

Single pulsars can radiate gravitational waves if they spin non-axisymmetrically. This may occur as a result of irregularities in the surface of the pulsar being 'frozen in' on formation. Another mechanism which can lead to a non-axisymmetrical situation and the subsequent radiation of gravitational waves, is when the pulsar is driven to precess by the accretion of angular momentum from a companion star. The degree of non-symmetry is defined in terms of the star's equatorial ellipticity, ϵ. A pulsar at a distance, r, produces gravitational waves of amplitude [9]

$$h \approx 6 \times 10^{-25} \left(\frac{f_{rot}}{500\,\mathrm{Hz}}\right)^2 \left(\frac{1\,\mathrm{kpc}}{r}\right) \left(\frac{\epsilon}{10^{-6}}\right) \tag{1.5}$$

at twice the frequency of rotation, f_{rot}.

Wagoner Stars

Wagoner described a method by which gravitational radiation can be emitted. If accretion onto a neutron star spins the star up to the Chandrasekhar-Friedman-Schutz instability point, the neutron star will become non-axisymmetric [10] and radiate any additional angular momentum away in the form of gravitational waves. Because the rate of accretion of angular momentum is proportional to the rate of accretion of mass, the gravitational wave luminosity of such a system will be proportional to its X-ray luminosity. This implies that the amplitude of the gravitational wave produced by such a system can be inferred from the X-ray flux without knowing the distance, r, to the source [6].

Recent discoveries by the Rossi X-Ray Timing Explorer [11] suggest that the gravitational wave signal strength of the X-ray source, Sco X-1, is $h \sim 2 \times 10^{-26}/\sqrt{\mathrm{Hz}}$ at 500 Hz at the surface of the Earth. Bildsten [11] reports that this source might be detected by long baseline detectors if integration times of the order of a year are used.

1.3.3 Stochastic Sources

There is a third class of potentially detectable signal – the stochastic background. The stochastic background appears as a gravitational wave signal that is both broadband in nature and ever present and is due to the superposition of signals from sources randomly distributed throughout the Universe.

One possible contribution to the stochastic background in a frequency band detectable by ground based interferometers results from primordial gravitational waves produced during or after an inflationary period immediately following the Big Bang [6]. Another possible source is cosmic string production. In string theory it is believed that random defects throughout the Universe will have reduced to linear 'strings' of enormous energy density as the Universe expands. As expansion continues, more of these strings enter from outside the horizon of observation. These strings evolve into loops which oscillate and gradually lose energy in the form of gravitational radiation [12].

The stochastic background is indistinguishable from detector noise in a single detector. Its frequency spectrum will however be identical for all detectors. By cross-correlating the outputs of two or more detectors, the stochastic background signal can be separated from random noise. Using detectors separated by reasonably large distances ensures that no other local, external influence can be mistaken as a gravitational cause of correlation. The distance of separation however should not be too large (i.e. no greater than $\frac{\lambda_{gw}}{4}$ where λ_{gw} is a typical gravitational wavelength). In this instance the two detectors cannot respond to the same 'set' of random gravitational waves at the same time. The result of this is that correlation is reduced and there follows a subsequent decrease in sensitivity.

1.4 Detection Schemes

All detection schemes employed in the detection of gravitational waves involve measuring the extremely small strains, h, produced in space by the wave. The two major types of ground based detectors that will be discussed are resonant bar detectors and laser interferometers. Ground based detectors operate in the region of a few tens of Hz to a

few kHz. These detection schemes will be discussed in section 1.4.1, 1.4.2 and section 1.6. By placing a laser interferometer into space, detection of much lower frequency signals can be achieved. The European proposal for a space-borne gravitational wave detector, LISA, is discussed briefly in section 1.7.

1.4.1 Resonant Bar Detectors

Resonant bar detectors were the first detectors to be developed and were based on the original concepts of Weber [13]. Such a detector usually consists of a massive ($\sim$ few tonnes), right circular cylinder of a material of low mechanical loss (or high quality factor, Q), typically aluminium or niobium. The passage of a gravitational wave of the correct frequency through a suitably oriented resonant bar detector will drive the fundamental longitudinal mode of the bar (at $\sim$ 1 kHz) causing small motions of its ends. This motion can then be sensed using a transducer and amplifier. The resulting signal is proportional to the induced gravitational strain.

The effects of seismic and acoustic noise sources on the resonant bar are minimised by suspending it from vibration isolation layers and placing the bar under vacuum. The sensitivity of the detector is then limited by noise in the sensors and the thermal noise of the bar itself. Reduction in the level of thermal noise is achievable by cooling the detector to cryogenic temperatures (a few kelvin or below). In addition, the bar is constructed from a material of low intrinsic loss (or high quality factor, Q). As a result, once the bar has been excited by a gravitational wave it will oscillate for a long period of time. This allows a measurement to be made over a long time interval which helps to average out the effect of sensor noise. However, this measurement is also made against a level of slowly varying thermal noise. To reduce the effect of the thermal excitation we need to shorten the measurement time interval (at the expense of an increase in sensor noise!). Clearly a compromise has to be found. With current technology this is typically set at a measurement bandwidth of $\sim \frac{1}{100}$ of the resonant frequency of the bar and leads to resonant bar detectors being intrinsically narrowband in nature.

Low temperature resonant bar detectors have been developed in Stanford, Louisana State University (ALLEGRO), Rome (NAUTILUS), CERN (EXPLORER), and Australia (NIOBE). Cryogenic versions of resonant bar detectors have achieved strain sen-

sitivites of $h \approx 6 \times 10^{-19}$ over bandwidths of a few Hz at $\sim 1\,\mathrm{kHz}$ [14, 15] at 4 K. It is believed that developments of the transducer and amplifier will improve sensitivity to a level that will allow detection of strains of $h \approx 1 \times 10^{-19}$. One proposed development is to improve the performance of the low-noise pre-amps. Another development is to increase detector bandwidth (to up to 70 Hz) and also detector sensitivity by cascading two small mechanical resonators (instead of using one as at present). The effect of this is to improve the impedance matching of the bar to the input port of the transducer.

Experimental groups in Padova (AURIGA) and the USA have developed techniques enabling the bars to be cooled further. By reducing the temperature from $\sim$4 K to ultracryogenic temperatures ($\sim$50 mK) it is expected that a strain sensitivity of the order $\sim 10^{-20}$ will ultimately be achieved [16].

It is possible to increase the sensitivity of a resonant bar detector further by increasing the mass of the detector (thus reducing the effect of thermal noise) and increasing the number of independent strain detectors present. Both of these criteria can be met by moving from a bar detector to one with a spherical configuration. A spherical detector has the advantage of being much more massive than a bar of the same resonant frequency without significantly increasing the overall size, and thus the cost of the cooling dewar. In addition a sphere has five usable quadrupole modes (as opposed to the bar's one) allowing the sphere to act as a multiple antenna when the sensors are positioned suitably. The ratio of the amplitudes of the modes can be used to determine the direction and polarisation of the passing gravitational wave. Spherical detectors have been proposed by experimental groups in the USA (TIGA) and the Netherlands (GRAIL).

An important limitation to the achievable sensitivity will be determined by the Heisenberg Uncertainty Principle [17, 18]. When a gravitational wave passes through a resonant bar detector, the resulting displacement is sensed by the unbalancing of an electrical bridge circuit and the resulting signal is amplified by an amplifier stage. The amplifier stage has electrical noise associated with it. This noise acts back through the transducer causing mechanical noise in the mass one quarter of a cycle later (i.e. this noise is associated with the momentum of the bar). With a standard, phase-insensitive method of detection, this noise causes an uncertainty in the measured displacement. It is possible to evade this 'back-action' by using a phase-sensitive method of detection. One method

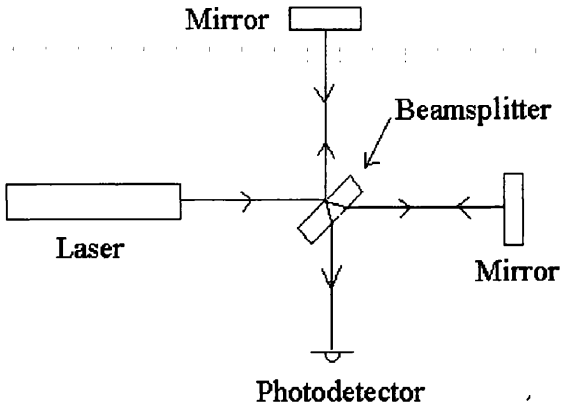

Figure 1.2: *Diagram of a simple Michelson Interferometer.*

might be to vary the amount of coupling between the amplifier and the bar. This can be achieved by modulating the drive signal on the bridge circuit and sensing the signal during one quarter of the cycle. The amplifier noise feeds back into the system during the next quarter cycle. However the coupling is reduced during this quarter of the cycle and as a result a measurement would not be made. The uncertainty in the measured displacement can therefore be reduced. This experimental technique is known as 'back-action evasion' and still requires further development before it can be successfully implemented in resonant bar detectors.

1.4.2 Laser Interferometric Gravitational Wave Detectors

The effect on a ring of test particles by the passage of a gravitational wave was shown in figure 1.1. It is easy to see that the orthogonal arms of a Michelson Interferometer might provide the ideal method for measuring the differential change in length caused by the quadrupole nature of a gravitational wave. Interferometric gravitational wave detectors were pioneered by Forward [19] and by Weiss [20]. The simplest configuration of a Michelson Interferometer is shown in figure 1.2. The interferometer is illuminated by light from a laser. The light incident on the beamsplitter is divided evenly between the two arms. The two beams traverse the lengths, L, between the beamsplitter and the end mirrors where they are reflected and returned for recombination at the beamsplitter. Changes in the resulting interference pattern due to the relative motion of the mirrors

caused by the passage of a gravitational wave are detected as changes in intensity at the output port by a photodiode. The optical components are suspended as pendulums under vacuum to isolate them from seismic and air pressure fluctuations. The use of pendulum suspensions allow interferometric gravitational wave detectors to be broadband in nature.

In more detail, the motion induced in a detector by an optimally orientated gravitational wave causes one of the interferometer arms to increase in length by δL whilst causing the orthogonal arm to decrease in length by the same amount. The result is a differential change in arm length of $2\delta L$. This motion causes a change in optical path length resulting in a relative phase shift in the interfering return beams which, in turn, causes a change in light intensity detected by the photodiode. In practice, since it can be shown that the best sensitivity of the interferometer can be achieved when the detector is operated close to a dark fringe, control electronics are used to hold the interferometer close to a minimum. The feedback signal that is required to keep the detector in this condition can be used as a measure of the relative displacement of the mirrors and hence the strain caused by the gravitational wave.

Clearly, an increase of the optical path length, $L_{optical}$, will result in a larger relative phase shift being generated for a given gravitational wave and hence will result in a more sensitive detector (provided other noise sources do not increase). The maximum sensitivity that can be achieved in an interferometer is obtained when the light is stored in the arms for half of the period of the gravitational wave. For example, this would correspond to an optical path length of $L_{optical} = \frac{\lambda_{gw}}{4} \approx 75\,\mathrm{km}$ using a typical value of $\lambda_{gw} \approx 3 \times 10^5\,\mathrm{m}$ for the gravitational wavelength. It is impractical to build an interferometer on Earth with a physical separation of the beamsplitter and end mirrors of much greater than $\sim 4\,\mathrm{km}$. It is however possible to increase the distance that the light travels by making it travel up and down the arms of the interferometer many times. There are two different methods for increasing the path length, and hence the light storage time, within the interferometer; the delay-line and the Fabry-Perot cavity. The basic principles behind these methods will now be discussed.

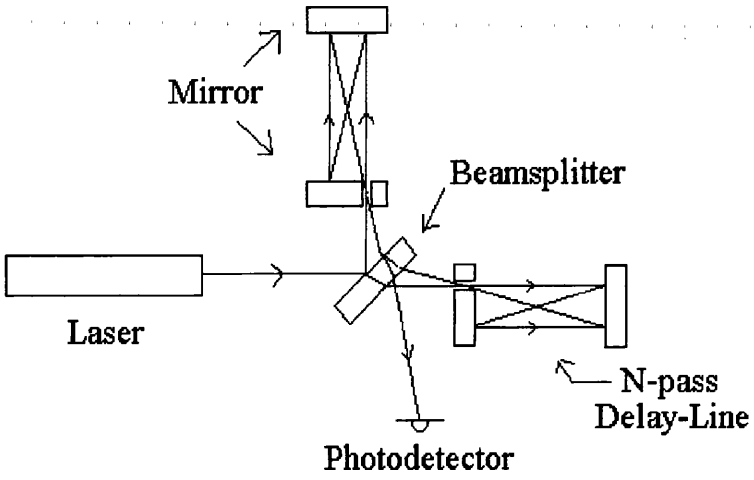

Figure 1.3: *Schematic diagram of a delay-line interferometer.*

The Delay-Line Interferometer

Delay-line detectors were first proposed by Weiss [20]. This type of detector has been developed by the group at the Max-Planck-Institut für Quantenoptik, Garching, Germany [21]. The optical path length in a delay-line interferometer is increased by the use of multiple non-overlapping beams that are reflected between two mirrors. The delay line is illuminated via a hole in a mirror placed in the interferometer arm close to the beamsplitter. In the arrangement developed at MPQ the light exits the delay-line by the same hole. A simplified schematic diagram of a delay-line interferometer can be seen in figure 1.3.

The maximum strain sensitivity achieved in a 30 m delay-line prototype interferometer at Garching was $h \approx 1 \times 10^{-19}\,\mathrm{m}/\sqrt{\mathrm{Hz}}$ above 1.5 kHz [22].

Fabry-Perot Interferometer

This method of increasing the storage time inside the interferometer was first developed at Glasgow [23]. In this example the light is injected into two Fabry-Perot cavities built into the arms of the interferometer. The light enters the cavities by partially transmitting input mirrors and in this scheme the reflecting beams lie one on top of

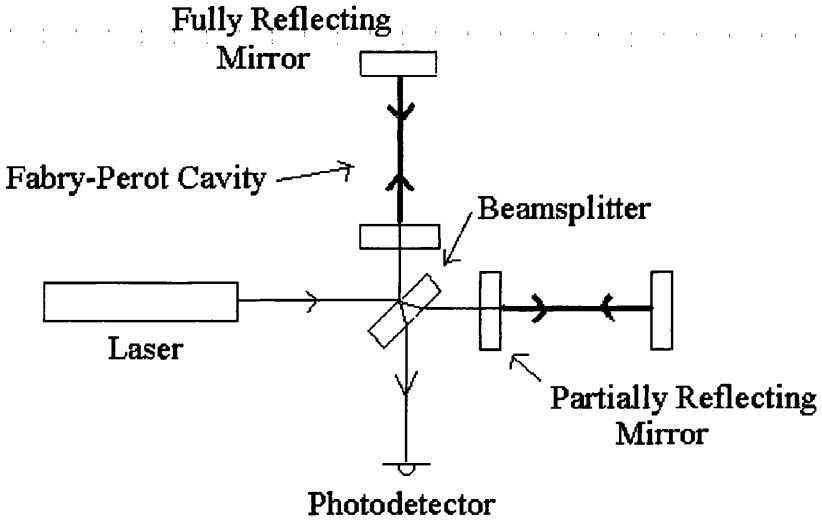

Figure 1.4: *Schematic diagram of a Faby-Perot interferometer.*

another. A schematic diagram of a Fabry-Perot interferometer can be seen in figure 1.4. In this type of interferometer, one of the Fabry-Perot cavities (the primary cavity) is held on resonance by adjusting the laser frequency using control electronics. Here it is assumed that the distances between the beamsplitter and the inboard cavity mirrors are such that there is a null output at the photodetector when both cavities are on resonance. The secondary cavity is then kept on resonance by feeding back some of the photodiode signal to an actuator at one of the mirrors. When a gravitational wave is present the wave changes the length of both of the interferometer arms. The change in length of the primary arm is compensated for (and the cavity kept on resonance) by a corresponding change in the laser wavelength. As a result of this, the change in wavelength of light used in both arms of the interferometer contains information about the change in arm length of the primary arm. The gravitational wave also changes the length of the secondary cavity by a length equal and opposite to the primary cavity. The size of signal required to keep the cavity on resonance and hence maintain the null fringe condition at the output (achieved by moving one of the mirrors in the secondary cavity) is proportional to $2\delta L$. In practice the distances between the beamsplitter and the inboard cavity mirrors has also to be controlled. A detailed description of the control electronics typically required in such a detection scheme can be found in Sigg [24].

The main disadvantage of the Fabry-Perot interferometer is the increased amount of

control electronics required to keep the cavities of the detector resonant and the output locked to a dark fringe. It does however have the advantage of requiring much smaller mirrors for operation since the multiple beams overlap one another. A further advantage of the Fabry-Perot interferometer is that the effect of scattered light within the interferometer arms is reduced [21].

The 10 m Fabry-Perot interferometer at Glasgow has reached a displacement sensitivity of $x \approx 6\times10^{-19}\,\mathrm{m}/\sqrt{\mathrm{Hz}}$, or a strain sensitivity of $h \approx 6\times10^{-20}\,/\sqrt{\mathrm{Hz}}$ at about 1 kHz [25].

1.5 Noise Sources

There are a number of noise sources present that limit the sensitivity that can be achieved by laser interferometric gravitational wave detectors.

1.5.1 Optical Readout Noise

The passage of a gravitational wave through a laser interferometer causes a change in the light power at the output port. A suitably positioned photodiode detects the gravitational wave as a change in this power. The minimum level of detectable change in light power is a fundamental limit to the sensitivity of the dectector. This is set by vacuum fluctuations [26] of the electromagnetic field which enter the interferometer through the output port. If these fluctuations in light have the correct phase to increase the amplitude of the light in one arm, they reduce the amplitude in the other – effectively causing a phase change at the photodiode. This source of noise is equivalent to that calculated by Poisson statistics when counting the number of detected photons. The vacuum fluctuations superposed on the laser light also produce a fluctuating force at the mirrors. The effect caused is radiation pressure noise.

- **Photon Counting Statistics**

  Light occurs in finite 'chunks' or *photons*. Measuring optical power is equivalent to counting the number of these photons arriving during a particular time interval, τ. The minimum detectable relative displacement in the time interval is determined by

the minimum detectable change in light power and is limited by the $\sqrt{N}$ uncertainty in counting N photons in time τ. This uncertainty gives rise to noise in the photocurrent of the photodiode – referred to as 'shot noise'. Because the output intensity is used as a measure of the gravitational wave amplitude, these statistical fluctuations in the detected signal will limit the sensitivity of the detector. In the case of a delay-line interferometer the sensitivity set by shot noise is given as [27]

$$h_{shot}(f) = \left(\frac{\pi\hbar\lambda}{\varepsilon P_{in} c}\right)^{\frac{1}{2}} \frac{f}{sin(\pi f \tau_s)} \quad /\sqrt{\text{Hz}} \tag{1.6}$$

where $\hbar$ is Planck's constant divided by 2π, λ is the wavelength of the laser light, ε is the quantum efficiency of the photodiode, P_{in} is the input power, c is the speed of light, and τ_s is the light storage time, i.e. the time that light spends in one arm of the interferometer. From equation 1.6 we can see that the effect produced by photon counting statistics can be reduced by setting the storage time equal to half of the period of the gravitational wave. The sensitivity can be improved by increasing the level of input power (it can also be shown that the sensitivity can be further improved by operating the detector close to a dark fringe).

- **Radiation Pressure Noise**

  The result of statistical fluctuations in the number of photons reflecting off the mirror surfaces causes the mirrors to recoil in a noisy manner. This is radiation pressure noise and has the effect of altering the phase difference in the recombined beam. It can be expressed as [28]

$$h_{r.p.}(f) = \frac{1}{mf^2 L}\sqrt{\frac{\hbar P_{in}}{2\pi^3 c\lambda}} \quad /\sqrt{\text{Hz}} \tag{1.7}$$

  where P_{in} is the input optical power, m is the mass of the mirror, L is the arm length, c is the speed of light and λ the laser wavelength. The level of radiation pressure noise falls off at higher frequency. Radiation pressure noise at a given frequency increases with increased P_{in} (as $P_{in}^{\frac{1}{2}}$).

The total optical noise is the quadrature sum of photon shot noise and radiation pressure noise and is known as the optical readout noise. Its spectrum is dominated by radiation pressure noise at low frequency and at high frequency by photon shot noise.

For a given gravitational wave frequency, f, there exists a minimum noise spectral density (due to the combined effects of photon shot noise and radiation pressure noise) which occurs when the input laser power is set to an optimum level, $P_{optimum}(f)$. At this optimum power we have the condition $h_{shot}(f) = h_{r.p.}(f)$ [28]. The locus of points of minimum noise is called the quantum limit. The quantum limit sets a limit to the minimum differential displacement of two masses that can be determined [29]. In interferometric detectors currently under construction the quantum limit is significantly below the other noise sources present.

It is difficult to reach the optimum laser power in a typical interferometer. At realisable laser powers the sensitivity of an interferometric detector will be limited at high frequency by the level of photon shot noise. The sensitivity set by radiation pressure noise at low frequencies is well below that of the other noise sources.

1.5.2 Thermal Noise

Thermal noise is generated by the random motion of the atoms of the test masses (or mirrors) and their suspensions, which are at some finite temperature and which have a number of resonant modes. Using the equipartition theorem we can assign a mean energy of k_BT to each mode (where k_B is Boltzmann's constant and T is the temperature in Kelvin). By designing low loss suspensions (i.e. suspensions with the energy of the modes packaged into narrow bands about their resonant frequencies) where the resonances are outside the detection band of the interferometer, we ensure that the off resonance thermal motion within the observation band is kept to a minimum. There are three main sources of thermal noise:

- **Thermal Noise Associated with the Pendulum Mode**

  The maximum thermal motion of a pendulum occurs at its resonant angular frequency, ω_0. For mirror suspensions used in interferometric detectors, ω_0 is typically around $2\pi \times 1$ rad s^{-1}. In the detection band of the interferometer, high above the resonant frequency, the spectral density of thermal motion associated with the pendulum mode is approximated to

$$\tilde{x}_{pend}(\omega) = \left(4k_BT\frac{\omega_0^2\phi_{pend_{total}}(\omega)}{m\omega^5}\right)^{\frac{1}{2}} \quad \mathrm{m}/\sqrt{\mathrm{Hz}} \qquad (1.8)$$

(refer to section 2.6) where k_B is Boltzmann's constant, T is the temperature in Kelvin, and $\phi_{pend_{total}}(\omega)$ is the mechanical loss factor associated with the pendulum mode (which will be discussed in further detail in Chapter 2).

- **Thermal Noise Associated with the Transverse (Violin) Modes of the Suspension Wires**

  The first few transverse (or *violin*) mode frequencies of the suspension wires typically occur within the detection band of the interferometer. By constructing the mirror suspensions from low loss materials, the loss associated with the violin modes is also very small. This implies that there will be several high, but narrow, peaks present within the detection band centred on these frequencies. It is likely that the wire resonances will therefore swamp any signal from a gravitational wave occurring at these frequencies. The small regions of frequency space affected by the violin modes will therefore be notched out of the data.

- **Thermal Noise Associated with the Internal Modes of the Test Masses**

  The dimensions of each test mass are chosen so that the lowest internal mode frequency is well above the upper frequency limit of the detection bandwidth (~few kHz). Most of the thermally induced motion is concentrated very close to the resonant frequencies.

  At frequencies well below the fundamental longitudinal mode the thermal motion due to the sum of the contributions from all of the significant internal modes will have a spectral density of [30]

$$\tilde{x}_{internal}(\omega) = \left[\sum_n \left(\frac{4k_BT\phi_{internal_n}(\omega)}{\alpha_n m\omega_n^2\omega}\right)\right]^{\frac{1}{2}} \quad \mathrm{m}/\sqrt{\mathrm{Hz}} \qquad (1.9)$$

  where $\phi_{internal_n}(\omega)$ is the loss associated with the internal mode (of order n) of the test mass. In this equation $\alpha_n m$ is the effective mass for each mode of the test mass, where α_n depends on the geometry of the laser beam, the mass of the mirror and the resonant frequency, ω_n.

A more comprehensive discussion of thermal noise can be found in Chapter 2. The study of thermal noise in GEO 600 and the methods employed to minimise its impact on the overall sensitivity of such a detector is the subject of this thesis.

1.5.3 Seismic Noise

There are two routes by which seismic noise can effect the mirrors.

- **Seismic Noise Introduced Through the Mirror Mounting**

  The level of seismic noise experienced by the interferometer is site dependent, and very often time-of-day dependent. At a quiet site the level of seismic motion present in the frequency range between 1 Hz and ~100 Hz is approximately $\left(\frac{10^{-7}}{f^2}\right)$ m/$\sqrt{\text{Hz}}$ in all directions at the surface of the ground [28].

  Each test mass must be isolated from the seismic motion of the ground in the range of frequencies over which the detector operates. Pendulums give attenuation of ground motion above the resonant frequency of the pendulum. A single, low loss pendulum attenuates ground motion by a factor of $\sim \left(\frac{f_0}{f}\right)^2$, where f_0 is its resonant frequency. Suspending two or more pendulums in series increases the horizontal attenuation with each additional pendulum. However the isolation provided by pendulums in the vertical direction is not as good as in the horizontal (since the vertical resonant frequency is much higher than the horizontal resonant frequency, the level of vertical isolation at a given frequency is much smaller than the horizontal isolation at the same frequency). Vertical displacement can couple into horizontal motion at some level and so additional vertical isolation must be included in the design to minimise the amount of this horizontal motion. This can be provided by incorporating cantilever springs into the final suspension design [31].

  Additional isolation is provided by suspending the double pendulum from a series of vibration isolation stacks – alternate layers of rubber and steel. Isolation stacks provide isolation in the vertical, horizontal and tilt directions by attenuating the seismic motion above the corresponding resonant frequencies of the stacks. In addition, since the rubber is of intrinsically high loss, the stack does not significantly amplify the seismic motion at its resonant frequencies.

- **Direct Coupling of Seismic Noise (or Gravity Gradient Noise)**

  The test mass can also couple with seismic motion directly through local fluctuations in the gravitational field (due to matter moving in the vicinity of the detector) [32, 33]. Vibration isolation systems have no effect on this noise source as gravity gradient noise effectively 'short circuits' the stacks and pendulums. The noise spectrum resulting from gravity gradient noise is too low to limit the sensitivity of the initial long base-line detectors. However as seismic isolation designs improve and other noise sources are reduced, gravity gradient noise may ultimately determine the achievable sensitivity of a detector at low frequency.

1.5.4 Displacement Noise Sources

Radiation pressure noise, thermal noise and seismic noise are all examples of displacement noise. Displacement noise sources cause noise in the form of mirror motion and therefore limit the displacement sensitivity that the detector can achieve. This form of noise is one of the main reasons against employing detectors with short baselines and aggressive beam folding. However the effect of displacement noise can be reduced by increasing the physical separation of the mirrors. This is one of the principal driving forces behind the building of detectors with long arm lengths. Consideration of levels of displacement noise likely to be present in a detector suggests that it is necessary to move to arm lengths of the order of a km to achieve the desired strain sensitivity of 10^{-21} to 10^{-22}.

1.5.5 Other Noise Sources

The main sources of noise have been discussed above. However there are a number of other noise sources which must be considered and controlled to reduce their effects to levels which are negligible.

Several of these are associated with the laser. They include frequency fluctuations of the laser light (caused by scattering) which introduces noise into the detector. These fluctuations can be stabilised by locking the laser frequency to one of the arms of the detectors. The effect of intensity fluctuations of the laser are reduced by modulation techniques (which ensures that the change in intensity to be detected is at a frequency

that is shot noise limited) and operating the detector at a dark fringe. Variation of laser beam position, orientation and geometry are also important. These variations can be minimised by using a mode cleaning device such as a single mode optical fibre or a mode cleaning cavity.

Fluctuations in the residual gas pressure of the vacuum system can lead to changes in the optical path length of the detector. This effect can be reduced by operating the detector at vacuum pressures of $\sim 10^{-8}$ mbar or less. Control systems are used to damp the various modes of the suspension systems. Care must also be taken so that electronic noise in these systems does not in itself cause significant motion of the masses.

1.6 The German-British project, GEO 600

There are a number of long baseline interferometric detectors currently under construction around the world. Scientists working on the LIGO [34] project in the USA are constructing two 4 km detectors at sites in Washington State and Louisiana. A French-Italian collaborative group, VIRGO [35], is building a 3 km detector near Pisa in Italy. TAMA, the Japanese 300 m detector project, is being built near Tokyo in Japan [36].

The German-British project is called GEO 600 [1] and it is a project being undertaken by groups from the Max-Planck-Institut für Quantenoptik at Hannover and Garching, the University of Glasgow, the University of Cardiff and the Albert Einstein Institut at Potsdam, together with contributions from the Laser-Zentrum, Hannover. This project is advancing rapidly at a site near Hannover, Germany.

GEO 600 is an interferometer with a four-bounce delay-line in each 600 m arm. The input laser power (of between 5 and 10 W) will be provided by a stabilised diode-pumped Nd:YAG laser. Before the light is sent into the interferometer it is passed through two modecleaners [37] to reduce the beam orientation and geometry noise. The mirrors within the mode-cleaner cavities are suspended to isolate them from the effects of ground vibrations. After passing through the modecleaners, the laser light is sent into the interferometer. To reduce random phase shifts of the light in the optical path due to fluctuations in gas density, the path lengths are entirely enclosed inside vacuum systems.

The suspension system for each test mass is likely to consist of a vibration isolation stack plus a triple pendulum, incorporating 2 layers of cantilever springs for extra vertical isolation. The additional vertical isolation is required to reduce the amount of cross-coupling that can occur. This is due to the mirrors used for the second and fourth bounces being positioned one above the other (and results in the laser beam making a small angle with the horizontal) allowing the sensing of a small amount of vertical motion. The whole suspension system is entirely closed within a vacuum system.

To ensure that the sensitivity of GEO 600 is competitive with that of 1^{st} stage LIGO and VIRGO detectors, the limitiations set by the shorter arm-length of GEO 600 must be compensated for from the outset. The advanced optical techniques employed include high factor power recycling and signal recycling. Firstly we shall consider power recycling. When the interferometer is locked to a dark fringe all of the recombined light at the beamsplitter is returned to the laser. To prevent this light from being lost, a mirror (the recycling mirror) is positioned between the laser and beamsplitter to form a resonant cavity between the mirror and the interferometer [38]. The optical power circulating in the interferometer is therefore increased and the effect is equivalent to using a more powerful laser [2]. This increases the phase sensitivity of the system. A power recycling factor of ~ 2000 will be employed in GEO 600 in comparison to a factor of ~ 30 in LIGO.

The passage of a gravitational wave through a suitably orientated detector phase modulates the carrier frequency of the laser light. This has the effect of encoding the gravitational signal in sidebands around the laser frequency. When the detector is locked to a dark fringe, the carrier frequency is returned towards the laser whilst the sidebands are emitted at the output of the interferometer. By suitable positioning of a partially transmitting mirror between the beamsplitter and the photodiode a cavity (referred to as the signal recycling cavity) can be formed for one of the sideband frequencies between this mirror and the two arms. This allows the sideband frequency to be returned to the interferometer and the technique is known as signal recycling [39]. This technique has the effect of resonant enhancement of the signal of a particular frequency thus improving the shot noise limited sensitivity in narrow bandwidth operation.

To minimise the effect of thermal noise in the frequency band of interest, synthetic fused

[2]This technique only works for mirrors of low optical loss.

silica (which exhibits particularly low levels of intrinsic loss) will be used as the mirror material. Because of its low loss we have developed suspension fibres made of fused quartz [3] to suspend the mirrors. This is an approach to test mass suspension which has not been proposed by the other major interferometer projects (all of 1^{st} stage detectors associated with the other projects intend to use steel wires). Methods of bonding the fused quartz fibres to the mirrors that do not degrade the obtainable levels of internal thermal noise have also had to be developed for use in GEO 600. The characterisation of fused quartz as a suitable low-loss suspension material and aspects of the design of the test mass suspension is the subject of this thesis.

The sensitivity curve of GEO 600 is shown in figure 1.5. The blue curve is the photon shot noise calculated for a four-beam delay-line (illuminated by 5 W of laser light (1.06 μm) and assumes a factor of 2000 in power recycling). The green curve is the total thermal noise (calculated for a 16 kg fused silica test mass, 25 cm in diameter, 15 cm long, and assuming an intrinsic loss $\phi_{internal}(\omega) = 2 \times 10^{-7}$ and structural damping). The red curve represents the seismic noise (the design specification at 50 Hz is to achieve a level of residual seismic noise at each test mass that is a factor of 10 lower than the thermal noise associated with the internal modes at 50 Hz) after filtering by the suspensions and the black curve is the total noise.

1.7 Space-Borne Detectors

LISA (Laser Inteferometric Space Antenna) [40] has been proposed as a cornerstone mission in the Post Horizon 2000 programme in ESA and is a space-borne Michelson Interferometer that should be able to observe gravitational waves occurring in the 0.1 mHz to 0.1 Hz frequency range. Gravitational waves emitted in this frequency band are undetectable by ground-based detectors due to gravity gradient noise. Typical sources of gravitational waves emitted in this frequency band range from stellar-mass binary systems with relativaly large separations, to interactions of massive black holes. LISA will consist of three identical spacecraft positioned in a heliocentric orbit 20° behind the Earth, with each spacecraft forming a vertex of an equilateral triangle. Each spacecraft

[3] The term fused quartz is used to refer specifically to SiO_2 produced from natural sources and fused silica used when either fused quartz or synthetic fused silica would be appropriate.

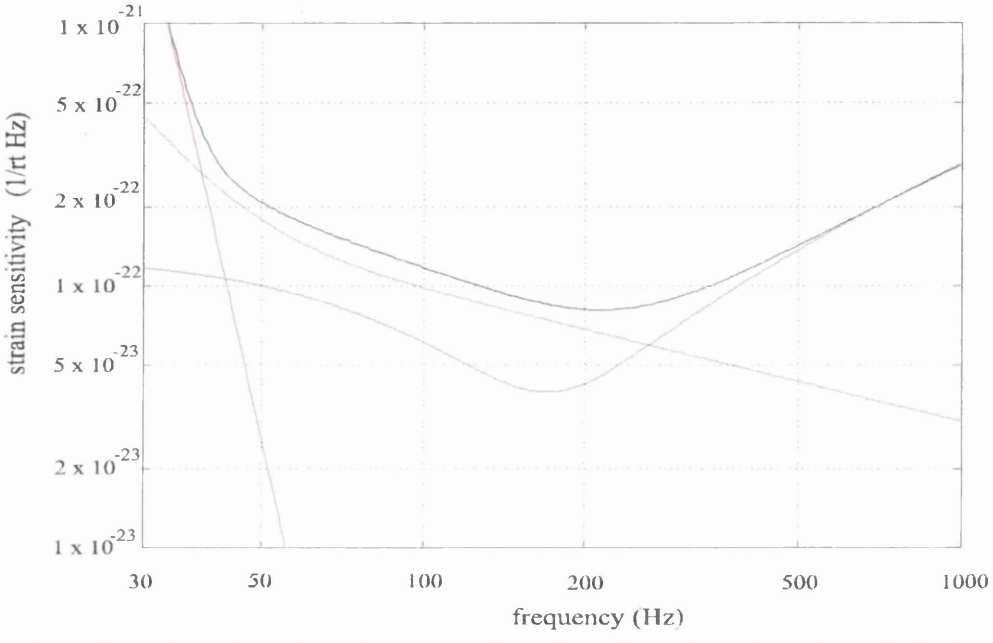

Figure 1.5: *The sensitivity curve of GEO 600. The blue curve is the photon shot noise calculated for a four-beam delay-line (illuminated by 5 W of laser light (1.06 μm) and assumes a factor of 2000 in power recycling). The green curve is the total thermal noise (calculated for a 16 kg fused silica test mass, 25 cm in diameter, 15 cm long, and assuming an intrinsic loss* $\phi_{internal}(\omega) = 2 \times 10^{-7}$ *and structural damping). The red curve represents the residual seismic noise (the design specification at 50 Hz is to achieve a level of seismic noise at each test mass that is a factor of 10 lower than the thermal noise associated with the internal modes at 50 Hz) after filtering from the suspensions and the black curve is the total noise. The data point on the plot represents the relative source strength of the Crab pulsar.*

in LISA will be separated from its neighbour by a distance of 5×10^9 m. Each spacecraft contains two test masses and two laser transponders (Nd:YAG) allowing the sides of the triangle to form two semi-independent interferometers. A gravitational wave strain sensitivity of $h \sim 10^{-21}$ $/\sqrt{\text{Hz}}$ is expected to be achieved. The proposed date of launch of a cornerstone mission is likely to be post 2015. However a joint ESA/NASA mission could be launched earlier.

Space-borne detectors will be complementary to ground-based detectors extending the frequency coverage over which observations of gravitational waves can be made.

1.8 Conclusions

The long baseline interferometric detectors such as GEO 600 and the 1^{st} stage LIGO, VIRGO and TAMA detectors are all currently under construction with aimed design sensitivities of $\sim 10^{-21}$ to $\sim 10^{-22}/\sqrt{\text{Hz}}$ over some of the detection band (between a few tens of Hz and a few kHz). It is intended that GEO 600 will be operational within the next three years when it will be possible to use this detector to perform searches for continuous sources such as pulsars. GEO 600 will also be used as one in a worldwide array of three or four detectors. This will allow coincidence observations of burst sources to be made. By comparing the arrival time of gravitational wave signals at the detectors in such an array, the position of a source will be determined. Space-borne detectors will complement observations made by ground-based detectors by increasing the frequency band over which searches for gravitational waves can be made.

Chapter 2

An Introduction to Thermal Noise

2.1 Introduction

A mirror, suspended as a pendulum by wires or fibres is a mechanical system which has many normal modes of oscillation. In accordance with the Equipartition Theorem, each normal mode of the suspension has a mean energy of k_BT Joules associated with it (where k_B is Boltzmann's constant and T is the temperature in Kelvin). This energy appears as thermally driven motion of the system. The combined effect of the thermal noise from all of the modes of the suspension means that thermally induced motion of the test mass and it's suspension fibres is a serious form of displacement noise in interferometric gravitational wave detectors; the rms displacement caused by thermal noise at the resonant frequencies of the last stage of the pendulum suspension system is much larger than that which might be expected by the passage of a gravitational wave. One might suggest that the effects of thermal noise could be reduced significantly by cooling the suspension in a manner similar to that used in resonant mass detectors. While this may be feasible for the next generation of advanced interferometric gravitational wave detectors, current detectors will not employ cooling. Because of this, the effect of thermal noise at frequencies of interest for gravitational wave detection must be reduced by other methods.

2.2 An Early Example of Thermal Noise

In his classic experiment of 1828, Brown [41] observed the random motion of pollen grains suspended in water. Many years later Einstein showed that this random motion resulted from fluctuations in the number of impacts of the water molecules with the pollen grains [42]. In doing so Einstein recognised that these impacts caused the grains to dissipate kinetic energy as they moved through the water. This was the first recognised relationship between fluctuation (which, in this instance, excites the system on a microscopic scale i.e. the random displacement of the pollen grains) and friction (which dissipates energy in this instance on a macroscopic scale i.e. the viscosity of water).

A general relationship between fluctuation and dissipation was established by Callen et. al. [43, 44] for any system that is linear and in thermal equilibrium. This is the fluctuation-dissipation theorem and is a useful tool in the study of thermal noise.

2.3 Fluctuation-Dissipation Theorem

The fluctuation-dissipation theorem relates the power spectral density of the fluctuating thermal driving force, $\tilde{F}^2_{therm}(\omega)$, of a mechanical system to the real (dissipative) part of the mechanical impedance, $\Re(Z(\omega))$, i.e:

$$\tilde{F}^2_{therm}(\omega) = 4k_B T \Re(Z(\omega)) \quad \text{per Hz} \tag{2.1}$$

The mechanical impedance is defined as $Z = \frac{F}{v}$ where v is the velocity response of the system resulting from an applied force, F.

The fluctuation-dissipation theorem is of importance because it lets us predict the effect on the thermal noise of manipulating the real part of the impedance (ie. the dissipation or damping).

The fluctuation-dissipation theorem can be rearranged and expressed in a more useful form. This is achieved by substituting the expression for the fluctuating driving force into

$$F^2 = Z^2 v^2 \tag{2.2}$$

and rearranging into the form of $\tilde{x}^2_{therm}(\omega)$ (the power spectral density of thermal displacement) to give

$$\tilde{x}^2_{therm}(\omega) = \frac{4k_B T}{\omega^2}\Re(Y(\omega)) \quad \text{per Hz} \tag{2.3}$$

where $Y(\omega)$ is mechanical admittance (and $Y(\omega) = \frac{1}{Z(\omega)}$).

2.4 Forms of External and Internal Damping

In a real suspension system there are many sources of dissipation present that can increase the level of thermal noise within the system. Some of the most significant are introduced below.

2.4.1 External Damping Mechanisms

- external viscous damping in the form of friction from residual gas molecules. This form of damping will be discussed in Chapter 3.
- The loss of energy from the pendulum suspension into a recoiling support structure (known as 'recoil damping'). A discussion of recoil damping can be found in Chapter 4.
- Energy loss due to eddy current and hysteresis damping. Whether either of these losses are present and to what extent they affect the pendulum loss depends on the materials used for the pendulum suspension and the proximity of naturally occurring magnetic fields or of magnets and feedback coils within the system. A discussion of these forms of damping can be found in Chapter 5.
- Frictional losses at the point of suspension and where the wires meet the test mass. Experimental evidence of the first of these losses (known as 'stick-slip' damping [45]) and how it was reduced is reported in Chapter 5.

- Finally, an unusual form of loss experienced in the course of this work – the effect caused by unexpected electrostatic charging of the pendulum. This will be discussed in Chapter 6.

With careful design, these forms of damping can usually be reduced to negligible levels.

2.4.2 Internal Damping

Let us assume for the moment that all sources of external damping have been reduced to levels where their contributions are no longer the dominant sources of loss. In this situation the largest source of thermal motion in the test mass suspension is internal friction in the material of the test mass and its suspension wires.

When a body is acted upon by some external force the material responds. The response is not instantaneous. Instead each of the affected degrees of freedom in the body relaxes into a new state of equilibrium after a time interval known as the 'relaxation time'. Causes of these lags in response include moving defects, shifting grain boundaries, thermal currents and other internal variables. The combined effect of these individual lags represents internal damping. The level of this damping can then be used to predict (by using the fluctuation-dissipation theorem) the level of thermal noise that will be generated in a pendulum hanging inside a gravitational wave detector at a given temperature.

Any resonant mode of a pendulum suspension e.g. internal mode of the test mass, pendulum mode or violin mode of the suspension wire, can be modelled as a damped harmonic oscillator represented by a mass, m, on a spring of constant, k. The combined effects of dissipation from internal friction can be included in this model by introducing a small imaginary term into the spring constant. The force associated with the spring is therefore of the form

$$F_{spring}(\omega) = -k\,(1 + i\phi(\omega))\,x. \tag{2.4}$$

The imaginary term, $\phi(\omega)$, is the loss angle (or loss factor) and represents the phase lag (in radians) of the response of the system, x, to the applied force, $F_{spring}(\omega)$. This

departure from the ideal case of elasticity is known as anelasticity [46].

The equation of motion of a harmonic oscillator subject to internal friction is

$$F(\omega) = m\ddot{x} + k\left(1 + i\phi(\omega)\right)x \tag{2.5}$$

where $F(\omega)$ is the internal thermal driving force.

We can obtain from the equation of motion, an expression for the motion induced in the oscillator due to the combined effects of internal friction. First, the equation of motion must be expressed in terms of velocity (using $\ddot{x} = i\omega v$ and $x = \frac{v}{i\omega}$) to give

$$F(\omega) = i\omega m v - i\frac{k}{\omega}\left(1 + i\phi(\omega)\right)v. \tag{2.6}$$

The fluctuating force, $F(\omega)$, is divided by velocity, v, to give the impedance, $Z(\omega)$, as

$$Z(\omega) = i\left(\omega m - \frac{k}{\omega}\right) + \phi(\omega)\frac{k}{\omega}. \tag{2.7}$$

The admittance is then obtained from the impedance,

$$Y(\omega) = \frac{\frac{k}{\omega}\phi(\omega) - i\left(\omega m - \frac{k}{\omega}\right)}{\left(\frac{k}{\omega}\phi(\omega)\right)^2 + \left(\omega m - \frac{k}{\omega}\right)^2}. \tag{2.8}$$

Finally, this is substituted into the fluctuation-dissipation theorem (in the form of equation 2.3) to give the power spectrum of thermal motion

$$\begin{aligned} \tilde{x}^2_{therm}(\omega) &= \frac{4k_BT}{\omega^2}\Re(Y(\omega)) \quad \text{per Hz} \\ &= \frac{4k_BT}{\omega^2}\frac{\phi(\omega)\frac{k}{\omega}}{\left(\frac{k}{\omega}\phi(\omega)\right)^2 + \left(\omega m - \frac{k}{\omega}\right)^2} \quad \text{per Hz} \end{aligned} \tag{2.9}$$

which, on substitution of $\omega_0^2 = \frac{k}{m}$ and suitable cancellation of terms reduces to

$$\tilde{x}^2_{therm}(\omega) = \frac{4k_B T\phi(\omega)\omega_0^2}{m\omega\left(\omega_0^4\phi^2(\omega) + (\omega_0^2 - \omega^2)^2\right)} \text{ per Hz.} \qquad (2.10)$$

2.4.3 Form of the Internal Loss Factor, $\phi(\omega)$

The internal loss factor may take one of many forms. One form of the loss factor is $\phi(\omega)$ proportional to frequency, f, in the form $\phi(\omega) = 2\pi\beta f$ (where β is a constant). It can be shown that when $\phi(\omega) = 2\pi\beta f$, the imaginary (or internal damping term) in equation 2.4 reduces to $F_{friction} = -bv$ (on substitution of $x = \frac{v}{i2\pi f}$ and $b = k\beta$). A loss factor of this form is described as a source of 'internal viscous damping'.

There is evidence to suggest that damping proportional to velocity is not the most common form of internal damping in materials. Experiments [47] have shown that a loss factor that is approximately constant with frequency is more realistic. A loss factor independent of frequency is known as 'structural damping'. Understanding the origin of a constant loss factor is however more complex. It is thought that the loss factor, $\phi(\omega)$, contains a number of distinct 'peaks'. These peaks occur at the 'characteristic frequencies' of the many contributing loss processes that happen simultaneously within the material. These peaks, known as 'Debye peaks', are usually separated in frequency by many orders of magnitude. In regions of frequency space away from the peaks of the individual loss mechanisms, the combined effect of the tails of the peaks is effectively constant with frequency [48]. The detection band of ground based interferometers usually lies within one such frequency region.

However there does exist one mechanism of internal friction which may exhibit a peak close to the detection band. In this instance the loss factor departs from the general case of structural damping. This source of loss is called thermoelastic damping and will be discussed in more detail in section 2.7.

Clearly the shape of the power spectrum for thermal displacement varies depending on which of the functional forms of loss factor is present within the suspension. The form of the loss factor must be determined if correct predictions of the limit set to the detector sensitivity by thermal noise are to be calculated. For the pendulum suspensions used in interferometric gravitational wave detectors the loss factors are very small and

it is therefore extremely difficult to measure $\phi(\omega)$ directly at all frequencies. The loss factor, $\phi(\omega)$, can however be measured at the resonant frequencies of the suspension (as is explained in section 2.5). Should a number of modes of a given type be measurable (e.g. vibrational modes of the suspension fibres or internal modes of the test mass), information can be gained on the form of $\phi(\omega)$.

It is useful to note that French [49] defines the quality factor, Q, of a resonant system in terms of the damping coefficient, b, and mass, m, as

$$Q(\omega_0) = \frac{m\omega_0}{b}. \tag{2.11}$$

The damping present within the suspension system is given by the real part of the mechanical impedance. Referring to equation 2.7 we can see that this is $\phi(\omega)\frac{k}{\omega}$ which is equivalent to the damping coefficient, b, in equation 2.11 (where b is a constant in the case of velocity damping but a function of frequency for structural damping). Substituting for b (at $\omega = \omega_0$) into equation 2.11 leads to a relationship between $Q(\omega_0)$ and $\phi(\omega_0)$ of

$$Q(\omega_0) = \frac{1}{\phi(\omega_0)}. \tag{2.12}$$

2.5 Measuring the Loss Factor of a Damped Harmonic Oscillator at the Resonant Frequency of one of its Modes, $\phi(\omega_0)$

The fluctuation-dissipation theorem allows all sources of thermal noise to be treated in a similar manner. If there are a number of different sources of dissipation present within a system (external as well as internal), they can all be considered by including their combined effects in an overall expression of the impedance of the system as a function of frequency. Effectively the total dissipation in a given system, at a frequency ω, is the sum of all of the individual loss angles i.e.

$$\phi_{total}(\omega) = \phi_1(\omega) + \phi_2(\omega) + \phi_3(\omega) + ... + \phi_n(\omega). \quad (2.13)$$

By measuring the 'total' loss factor exhibited by the suspension at an angular frequency, ω_0, (the resonant frequency of one of its modes) and knowing the functional form of the internal loss mechanism, the level of the loss factor at a frequency ω can be determined. This loss factor can be substituted with the relevant parameters of the test mass into the fluctuation-dissipation theorem to predict the level of thermal noise (at a frequency ω) present within our suspension. This section contains a discussion of one method of measuring the loss factor.

In our experiments we first excite a normal mode by some means. The mode is then allowed to decay freely subject to the losses present in the system. The displacement of the mode can be represented by

$$x(t) = x_0 e^{-\frac{1}{2}\phi_{total}(\omega_0)\omega_0 t} e^{i\omega_0 t} \quad (2.14)$$

where $x(t)$ is the amplitude at time, t, x_0 is the initial amplitude, ω_0 is the resonant angular frequency of the mode and $\phi_{total}(\omega_0)$ is the combined effects of the loss mechanisms present. We can determine the loss by measuring the amplitude decay envelope of the free oscillation as a function of time.

Consider the amplitude decay term of equation 2.14

$$A(t) = x_0 e^{-\frac{1}{2}\phi_{total}(\omega_0)\omega_0 t} \quad (2.15)$$

rearranging this we find

$$\phi_{total}(\omega_0) = \frac{2ln\left(\frac{x_0}{A(t)}\right)}{\omega_0 t}. \quad (2.16)$$

If one measures the relaxation time, τ, taken for the amplitude to decay to $A(t) = \frac{x_0}{e}$, equation 2.16 reduces to

$$\phi_{total}(\omega_0) = \frac{2}{\omega_0 \tau} \tag{2.17}$$

which is recognisable as being equal to the reciprocal of a commonly used definition of the quality factor, $Q(\omega_0)$ (Refer to French [49]). Once again we see that $\phi(\omega_0) = \frac{1}{Q(\omega_0)}$.

In terms of the parameters $A(t)$ and t measured in our experiment, it is more useful to express equation 2.16 in the following way;

$$ln(A(t)) = -\frac{\phi_{total}(\omega_0)\omega_0}{2}t + ln(x_0) \tag{2.18}$$

which has the form of a straight line when the natural logarithm of the amplitude, $A(t)$, is plotted with respect to t. By calculating the gradient of the resulting plot and multiplying it by $-\frac{2}{\omega_0}$, it is possible to obtain a value for the loss factor at the resonant frequency.

Once again let us assume that all external loss mechanisms have been minimised and that internal friction is the dominant loss mechanism present. Measurement of the internal loss factor at the resonant frequency tells us nothing about the frequency dependence of the internal loss angle. However, as was discussed in section 2.4.3, it is usually possible to infer the functional form of the loss, $\phi(\omega)$, by measuring higher order modes of the system. Measurements of the loss factor associated with the internal modes of fused silica test masses have been performed by Gillespie [30], Braginsky [50] and Traeger [51] over a range of frequencies in the tens of kHz region. The measured loss factor of fused quartz will be taken to be $\sim 2 \times 10^{-7}$ and results have suggested that the material exhibits structural damping. These results show that the loss was a measure of internal friction, i.e. the 'intrinsic' loss factor set by the material itself and cannot be improved upon. The level of thermal motion within the detection band resulting from this level of intrinsic loss is discussed in the following section. A further example of this type of measurement is discussed in Chapter 3. There a report is given of experiments performed to measure the intrinsic material loss factor of an oscillating ribbon fibre at four frequencies in the detection band of interest.

A point to note about the description given above for calculating the loss factor is that

it assumes that the oscillator decays to a negligible amplitude. This however is not always the case. In the example of measurements made in Chapter 3, the amplitude tends to some background value, A_B, significantly greater than zero. Calculating the loss factor by the simple method above would result in a loss that is less than the real loss. A correction factor must be included in these instances. It is relatively straight forward to prove that a better estimate of the loss factor can be calculated from a plot of $ln\sqrt{A(t)^2 - A_B^2}$ versus time, t, instead of simply $lnA(t)$ versus t. The gradient is then calculated a$A(t)^2 - A_B^2$ versus time, t, btain the loss factor on resonance, $\phi(\omega_0)$.
ted and multiplied by $-\frac{2}{\omega_0}$

2.6 Comments on the Fluctuation-Dissipation Theorem

Consider again the general expression for the power spectral density of thermal motion of one of the modes of our suspension, $\tilde{x}^2_{therm}(\omega)$, in terms of internal dissipation as given in equation 2.10. The level of thermal motion, $\tilde{x}_{therm}(\omega)$, can be altered by changing the level of internal damping, $\phi(\omega)$, present in the suspension.

This statement however appears to be at odds with the Equipartition Theorem which states that every velocity component in a system has associated with it an average of $\frac{1}{2}k_BT$ of energy. For example, in a 1 dimensional oscillator, the Equipartition Theorem requires that

$$\frac{1}{2}m\overline{v^2} = \frac{1}{2}k_BT \tag{2.19}$$

which can be rearranged to give

$$\overline{x^2} = \frac{k_BT}{m\omega_0^2} \tag{2.20}$$

which is independent of loss, $\phi(\omega)$. The fluctuation - dissipation theorem and the Equipartition Theorem however do not disagree, they just give us different information. The Equipartition Theorem refers to the mean square thermal displacement calculated over all frequencies. This is equal to the square of the thermal motion calculated at each frequency by the fluctuation - dissipation theorem then summed over all frequencies.

Knowing that there is a 'total' mean squared displacement (given by the Equipartition Theorem) allows us to refine our understanding of the information obtained from the fluctuation-dissipation theorem. Let us examine the power spectral density of displacement in three distinct regions of frequency as given by the fluctuation-dissipation theorem. Refer to equation 2.10 and consider first the case when $\omega \ll \omega_0$:

$$\begin{aligned} \tilde{x}^2_{therm}(\omega) &\approx \frac{4k_B T\phi(\omega)\omega_0^2}{m\omega(\omega_0^4\phi^2(\omega)+\omega_0^4)} \text{ per Hz} \\ &\approx \frac{4k_B T\phi(\omega)}{m\omega\omega_0^2(\phi^2(\omega)+1)} \text{ per Hz} \end{aligned} \tag{2.21}$$

and assuming $\phi(\omega)^2 \ll 1$ then

$$\tilde{x}^2_{therm}(\omega) \approx \frac{4k_B T}{m\omega_0^2}\left(\frac{\phi(\omega)}{\omega}\right) \text{ per Hz.} \tag{2.22}$$

Consider also $\omega \gg \omega_0$

$$\tilde{x}^2_{therm}(\omega) \approx \frac{4k_B T\omega_0^2\phi(\omega)}{m\omega\left((\omega^2)^2+\omega_0^4\phi^2\right)} \text{ per Hz} \tag{2.23}$$

and once again, assuming that $\phi(\omega)^2 \ll 1$

$$\tilde{x}^2_{therm}(\omega) \approx \frac{4k_B T\omega_0^2}{m}\left(\frac{\phi(\omega)}{\omega^5}\right) \text{ per Hz.} \tag{2.24}$$

Examining equation 2.22 and equation 2.24 we see that it is possible to minimise the levels of thermal motion at frequencies away from the resonances of the suspension system by designing the suspension to have very low levels of mechanical loss ($\phi(\omega) \ll 1$). However, to conserve the 'total' squared displacement over all frequencies (as given by the Equipartition Theorem) there must be a correspondingly high response at the resonant frequency, namely

$$\tilde{x}^2_{therm}(\omega_0) = \frac{4k_B T\phi(\omega_0)\omega_0^2}{m\omega_0\omega_0^4\phi^2(\omega_0)} \text{ per Hz}$$

$$= \frac{4k_BT}{m\omega_0^3}\left(\frac{1}{\phi(\omega_0)}\right) \quad \text{per Hz} \tag{2.25}$$

which results in a very large $\tilde{x}^2_{therm}(\omega_0)$ if $\phi(\omega) \ll 1$!

It was discussed in section 2.5 that the loss factor associated with the internal modes of a fused silica mass is believed to be the intrinsic loss factor of the material (i.e. $\phi_{intrinsic}(\omega) = 2 \times 10^{-7}$) and that it is structurally damped. The thermal noise contribution from one internal mode can be calculated at frequencies within the detection band, well below the resonant frequency, by using equation 2.22. This equation can be generalised to include all of the relevant internal modes as

$$\tilde{x}^2_{internal}(\omega) = \left[\sum_n \left(\frac{4k_BT\phi_{internal_n}(\omega)}{\alpha_n m\omega_n^2\omega}\right)\right] \tag{2.26}$$

where $\phi_{internal_n}(\omega)$ is the loss factor associated with the n^{th} order internal mode and $\alpha_n m$ is the effective mass of the same mode (α_n is an empirical factor that characterises the coupling between the internal mode and the optical mode and depends on the size of the laser beam, the mass of the mirror and the resonant frequency, ω_n). The GEO 600 thermal noise specification at 50 Hz is set by the thermal noise contribution from the combined effect of the internal modes and corresponds to a rms thermal displacement of $\tilde{x}_{internal}(\omega) = 7 \times 10^{-20}\,\mathrm{m}/\sqrt{\mathrm{Hz}}$ [52].

The test mass is suspended as a pendulum to attenuate seismic noise in the detection band of the interferometer. This is achieved by choosing the length of the suspension wire so that the resonant frequency of the pendulum mode is below the low frequency end of the detection band. The pendulum mode also has thermal noise associated with it. However we can construct pendulums in such a manner that the thermal noise associated with the pendulum mode does not contribute significantly to the overall level of thermal noise in the frequency band of interest (the specification for the thermal noise associated with the pendulum mode at 50 Hz is discussed in section 2.8). This is achieved in two ways. Firstly, the low resonant frequency of the pendulum mode ensures that the maximum thermal displacement occurs at a frequency outwith the detection band of the interferometer. At 50 Hz the thermal displacement will have reached a level predicted by equation 2.24 (with the loss factor associated with the pendulum mode, $\phi_{pend_{total}}(\omega)$,

substituted for $\phi(\omega)$). Secondly, the pendulum mode has associated with it a loss factor that is significantly below the intrinsic loss of the material of the suspension wires or fibres.

The reason for this decrease in loss factor is as follows. Consider a simple pendulum of mass, m, suspension wire/fibre length, l, hanging from a rigid support structure. Assume also that all external damping mechanisms are negligible. The test mass hangs in equilibrium at a position where the weight of the test mass is balanced by the elastic restoring force of the wire (related to the wire stiffness).

Consider what happens when the pendulum is pushed to one side. Two restoring forces act on the pendulum – that provided by the transverse elasticity of the tensioned wire, and gravity. The wire bends in a small region at the top and providing the wire is thin, the gravitational restoring force plays the dominant part. Gravity provides a 'spring constant' of $k_{grav} = \frac{mg}{l}$ and is lossless. The only loss of energy from the pendulum is due to the small dissipative fraction of the transverse elastic spring constant of the suspension wires, which is itself only a very small fraction of the total effective spring constant. We can derive an expression for the loss factor of the pendulum mode in terms of the loss associated with wire bending using the proof below.

2.6.1 An Advantage of Employing a Pendulum Suspension

First, consider an alternative definition of loss [49],

$$\begin{aligned} \phi(\omega_0) &= \frac{1}{Q(\omega_0)} \\ &= \frac{E_{lost/cycle}}{2\pi E_{stored}}. \end{aligned} \tag{2.27}$$

The energy lost per cycle is dissipated in the bending of the wire; the energy stored in bending the wire is $E_{stored_{wire}} = \frac{1}{2}k_{wire}x^2$ (where x is the horizontal displacement of the pendulum from it's equilibrium position) and the energy lost per cycle is some fraction, α, of the total elastic energy i.e. $E_{lost/cycle} = \frac{1}{2}\alpha k_{wire}x^2$. The total energy stored in a cycle of the swinging pendulum is $E_{stored_{pend}} = \frac{1}{2}(k_{wire} + k_{grav})x^2$. Expressions can be derived

for the wire loss, $\phi_{mat_{total}}(\omega_0)$, and the pendulum loss, $\phi_{pend_{total}}(\omega_0)$, by substitution of the appropriate energies into equation 2.27. Dividing one expression by the other gives the relationship

$$\frac{\phi_{pend_{total}}(\omega_0)}{\phi_{mat_{total}}(\omega_0)} = \frac{k_{wire}}{k_{wire} + k_{grav}}. \tag{2.28}$$

We know that $k_{grav} \gg k_{wire}$ which allows for the simplification

$$\phi_{pend_{total}}(\omega_0) \approx \phi_{mat_{total}}(\omega_0)\frac{k_{wire}}{k_{grav}}. \tag{2.29}$$

We can see from equation 2.29 that because $k_{grav} \gg k_{wire}$, the value of loss factor that the pendulum mode displays is a reduced level of the loss factor of the suspension wire material.

Let us move now to the more general case of a pendulum of mass, m, suspended by n wires of length l. Saulson [53] gives the elastic spring constant of a bending wire under tension as $k_{wire} = \frac{n\sqrt{TEI}}{2l^2}$ where T is the tension per wire, E is Young's modulus of the wire material and I is the moment of cross-sectional area ($I = \frac{\pi r^4}{4}$ for a cylindrical wire of radius, r). Substituting for k_{wire} and k_{grav} into equation 2.29 gives

$$\phi_{pend_{total}}(\omega_0) = \phi_{mat_{total}}(\omega_0)\frac{\xi n\sqrt{TEI}}{2mgl} \tag{2.30}$$

where ξ is an additional term that takes the value 1 or 2 depending on whether the positions of the wires constrains them to bend at the the top, or top and bottom, respectively. Although equation 2.30 is defined at the resonant frequency, ω_0, the relationship between the pendulum loss at any frequency, ω, and the material loss at the same frequency, ω holds.

2.7 Thermoelastic Damping

The material loss of the suspension fibres discussed in the previous section was expressed in terms of a total material loss, $\phi_{mat_{total}}(\omega)$, and not the intrinsic loss of the material, $\phi_{mat_{intrinsic}}(\omega)$, as might have been expected. This is because there exists a source of internal friction which, due to the dimensions of the wire/fibre, may exhibit its maximum of damping at a frequency in (or near) the frequency band of interest. The loss angle for the thermoelastic effect is $\phi_{mat_{t.e.}}(\omega)$. The frequency at which the maximum loss occurs (the 'characteristic frequency') is a function of the radius/thickness of the suspension wire (or fibre) and the properties of the material. The maximum level of loss at the characteristic frequency is a function of the material alone. If the loss is found to contribute strongly at frequencies of interest it must be added to the constant, 'intrinsic' loss factor in order to obtain a realistic value of loss (i.e. $\phi_{mat_{total}}(\omega) = \phi_{mat_{intrinsic}}(\omega) + \phi_{mat_{t.e.}}(\omega)$). The level of thermoelastic damping present at a frequency ω affects the level of pendulum loss factor achievable through the relationship given in equation 2.30.

Consider measuring the material loss factor associated with the vibrational mode of a wire or fibre clamped at one end. As it oscillates a periodic stress is applied to the wire or fibre, and as a result a local temperature gradient is induced across the sample. This is because the compressed region of the wire or fibre increases in temperature whilst the extended region decreases. Heat then flows across the sample in an attempt to restore equilibrium. At very low frequencies, the process is essentially isothermal and the sample is never far from equilibrium. No energy loss will occur in this situation because there is no significant time lag involved in the material reaching equilibrium. At high frequencies the stress is removed (or reversed) on a time scale much less than the relaxation time of the sample, and therefore no significant heat flows. At these frequencies the process is approximately reversible and no significant vibrational energy is lost. At an intermediate frequency, the frequency of oscillation of the sample will be comparable to $\frac{1}{2\pi}\times$ (relaxation time)$^{-1}$ of the material. In this instance the process of heat flow is irreversible. Accompanying this is an increase in entropy and hence in dissipated power. This occurs as a conversion of vibrational energy (at the characteristic frequency) to heat. The increase in the level of loss factor, $\phi_{mat_{t.e.}}(\omega)$, results in an increase in the level of thermal noise at this frequency.

Thermoelastic loss is similar to other forms of internal loss in that it is defined [46] in terms of its relaxation time, τ, and relaxation strength, Δ, by

$$\phi_{mat_{t.e.}}(\omega) = \Delta \frac{\omega\tau}{1+(\omega\tau)^2}. \tag{2.31}$$

In the case of thermoelastic damping, the strength of the relaxation is given by Nowick [46] as

$$\Delta = \frac{E\alpha^2 T}{\rho c} \tag{2.32}$$

where E is Young's modulus, α is the coefficient of thermal expansion, ρ is the density and c is the specific heat at constant volume of the suspension wire or fibre material. The frequency at which the maximum loss occurs (the 'characteristic frequency') is determined by the relaxation time and is given by

$$\begin{aligned} f_{char} &= \frac{1}{2\pi\tau} \\ &= 2.16\frac{k}{\rho c d^2} \end{aligned} \tag{2.33}$$

for a cylindrical fibre where k is the thermal conductivity of the material and d the diameter of the sample.

The effect that thermoelastic damping has on the loss factor associated with the pendulum mode can be altered. This is achieved by changing the shape of the wire/fibre cross-section whilst maintaining the tension in each wire/fibre. This results in a change in the frequency at which the maximum loss occurs. An example of this might be to use a thin ribbon (or flexure) of thickness, t. In this instance the 'characteristic frequency' occurs at

$$f_{char} = \frac{\pi k}{2\rho c t^2}. \tag{2.34}$$

From equation 2.31, it can be seen that the level of the maximum loss (for any wire or fibre shape) is given by

$$\phi_{mat_{t.e.}}(\omega_{char}) = \frac{\Delta}{2}. \tag{2.35}$$

Whether or not the thermoelastic loss resulting from the sample in question contributes significantly to the overall level of loss, and as a result to the overall level of thermal noise, depends on the material properties and dimensions of the sample.

Thermoelastic damping is not in evidence in torsional modes since this type of mode only involves shear motion and does not involve local volume changes that result in changes in thermal energy [54].

2.8 Important Normal Modes of the Suspension

Some types of the normal modes present within the suspension system of an interferometric detector have already been discussed. Listed below is a summary of all of the various normal modes. In addition, the effect that the levels of associated thermal noise have on the achievable sensitivity of GEO 600 is discussed.

The first class of normal modes contributing to the level of thermal noise present within the detector consists of the vibrational (or internal) modes of the test mass. In this instance the test mass must be treated as an elastic body. The centre of mass remains still, but the shape of the test mass itself changes. There is a variety of different mode shapes that can be excited in the mass, some of which couple into the inteferometer signal and others which do not. Whether the mode shape can be sensed by the interferometer and therefore contribute to the level of thermal noise is discussed further in section 7.4.4.

The thermal noise associated with the combined effects of the internal modes of the test mass is intrinsic to the material and cannot be improved upon. This source of thermal noise sets the thermal noise limit to the achievable sensitivity of a detector. Much research has been performed around the world to find materials of suitably low 'intrinsic' loss. The dimensions and mass of the test mass are such that the internal

mode frequency is well above the detection band of GEO 600. The measured value for the internal loss ($\phi_{internal}(\omega) = 2 \times 10^{-7}$) is equivalent to a spectral density of thermal displacement of $\tilde{x}_{internal}(\omega) = 7 \times 10^{-20}\,\mathrm{m}/\sqrt{\mathrm{Hz}}$ at 50 Hz (as was discussed in section 2.6) and is very easily degraded. The loss factor associated with the internal modes can be increased by friction occurring between the mass and suspension wires or fibres and by the method employed to attach the wires or fibres to the test mass. In Chapter 7 there is a discussion of experiments performed to develop low-loss jointing techniques in an attempt to preserve the low internal thermal noise characteristics of the fused quartz masses.

The second class of vibrational modes consists of the suspension modes. These are modes in which the test mass can be treated as a rigid body. The most important of these modes are those whose associated thermal noise causes motion of the centre of mass. The suspension modes include the pendulum modes, the transverse vibrations (or violin modes) of the suspension wires (which causes small recoil motions of the test mass), as well as the vertical modes, torsional and tilt modes of the pendulum.

The thermal motion associated with the pendulum mode excited in the direction of the interferometer arm will couple directly into the interferometer signal reducing the interferometer sensitivity. This happens because the thermally induced mirror motion changes the relative separation of the test masses. As was discussed in section 2.6, the suspension can be designed so that the maximum displacement can be forced to occur at frequencies below the lowest frequency of the detection band of the interferometer.

To ensure that thermal noise associated with the longitudinal pendulum mode does not contribute significantly to the overall sensitivity, an acceptable figure is set for the power spectral density of thermal motion for this mode, $\tilde{x}^2_{pend_{total}}(\omega)$. This figure is a factor of 10 lower than $\tilde{x}^2_{internal}(\omega)$ at 50 Hz and is referred to as the GEO 600 thermal noise specification. Substituting the GEO 600 thermal noise specification for the pendulum mode and the parameters of a GEO 600 suspension into equation 2.24 (i.e. where $\omega \gg \omega_0$) allows calculation of the acceptable level of loss factor associated with the pendulum mode. This is calculated to be 3.7×10^{-8} at 50 Hz. Experiments performed to develop test mass suspensions that exhibit this level of loss are reported in chapters 5 and 6.

One GEO 600 test mass is 16 kg. If we decide to include a safety factor in the loading of

the wires or fibres and tension them to $\frac{1}{3}$ of their known tensile strength, we can calculate the radius of the suspension wire or fibre required. These two pieces of information can be substituted, together with the pendulum mode loss factor associated with the GEO 600 thermal noise specification, into equation 2.30 to allow calculation of the level of material loss, $\phi_{mat_{total}}(\omega)$, required from a given material. A discussion can be found in Chapter 3 of experiments conducted to find a material of low enough intrinsic loss factor to be used in GEO 600.

The violin modes of the suspension wires or fibres form a harmonic series that unfortunately lie within the detection band of the detector. The violin modes have associated with them a loss that is a reduced level of the intrinsic loss of the suspension wire (and which are of the same order as the loss associated with the pendulum mode for exactly the same reasons). The thermally induced displacement of the test mass resulting from the violin modes is the noise associated with the violin mode suppressed by the factor $\frac{m}{m_{wire}}$ (where m is the mass of the pendulum and m_{wire} the mass of the wire) and off resonance is much smaller than motion resulting from the thermal noise associated with the other modes. Although the off resonance thermal noise is very much smaller than the thermal noise associated with the other modes of the pendulum suspension, we cannot afford to relax the level of violin mode loss factor. This is because the violin mode loss and the pendulum mode loss factor are related by $\phi_{violin}(\omega) = 2\phi_{pend}(\omega)$ (when the rocking mode of the pendulum has been constrained) [55, 56]. Because the suspension is designed to be of low loss most of the thermally induced motion will be concentrated into very narrow frequency bands around the resonant frequencies. Therefore the resonant frequencies are likely to be the only frequencies that will contribute significantly to the overall level of thermal noise. However because of their low loss factor the amount of detection band occupied by the violin modes is small. These narrow bands are notched out of the resulting data.

With careful design of the suspension system the thermal noise associated with the pendulum and violin modes at 90° to the direction of the laser beam will not contribute significantly to the overall level of thermal noise present in GEO 600. Positioning of the laser beam on the centre of a suspended mass allows the thermal noise associated with the vertical spring modes, torsional modes and tilt modes to be kept within acceptable levels.

2.9 Conclusions

We have seen that the fluctuation-dissipation theorem is a useful equation that relates the level of microscopic thermal noise generated in the modes of the suspension to the macroscopic loss and which can be used as a tool in the design of suspensions in gravitational wave detectors. We see that by measuring and then reducing the levels of loss present in the suspension, we can predict and then improve upon the associated levels of off resonant thermal noise.

We have touched on the need for low loss methods of attaching the suspension wires or fibres to the mass to preserve the low internal losses of the test mass. We have also introduced an acceptable level of thermal displacement associated with the most important of the suspension modes – the longitudinal pendulum mode. This level is such that the loss contribution from this mode is not a significant factor in the overall level of thermal noise and corresponds to a pendulum mode loss factor of $\phi_{pend_{total}}(\omega) = 3.7 \times 10^{-8}$ at 50 Hz. Much of the work presented in this thesis deals with identifying and reducing the excess loss present (from a number of loss mechanisms) to levels that allow us to achieve the GEO 600 thermal noise specification.

Chapter 3

The Determination of a Material Suitable for Suspending the GEO 600 Test Masses

3.1 Introduction

In Chapter 2 the subject of thermal noise in the suspensions of the test masses in laser interferometric gravitational wave detectors was introduced. It was explained that the sensitivity of GEO 600 at 50 Hz will be limited by the thermal noise source that is hardest to reduce further – the thermal noise associated with the internal friction in the material of the test masses. In addition to this there are other sources of thermal noise present within the suspension system. However, the level of noise contribution from each of these sources can, to some extent, be controlled. One such source of thermal noise is due to the loss associated with the pendulum mode.

The GEO 600 thermal noise specification is given in section 2.8. It implies that a loss factor at 50 Hz for the pendulum mode of $\phi_{pend_{total}}(\omega) = 3.7 \times 10^{-8}$ is acceptable; with this level of loss associated with the pendulum mode, the detector sensitivity will remain limited by the internal losses of the test masses.

In a carefully designed suspension (where all external damping mechanisms and the losses

associated with attaching the wires/fibres to both the point of suspension and mass have been reduced to negligible levels) the loss factor associated with the pendulum mode, $\phi_{pend_{total}}(\omega)$, is related to the loss factor of the suspension wire/fibre material, $\phi_{mat_{total}}(\omega)$, by equation 2.30 i.e.

$$\phi_{pend_{total}}(\omega) = \phi_{mat_{total}}(\omega)\frac{\xi n\sqrt{TEI}}{2mgl}.$$

The term $\phi_{mat_{total}}(\omega)$ consists of the sum of the intrinsic loss factor of the wire or fibre material, $\phi_{mat_{intrinsic}}(\omega)$, (due to the combined effects of the various internal loss mechanisms - refer to section 2.4.3) and a possible contribution from thermoelastic damping, $\phi_{mat_{t.e.}}(\omega)$, (an internal damping mechanism that may 'peak' close to the frequency band of interest). The definition of the terms included in the 'multiplication factor' (i.e. $\frac{\xi n\sqrt{TEI}}{2mgl}$) are given in section 2.6.1. To reach the target level of $\phi_{pend_{total}}(\omega)$, a suspension wire/fibre with a low material loss contribution at the target frequency of $\omega = 2\pi \times 50\,\mathrm{rad\,s^{-1}}$, and a small multiplication factor is desirable. One method of achieving a small multiplication factor is to employ a wire/fibre material with a high tensile strength thus allowing the use of samples of small radii (where $I \propto r^4$).

This chapter contains a discussion of the experiments performed to find a material that exhibits losses of a value low enough to be used as the suspension wires/fibres in GEO 600.

3.2 Experiments to Determine the Material Loss Factor of Carbon Steel Wires

Carbon steel is a commonly chosen material for the suspension wires in prototype interferometric detectors. If a 16 kg GEO 600 sized test mass is to be suspended by four carbon steel wires tensioned to $\frac{1}{3}$ of their breaking stress, the required wire radius can be calculated (Chapter 7 contains a discussion about how one might choose the number of suspension wires/fibres to employ in the final design). Taking the breaking stress of carbon steel to be 3×10^9 Pa allows calculation of a suitable wire radius of r= 111 μm. This radius, together with a wire length of $l = 0.25\,\mathrm{m}$, a Young's modulus of

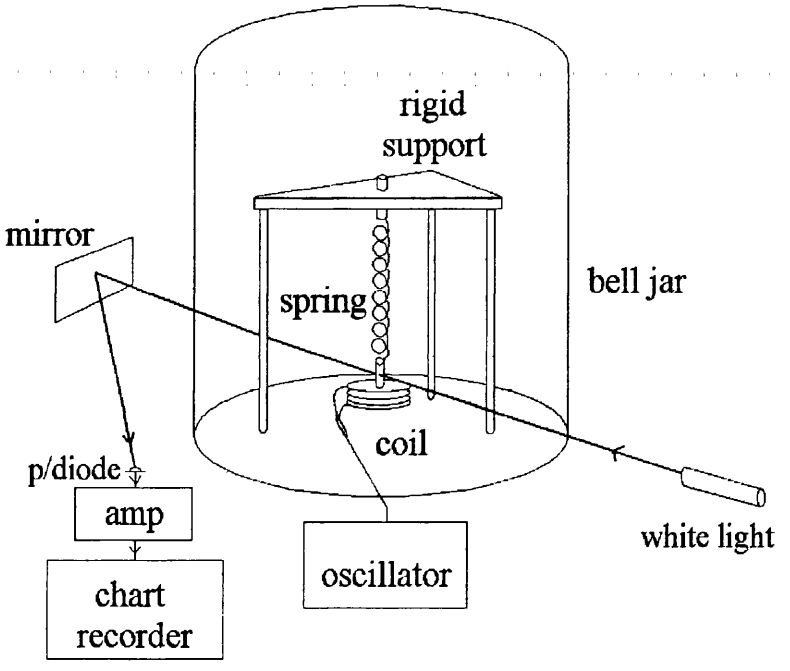

Figure 3.1: *Experimental apparatus for the measurement of* $\phi_{mat_{total}}(\omega_0)$ *of carbon steel wire.*

$E = 2.1 \times 10^{11}$ Pa and the loss factor specification associated with the pendulum mode at 50 Hz are substituted into equation 2.30 to allow calculation of the required wire loss factor of $\phi_{mat_{total}}(\omega) = 1.2 \times 10^{-5}$ at 50 Hz.

Experiments were conducted to measure the total material loss on resonance of samples of carbon steel wire of two different thicknesses – 127 μm diameter and 178 μm diameter. Lengths of the carbon steel wire were first coiled into springs by drawing a sharp edge along the length [1]. A small steel bob was then attached to one end of each wire. The other end of the wire was clamped firmly into a precision engineered pin-vice in order to reduce losses at the point of suspension. This mounting point was an integral part of a rigid support structure designed to minimise the effect of recoil back into the system. The structure was in turn placed inside a vacuum bell jar that could be evacuated to pressures at which the effect of gas damping was negligible; typically pressures of 2×10^{-5} mbar or below were used (refer to Appendix A). A diagram of the experimental apparatus used in measuring the material loss, $\phi_{mat_{total}}(\omega_0)$, can be seen in figure 3.1.

[1] It should be noted that it is possible that coiling the wire in this manner may introduce surface damage and therefore increase the material loss factor. For the purpose of this measurement it has been assumed that any increase in loss factor is negligible. This assumption however is open to discussion.

The fundamental vertical mode of each spring was excited by applying an alternating current to the coil positioned around the bob at half of the frequency of the vertical resonance of the wire and bob suspension. When a reasonable amplitude of motion had been obtained the current was switched off and the coil uncoupled from the oscillator to prevent eddy current damping of the oscillation. The vertical mode was then allowed to decay freely with time. A stopwatch was used to measure the period of the vertical mode from which the frequency was determined. A white light source was shone across the bell jar. The light beam was partially obscured by the bob. A photodiode positioned on the far side of the bell jar (behind the bob) permitted a shadow sensing technique to be employed to detect the amplitude, $A(t)$, and hence the decay of the vertical motion. The signal from the photodiode was filtered, amplified and passed to a chart recorder.

The charts obtained for the amplitude decays of the carbon steel wires showed that the amplitude decreased towards some background level, A_B, instead of zero. This was due to mechanical noise (from the vacuum pumps) driving the vertical mode (as was discussed in section 2.5). To correct for this a graph of $ln\sqrt{A(t)^2 - A_B^2}$ versus time, t, was plotted instead of simply $lnA(t)$ versus t. A value for the loss factor was calculated by multiplying the gradient of the graph by $-\frac{2}{\omega_0}$ (where ω_0 is the resonant angular frequency). If an uncorrected decay is used to calculate the loss, the offset will result in an artificially low value of $\phi_{mat_{total}}(\omega_0)$.

Applying this technique of obtaining $\phi_{mat_{total}}(\omega_0)$ to the results generated average values for the loss of $\phi_{mat_{total}}(\omega_0) = (1.58 \pm 0.15) \times 10^{-4}$ at 2.6 Hz for the sample of 127 μm diameter wire and $\phi_{mat_{total}}(\omega_0) = (4.54 \pm 0.40) \times 10^{-4}$ at 1.75 Hz for the 178 μm diameter wire.

The material constants for carbon steel are $E = 2.1 \times 10^{11}$ Pa

$k = 50\,\mathrm{W\,m^{-1}K^{-1}}$

$\rho = 7800\,\mathrm{kg\,m^3}$

$c = 420\,\mathrm{J\,kg^{-1}K^{-1}}$

and $\alpha = 15 \times 10^{-6}\ \mathrm{K^{-1}}$

at a temperature of $T = 300\,\mathrm{K}$.

From these numbers we can calculate the thermoelastic damping contribution at the measurement frequencies using the equations given in section 2.7[2]. The level of thermoelastic damping present in both of the wire samples (i.e $\phi_{mat_{t.e.}}(\omega_0) = 5.5 \times 10^{-6}$ for the 127 μm diamter wire and $\phi_{mat_{t.e.}}(\omega_0) = 7.28 \times 10^{-6}$ for the 178 μm diameter wire) was considered to be negligible since it contributed towards no more than 3% of the total loss at the measurement frequencies. If we assume that loss contributions from external sources are negligible, the measured loss factor can be taken as the intrinsic loss factor of the material, $\phi_{mat_{intrinsic}}(\omega_0)$, (which, as a property of the material itself is independent of wire diameter). If we also assume that the loss mechanism present within carbon steel is structural in nature [57], the loss $\phi_{mat_{intrinsic}}(\omega_0)$ will be constant at all frequencies. Because the two wires are the same material, it follows that the value obtained for $\phi_{mat_{intrinsic}}(\omega_0)$ should be the same for both samples. This however was not the case. We infer that there was a source of external loss present in the results obtained from the 178 μm diameter wire. This was believed to be a result of frictional losses in an undertightened pin-vice. We therefore conclude that the results obtained from the 127 μm diameter wire give a more realistic value of the intrinsic loss, $\phi_{mat_{intrinsic}}(\omega_0)$. This is confirmed in section 5.5.

Using the value of $\phi_{mat_{intrinsic}}(\omega)$ obtained from the 127 μm diameter wire plus the thermoelastic contribution at 50 Hz, calculated for a 222 μm diameter wire suitable for suspending a GEO 600 mass (i.e. $\phi_{mat_{t.e.}}(\omega) = 3.2 \times 10^{-4}$), we can calculate the expected $\phi_{mat_{total}}(\omega)$ at 50 Hz associated with the carbon steel wire. This number is $(4.75 \pm 0.15) \times 10^{-4}$, a factor of ~ 40 higher than the GEO 600 specification for the material loss factor. Thus a material of intrinsically lower loss factor is required if we are to meet the GEO 600 pendulum thermal noise specification.

[2]The motion of the body of the spring results from a shearing action. Bending however occurs at the top and bottom of the wire (at the point where the spring enters the pin-vice and where it is attached to the mass) and therefore a contribution due to thermoelastic damping is believed to exist.

3.3 The Use of Fused Quartz as a Suspension Fibre Material

Braginsky [58] has shown that ultra high grade fused silica is of low enough intrinsic loss, $\phi_{mat_{intrinsic}}(\omega)$, to be suitable for the suspension of the test masses in laser interferometric gravitational wave detectors. As well as its intrinsically low loss factor, fused silica has a further advantage: the use of fused silica fibres allows the construction of monolithic suspensions. This can help to maintain the low level of internal thermal noise by minimising any excess loss that is associated with the attachment of the suspension fibres to the fused silica test mass or to the point of suspension. The subject of minimising the losses at the joint between the fibres and the test mass will be discussed further in Chapter 7.

We propose to suspend the GEO 600 sized test masses on four fused quartz fibres tensioned to $\frac{1}{3}$ of the breaking stress [3]. Knowing this we can calculate a suitable fibre radius to be $r = 220\,\mu$m. From this radius, a fibre length of 0.25 m, a Young's modulus of 7×10^{10} Pa and the desired level of pendulum mode loss, $\phi_{pend_{total}}(\omega)$, for a GEO 600 test mass at 50 Hz, a maximum acceptable level of $\phi_{mat_{total}}(\omega) = 5.1 \times 10^{-6}$ at 50 Hz can be calculated using equation 2.30 [4].

The remainder of this chapter contains a discussion of the experiments performed to determine if samples of an inexpensive, 'standard grade' fused quartz are of low enough $\phi_{mat_{total}}(\omega)$ to be considered as the suspension fibre material for GEO 600.

3.4 Methods of Production of Fused Quartz Fibres

Three methods of producing fused quartz fibres will be discussed in this section; pulling fibres using either an oxy-hydrogen burner or an RF furnace, and etching fused quartz

[3] Experiments to measure the breaking stress of fused quartz fibres conducted by the author (on samples of 'standard grade' fused quartz) and by Braginsky (private communication) have suggested that 800 MPa is a reasonable value to assume.

[4] The loss factor resulting from the shearing action of the wire is assumed to be the same as that due to bending.

rods with hydrofluoric acid.

3.4.1 Pulling Fused Quartz Fibres in an Oxy-Hydrogen Flame

Pulling fused quartz fibres by this method involves holding small sections of fused quartz rod (typically 3 mm in diameter) in the hottest region of an oxy-hydrogen flame. Once the material softens and the flame is removed, a quick motion outwards from the ends pulls a thin fused quartz fibre. Sections of 3 mm rod are left attached to both ends. It should be noted that the existence of the rod-ends or 'stubs' on the fibres is an advantage in minimising the excess loss known as 'stick-slip' damping that can occur at points of attachment [45]. 'Stick-slip' damping is discussed in section 5.4. This method of fibre production has the advantages of being both quick and easy. There are however two disadvantages associated with this pulling method. The first is the difficulty of pulling the matched set of fibres required for the construction of a test mass suspension. The second problem is the difficulty of pulling ribbon shaped fibres with the oxy-hydrogen burner. As was previously discussed in section 2.7, this fibre configuration has thermal noise advantages over cylindrical fibres.

3.4.2 Pulling Fused Quartz Fibres in an RF Furnace

The RF furnace consists of an 8 kV power oscillator which produces a varying electromagnetic field (at 400 kHz) in an external drive coil. This field induces a current in a graphite ring that sits centrally within the coil thus heating it. Graphite is used as the heating element because it can withstand the temperature of 1800 °C+ that is required to soften the fused quartz rod without reacting with it. Before operating the RF furnace, a fused quartz rod (typically 3 mm in diameter) is passed through the centre of the furnace and clamped to geared motors above and below. The settings of these motors determines the rate of feed of fresh material into the furnace and the rate of pull of the fibre from beneath (and hence the fibre thickness) during the fibre pulling process. The fibres are pulled in an argon atmosphere to prevent a reaction of the graphite element with the air. It takes approximately 90 s to heat the graphite element and subsequently radiate enough heat onto the fused quartz rod so that it reaches its softening temperature. Once

the fused quartz rod has been heated sufficiently, the pull and feed motors are switched on and a fibre pulled.

Situated beneath the furnace is a series of microswitches. These are triggered by the moving carriage attached to the pull motor and turn the furnace and the two motors off in a predetermined sequence. The positions of the microswitches and hence the timing of the switching sequence is variable giving control of the fibre pulled.

Fibres produced by this method also have sections of the 3 mm diameter rod attached at each end.

Advantages of the RF furnace include firstly, the ability to produce matched sets of fibres required for the construction of pendulums. Secondly, ribbon fibres can be pulled by replacing the length of 3 mm fused quartz rod positioned within the heating element with a section of fused quartz slide. One disadvantage of pulling fibres in this manner is the time required to set up the furnace, pull the fibre and allow the system to cool to a manageable temperature before repeating the process. A further disadvantage is the possible contamination of the fused quartz with graphite from the heating element should the two touch during the pulling process. A photograph of the RF furnace taken during the inital stage of heating the fused quartz rod can be found in figure 3.2.

3.4.3 Fibres Formed by Etching Fused Quartz Rods

There is a third method that can be used to form fused quartz fibres which, although not employed for any of the experiments reported in this text, should be mentioned. This involves etching the fused quartz rods down to the desired radii by submersing them in hydrofluoric (HF) acid. By coating the ends of the fused quartz rods with a substance that is impermeable to hydrogen fluoride, for example paraffin wax, sections of thicker rod can be left attached to both ends of the etched fibre.

The discussion contained in sections 3.5 - 3.7.3 relates to experiments conducted on samples of fused quartz ribbons pulled in the RF furnace. Ribbons were used for reasons of simplicity – it proved easier to measure the amplitude decay of ribbon fibres because ribbons are constrained to oscillate in one sense only. A consistency check on the level

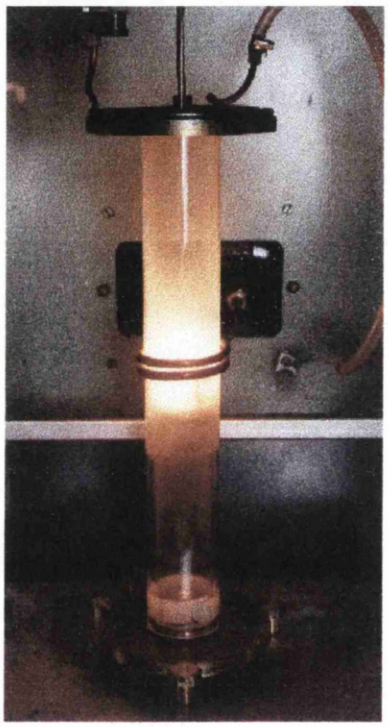

Figure 3.2: *Photograph of the RF induction furnace during its operation. The fused quartz rod runs vertically through the quartz cylinder (in which argon flows) and is clamped to geared motors top and bottom (outwith photo). The graphite heating element sits in the centre of the copper drive coil. The plates at the ends of the quartz cylinder are water cooled.*

of loss factor of a cylindrical fibre sample is discussed in section 3.7.4.

3.5 Expected Limitations to the Measurement of the Material Loss Factor of Fused Quartz Ribbons

In the same way as for the carbon steel wires discussed previously, the measured loss factor of fused quartz ribbons, $\phi_{mat_{total}}(\omega_0)$, will contain contributions from all of the significant loss mechanisms present. Possible contributions to the overall loss may include:

- Energy lost into a recoiling support structure. This can be reduced to negligible levels by careful design of the test structure and is further discussed in section 3.6.
- Losses in the clamp ('stick-slip' damping). This is minimised by the method of fibre production and by careful clamping and is further discussed in section 3.6.
- Any loss caused by the fibre becoming electrostically charged (e.g. by UV radiation from the ion pump or gauge) is reduced to insignificant levels by careful positioning of the fibre within the vacuum tank.

The measured loss factor will therefore be mainly the sum of contributions from the following loss mechanisms (at a frequency ω_0) i.e.

$$\phi_{mat_{total}}(\omega_0) = \phi_{mat_{intrinsic}}(\omega_0) + \phi_{mat_{t.e.}}(\omega_0) + \phi_{mat_{gas}}(\omega_0). \quad (3.1)$$

These losses are; $\phi_{mat_{intrinsic}}(\omega_0)$ and $\phi_{mat_{t.e.}}(\omega_0)$ which have both been discussed in section 3.1 and $\phi_{mat_{gas}}(\omega_0)$, a contribution due to external damping from the residual gas present. It is possible to estimate the contribution due to gas damping, $\phi_{mat_{gas}}(\omega_0)$, at a pressure, P, by substituting the relevant parameters into equation A.13 (which can be found in Appendix A). This is discussed more fully in section 3.6.1.

3.6 Experiments to Determine the Material Loss Factor of Fused Quartz Ribbons

A fused quartz slide (1 mm thick) was pulled into a ribbon fibre of length 12.5 cm, width 3 mm and thickness ~54 μm using the RF furnace. A portion of the 1 mm thick slide was left attached to one end of the fibre. To protect it, thin strips of steel (cut from a feeler gauge) were attached above and below the slide with a thin layer of the vacuum epoxy, Torrseal. The fused quartz slide and stainless steel sandwich was clamped horizontally between two aluminium plates (with the plates exerting pressure on the steel). Clamping on the thicker portion of the fused quartz, and not the fibre itself, helps to minimise the problems associated with 'stick-slip' damping (refer to section 5.4). The aluminium clamp was mounted on a rigid aluminium table of thickness 25 mm. The table top was supported by four aluminium legs of diameter 50 mm, each of which was braced against the wall of a stainless steel vacuum tank in which the table stood. This massive, stable structure was designed to reduce the effects of recoil damping of the fibre back into the surroundings to a negligible level.

The vacuum tank was evacuated by an ion pump that worked in parallel with a turbo-molecular pump backed by a rotary pump. The system could reach vacuum pressures of $\sim 1 \times 10^{-7}$ mbar. A laser beam was shone across the vacuum tank so that the oscillating fibre partially obscured the beam. The motion of the fibre was sensed by detecting the resulting diffraction pattern on a split photodiode positioned at the far side of the vacuum tank. The resulting signals from the halves of the split photodiode were subtracted, filtered, amplified and recorded on a data acquisition program which had been developed in-house [59]. A fraction of the signal resulting from the photodiode was passed through a phase shifter, amplified and superimposed upon a 750 V d.c. bias to create an a.c. drive signal which alternated between ~100 V and ~1400 V. This voltage was then applied between two metal strips, the 'drive plate', situated beneath the free end of the fibre.

In order to protect the high voltage amplifier in case the strips should short circuit, a large resistor, R_1, was inserted in series between the amplifier and the drive plate. The value of R_1 was chosen such that $\frac{1}{2\pi R_1 C_1} \gg f_0$, where C_1 was the estimated value of the

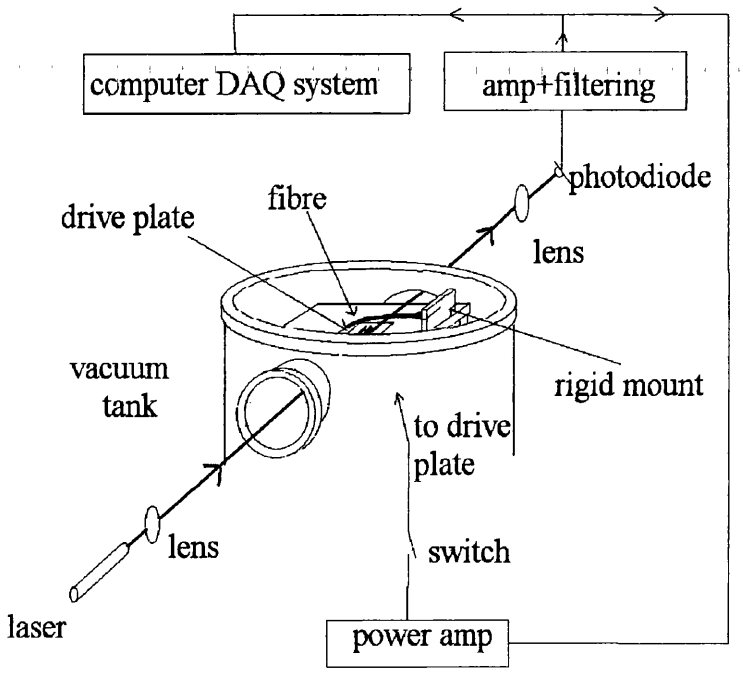

Figure 3.3: *Experimental apparatus for the measurement of* $\phi_{mat_{total}}(\omega_0)$ *of fused quartz fibres.*

capacitance between the two strips and f_0 was the resonant frequency of the fibre.

When the phase of the feedback signal was correctly adjusted, the fibre resonance could be excited by positive feedback. The resonances of this fibre occurred at [5] 6.06 Hz, 22.8 Hz, 59.6 Hz and ~106 Hz. Once a suitable amplitude of fibre motion had been achieved, the drive signal was disconnected and the drive plate grounded by means of a second resistor, R_2, in parallel with the drive plate. The size of the resistor was chosen such that the time constant of the R_2C_1 filter was much shorter than the period of the fibre resonance (and $R_2 \gg R_1$). The amplitude of motion was sensed and recorded by the equipment described above. A diagram of the experimental equipment used in measuring $\phi_{mat_{total}}(\omega_0)$ can be seen in figure 3.3.

[5] At initial, large amplitudes of excitation of the fourth harmonic, the frequency was ~104 Hz. As the amplitude decayed the frequency increased to ~106 Hz. This may be understood by the following: At large amplitudes the point of bending occurs high up in the necked section of the fibre. As the amplitude decreases the point of bending moves further down the neck. This has the effect of decreasing the fibre length and results in an increase in frequency.

3.6.1 Determining the Level of Residual Gas Damping Within the System

Prior to performing the loss experiments a suitable working pressure was estimated which should allow the measurements taken to be free from any significant effects of gas damping. A value of $\phi_{mat_{total}}(\omega_0) = (0.2 - 1) \times 10^{-6}$ was assumed reasonable for fused quartz (by comparison with the values of internal loss measured on bulk samples of fused quartz [30, 51]). For gas damping to be considered negligible we require that it adds no more than a 10% contribution to this number i.e. $\phi_{mat_{gas}}(\omega_0) = (0.2 - 1) \times 10^{-7}$. The required pressure was estimated by substitiuting the following parameters into equation A.13.

1. $\omega_0 = 2\pi \times 22.8\,\mathrm{rad\,s^{-1}}$ (the frequency of the first enharmonic overtone of the fibre).
2. The effective area, $A_{effective}$, and effective mass, $m_{effective}$, of the section of fibre involved in the oscillation. Because we were considering a higher order harmonic, we estimated these by assuming that all of the fibre was involved in the oscillatory motion and thus that the required area and mass equalled the surface area, A, and the mass, m, of the fibre. Due to the taper of the fibre only a rough estimate of the total area, A, and total mass, m, was made. The maximum value of A and minimum value of m were calculated using the dimensions of the fibre given in section 3.6.
3. the gram molar mass of hydrogen, $M = 2 \times 10^{-3}\,\mathrm{kg}$, (in a high vacuum system, once the tank had been baked, hydrogen would be expected as the dominant molecule present).

The result is that a pressure in the range $(0.4 - 2) \times 10^{-5}\,\mathrm{mbar}$ should be sufficient to reduce the level of residual gas damping to acceptable proportions. Preliminary measurements taken at a vacuum pressures of $2 \times 10^{-5}\,\mathrm{mbar}$ resulted in an average loss factor of $\phi_{mat_{total}}(\omega_0) = (3.39 \pm 0.40) \times 10^{-6}$ for the 22.8 Hz resonance. This level of loss is almost 3.5× greater than the highest expected loss factor of 1.1×10^{-6}. A similar calculation can be performed if it is assumed that N_2 is the dominant molecule present (due to a small air leak in the system). This calculation suggests that measurements

made at pressures in the range of $(1-5)\times 10^{-6}$ mbar would be free of any significant effects of gas damping. Measurements made in this pressure range also resulted in losses higher than were expected. Because great care had been taken to minimise all additional sources of loss when designing the experimental system, it was believed that excessive gas damping (i.e. from much heavier molecules then either H_2 or N_2) was responsible. The relationship between the measured loss factor and pressure was therefore investigated.

The system was evacuated to $\sim 1\times 10^{-7}$ mbar. The system was then isolated and the vacuum pumps stopped. The 22.8 Hz resonance was excited and its amplitude allowed to decay freely whilst being recorded by the data acquisition program. During the amplitude decay the vacuum tank and its contents slowly outgassed. The increase in pressure as a function of time was simultaneously recorded.

A plot of measured loss factor, $\phi_{mat_{total}}(\omega_0)$, against pressure, P, was generated from the plots of $ln\sqrt{A(t)^2-A_B^2}$ versus time, t, and pressure, P, versus time, t. This is shown in figure 3.4.

The equation of the line in figure 3.4 is expected to be of the form

$$\phi_{mat_{total}}(\omega_0) = \alpha_{outgas}P_{mbar} + (\phi_{mat_{intrinsic}}(\omega_0) + \phi_{mat_{t.e}}(\omega_0)) \tag{3.2}$$

where

$$\alpha_{outgas} = \frac{A}{m\omega_0}\sqrt{\frac{M}{\mathcal{R}T}}(1\times 10^2) \tag{3.3}$$

is the gradient and P_{mbar} is the pressure measured in mbar. The term $\alpha_{outgas}P_{mbar}$ is the loss due to residual gas damping $(\phi_{mat_{gas}}(\omega_0))$.

The intercept of the line with the y axis equals the material loss factor, $\phi_{mat_{total}}(\omega_0)$, with the contribution due to residual gas damping removed. From examination of the results shown in figure 3.4, the intercept occurs at $\phi_{mat_{total}}(\omega_0) = \phi_{mat_{intrinsic}}(\omega_0)+\phi_{mat_{t.e}}(\omega_0) = 3.3\times 10^{-7}$.

Further examination of the equation of the line suggests that measurements of loss conducted at pressures below $\sim 5\times 10^{-7}$ mbar will contain a contribution from gas damping

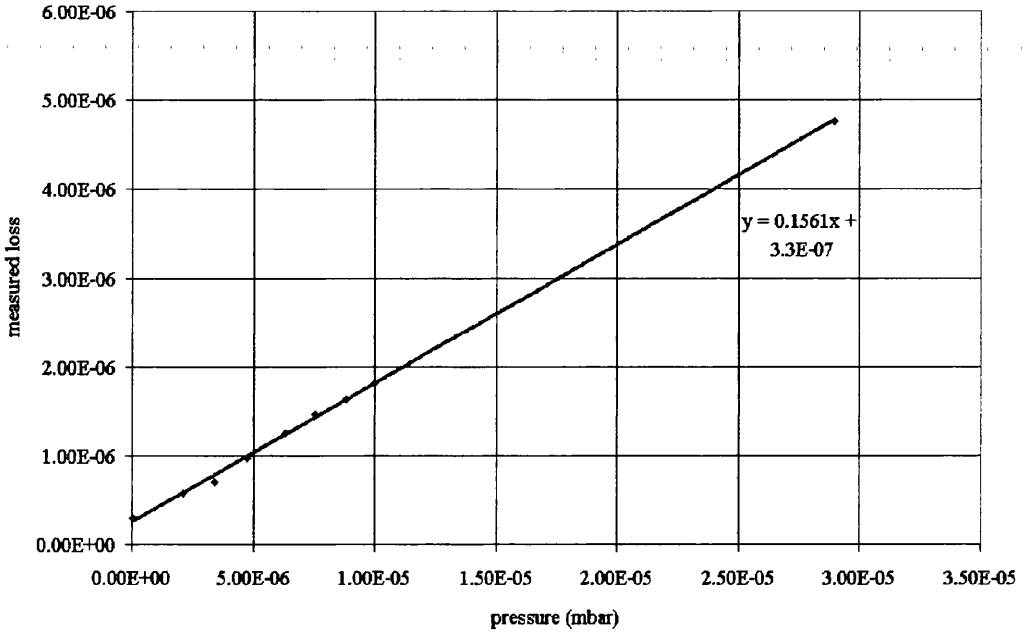

Figure 3.4: *Composite plot of* $\phi_{mat_{total}}(\omega_0)$ *vs pressure as tank outgasses.*

of less than 10%. Measurements taken at pressures below $\sim 5 \times 10^{-7}$ mbar therefore are considered to have a negligible effect from gas damping.

Before continuing with measurements of material loss, it seemed desirable to investigate further the unexpectedly high level of gas damping. The most likely explanation of this was that a partial pressure of molecules of large molecular weight was present.

3.6.2 Experiments to Determine the Molecular Species Responsible for the Excess Levels of Gas Damping within the Experimental System

Unfortunately, for a number of reasons, the mass, M, of the molecules responsible for the excess levels of gas damping cannot be calculated directly from equation 3.3. Firstly, it was difficult to determine the values of the effective area, $A_{effective}$, and the effective mass, $m_{effective}$, accurately. Secondly, the values of pressure read from the vacuum gauge, and hence the value calculated for the gradient, α_{outgas}, were obtained from a gauge that was calibrated with respect to nitrogen and not the gas present within the vacuum tank. We therefore had to try to determine the molecular mass, M, experimentally.

We start by expressing the measured gradient, α_{outgas}, of the graph in figure 3.4 as

$$\begin{aligned} \alpha_{outgas} &= \alpha_{measured} \\ &= \frac{\beta}{\eta}\sqrt{M} \end{aligned} \tag{3.4}$$

where η is the 'gas correction factor'. This corrects the pressure reading obtained from the vacuum gauge (which was calibrated to read for nitrogen) to that of the gas present in the system. Values of η can be found found for various molecules in the manual for the vacuum gauge used [60]. β is a constant which was evaluated by the following method.

Nitrogen was slowly bled into the vacuum tank thus ensuring that it was the dominant molecule present within the system. The butterfly valve on the turbo pump was used as a throttle and adjusted so that the rate of pumping balanced the rate of nitrogen being backfilled into the tank. By employing this method, the pressure inside the tank was kept constant during the time required to measure the amplitude decay of the 22.8 Hz resonance. By further adjustment of the butterfly valve, the rate of pumping from the turbo pump was altered to allow the measurement of the same resonance to be repeated at a number of different vacuum pressures. Values of $\phi_{mat_{total}}(\omega_0)$ were calculated from each of the amplitude decays and plotted against the value of pressure at which each experiment was performed (see figure 3.5).

The gradient of this graph is $\alpha_{N_2} = 0.066 \pm 0.014$. Using the value of the gradient, the gram molar mass of nitrogen, $M = 28 \times 10^{-3}$ kg, and $\eta = 1$ in the case of nitrogen, a value for the constant, $\beta = 0.39 \pm 0.08$, was calculated.

To check this value of β, the above procedure was repeated using hydrogen. Again, the resonance was excited at a number of different vacuum pressures and values for $\phi_{mat_{total}}(\omega_0)$ obtained. These were then plotted on a graph of $\phi_{mat_{total}}(\omega_0)$ versus P shown in figure 3.6.

The gradient of this graph was calculated as $\alpha_{H_2} = 0.040 \pm 0.014$. The manual for the pressure gauge [60] gives $\eta = 0.42$ for the gas correction factor of hydrogen. Substituting this, the measured gradient and the gram molar mass of hydrogen into equation 3.4, gives a β of 0.38 ± 0.13. The two values of β determined are consistent within experimental

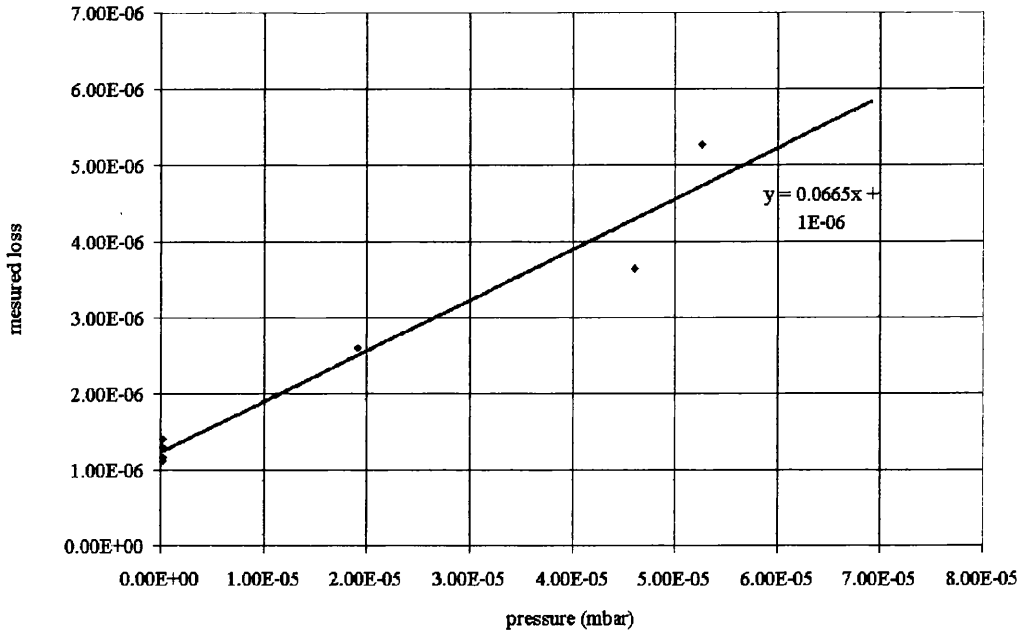

Figure 3.5: $\phi_{mat_{total}}(\omega_0)$ *vs pressure; nitrogen backfill.*

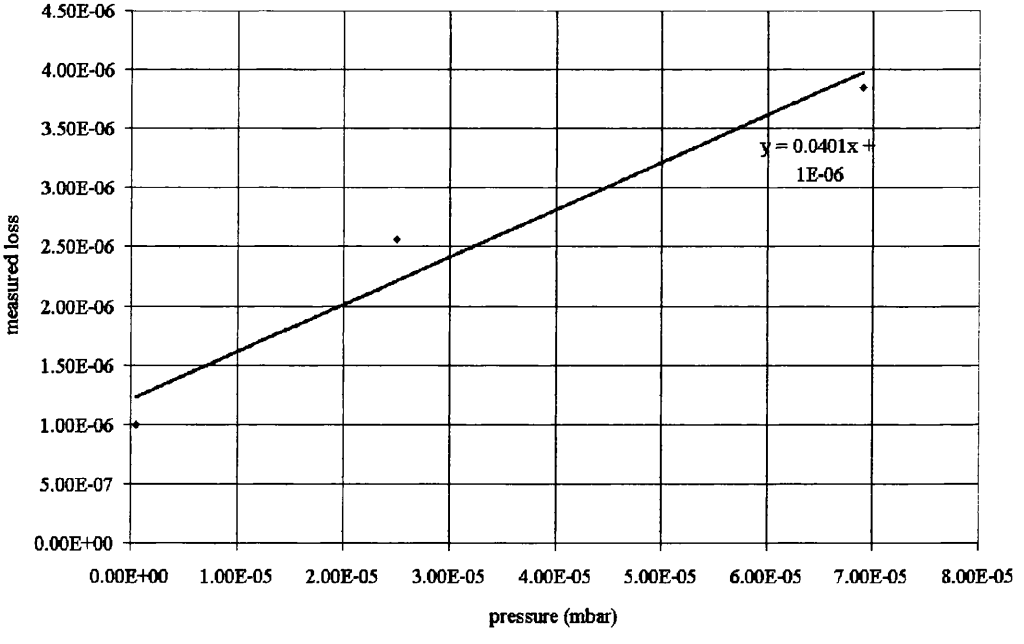

Figure 3.6: $\phi_{mat_{total}}(\omega_0)$ *vs pressure; hydrogen backfill.*

error.

We now return to the question of what gas was present within the vacuum tank during the outgassing test shown in figure 3.4. A gradient of $\alpha_{outgas} = 0.156 \pm 0.008$ was obtained from this graph. Substitution of the gradient and the average value of $\beta = 0.39 \pm 0.08$ into equation 3.4 leads to

$$\frac{\sqrt{M}}{\eta} = 0.40 \pm 0.08 \tag{3.5}$$

which contains two unknowns. A residual gas analyser was attached to the vacuum system and the contents of the tank examined up to a molecular mass of 80 a.m.u. (the upper working limit of the gas analyser). No combination of gram molar mass, M, detected by the analyser and its corresponding gas correction factor, η, (obtained from the ion gauge manual) could be found that gave the constant given in equation 3.5.

It was concluded that the gas contributing to the excess levels of gas damping within the vacuum system was of molecular mass greater than 80 a.m.u. and was probably produced by the vacuum epoxy, Torrseal, or the board onto which the drive plate was etched.

It is worth noting that the predicted levels of material loss, $\phi_{mat_{total}}(\omega_0)$, containing a zero contribution from gas damping were different when the vacuum tank was allowed to outgas and when nitrogen and then hydrogen backfilled the system. The results obtained when the tank outgassed were separated in time by several weeks from the results obtained by backfilling the tank. During the intervening time there was a significant change in laboratory temperature which had a clear effect on the measurements of material loss, $\phi_{mat_{total}}(\omega_0)$. This will be further discussed in the following section.

3.7 Measurement of Material Loss Factor at Pressures Below the Residual Gas Damping Region

A series of measurements of the material loss factor, $\phi_{mat_{total}}(\omega_0)$, of the first four resonances of the ribbon fibre were performed at pressures that were free from the significant

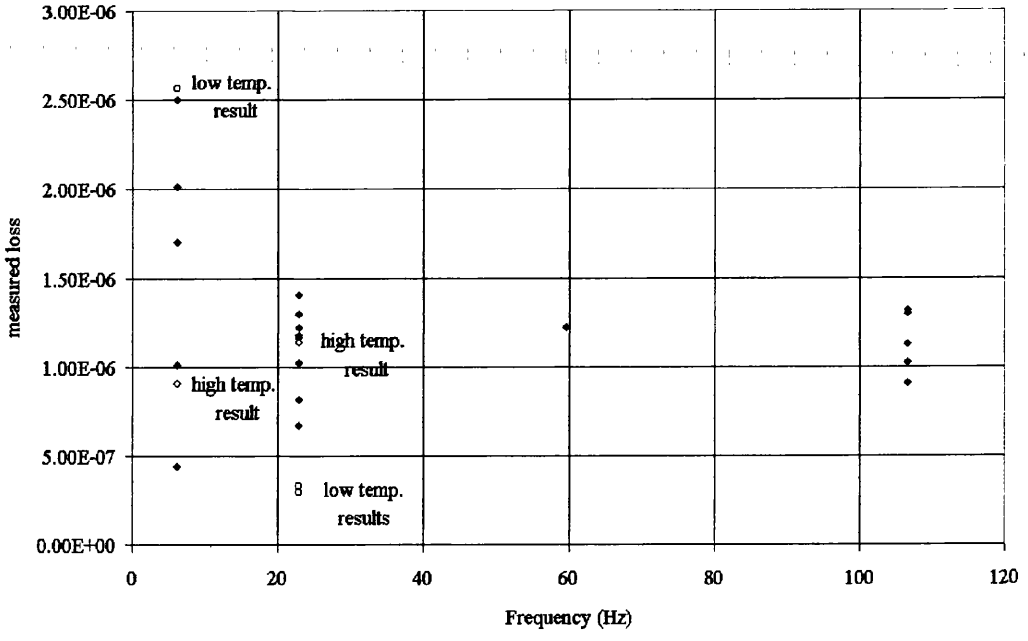

Figure 3.7: *Spread of measured $\phi_{mat_{total}}(\omega_0)$ for the first four resonances of the fused quartz ribbon fibre.*

effects of gas damping. The loss factors obtained from the amplitude decays range between $\sim 2.5\times10^{-6}$ and $\sim 3\times10^{-7}$ and are plotted as a function of frequency in figure 3.7.

The results were obtained over a period of some weeks during which time the temperature within the laboratory changed significantly. The measurements of the lowest loss factor for the resonance at 22.8 Hz and the highest loss factor for the fundamental were observed on the coldest days in the laboratory. The temperature subsequently rose and a higher value of loss factor for the 22.8 Hz resonance and a lower value of loss factor at the fundamental frequency were measured. It was postulated that there was some nonlinear coupling between the resonant modes of the fibre and that this coupling was temperature dependent [6]. The coupling could be between the observed mode and a torsional mode for example which could not be sensed, or in some cases the coupling could be between the observed mode and another mode which could be observed; for example there was difficulty experienced in exciting the 59.6 Hz resonance as the temperature in the laboratory rose. When this resonance was excited the energy of the mode could be

[6] Young's modulus is strongly temperature dependent. Consider a temperature increase. One would expect a corresponding decrease in Young's modulus, and as a direct consequence, a shift in the point of fibre bending further up the necked region. This could alter the amount of coupling present.

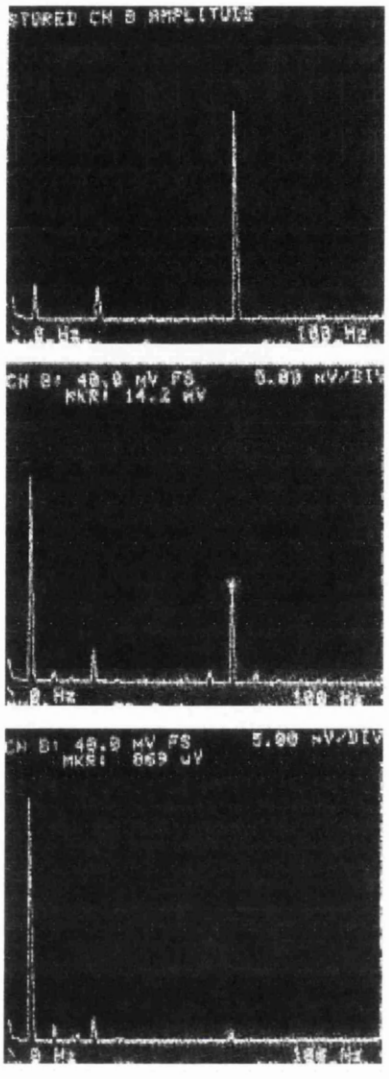

Figure 3.8: *Sequence of photographs showing the coupling of energy between the 59.6 Hz resonance and the fundamental mode over a period of ~2 min.*

seen to leave the 59.6 Hz resonant frequency and transfer into the fundamental mode over a time period of approximately two minutes. The photos in figure 3.8 are a sequence of frames taken from the spectrum analyser showing the energy transfer between modes over this period of time.

3.7.1 The Effect of Thermoelastic Damping on the Ribbon Fibre Tested

It was explained in section 2.7 that thermoelastic damping is an internal loss mechanism that can cause the total loss to depart from the intrinsic loss in the frequency band

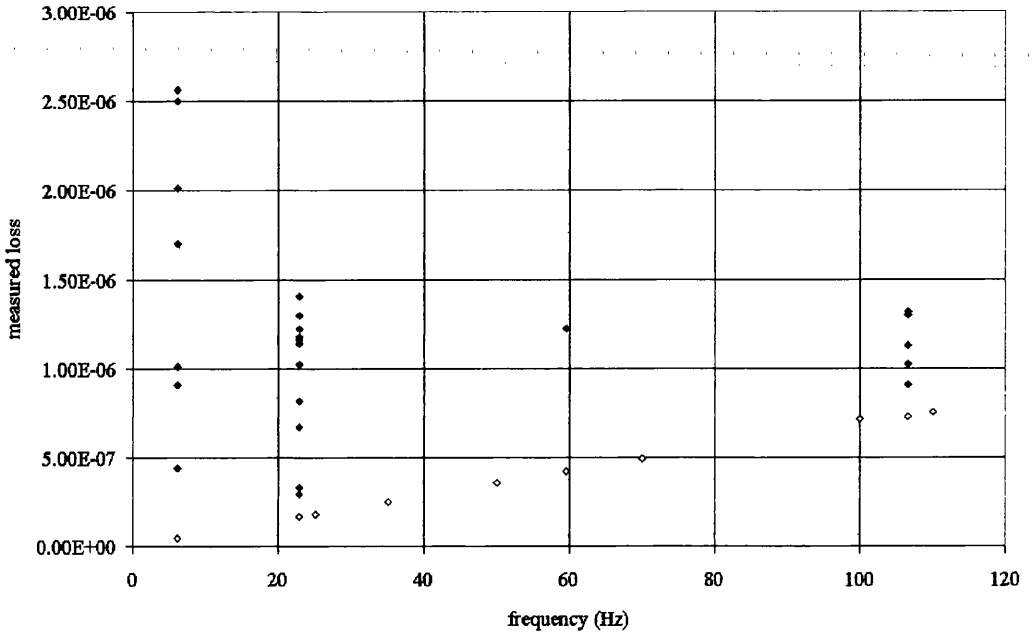

Figure 3.9: *Spread of measured loss, $\phi_{mat_{total}}(\omega_0)$, for the first four resonances of a fused quartz ribbon (solid data points) together with the limit set to the measureable $\phi_{mat_{total}}(\omega_0)$ due to thermoelastic damping ('unfilled' data points).*

of interest. It is therefore interesting to examine the possible effect that thermoelastic damping had on the results presented in section 3.7.

In figure 3.9 the results previously presented in section 3.7 are plotted together with the thermoelastic limit calculated for a ribbon fibre of thickness, t = 54 μm. The thermoelastic limit is obtained using the equations in section 2.7 and the material constants of fused quartz given below.

The material constants of fused quartz are $E = 7 \times 10^{10}\,\mathrm{Pa}$

$$\rho = 2200\,\mathrm{kg\,m^3}$$

$$c = 772\,\mathrm{J\,kg^{-1}K^{-1}}$$

$$\alpha = 5.1 \times 10^{-7}\,\mathrm{K^{-1}}$$

and $k = 1.38\,\mathrm{W\,m^{-1}K^{-1}}$

at a temperature of $T = 300\,\mathrm{K}$.

It can be seen from figure 3.9 that thermoelastic damping is a significant contribution

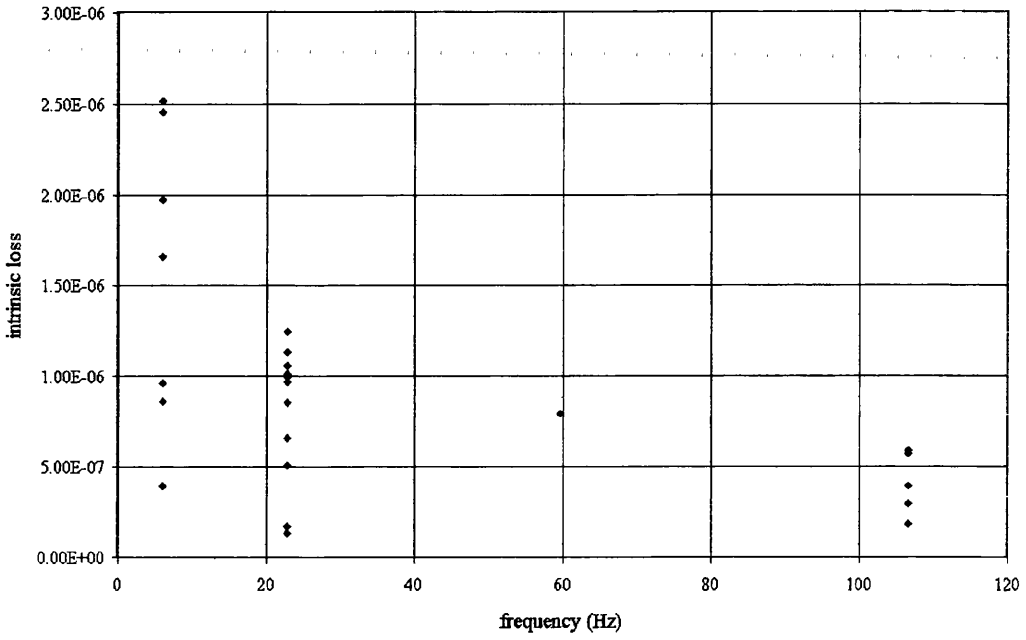

Figure 3.10: *Measured material loss with the thermoelastic contribution removed.*

for the material loss factor measured at ~106 Hz.

It is interesting to replot the experimental results after removing the thermoelastic damping contribution at each of the resonant frequencies. This is shown in figure 3.10. The data points plotted in figure 3.10 represent the level of intrinsic loss associated with the fused quartz ribbon, $\phi_{mat_{intrinsic}}(\omega)$. Consider the lower values of measured loss factors at each frequency only (because these are the results believed to have been least affected by mode coupling). The loss measured for all four modes in the examples of reduced levels of coupling is consistent with the loss mechanism being independent of frequency i.e. the sample of fused quartz appears to be subject to structural damping.

3.7.2 The Effect on the Measured Loss Factor Caused by Welding the Fused Quartz Ribbon

When constructing a pendulum suspension, the method used to attach the suspension fibres to the mass can affect the level of internal loss associated with the test mass [7]. Welding fused quartz fibres directly to the fused quartz test mass is one method of

[7] the effects on the internal loss introduced by various methods of attaching fused quartz fibres to small masses will be discussed fully in Chapter 7.

attachment which produces a monolithic suspension and which should have a potentially minimal effect on the achievable level of internal loss factor. However it is also important to check whether welding has any effect on the loss factor of the suspending fibre. The apparatus used in this experiment gave us an opportunity to test the effect of welding on the intrinsic loss associated with the fibre material. The ribbon used in the previous experiments was broken in the region where the fused quartz slide necked down into the fibre. The two pieces were then welded back together with an oxy-hydrogen burner. The whole process was performed with the sandwiched end of the ribbon left within the aluminium clamp. This was done to avoid altering any contribution to the loss factor, $\phi_{mat_{total}}(\omega_0)$, which might have arisen due to changes in the loss associated with adjustments of the clamp.

The loss factors, $\phi_{mat_{total}}(\omega_0)$, of the first four resonant frequencies of the ribbon fibre were remeasured using the method described in section 3.6. The frequencies of the resonances were seen at 6.08 Hz, 22.9 Hz, 60 Hz and $\sim$ 104 Hz, having changed only slightly.

The results presented in figure 3.11 show that although the welding process appears to have degraded the measured loss factor slightly, the change is not a significant one.

3.7.3 A Check on the Level of Material Loss Factor Using a Second Ribbon Fibre Sample

To check the level of consistency between samples of fused quartz, a second ribbon fibre was tested. This fibre necked down from the quartz slide from which it was pulled into a ribbon 14 cm in length, 1 mm wide and of thickness $\sim$90 μm. The thick end was sandwiched between two pieces of feeler gauge by a thin layer of Torrseal and clamped into the test structure.

The amplitude decays of the first four resonances, at frequencies of 5.04 Hz, 31 Hz, 84.4 Hz and 160 Hz, were measured at a vacuum pressure where the effect of gas damping was negligible. The intrinsic loss factors, $\phi_{mat_{intrinsic}}(\omega_0)$, were calculated by subtracting the thermoelastic damping contribution (for a $\sim$ 90 μm thick fibre) from the measured loss factors. These are plotted as a function of frequency in figure 3.12.

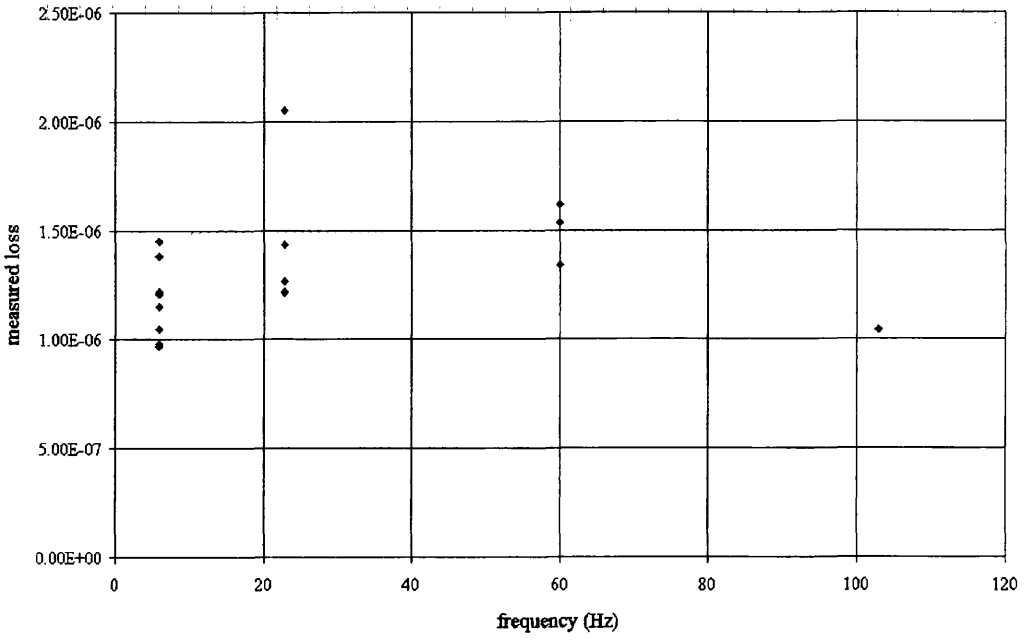

Figure 3.11: *Spread of measured $\phi_{mat_{total}}(\omega_0)$ of first four resonances of welded ribbon fibre.*

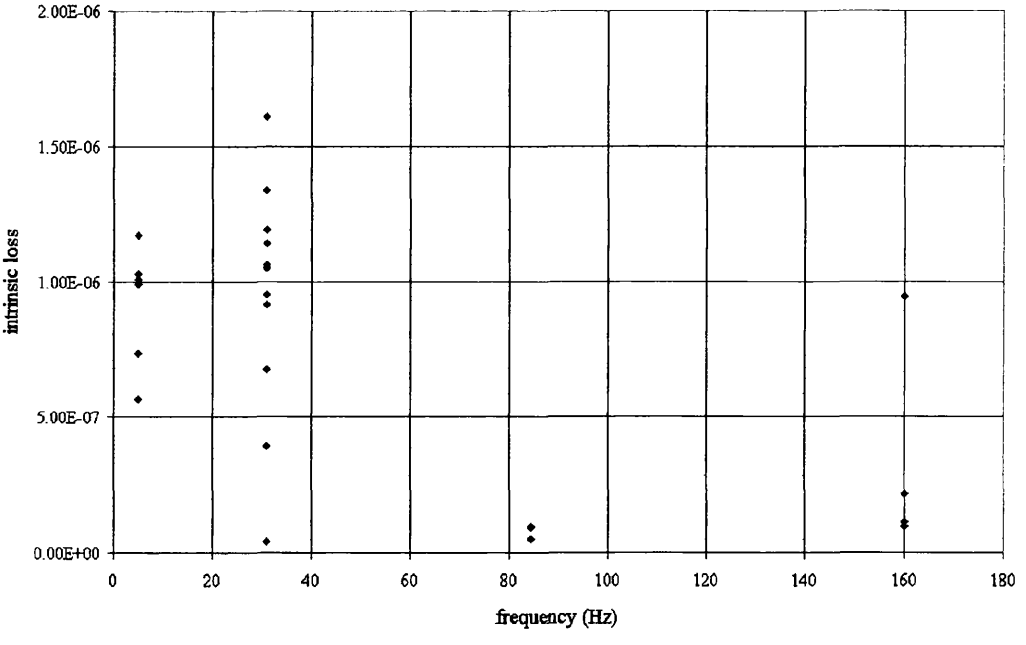

Figure 3.12: *Spread of $\phi_{mat_{intrinsic}}(\omega_0)$ for first four resonances of second ribbon fibre (with thermoelastic contribution removed).*

Examine the results presented in figure 3.12. The lowest measured value of intrinsic loss of the material (i.e. the value of loss exhibiting negligible mode coupling), can be seen to be consistent with the lowest level of intrinsic loss factor obtained from the previous ribbon sample (refer to figure 3.10).

3.7.4 Measurement of Material Loss Factor of a Cylindrical Fused Quartz Fibre

The material loss factor associated with a cylindrical fibre was measured to check that the geometry of the ribbon fibre was not a significant contributing factor in obtaining the levels of $\phi_{mat_{total}}(\omega_0)$ reported in section 3.7.

A cylindrical fibre of length 14 cm, and diameter $\sim$280 μm (at the point of bending) was pulled from a 3 mm fused quartz rod. A small length of 3 mm rod was left attached to the end. This was inserted into a length of protective brass sleeving with a split cut down its full length. This brass sleeve was inserted into a clamp that was mounted within the experimental apparatus. The clamp was tightened, squeezing the brass down onto the fused quartz rod and gripping it firmly, thus minimising the effect of 'stick -slip' damping (discussed in section 5.4).

The fibre resonance (at 15.4 Hz) was excited by the same method used in all previous tests. Unlike the ribbon fibre, the cylindrical fibre is not constrained to oscillate in one sense only. As a result, the sense of the fibre oscillation tends to precess. This motion can be separated into two orthogonal components; horizontal and vertical. To analyse the fibre motion rigorously, a method of sensing the fibre motion should detect both of these components and combine them in quadrature. Because this test was merely a consistency check, it was decided that using the existing experimental apparatus and hence sensing the vertical component only, was sufficient. The detected component of motion was, in this instance, recorded on a chart recorder. The resulting amplitude decay contained a large beat due to the precession of the fibre oscillation. A logarithmic fit to the maxima of the beat signal was plotted, and from this a value of $\phi_{mat_{total}}(\omega_0) = (1.7 \pm 0.5) \times 10^{-6}$ was calculated. The measured material loss was found to be consistent with the values obtained for the fused quartz ribbons.

3.8 Conclusions

It was shown that measurements of the intrinsic loss factor, $\phi_{mat_{intrinsic}}(\omega_0)$, obtained from samples of fused quartz ribbons (produced by an RF induction furnace) were reproducibly in the range of $(0.5 - 1) \times 10^{-6}$ in the frequency range 6 Hz to 160 Hz. Measurements made on a cylindrical fibre yielded results of the same order. Welding fused quartz was shown to have an insignificant effect on the material loss factor. It was also shown that the internal loss mechanism of fused quartz is consistent with structural damping (i.e. that the intrinsic loss factor, $\phi_{mat_{intrinsic}}(\omega)$, is independent of frequency).

The specification for fused quartz to be a suitable material for the suspension fibres in GEO 600 is a material loss factor of $\phi_{mat_{total}}(\omega_0) \leq 5 \times 10^{-6}$. From the best results obtained it can be concluded that standard grade fused quartz should be an ideal candidate, being potentially a factor of 10 better than the maximum acceptable material loss. Even lower material loss factors have been measured for samples of synthetic fused silica of higher quality [61]. It is therefore our intention to employ fused quartz/silica as the material for the suspension fibres of the final stage (i.e. main mirrors) of the GEO 600 suspensions.

Chapter 4

Characterisation of the Test System Used in the Measurement of Pendulum Mode Loss Factor

4.1 Introduction

The desirable level of thermal noise associated with the pendulum mode of one GEO 600 test mass was given in Chapter 2 as equivalent to a loss factor of $\phi_{pend_{total}}(\omega) = 3.7 \times 10^{-8}$ at 50 Hz. Pendulums have been constructed and tested in the laboratory in an attempt to build a pendulum, the pendulum mode of which exhibits low enough losses to be suitable for use in GEO 600.

Measurements of the loss factors of the longitudinal modes of pendulums of small mass, made previously by J. Logan [62], yielded a measured loss factor of $\phi_{pend_{total}}(\omega_0) = (2.15 \pm 0.45) \times 10^{-7}$ for a 1 Hz, 70 g pendulum suspended on two fused quartz fibres. A ~200 g pendulum, on the same fibres, had a loss factor of $\phi_{pend_{total}}(\omega_0) = (1.59 \pm 0.35) \times 10^{-7}$. If these losses were due solely to the loss factor associated with that of the suspension fibres (i.e. $\phi_{mat_{total}}(\omega_0)$), the three-fold increase in mass would have decreased the loss factor, multiplying it by the factor $\frac{1}{\sqrt{3}}$, to the value $\phi_{pend_{total}}(\omega_0) = 1.24 \times 10^{-7}$ (as can be seen with reference to equation 2.30). The actual loss is some 30 % higher than the

calculated figure.

Damping of the pendulum mode by recoil of the structure from which the pendulum was suspended is a possible explanation for this increase in loss. In this chapter, measurements are presented which show that recoil of the structure is present at a level which justifies taking measures to improve the stiffness of the structure.

Masses of $\sim$ 200 g were chosen for the test pendulum for two reasons. Using masses larger than $\sim$ 200 g would have meant that our measurements would have been limited by much larger recoil losses and as a result the GEO 600 specification would become more difficult to reach. Using smaller masses would require the use of proportionally thinner fibres to achieve a loss equivalent to the GEO 600 specification. These fibres are more difficult to produce.

4.2 Description of the Original Experimental Apparatus to Measure the Pendulum Mode Loss Factor

The original experimental system consisted of a vacuum tank mounted on three halved ball bearings bedded into a steel plate 1 cm thick which covered a concrete block of mass 1080 kg. An ion pump (which sat on a wheeled trolley) was also attached to the vacuum tank by means of a short length of 13 cm diameter rigid pipe. It was hoped that this would be a mechanically stable base for a rigid pendulum support structure. This support structure consisted of an aluminium table, with top 1.6 cm thick supported by four cylindrical legs of 5 cm diameter braced against the inside walls of the vacuum tank. On this a rigid box structure, or 'top-hat', was mounted and stiffened by the addition of aluminium buttresses. Slots were cut through the upper surface of the top-hat structure and through the table top directly underneath. Figure 4.1 shows the pendulum support structure in its original state.

The 3 mm diameter fused quartz rods at the ends of the suspension fibres of the test pendulum were glued into tightly fitting sections of brass cylinders which were tightened into an aluminium clamp. A schematic of this arrangement can be seen in figure 4.2. The bob was then lowered through the slots cut into the support structure until the

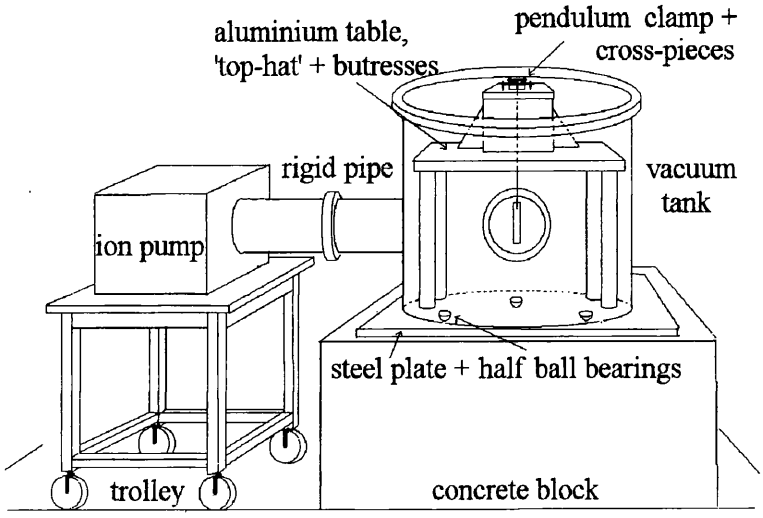

Figure 4.1: *Original structure for the suspension of test pendulums.*

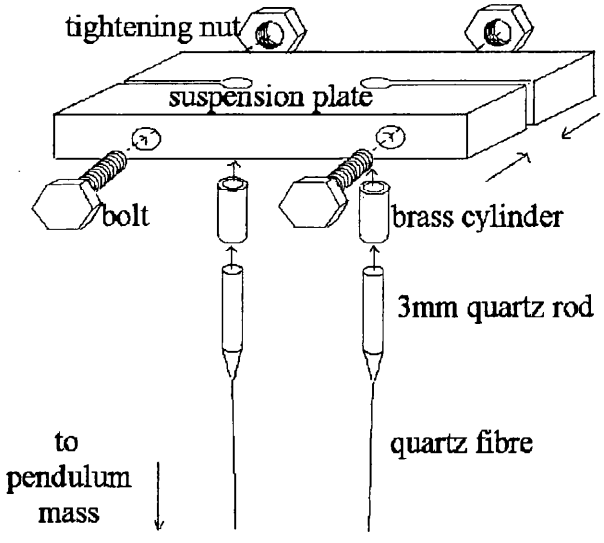

Figure 4.2: *Diagram of the suspension plate and the method of attaching the fibres.*

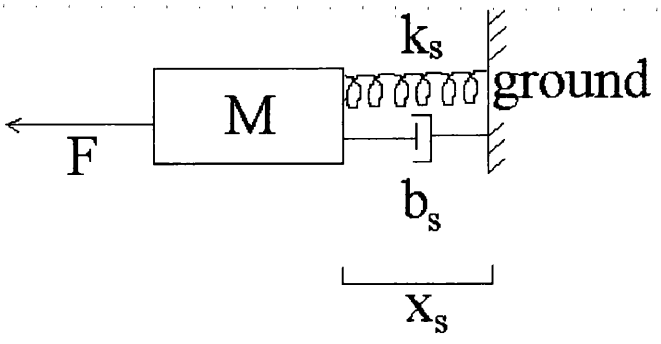

Figure 4.3: *Schematic representation of the lossy pendulum support structure.*

aluminium plate rested on the top-hat. The aluminium clamp was in turn clamped onto the top-hat by means of cross-pieces that passed over the clamp and tightened down into the top-hat.

4.3 Introduction to Recoil Damping

An estimate of the level of damping present within the lossy support structure can be obtained from modelling the support structure as a heavy mass, M. This mass is connected to ground by a spring of elastic constant, k_s, and dashpot (of damping coefficient b_s) representing the loss. The structure can therefore be represented diagramatically in the form of figure 4.3.

In the general case of a damped mechanical oscillator driven by a sinusoidal force where the angular frequency of the force, ω_0, is small compared with the natural frequency of free oscillation, the oscillator's response is controlled by the stiffness of the spring, k_s [49]. This means that the frequency of the structure is that of the driving force. It is also clear from French [49] that the phase of the displacement, x_s, lags that of the driving force, F, by a small angle δ. We can write

$$x_s = \frac{F}{k_s} e^{i\delta} \tag{4.1}$$

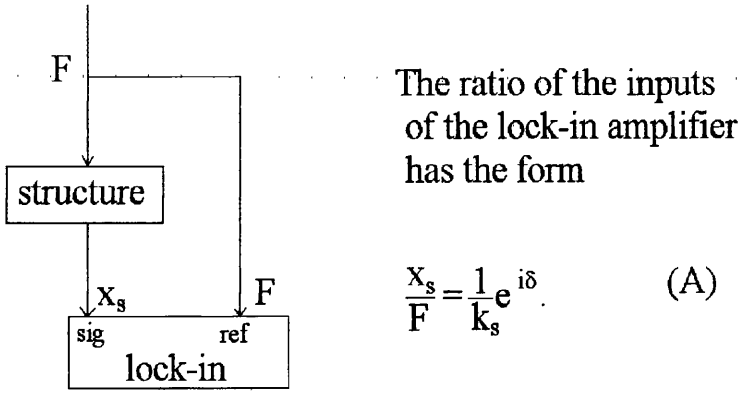

Figure 4.4: *Direct process for measuring x_s with respect to F.*

where δ is negative for a phase lag.

It is shown in Appendix B.1 that when the driving force is supplied by a swinging pendulum of mass, m_p, and angular frequency, ω_0, the limit to the measurable value of pendulum mode loss factor is given by

$$\phi_{recoil}(\omega_0) = -\frac{m_p \omega_0^2}{k_s}\delta$$

(refer to equation B.12).

To determine the limiting loss, $\phi_{recoil}(\omega_0)$, it is therefore necessary to know k_s and δ. The stiffness constant, k_s, can be found from the driving force, F, and the resulting displacement, x_s, of the structure whilst the phase angle δ can be determined by measuring the phase between x_s and F.

4.3.1 Measurement Principle 1

If there existed some straight-forward method of measuring both the applied force, F, and the structure's response, x_s, we would be able to obtain the required values of k_s and δ directly. This measurement might be performed with a lock-in amplifier. Figure 4.4 shows schematically the process involved in this measurement.

The lock-in amplifier measures the magnitude of a signal (in this instance the signal

representing the displacement, x_s) and also the phase by comparing this signal with a reference signal (that of the applied force, F). However, as yet we have neither identified how to make measurements of F and x_s, both of which are required to determine k_s, nor addressed how we might obtain signals proportional to F and x_s which would be adequate for determining δ. The method as shown in figure 4.4 is insufficient for the determination of k_s and δ.

4.3.2 Measurement Principle 2

The displacement of the structure cannot easily be sensed directly. Instead, the displacement is deduced from the acceleration. There was available an inverted pendulum accelerometer which had the required sensitivity and linearity at low frequency [1]. The accelerometer was placed on top of the support structure. An explanation of the operation of the inverted pendulum accelerometer can be found in Appendix B.2. The magnitude of the displacement, $|x_s|$, can be found from the magnitude of the acceleration, $|\ddot{x}_s|$, by dividing it by ω_0^2.

In the case where the force is applied to the structure by a viscously damped oscillator, the variation of amplitude of the force with respect to time introduces an additional phase angle between the displacement of the structure and its acceleration. Since the acceleration is being used to find the displacement, this additional phase angle appears in the measured phase and will be denoted by L. The occurrence of this angle can be shown by considering equation 4.1 i.e.

$$x_s = \frac{F}{k_s} e^{i\delta}$$

where the applied force is of the form, $F = F_0 e^{i\omega_0 t} e^{-\frac{\gamma_p}{2}t}$ (F_0 is the maximum force and $\frac{\gamma_p}{2}$ is the decay constant of the oscillator's amplitude), and implies that the displacement of the structure can be rewritten as

[1] An accelerometer was chosen because the accelerometer does not require an external reference signal.

$$x_s = \frac{F_0}{k_s} e^{i\omega_0 t} e^{-\frac{\gamma_p}{2}t} e^{i\delta}. \tag{4.2}$$

Differentiating x_s twice will give the acceleration, $\ddot{x}_s$, in terms of the displacement of the structure

$$\ddot{x}_s = -\left((\omega_0^2 - \frac{\gamma_p^2}{4}) + i\omega_0\gamma_p \right) x_s. \tag{4.3}$$

If it is assumed that $\frac{\gamma_p^2}{4}$ is very small compared to ω_0^2, equation 4.3 can be approximated to

$$\ddot{x}_s = -(\omega_0^2 + i\omega_0\gamma_p)x_s. \tag{4.4}$$

In equation 4.4, the real part of $\ddot{x}_s$ (i.e. $-\omega_0^2 x_s$) is exactly opposite in phase to x_s as expected, but there is also an imaginary term $-i\omega_0\gamma_p$ which shows that $\ddot{x}_s$ leads its real component by a small angle L where

$$\begin{aligned} tanL &= \frac{\omega_0\gamma_p}{\omega_0^2} \\ &= \frac{1}{Q} \end{aligned} \tag{4.5}$$

and Q is the quality factor of the viscously damped oscillator.

For consistency in the analysis that will follow, equation 4.4 will be rearranged and then expressed as

$$\begin{aligned} \frac{\ddot{x}_s}{x_s} &= \alpha e^{i(\pi+L)} \\ &= -\alpha e^{iL}. \end{aligned} \tag{4.6}$$

Schematically, the experimental configuration discussed in the preceding section is shown

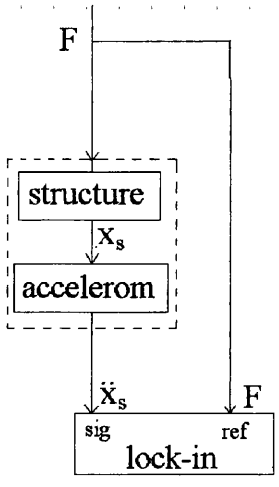

The ratio of the inputs of the lock-in amplifier has the form

$$\frac{\ddot{x}_s}{F} = A e^{i\delta'} \qquad \text{(B)}$$

which, by substitution, can be expressed in terms of the original parameters, F and x_s, as

$$\frac{x_s}{F} = \frac{-A}{\alpha} e^{i(\delta' - L)} \qquad \text{(C)}$$

where $A = \frac{-\alpha}{k_s}$ and $\delta' - L = \delta$

Figure 4.5: *Initial adaptation made to the experimental apparatus to allow the indirect measurement of x_s with respect to F.*

in figure 4.5. However it should be noted that we have still to address the problem of how to detect the applied force, F.

4.3.3 Measurement Principle 3

An initial attempt to detect the applied force, F, was made by adopting an experimental arrangement which involved applying a sinusoidal force (in the horizontal direction) to the point of suspension by means of a cable, attached at one end to the support structure, passing over a pulley and attached at the other end to a mass which oscillated on a spring balance. This arrangement can be seen in figure 4.6.

A reference signal for use by the lock-in amplifier which represented the applied force was obtained by a coil and magnet sensor. The magnet was situated on the cable (between the support structure and the pulley) and moved into and out of a stationary coil. From the accelerometer on the top-hat, and the associated calibration constant (refer to Appendix B.2), an average value of $\ddot{x}_s = (1.10 \pm 0.14) \times 10^{-3}\,\mathrm{m\,s^{-2}}$ was obtained for a driving force of $2.8\,\mathrm{N}_{rms}$ (obtained from a force of $8\,\mathrm{N}_{pk/pk}$ measured from the

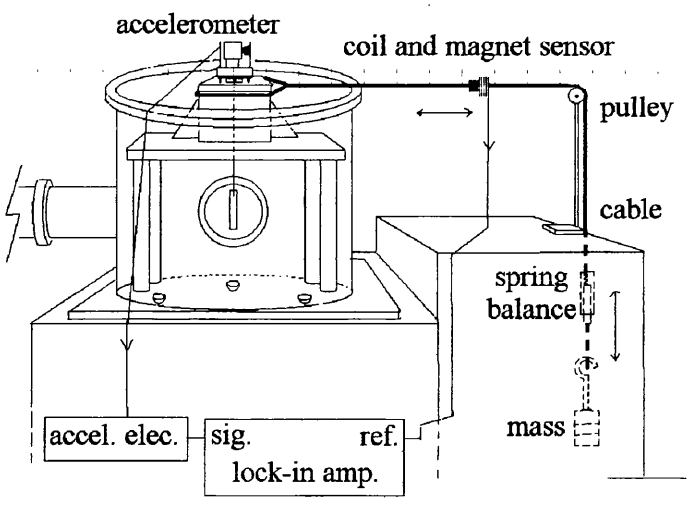

Figure 4.6: *Experimental arrangement for measuring k_s of the original apparatus.*

spring balance). The angular frequency of the force was found to be $\omega_0 = 12.56\,\mathrm{rad\,s^{-1}}$, which, on substitution into the equation $|x_s| = |\frac{\ddot{x}_s}{\omega_0^2}|$, gives the magnitude of the recoil displacement as $|x_s| = (6.97 \pm 0.87) \times 10^{-6}\,\mathrm{m}$. Hookes's Law can then be used to determine the magnitude of stiffness of the support, $k_s = (4.0 \pm 0.5) \times 10^5\,\mathrm{N\,m^{-1}}$.

To achieve a measurable δ required a large amplitude of the oscillating mass to be made. These large movements caused jerking of the cable and degrading of the sensed signal, and as a result, a situation arose where there was no accurate method for sensing the applied force. It was decided that an alternative method of applying the force to the 'top-plate' should be used.

This was achieved by suspending a pendulum (of mass, $m_p = 1.2\,\mathrm{kg}$, and suspension wire length, $l = 25\,\mathrm{cm}$) from the support structure. The pendulum applied a sinusoidal force to the structure (this force being viscously damped). The displacement of the pendulum is shown in Appendix B.3 to be in phase with the force applied to the support structure by the tension in the suspension wire. An input signal, which represented this force, could be obtained for use as the reference of the lock-in amplifier by shadow sensing the pendulum displacement, x_p. This was done by shining a strong white light through the port-holes of the vacuum tank across the pendulum mass and detecting the shadow cast on a photodiode. The resulting signal contained a d.c. component due to the residual

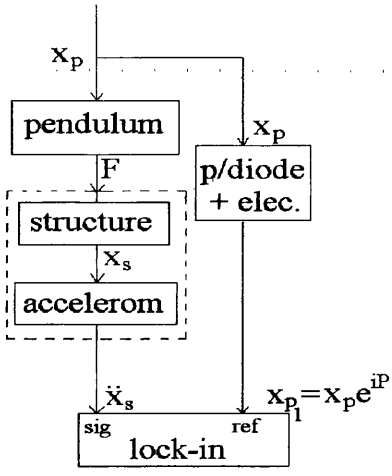

The ratio of the inputs of the lock-in amplifier has the form

$$\frac{\ddot{x}_s}{x_{p_1}} = Be^{i\delta''} \qquad (D)$$

which, on substitution of $\frac{\ddot{x}_s}{x_s} = -\alpha e^{iL}$, $x_{p_1} = x_p e^{iP}$ and $F \simeq \frac{m_p g x_p}{l}$, can be expressed in terms of the original parameters as

$$\frac{x_s}{F} = \frac{-Bl}{\alpha m_p g} e^{i(\delta''+P-L)} \qquad (E)$$

where $\frac{-\alpha m_p g}{Bl} = k_s$ and $\delta''+P-L = \delta$

Figure 4.7: *Further adaptations made to the experimental apparatus to allow the indirect measurement of x_s with respect to F.*

light present when the pendulum was at rest and this component was removed by adding to it a d.c. signal of the same magnitude and opposite sign. The a.c. component which remained was amplified and fed into the reference input of the lock-in amplifier. However, this signal lags the actual pendulum displacement, x_p, by an angle P. This is due to a phase angle being introduced by the electronics in the shadow sensor.

With the pendulum suspended from the support structure, a schematic of the equipment is shown in figure 4.7.

Referring to figure 4.7, it can be seen that a value for δ'' can be obtained directly from the measurement made by the lock-in amplifier. Recording the shadow sensed amplitude decay of the viscously damped pendulum allows a value to be calculated for its Q factor. From this Q, a value for L can be determined (using equation 4.5). A value for P can be calculated from the electronics of the shadow sensor and hence δ can be found. The lock-in amplifier is also used to measure the magnitude of the acceleration, $|\ddot{x}_s|$ using the calibration constant of the accelerometer (refer to Appendix B.2). This value can then be used to find the magnitude of the stucture's displacement, $|x_s|$, using $|x_s| = |\frac{\ddot{x}_s}{\omega_0^2}|$. A value for the peak force applied can be determined from $F_{pk} \approx \frac{m_p g x_p}{l}$ (where x_p is the maximum horizontal displacement of the pendulum swing). From this a value of the rms force can be found and then, once again, Hooke's Law can be used to determine k_s.

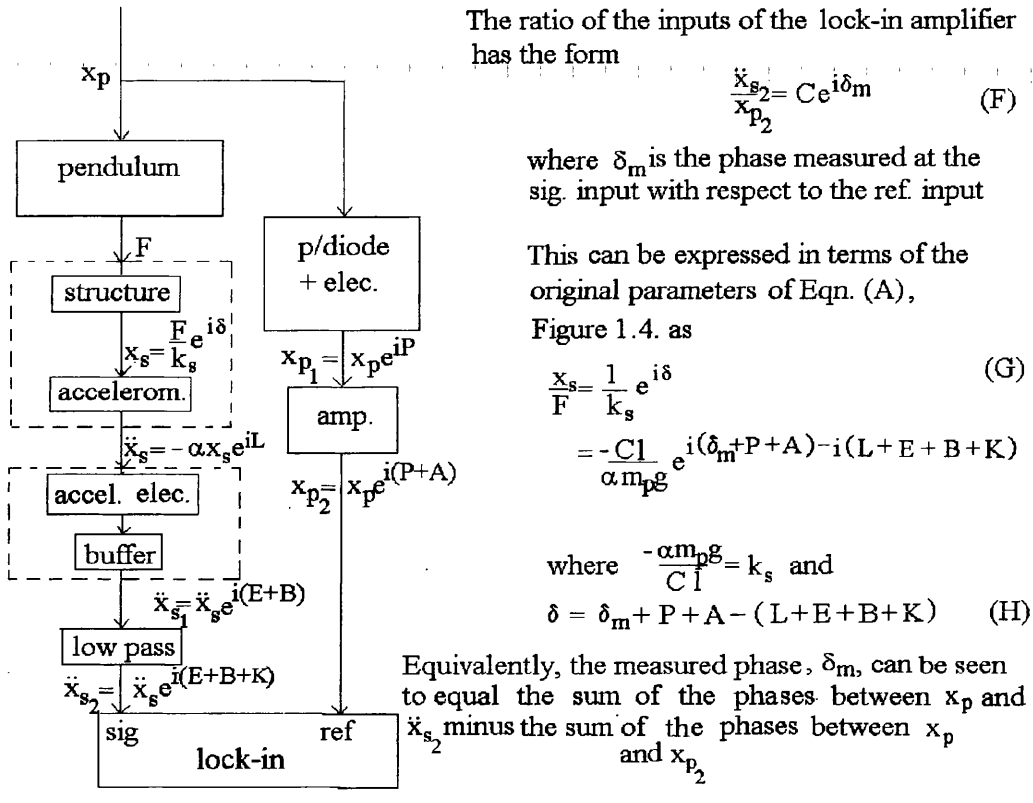

Figure 4.8: *Final configuration of experimental apparatus allowing the indirect measurement of x_s with respect to F.*

4.3.4 Measurement Principle 4

In practice, the apparatus as shown in figure 4.7, is not yet complete. A number of additional pieces of equipment are required to perform the measurement suggested in the diagram. Each of these pieces of equipment introduces additional phase shifts. These components are now included in figure 4.8.

The measurement made by the lock-in amplifier gives a value for $|\ddot{x}_s|$ from which k_s can be calculated. It also supplies a value for δ_m (where δ_m is the phase measured at the signal input of the lock-in amplifier with respect to the signal at the reference input of the lock-in amplifier). The value of k_s found from the method of the mass oscillating on the spring was checked using this experimental configuration. The value obtained using the new experimental method was found to coincide with the original value within the accuracy of the experiment. The parameter, δ, can be obtained from the measurement of δ_m (using equation (H) in figure 4.8) once the values of all the additional phase shifts

have been determined. These additional phase shifts will be the subject of the following section.

4.4 The Evaluation of the Additional Phase Shifts Present Within the Measurement of δ_m

4.4.1 Evaluation of P, the Phase Shift Associated with the Photodiode Circuit

The phase shift accumulated through the photodiode circuit was calculated to introduce a phase lag of $P = (-0.395 \pm 0.079)°$ for the photodiode circuit used in the initial phase measurement. At the time of the improvements made to stiffen the experimental system (section 4.5), alterations were also made to the reference photodiode circuit which included removing a capacitor from across the output of the circuit. This resulted in a decrease in the phase shift to one of negligible size, ($P \sim -10^{-5°}$).

4.4.2 Evaluation of E, the Phase Shift Associated with the Phase Lead Filter

The theory of the inverted pendulum accelerometer is discussed in Appendix B.2. There it is explained that in the ideal case of infinitely high loop gain, the acceleration fedback, $\ddot{x}_f$, is equal in magnitude and phase to the acceleration of the structure, $\ddot{x}_s$. However, in the real condition of non-infinite loop gain, an additional small phase shift is introduced between the two accelerations by the phase lead (or damping) filter. We can evaluate the additional phase shift generated at the 1 Hz measurement frequency by the phase lead filter by studying the closed loop transfer function of the accelerometer electronics taken as a whole.

An expression is given in Appendix B.2 for the ratio of the acceleration fedback to that of the acceleration of the structure;

$$\left(\frac{\ddot{x}_f}{\ddot{x}_s}\right)_f = \frac{GH}{1+GH} \tag{4.7}$$

In this expression, G is the transfer function relating relative displacement of the accelerometer mass, x_r, to the acceleration of the structure, $\ddot{x}_s$,

$$\begin{aligned} G &= \frac{x_r}{\ddot{x}_s} \\ &= \frac{1}{s^2 + \frac{\omega_{0_{accel}}}{Q}s + \omega_{0_{accel}}^2} \end{aligned} \tag{4.8}$$

(where Q is the quality factor of the accelerometer mass and $\omega_{0_{accel}}$ is the natural frequency of the inverted pendulum) and where H is the overall gain of the feedback of the accelerometer (with $s = i\omega$). H can be expressed as the product of the gains of the individual components of the feedback system. These are the gain of the phase lead filter, H_{filter}, and the gain of the other circuit components which, when multiplied together, give H_{other}. The H_{filter} term not only contributes to the overall magnitude of the gain, but is also responsible for the introduction of an additional phase shift present in the case of non-infinite loop gain. The H_{other} term contributes only to the magnitude of the gain and not the phase. The gain H can therefore be expressed as

$$H = H_{filter}H_{other}. \tag{4.9}$$

The circuit diagram of the phase lead (or damping) filter is shown in figure 4.9. From this diagram an expression for the gain of the phase lead filter can be generated

$$\begin{aligned} H_{filter} &= \frac{V_{out}}{V_{in}} \\ &= \frac{R_2}{R_1}\frac{s\tau + 1}{sC_1 r + 1} \end{aligned} \tag{4.10}$$

where $\tau = (R_1 + r)C_1 = 6.16 \times 10^{-3}$s. As a result of substituting equation 4.10 into equation 4.9, the overall gain, H can be expressed as

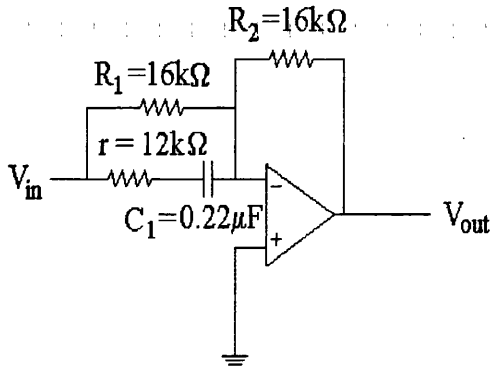

Figure 4.9: *Diagram of phase lead filter.*

$$H = H_{dc}\frac{s\tau + 1}{sC_1 r + 1} \tag{4.11}$$

where H_{dc} is the dc gain contribution and equals $H_{other}\frac{R_2}{R_1}$.

Substituting for G and H into equation 4.7 gives

$$\left(\frac{\ddot{x}_f}{\ddot{x}_s}\right)_f = \frac{H_{dc}(1+s\tau)}{s^3C_1r + s^2(1+\frac{\omega_{0_{accel}}}{Q}C_1r) + s(\frac{\omega_{0_{accel}}}{Q} + \omega_{0_{accel}}^2 C_1 r + H_{dc}\tau) + \omega_{0_{accel}}^2 + H_{dc}} \tag{4.12}$$

which can be simplified, using $\omega_{f_{accel}}^2 = \omega_{0_{accel}}^2 + H_{dc}$, to

$$\left(\frac{\ddot{x}_f}{\ddot{x}_s}\right)_f = \frac{sH_{dc}\tau + H_{dc}}{s^3rC_1 + s^2(1+\frac{\omega_{0_{accel}}}{Q}C_1r) + s(\frac{\omega_{0_{accel}}}{Q} + \omega_{0_{accel}}^2 rC_1 + H_{dc}\tau) + \omega_{f_{accel}}^2}. \tag{4.13}$$

The additional phase angle generated by the phase lead filter can be evaluated from this transfer function once the coefficients of s have been evaluated. These coefficients were either already known (i.e. R_1, R_2, r, and C_1 thus allowing the calculation of τ), or were measured (i.e. Q, as well as $\omega_{0_{accel}}$ and $\omega_{f_{accel}}$, from which H_{dc} was calculated).

- **the evaluation of $\omega_{0_{accel}}$ and Q**

  The accelerometer circuit was left in open loop mode for measurement of the natural angular frequency, $\omega_{0_{accel}}$, and the quality factor, Q, of the inverted pendulum. The pendulum was first displaced gently to one side to start it oscillating. The resulting sinusoidal oscillation was then allowed to decay freely. The magnet attached to the swinging pendulum induced a signal in the coil normally used for feedback and this signal was plotted on a chart recorder. From this information calculated values of $\omega_{0_{accel}} = 15.7 \text{ rad s}^{-1}$ and $Q = 52$ were obtained.

- **the evaluation of $\omega_{f_{accel}}$**

  To measure $\omega_{f_{accel}}$ the accelerometer circuit was operated in closed loop mode. The inverted pendulum was mounted on top of a shaker table driven by a white noise source. The response of the accelerometer was monitored on a spectrum analyser. The resulting power spectrum revealed that the resonant frequency of the accelerometer, with feedback, was $\omega_{f_{accel}} = 150.8 \,\text{rad s}^{-1}$.

- **the evaluation of H_{dc}**

  As has been previously stated,

$$\omega_{f_{accel}}^2 = \omega_{0_{accel}}^2 + H_{dc}. \tag{4.14}$$

  Thus with $\omega_{0_{accel}} = 15.7 \,\text{rad s}^{-1}$ and $\omega_{f_{accel}} = 150.8 \,\text{rad s}^{-1}$, a value of $H_{dc} \approx 20000$ was calculated.

The phase associated with the transfer function given in equation 4.13 can now be evaluated using the Bode function in MatLab. The Bode phase plot generated showed that the feedback acceleration, $\ddot{x}_f$, leads the acceleration of the structure, $\ddot{x}_s$, by an angle $E = (+0.025 \pm 0.003)^\circ$ at the 1 Hz measurement frequency.

4.4.3 Evaluation of B, the Phase Shift Generated Across the Buffer Amplifier and the Coil Driver

The phase shift B is present due to the necessity of making the measurements required to obtain k_s and δ with a signal obtained from a point earlier in the accelerometer circuitry

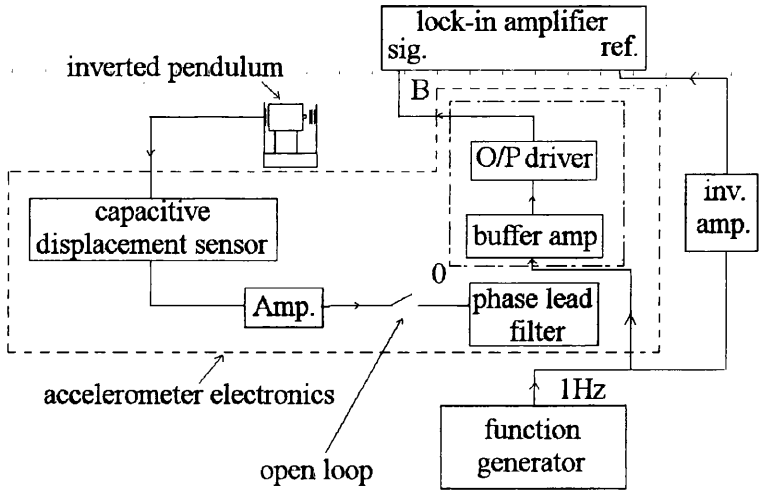

Figure 4.10: *Diagram showing the method of measuring B.*

than that of the desired signal. This was because the signal out of the coil driver was not grounded (as can be seen by referring to Figure B.2 in Appendix B.2). The relevant phase shift is that caused by the buffer amplifier and output driver.

To measure this phase the accelerometer was operated in open-loop mode. The leads from the output driver were disconnected from the coil and connected to the signal input of the lock-in amplifier. The signal from the output driver could be sent directly into the lock-in amplifier since the latter has a floating earth facility (this could not be used during the actual phase measurements because of the presence of other essential mains-earthed equipment connected in parallel e.g. an oscilloscope). A 1 Hz signal (approximating the pendulum swing) from a function generator was fed through the buffer amplifier and output driver and into the signal input of the lock-in amplifier. By comparing this signal with the 1 Hz signal from the function generator, passed through an inverting amplifier (which was assumed not to introduce any additional phase) and into the reference input of the lock-in amplifier, a measurement of the phase accumulated through the buffer amplifier and output driver could be made. This experimental configuration is shown schematically in figure 4.10. The result obtained from this measurement showed that the signal from the output driver leads the signal into the buffer amplifier by an angle of $(+0.20 \pm 0.05)°$.

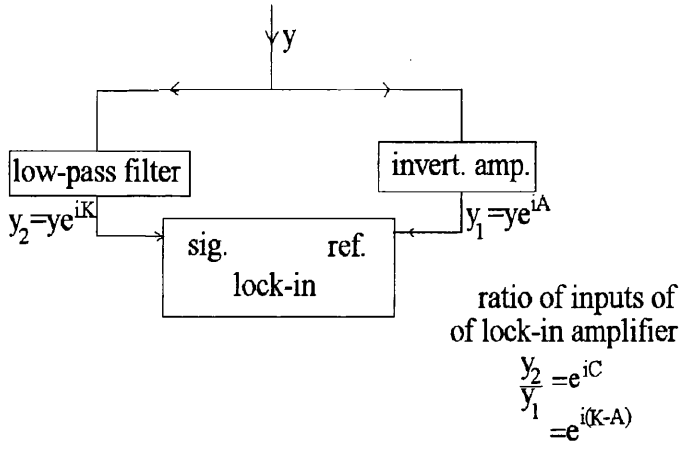

Figure 4.11: *Diagram showing the method of determining the phase contributions A and K.*

4.4.4 Evaluation of K and A, the Combined Phase Shift Accumulated Through the Low-Pass Filter, K, and the Inverting Amplifier, A

The phase shifts accumulated through the low pass filter, K, and through the inverting amplifier, A, shown in figure 4.8 can in fact be determined in combination. This was performed by first disconnecting the inputs of both the low-pass filter and the inverting amplifier from the equipment that came before it. A common 1 Hz signal (denoted by 'y' on figure 4.11) was then inserted into the inputs of both the low-pass filter and the inverting amplifier. The signal leaving the low-pass filter (which included the phase accumulated through the filter, K) was fed into the signal input of the lock-in amplifier whilst the output of the inverting amplifier (which contained the phase shift A) was connected to the reference input. Figure 4.11 shows the experimental configuration employed in this measurement. It also shows that the resultant phase, C, measured by the lock-in amplifier is the difference between the two accumulated phases i.e.

$$C = K - A \tag{4.15}$$

The combined phase angle C was determined for each new measurement of δ_m. This

was carried out to remove any effect on the measured phase resulting from any ambient temperature variations present.

It is useful to note that substitution of $C = K - A$ into equation (H) of figure 4.8 leads to the desired phase lag, δ, being expressed alternatively as

$$\delta = \delta_m + P - C - L - E - B. \tag{4.16}$$

4.4.5 Evaluation of δ for the Original Test System

Now that the various methods required to evaluate the additional phase shifts have been addressed, an experiment could be performed to determine the recoil phase lag, δ, present in the original test system.

The signal representing the force applied to the top-plate (obtained from the amplified signal from the shadow sensing of the pendulum motion) was fed into the reference channel of the lock-in amplifier. The signal representing the motion of the top-plate obtained from the accelerometer (after undergoing suitable filtering and amplification) was fed into the signal input. A phase measurement of $\delta_m = (-4.75 \pm 0.34)°$ was measured suggesting that the signal measured at the signal input lags that at the reference input of the lock-in amplifier. This measurement contains the required phase lag, δ, and all of the additional phase shifts accumulated through the various stages of the measurement.

A phase shift of $C = K - A = (-4.20 \pm 0.05)°$ was measured using the method discussed in the previous section (and represents the phase angle by which the output of the low-pass filter lags the output of the amplifier). A phase angle of $P = (-0.395 \pm 0.079)°$ was calculated in section 4.4.1 for the angle by which the output of the photodiode circuit lags the input. Section 4.4.2 contains the value of the phase introduced between the feedback acceleration and the acceleration of the structure due to operating the accelerometer in the condition of non-infinite loop gain. The value calculated shows that the feedback acceleration leads the acceleration of the structure by the angle $E = (+0.025 \pm 0.003)°$. The signal from the output driver is found to lead the signal into the buffer amplifier by an angle $B = (+0.20 \pm 0.05)°$ (refer to section 4.4.3). Finally, the decreasing amplitude

of the viscously damped pendulum swing was detected by the shadow sensor with the resulting signal recorded on a chart recorder allowing the Q to be calculated. This was then substituted into equation 4.5 to calculate the excess phase angle, L, between x_s and $\ddot{x}_s$. The resultant angle was $L = (+4.90 \pm 0.89) \times 10^{-3°}$.

The recoil phase shift, δ, by which the recoil displacement of the support structure, x_s, lags the applied force, F, can now be calculated from equation 4.16 where

$$\begin{aligned} \delta &= \delta_m + P - C - L - E - B \\ &= -(1.17 \pm 0.36)° \\ &= -(20.41 \pm 6.23) \times 10^{-3}\,\text{rad}. \end{aligned} \tag{4.17}$$

- **Recoil Limit for Original ~200 g Pendulum**

  We are now in a position to calculate the contribution to the loss factor of the original pendulum due to recoil damping. This can be done by substituting the value calculated for δ above, and the value obtained for the spring constant of the support structure, $k_s = (4.0 \pm 0.5) \times 10^5\,\text{Nm}^{-1}$ into equation B.12, together with the pendulum mass, $m \approx 0.2$ kg, and resonant angular frequency, $\omega_0 = 6.28$ rad s^{-1}. The recoil loss factor was calculated to be

$$\phi_{recoil}(\omega_0) = (4.0 \pm 1.9) \times 10^{-7}. \tag{4.18}$$

  We can also calculate what the minimum level of measurable loss factor (i.e. $\phi_{pend_{total}}(\omega_0) = \phi_{recoil}(\omega_0) + \phi_{pend_{intrinsic}}(\omega_0) + \phi_{pend_{t.e.}}(\omega_0)$) of a pendulum hanging in this structure would be. First, assume that the intrinsic loss of the material of the suspension fibres is $\phi_{mat_{intrinsic}}(\omega) \approx 5 \times 10^{-7}$. Also assume that the diameter of the fibres is $\sim 200\,\mu$m from which the thermoelastic damping contribution can be calculated (using the equations in section 2.7). The two contributions to the material loss factor can be combined and substituted into equation 2.30 to give an approximate value of

$$\phi_{pend_{intrinsic}}(\omega_0) + \phi_{pend_{t.e.}}(\omega_0) = 3 \times 10^{-9} \tag{4.19}$$

which, being less than $\frac{1}{10}\phi_{recoil}(\omega_0)$ is a negligible contribution.

The measurable loss of this pendulum is therefore

$$\begin{aligned} \phi_{pend_{total}}(\omega_0) &= \phi_{recoil}(\omega_0) \\ &= (4.0 \pm 1.9) \times 10^{-7}. \end{aligned} \tag{4.20}$$

The total measured pendulum loss for a 200 g mass reported by J. Logan was $\phi_{pend_{total}}(\omega_0) = (1.59 \pm 0.35) \times 10^{-7}$ which, within experimental accuracy, is approximately that predicted and given in equation 4.20.

There are two points worth noting from this result; firstly, recoil damping is probably the significant loss present, and secondly, the level to which the recoil limit was determined in this experiment was of very low accuracy. The reason for performing the pendulum mode loss factor experiments is to examine whether pendulums suspended by fused quartz fibres can exhibit low enough losses to be considered suitable for GEO 600. The GEO 600 specification however lies below the experimental limit to which measurements could be made in the present structure. Before any further pendulum loss experiments were performed, the rigidity of the system would need to be increased and the measurement system improved, allowing the recoil limit to be lowered and determined with far greater confidence. In an ideal system we would reduce the contribution from recoil damping to negligible proportions (i.e. $\phi_{recoil}(\omega_0) < \frac{1}{10}\phi_{pend_{total}}(\omega_0)$). However, if we can determine the level of recoil damping present to high accuracy, it is not essential to reduce its contribution to this level. Instead we can subtract the accurately known recoil contribution from the total measured loss factor to give a reliable value for the actual loss factor associated with the pendulum mode.

4.5 Improvements Made to the Experimental Apparatus

With reference to the original apparatus shown in figure 4.1, it can be seen that the vacuum tank was attached to the ion pump by a length of rigid pipe. The ion pump sat on a relatively stable trolley. However the overall stiffness was not high enough. In particular the trolley legs could flex causing the vacuum tank to rock on its ball

mountings which were distorting the bottom plate of the vacuum tank. To prevent this the ion pump was remounted on a ~700 kg concrete block. The three halved ball bearings underneath the tank were also removed and replaced by two steel discs with the third mounting point of the support being supplied by the connection to the ion pump (which was itself mounted on three points).

Once the support structure had been stiffened a greater force applied to the point of suspension was needed for a measurable magnitude of recoil acceleration. This was achieved by replacing the 1.2 kg pendulum originally used with one of 10 kg. As a result of stiffening the structure, the phase shift, δ, decreased and a more stable digital lock-in amplifier (with a phase resolution of 0.05°) had to be substituted for the analogue one (phase resolution of $\sim 0.5°$) used previously since the latter was unable to measure the smaller δ with sufficient accuracy. For reference signals of ≤ 1 Hz the digital lock-in amplifier required a TTL input. To obtain this a He-Ne laser was focussed onto a 200 μm slit cut into a flag mounted on the top of the pendulum. The pendulum was then swung. A photodiode was positioned on the opposite side of the pendulum to detect the pulses of transmitted light. The resulting signal, at twice the pendulum frequency, was amplified, sharpened with a comparator and used to trigger a JK flip-flop which generated a 1 Hz TTL output suitable for use as the reference signal of the lock-in amplifier [59].

4.6 Evaluation of k_s for the Stiffened System

A number of values of the magnitude of recoil acceleration were noted and the average calculated as $\ddot{x}_s = (3.52 \pm 0.43) \times 10^{-5}\,\mathrm{m\,s^{-2}}$. The magnitude of the recoil acceleration and the frequency of the pendulum swing can be used to find the magnitude of the displacement, $|x_s|$. The horizontal component of the applied force was evaluated by substituting the value of the maximum horizontal displacement of the pendulum, $x_p = 17.5\,\mathrm{mm}$, and the length of the suspension wire, $l = 250\,\mathrm{mm}$, into the equation $F_{pk} \approx \frac{m_p g x_p}{l}$, where m_p is the mass of the pendulum. From this a value of the rms force could be found. Using F_{rms} and $|x_s|$, the average stiffness of the structure could be calculated (by the same method as before) as $k_s = (5.49 \pm 0.67) \times 10^6\,\mathrm{N\,m^{-1}}$.

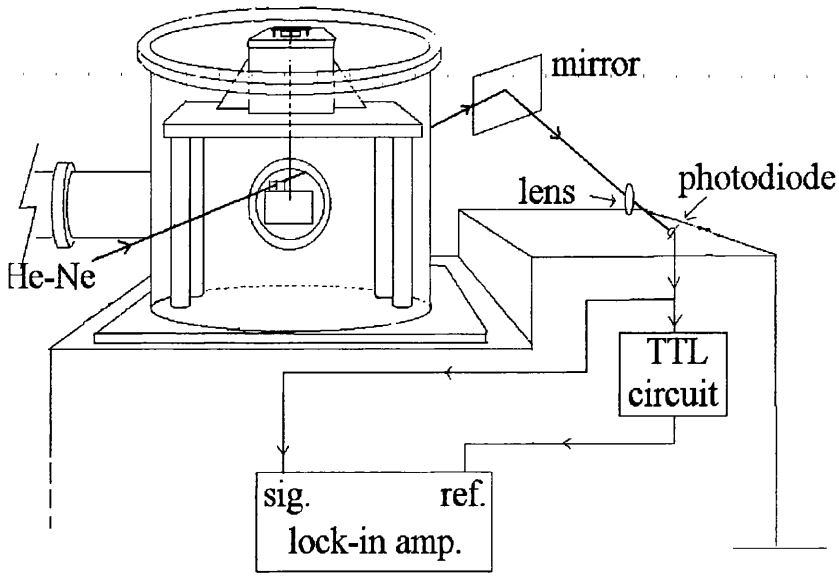

Figure 4.12: *Initial experimental method for measuring T.*

4.7 Measurement of δ for the Stiffened System

The inclusion of the TTL circuit in the apparatus raised the question of how to determine T, the phase accumulated through the TTL circuit. The most obvious method was to split the signal from the photodiode, and pass the signal into i) the TTL circuit and then on into the reference channel of the lock-in amplifier and ii) directly in to the signal channel of the lock-in amplifier. This is shown schematically in figure 4.12.

A difficulty arising from this arrangement is that the two signals fed in to the lock-in amplifier would be at different frequencies; a 2 Hz signal at the signal channel and a 1 Hz signal at the reference channel. This was remedied by creating an alternative 1 Hz input for the signal channel (representing the same information as the photodiode signal used to generate the 1 Hz TTL signal) by shadow sensing the pendulum motion using a flag and white light source as in section 4.3.3. This gives a measurement of phase between the signals from the shadow sensed pendulum (once having passed through the amplifier and filter stage and accumulating a phase K) at the signal channel of the lock-in amplifier and the output of the TTL circuit at the reference channel (having accumulated a phase shift T) and is equal to $J = K - T$. The derivation of the phase shift J is a direct analogy of the determination of the phase shift C in section 4.4.4. By switching between

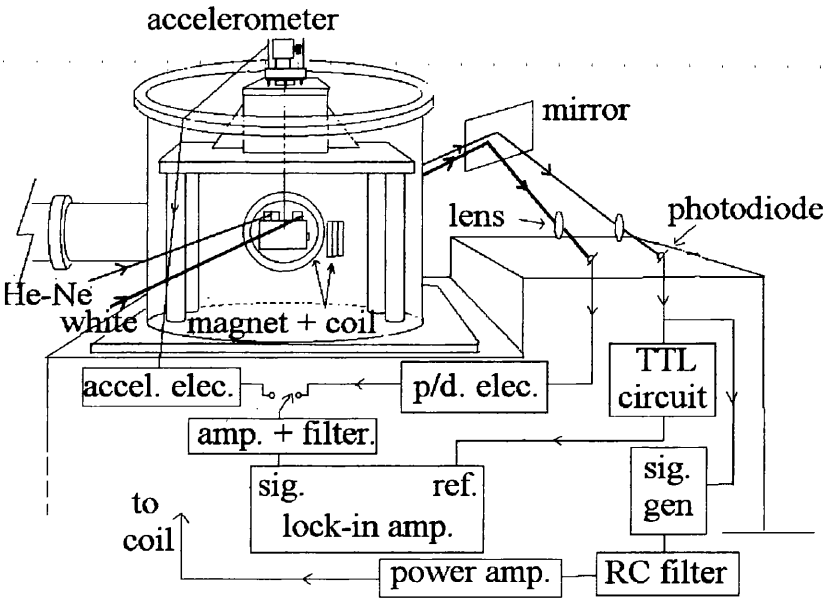

Figure 4.13: *Experimental arrangement for measuring J and δ_m.*

the signals obtained from the sensed pendulum motion using the white light source and the signal from the accelerometer, a series of successive measurements of J and δ_m (the total measured phase) could, in principle be obtained.

A further complication with this experimental arrangement resulted however from the decreasing amplitude of pendulum swing. At small swing amplitudes the phase angles J and δ_m were found to drift thus making it difficult to obtain consistent values. To overcome this problem, the pendulum swing was maintained at a constant amplitude by means of a servo system using a coil and magnet drive. The magnet was attached to one face of the pendulum with the coil positioned in front of it. A fraction of the TTL signal was used to trigger a signal generator to produce a 1 Hz signal which was then fed into the coil. To get this force in phase with the pendulum velocity an RC filter was introduced to allow adjustment of the phase of the drive signal so that the force was applied to the pendulum at the lowest point of its swing. Although the coil and magnet drive removed the problem of phase drift it introduced a further complication, that of magnetic pick-up of the drive signal by the accelerometer. This problem was overcome by switching the drive coil off during measurements involving the accelerometer (i.e. δ_m) and switching it on again for measurements of J. The final arrangement of the

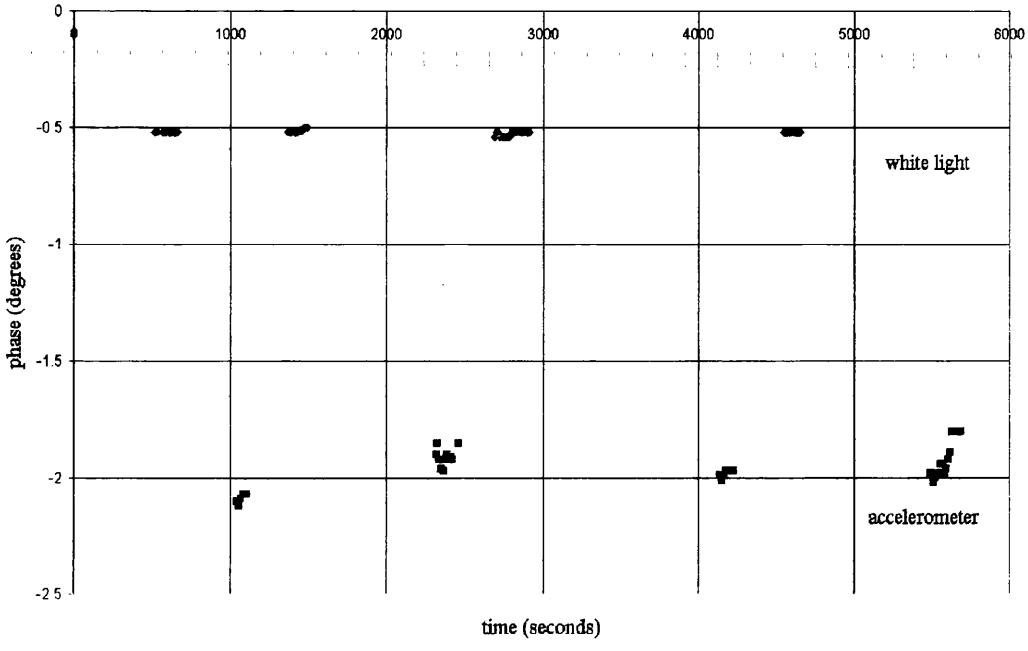

Figure 4.14: *Plot of phase data where* $J = -0.52°$ *and* $\delta_m = -1.91°$.

experimental apparatus can be seen in figure 4.13. The experimental results are shown in figure 4.14. Phase shifts, averaged over a number of successive measurements, were obtained of $J = (-0.52 \pm 0.01)°$ and $\delta_m = (-1.91 \pm 0.01)°$. A new measurement was made of the phase L, the excess phase angle between x_s and $\ddot{x}_s$, and was found to be $L = (+3.17 \pm 0.55) \times 10^{-3°}$. These phase shifts, together with the other phase shifts determined previously, were substituted into the following equation thus allowing us to find δ (the phase angle by which the displacement of the top-plate lags the applied force).

$$\begin{aligned} \delta &= \delta_m + P - J - L - E - B \\ &= -(1.61 \pm 0.06)° \\ &= -(28.06 \pm 1.05) \times 10^{-3}\,\text{rad}. \end{aligned} \tag{4.21}$$

- **Recoil Limit for a 200 g Pendulum Hung in Stiffened System**

  On substitution of the values of δ and k_s into equation B.12, the value of the contribution to the total measured loss factor due to recoil damping (for a 200 g pendulum) can be calculated as

$$\phi_{recoil}(\omega_0) = (4.00 \pm 0.48) \times 10^{-8}. \quad (4.22)$$

Knowing this, it is possible to calculate the theoretical limit to the measureable loss factor of a 200 g pendulum hung in this system. Again the pendulum mode loss associated with the suspension fibres (given in equation 4.19) is $< \frac{1}{10}\phi_{recoil}(\omega_0)$ and is considered negligible. Therefore the limit to the pendulum mode loss factor measurable in this system (for a 200 g mass) is

$$\begin{aligned} \phi_{pend_{total}}(\omega_0) &= \phi_{recoil}(\omega_0) \\ &= (4.00 \pm 0.48) \times 10^{-8} \end{aligned} \quad (4.23)$$

assuming no other losses are present. The system has thus been stiffened sufficiently to allow loss factors of the order required for GEO 600 to be measured on 200 g masses.

More importantly, now that the stiffness, k_s, and phase lag of the systems response, δ, have been determined to a far greater level of accuracy than in the first experiment, the level of recoil damping present in the system, $\phi_{recoil}(\omega_0)$, can be determined with a higher degree of confidence. We can thus subtract the accurately known contribution due to recoil damping from the measured loss factor, allowing us to determine the level of remaining loss factor associated with the pendulum mode with certainty.

4.8 Conclusions

Experiments have suggested that the original pendulum mode loss factor measurements conducted were limited by energy being lost into a recoiling pendulum support structure. The support structure was subsequently stiffened sufficiently to allow measurable losses of $\phi_{pend_{total}}(\omega_0) \approx 4 \times 10^{-8}$ for a 200 g mass (suspended by fibres of $\sim 200\,\mu$m diameter) – of the order required for a GEO 600 test mass.

By improving the measurement process, it was possible to determine the mechanical properties of the support structure (i.e. k_s, δ and hence the loss contribution, $\phi_{recoil}(\omega_0)$)

to a higher level of accuracy for the stiffened system. This has afforded us the possibility of safely subtracting the recoil contribution, $\phi_{recoil}(\omega_0)$, from all subsequent measurements of the pendulum mode loss factor, thereby allowing a more accurate prediction of the remaining losses present in the measured loss factor.

Chapter 5

Loss Factor Measurements of Pendulums Suspended from Carbon Steel Wires

5.1 Introduction

A discussion which outlines the GEO 600 specification for the acceptable level of thermal noise at 50 Hz associated with the pendulum mode of one full sized test mass suspension (i.e. 16 kg) can be found in section 2.8. The level of the power spectral density of thermal motion, $\tilde{x}^2_{pend}(\omega)$, associated with this mode was specified to be an order of magnitude lower than the estimated power spectral density of thermal motion associated with the internal modes of the test mass and is equivalent to a rms thermal displacement of $\tilde{x}_{pend}(\omega) = 2.2 \times 10^{-20}\,\mathrm{m}/\sqrt{\mathrm{Hz}}$ at 50 Hz. This noise level can also be expressed as a total loss factor due to the pendulum mode of $\phi_{pend_{total}}(\omega) = 3.7 \times 10^{-8}$ at 50 Hz. Recall from Chapter 2 that the theoretical limit to the level of loss that is obtainable for the pendulum mode is given by equation 2.30 i.e.

$$\phi_{pend_{total}}(\omega) = \phi_{mat_{total}}(\omega)\xi n\frac{\sqrt{TEI}}{2mgl}$$

where $\phi_{mat_{total}}(\omega)$ is the total material loss factor of the suspension wire or fibre material and the remaining terms are defined in section 2.6.1. From equation 2.30 it is clear that one of the factors that determines the level of $\phi_{pend_{total}}(\omega)$ that can be achieved at a given frequency is the total loss of the material, $\phi_{mat_{total}}(\omega)$, used to suspend the test mass. The maximum acceptable total material loss factor for a given suspension material can be calculated from equation 2.30 using the appropriate parameters for a GEO 600 suspension, and has the values

- $\phi_{mat_{total}}(\omega) = 1.2 \times 10^{-5}$ at 50 Hz for carbon steel
- $\phi_{mat_{total}}(\omega) = 5.1 \times 10^{-6}$ at 50 Hz for fused quartz

(these numbers were calculated for four suspension wires/fibres tensioned to $\frac{1}{3}$ of the tensile strength of the material in question – refer to Chapter 3). Assuming that all external loss mechanisms are negligible, the total material loss is the sum of the intrinsic loss factor of the material, $\phi_{mat_{intrinsic}}(\omega)$, and a possible contribution $\phi_{mat_{t.e.}}(\omega)$ due to thermoelastic damping (both of which have been discussed in Chapter 2). Measurements have shown that it is likely that the material loss factor is structural [47] in nature (i.e. $\phi_{mat_{intrinsic}}(\omega)$ is constant at all frequencies). The magnitude of the thermoelastic loss however varies with frequency about a maximum value defined by the properties of the material.

The level of loss due to thermoelastic damping in a 222 μm diameter wire made of carbon steel (suitable for suspending a GEO 600 test mass) was calculated to be $\phi_{mat_{t.e.}}(\omega) = 3.21 \times 10^{-4}$ at 50 Hz. This loss is considerably higher than the required material loss factor already quoted for carbon steel showing that carbon steel cannot meet the GEO 600 specification. The contribution at 50 Hz due to thermoelastic damping from fused quartz (for a fibre of 440 μm diameter suitable for use in GEO 600) is much lower than carbon steel i.e. $\phi_{mat_{t.e.}}(\omega) = 5.6 \times 10^{-7}$. Its intrinsic loss factor, $\phi_{mat_{intrinsic}}(\omega)$, is also low (as calculated from the measured $\phi_{mat_{total}}(\omega)$ in Chapter 3). This means that the total material loss factor of fused quartz at 50 Hz is below the maximum acceptable loss for fused quartz, $\phi_{mat_{total}}(\omega) = 5.10 \times 10^{-6}$, therefore making it a suitable candidate for the suspension material of the GEO 600 test masses.

Even although carbon steel does not meet the GEO 600 specification there are two reasons

for studying the use of carbon steel as a suspension material;

- with the exception of GEO 600, all of the first stage detectors belonging to the major laser interferometric gravitational wave detector projects around the world are being constructed with the suspended components being hung on steel wires.
- there are many suspended elements in GEO 600 other than the test masses (e.g. the reaction masses and intermediate masses) whose thermal noise requirements are not as stringent as those of the test masses. These will be hung on steel wires.

It is therefore interesting to study the level of loss factor that is obtainable experimentally from such suspensions.

Measurements of the material loss factor made on a spring formed from carbon steel wire of 127 μm diameter were reported in Chapter 3. The measured loss factor was $\phi_{mat_{total}}(\omega) = (1.58 \pm 0.15) \times 10^{-4}$ (measured at a resonant frequency of 2.6 Hz). To translate this into the loss factor associated with the pendulum mode that is achievable by a GEO 600 test mass suspension at 50 Hz we must

- calculate the thermoelastic damping contribution within the measured material loss factor for a wire of diameter and resonant frequency the same as the tested wire. This was shown (in section 3.2) to be negligible. The measured loss is therefore assumed to be the intrinsic loss factor, $\phi_{mat_{intrinsic}}(\omega)$.
- add to this the thermoelastic loss factor calculated for a 222 μm diameter GEO 600 suspension wire at 50 Hz (i.e. $\phi_{mat_{t.e.}}(\omega) = 3.21 \times 10^{-4}$) to give a $\phi_{mat_{total}}(\omega) = (4.79 \pm 0.15) \times 10^{-4}$ at 50 Hz
- finally, substitute this into equation 2.30 to calculate the lowest achievable loss factor associated with the pendulum mode at 50 Hz, $\phi_{pend_{total}}(\omega) = (1.53 \pm 0.05) \times 10^{-6}$.

This value of the pendulum mode loss factor is equivalent to a rms thermal displacement of $(1.43 \pm 0.05) \times 10^{-19}$ m/$\sqrt{\text{Hz}}$ at 50 Hz, a factor of $\sim 6.5 \times$ higher than the GEO 600 specification.

By measuring the loss factor associated with the pendulum mode of pendulums suspended from carbon steel wires it was hoped that information would be obtained about how best to construct suspensions of this kind without introducing excess losses (such as losses in the clamps) and thus degrading the thermal noise levels further.

5.2 Construction of the Initial Test Pendulums Suspended by Carbon Steel Wires

Before embarking on the construction of a test pendulum suspended from carbon steel wires, care was taken to find a method of clamping the wire ends that allowed a reasonable amount of clamping pressure to be applied to the wire in an attempt to minimise losses associated with the clamp. Precision engineered pin-vices appeared to provide a suitable solution. Pin-vices are obtainable in a variety of different bore sizes. It is therefore possible to find a pin-vice that fits tightly the wire diameter in question. The precision engineering of the bore of the pin-vice further ensures that there is good contact between the wire and pin-vice. Figure 5.1 shows a photograph of the type of pin-vice used to clamp the ends of the carbon steel wire. The test pendulum was constructed by first inserting the ends of two 25 cm lengths of 178 μm diameter carbon steel wire into the pin-vices. These were tightened onto the wire by hand. The pin-vices at the bottom ends of both wires were glued to opposite edges of a 210 g glass plate that formed the pendulum mass as shown in figure 5.2. The pin-vices at the opposite ends of the wires were inserted into two clamps machined from an aluminium plate. A schematic diagram of these clamps can be seen in figure 5.3. Tightening the nuts (shown in the diagram) squeezed the jaws of the clamps onto the pin-vices thus clamping them firmly into position. Finally, a small flag was attached to the underside of the pendulum.

The pendulum was lowered into position inside the vacuum tank (as can be seen with reference to figure 5.4). The suspension plate, now resting on the 'top-hat', was prevented from moving by two aluminium cross-pieces tightened into the top-hat. The tank was evacuated by an oil diffusion pump (backed by a rotary pump) in parallel with an ion pump, to a pressure of the order of 10^{-7} mbar. This level of vacuum pressure was employed to ensure that the longitudinal pendulum mode was not subject to significant

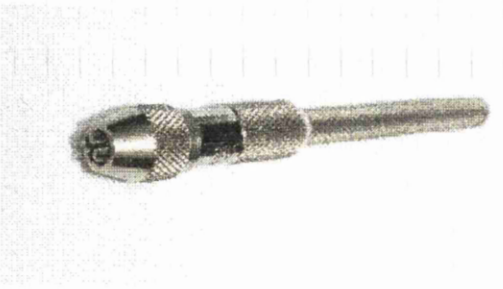

Figure 5.1: *Photograph of pin-vice used to clamp the ends of the carbon steel wires (length of pin-vice is* $\sim 7\,cm$*).*

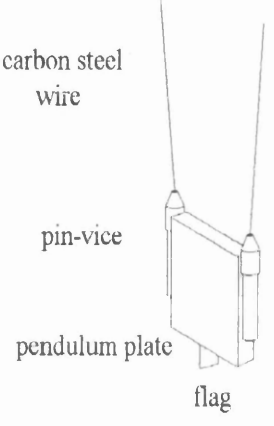

Figure 5.2: *Pendulum suspended by carbon steel wire with wire attachments made using pin-vices.*

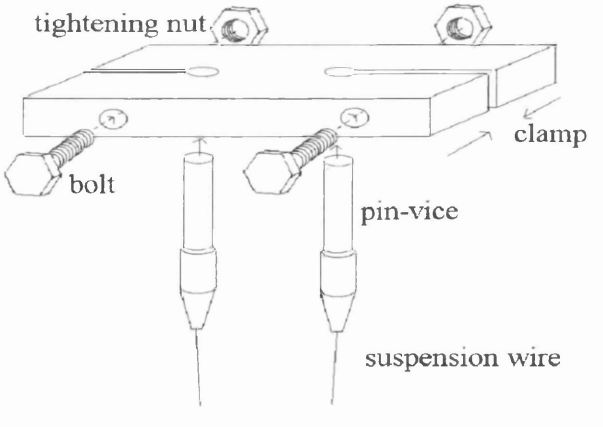

Figure 5.3: *Diagram of the suspension plate.*

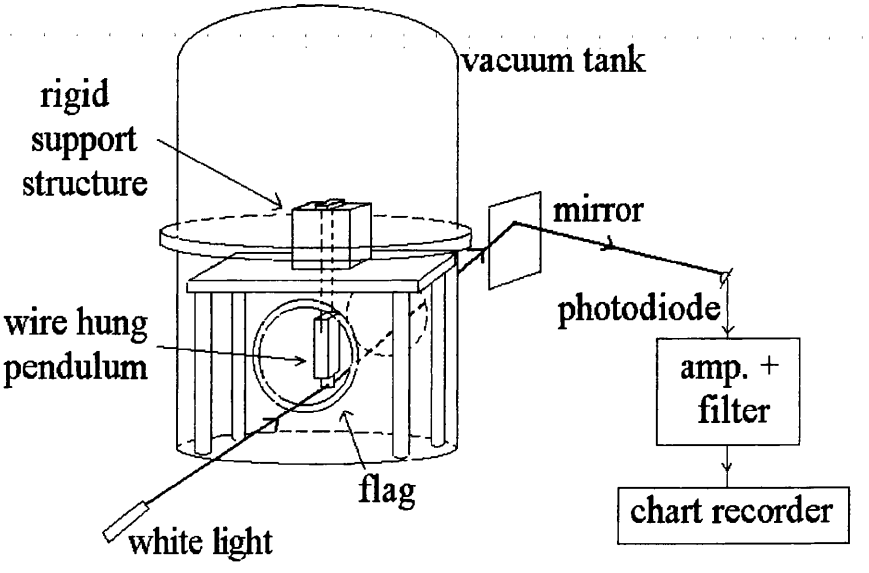

Figure 5.4: *Experimental apparatus used in the measurement of the pendulum mode loss of pendulums suspended by carbon steel wires.*

levels of gas damping (this can be checked by substitution of the parameters of this experimental system into equation A.13).

5.3 Initial Results Obtained from Measurement of the Pendulum Mode Loss Factor of a Pendulum Suspended by Carbon Steel Wires

5.3.1 Experimental Apparatus

The pendulum mode was excited by means of a coil and magnet 'pusher' inside the vacuum tank. This was constructed from a thin metal lever attached at one end to a point half way down the length of a small retort stand. A magnet was mounted on one side of the lever whilst a short length of fused quartz rod was attached to the other. A small conducting foam pad was mounted to the end of the fused quartz rod. A coil was then positioned on the retort stand behind the magnet. Figure 5.5 is a schematic diagram of the pendulum pusher. The passage of current through the coil repelled the

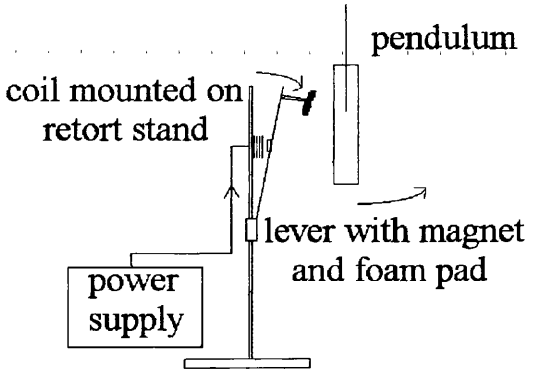

Figure 5.5: *Diagram of the pendulum 'pusher'.*

magnet. This in turn caused the foam pad to push the pendulum. The current in the coil was cut off rapidly enough to allow the lever to spring back into its initial position ensuring that the pendulum could swing freely.

The amplitude decay of the longitudinal pendulum mode was detected by the use of a shadow sensing technique in which a beam of white light was shone across the vacuum tank. The light beam was partially obscured by the flag attached to the underside of the swinging pendulum. A photodiode positioned behind the pendulum was used to detect the change in intensity of the light passing the flag. The signal from the photodiode was filtered, amplified and recorded on a chart recorder. A diagram of the apparatus used can be seen in figure 5.4.

5.3.2 Experimental Results

In figure 5.6 a plot of $ln(amplitude)$ versus time, t, is shown for a typical amplitude decay. The initial amplitude of the swinging pendulum was measured to be $\sim 4\,\mathrm{mm}$.

The total loss factor, $\phi_{pend_{total}}(\omega_0)$, measured at the pendulum mode frequency, is proportional to the gradient of this graph and can be found from $\phi_{pend_{total}}(\omega_0) = -\frac{2}{\omega_0} \times gradient$ where ω_0 is the resonant angular frequency of the pendulum (refer to section 2.5).

The plot in figure 5.6 is divided into two sections of different gradients. The best fit line through the first section of the plot corresponds to a loss factor of $\phi_{pend_{total}}(\omega_0) =$

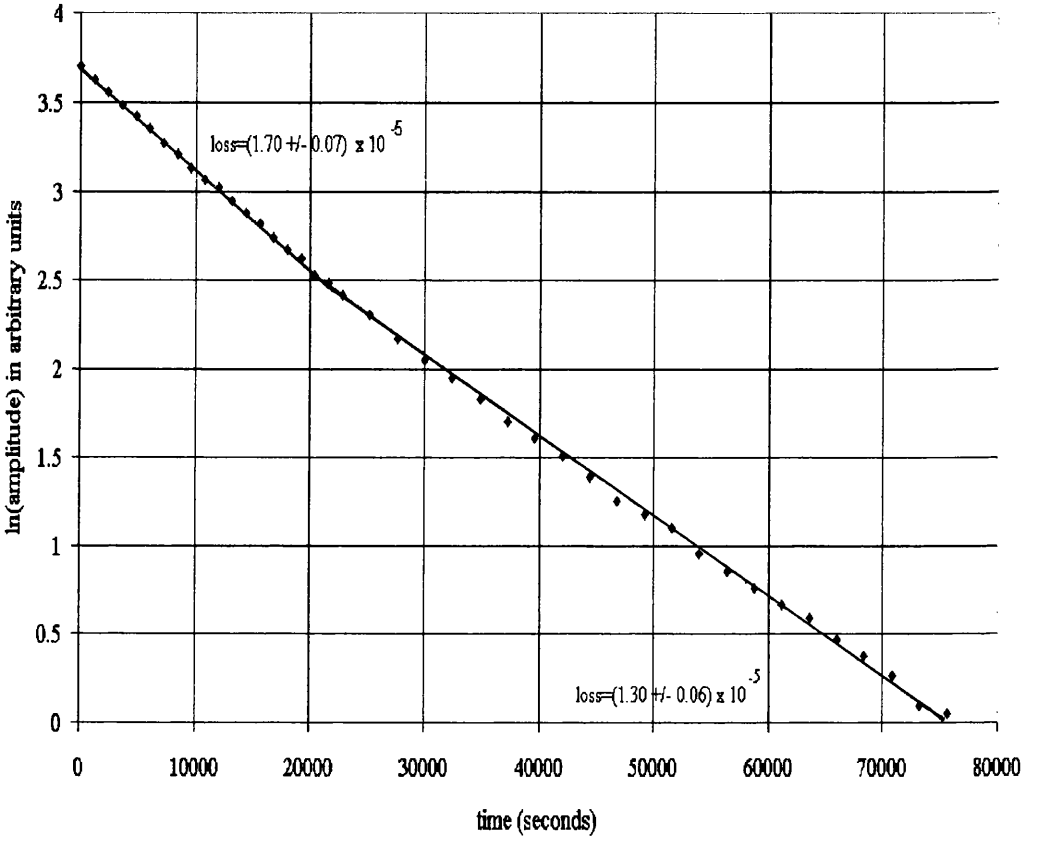

Figure 5.6: *Logarithmic fit to amplitude decay of 210 g pendulum suspended by 178 μm diameter carbon steel wires.*

$(1.70 \pm 0.07) \times 10^{-5}$. The gradient decreases in the second section of the plot and corresponds to a loss factor of $\phi_{pend_{total}}(\omega_0) = (1.30 \pm 0.06) \times 10^{-5}$. From this we can conclude that there exists an additional, excess loss in the first section of the graph. By extrapolating the best fit lines of both sections of the graph to the point where they intersect, an approximate time can be found where the effect of the excess damping ceases to have a significant effect. This 'knee' occurs at a time ~21600 s after the pendulum was set in motion. Over this time interval the swing amplitude was found to have decreased from the initial amplitude of ~ 4 mm to ~ 1 mm. Two possible explanations were considered for the change in the decay constant of the amplitude decay. These will be discussed in the following section.

5.4 Possible Explanations for the Observed Change in Decay Constant of the Amplitude Decay

The two explanations considered were

1. a non-linearity in the method employed to sense and record the amplitude decay of the pendulum motion
2. the possibility of an amplitude dependent damping originating at the interface between the suspension wire and the pin-vice.

1. Non-linearities can be introduced by the chart recorder, the amplifier, the shape of the light beam itself and the photodiode sensing the light. These will be considered in turn.

1(A). The photodiode signal was amplified and then passed to the chart recorder. In the course of an experiment, the amplitude of the photodiode signal decreased and the gain of the amplifier was increased at various points to maintain a chart recorder trace that was of approximately constant amplitude throughout. This was done to ensure that the chart recorder operated in the same amplitude range during the experiment therefore eliminating any non-linearity that may have been introduced by it. It was postulated however that a non-linearity may have been introduced at the gain switching points of

the amplifier. To check for this, an accurately known voltage at the pendulum frequency was applied to the amplifier. The output voltages were found to be in accordance with the gain settings. Switching the gain of the amplifier was therefore ruled out as a cause of the change in decay constant.

1(B). Variation in intensity across the diameter of the light spot could introduce a non-linearity, however, an effort was made (by using a light bulb with a small filament and a focussing collimator) to ensure that the light source produced a beam that was of approximately constant intensity across the field. The circular profile of the light beam could however mean that the intensity of the light detected passing the flag was not directly proportional to the amplitude of swing at large amplitudes. Consider the following:

The signal intensity at the photodiode is proportional to the 'area' of light passing the flag, A_{pass}. This area is

$$A_{pass} = \int_x^R \sqrt{R^2 - x^2} dx. \tag{5.1}$$

where x is the swing amplitude and R is the radius of the light beam. This signal intensity oscillates about a d.c. offset. The level of this offset is determined by the signal intensity when the pendulum is at rest i.e.

$$A_0 = \int_0^R \sqrt{R^2 - x^2} dx. \tag{5.2}$$

The signal that was sent to the chart recorder however was the detected signal minus the d.c. offset (which was removed by adding to the detected signal a d.c. signal of equal magnitude and opposite sign to that of A_0):

$$\begin{aligned} A &= \int_0^R \sqrt{R^2 - x^2} dx - \int_x^R \sqrt{R^2 - x^2} dx \\ &= \int_0^x \sqrt{R^2 - x^2} dx \end{aligned} \tag{5.3}$$

which is equivalent to the 'area' of the light beam obscured by the flag (and is marked A on figure 5.7).

We can compare the real case of the circular beam profile to that of the 'ideal' case of a square beam profile. The area of light obscured by the flag in the case of a square beam would be directly proportional to the swing amplitude e.g. $\frac{dA}{dx} = constant$. This can be seen with reference to curve (i) in figure 5.8. However, using equation 5.3 we see that $\frac{dA}{dx} \neq constant$ for the case of the circular beam profile. We can find the actual relationship between A and x by using equation 5.3 to calculate A as a function of x. For ease we use the substitution $x = Rsin\theta$ in equation 5.3 which gives

$$A = \int_0^{Rsin\theta} \left(\sqrt{R^2 - R^2 sin^2\theta}\right) Rcos\theta d\theta \tag{5.4}$$

which can be solved to give

$$A = \frac{R^2}{2}\left(\frac{1}{2}sin2\theta + \theta\right)_0^{Rsin\theta}. \tag{5.5}$$

Transforming back into 'x' (using the substitution $sin\theta = \frac{x}{R}$) we find

$$\begin{aligned} A &= \frac{R^2}{2}\left(\frac{x}{R}\sqrt{1 - \left(\frac{x}{R}\right)^2} + sin^{-1}\frac{x}{R}\right)_0^x \\ &= \frac{R^2}{2}\left(\frac{x}{R}\sqrt{1 - \left(\frac{x}{R}\right)^2} + sin^{-1}\frac{x}{R}\right). \end{aligned} \tag{5.6}$$

Curve (ii) in figure 5.8 is a plot of the area of the obscured beam, A, versus swing amplitude, x, (where $R \sim 1.5$ cm is a typical radius of the circular light beam).

By examining figure 5.8, two points can be noted for the case of large swing amplitudes:

- the area, A, obscured by the flag for a given x is less than that obscured in the ideal case

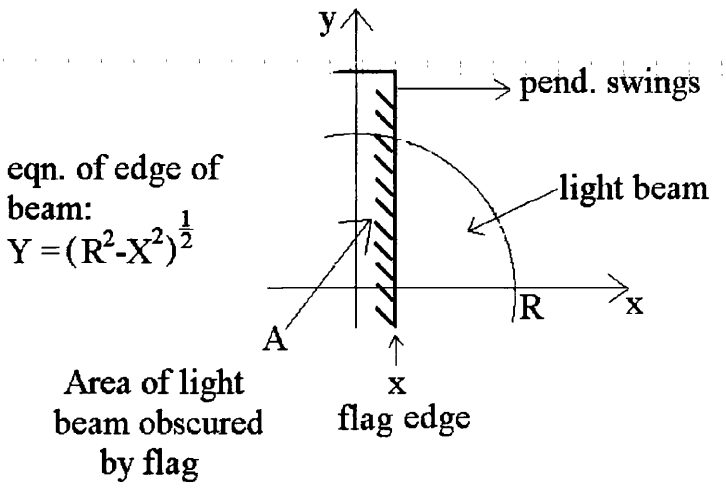

Figure 5.7: *Diagram of half of the light beam shone across the flag of the swinging pendulum.*

- the change in A for a given change in x is smaller than that observed in the ideal case.

The second point allows us to deduce that if the initial amplitude had fallen in the strongly non-linear region, the loss factor measured would have been smaller than the actual loss factor associated with the pendulum mode. This would have eventually increased to the expected value once the pendulum had decayed into the region that gave a response that was approximately linear. This effect is opposite to that observed (refer to figure 5.6) and was therefore dismissed as the source of change in measured loss [1].

1(C). As the pendulum swings the position of the light beam that passes the flag shifts on the photodiode. The response of the photodiode cannot be assumed to be linear over the entire surface. To ensure that the observed change in loss factor was not due to the light falling on a region of the photodiode with a different response, the light was focussed onto the central region of the photodiode. A nonlinearity introduced by the photodiode was therefore disregarded as the source of the change in measured loss factor.

[1] It should be noted that at amplitudes $<\sim 5$ mm the response is essentially linear.

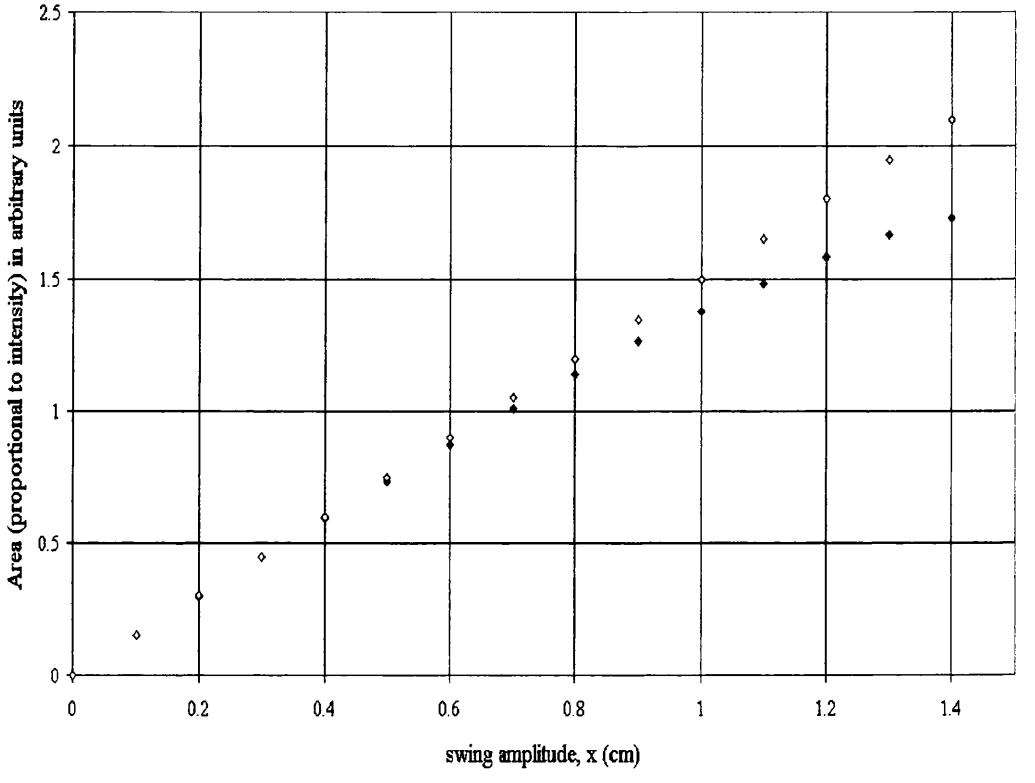

Figure 5.8: *Plot of A as a function x. Curve (i) ('unfilled' points) shows the 'ideal case' (dimensions of the square beam profile are taken as 2R, where $R \sim 1.5\,cm$). Curve (ii) ('solid' points) shows the real case of a circular beam profile of radius, R.*

2. Our attention was then turned to the possibility of additional damping arising between the pin-vice and the suspension wire, also referred to as 'stick-slip' damping [45]. As the pendulum swings in the longitudinal mode the suspension wires bend at the point where they enter the upper pin-vices. 'Stick-slip' damping arises in the pin-vices at the point of suspension of the pendulum; for amplitudes above a particular value, x, the shear stress required to hold the wire in the clamp exceeds the value that can be provided by the clamp due to the material having a finite coefficient of static friction. At swing amplitudes greater than x the bending wire rubs within the clamp. This friction causes an excess loss and thus an increase in the value of observed $\phi_{pend_{total}}(\omega_0)$. One would therefore expect two levels of damping to be observable depending on whether the neccessary clamping stresses were overcome or not.

To estimate the level of amplitude, x, below which 'stick-slip' damping is negligible we need to calculate the magnitude of the shear force per unit area existing in the clamp.

As the pendulum swings the wire applies a peak shear stress averaged over the surface of the pin-vice of

$$S = \frac{4rG}{\pi R} \tag{5.7}$$

(derived in figure 5.9) where G is the shear modulus of carbon steel, r is the radius of the suspension wire and R is the bending radius of the wire in the region near the point of suspension. R is of the form [45]

$$R = \frac{EI}{C_f \theta}. \tag{5.8}$$

In equation 5.8, E is the Young's Modulus of carbon steel ($E = 2.1 \times 10^{11}$ Pa) and I is the moment of cross sectional area ($I = \frac{\pi r^4}{4}$). θ is the angular displacement of the pendulum from its equilibrium position and $C_f\theta$ is the sum of the elastic and gravitational restoring torques (where C_f takes the form $C_f \approx \sqrt{TEI}$ for small θ, and T is the tension per wire) [45].

Substituting equation 5.8 into equation 5.7 gives the expression

1. At the peak displacement of the pendulum swing the max. shear stress occurs at the point of max. bending (marked 'A' on figure). The max. shear stress can be calculated:

from geometry

$$\frac{y-x}{x} = \frac{b-a}{a}$$

$$\frac{2r}{R} = \frac{b-a}{a}$$

shear strain = $\tan\theta = \frac{b}{y} = \frac{e}{2r}$

and $\tan\theta \sim \theta$ when $a \ll R$.

We know that $2r \ll R$.

We can consider a 'square' element of the wire such that $2r \sim a$ and thus

$$\theta = \frac{b}{y} = \frac{2r+e}{R+2r}$$

(where $2r \gg e$ and $R \gg 2r$)

$$\Rightarrow \theta = \frac{2r}{R}$$

and shear stress = $S_{max} = G\dot{\theta} = \frac{2Gr}{R}$ at peak x.

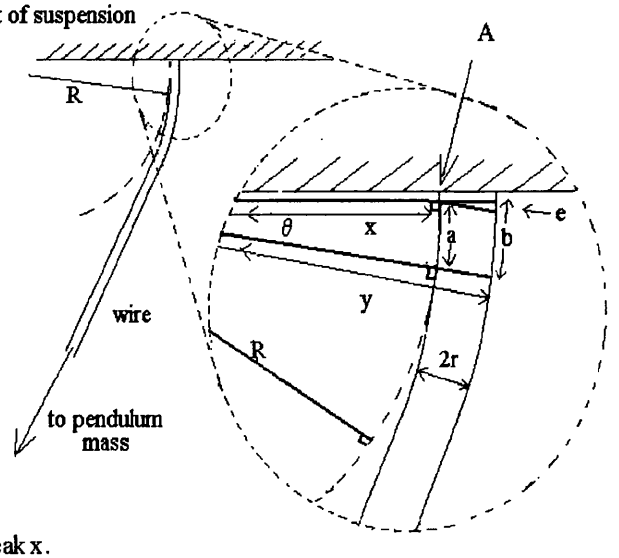

2. A quarter of the way around the wire from position 'A' the shear stress is at a minimum. We can calculate the average shear stress, S over half of the wire (during half of the pendulum cycle):

stress at element 'B' is $\frac{2hG}{R} = \frac{2Gr}{R}\sin\alpha$

Average stress over half wire, $S = \dfrac{\frac{2Gr}{R}\int_0^{\pi}\sin\alpha\, d\alpha}{\int_0^{\pi} d\alpha} = \frac{4Gr}{\pi R}$.

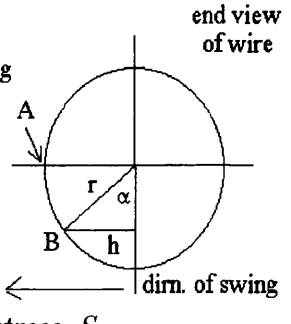

Figure 5.9: *Derivation of expression of the shear stress, S.*

$$S = \frac{8G\theta\sqrt{T}}{\pi r\sqrt{\pi E}}. \tag{5.9}$$

Further substitution of $\theta \approx \frac{x}{l}$ (where x is the swing amplitude and l the length of the suspension wire) leads to

$$S = \frac{8Gx\sqrt{T}}{\pi rl\sqrt{\pi E}} \tag{5.10}$$

where the shear stress applied to the clamp can be seen to be amplitude dependent.

The actual shear reaction force per unit area that can be applied by the pin-vice to the wire, $\frac{F_{actual}}{A_c}$, is

$$\begin{aligned} \frac{F_{actual}}{A_c} &= \frac{\mu F_N}{A_c} \\ &= \frac{T\gamma}{A_c} \end{aligned} \tag{5.11}$$

where A_c is the area of over which the normal force, F_N, acts and equals the area of contact between the wire and clamp, μ is the coefficient of static friction and γ is a measure of tightening of the pin-vice.

If there is to be no significant additional loss exhibited due to the effect of 'stick-slip' damping, the actual clamping force per unit area applied to the wire, $\frac{F_{actual}}{A_c}$, must be greater than the average shear stress applied by the wire, S, i.e.

$$\frac{F_{actual}}{A_c} > S \tag{5.12}$$

which, on appropriate substitutions for the two terms, leads to

$$\frac{T\gamma}{A_c} > \frac{8Gx\sqrt{T}}{\pi rl\sqrt{\pi E}}. \tag{5.13}$$

The above inequality can be rearranged to give the size of the swing amplitude at which the effect of 'stick-slip' damping in the pin-vice no longer causes significant additional damping. In other words, a 'knee' will occur at an amplitude

$$x < \frac{\gamma r l \pi \sqrt{\pi E T}}{8 G A_c}. \tag{5.14}$$

There are two unknown parameters, γ and A_c, that must first be determined before it is possible to calculate the swing amplitude, x, below which there is a negligible contribution to the overall level of damping from 'stick-slip'.

- Determination of the Tightening Factor, γ

  A length of the suspension wire was attached to an empty container. The other end of the wire was inserted into a pin-vice identical to that used to clamp the wires in the pendulum loss measurements. The pin-vice was tightened on to the wire in a manner similar to that used during the construction of the test pendulum. The empty container was then suspended from the pin-vice and wire. Further mass was slowly added to the suspended container until the wire began to slip from the clamp. This happened when a total of 270 g was suspended from the wire. The tightening factor is therefore $\gamma = 2.6$ since the mass required to cause the wire to slip was $2.6\times$ larger than the mass suspended by one wire during the loss experiments. An error of $\pm 10\,\%$ was added to this factor to represent the uncertainty involved in tightening the pin-vice onto the test wire to the same degree as was used in the loss experiments.

- Determination of the Area, A_c, over which the Clamping Force Acts

  A piece of enamelled copper wire (of approximately the same diameter as the steel wire) was inserted into a pin-vice. The pin-vice was tightened onto the wire to leave an indentation in the softer wire. The pin-vice was then undone and the wire removed. The length of the indent left in the wire was measured as $l_{indent} = (270 \pm 27)\,\mu$m. From this length and the diameter of the suspension wire, $d = 178\,\mu$m, the area, A_c, was obtained. This area, approximating the area of contact between the pin-vice and the wire, can be obtained from $A_c = \pi d l_{indent}$ and is equal to $(1.51 \pm 0.15) \times 10^{-7}\,\mathrm{m}^{-2}$.

We now have values for all of the parameters in equation 5.14.

These are $E = 2.1 \times 10^{11}\,\mathrm{Pa}$

$T = 1.03\,\mathrm{N}$

$\gamma = 2.6 \pm 0.3$

$r = 89\,\mu\mathrm{m}$

$l = 0.250 \pm 0.003\,\mathrm{m}$

$G = 8.1 \times 10^{10}\,\mathrm{Pa}$

and $A_c = (1.51 \pm 0.15) \times 10^{-7}\,\mathrm{m}^{-2}$.

Substituting these values into equation 5.14 gives an estimate of the upper limit to the amplitude where the 'knee' occurs. The amplitude is found to be $x = 1.5 \pm 0.3$ mm.

This approximately corresponds to the amplitude at which the level of damping changed in the experimental results shown in figure 5.6. It was concluded that 'stick-slip' damping was the cause of the additional loss in the first 21600 s of the experimental run. This source of loss had a negligible effect at an amplitude of less than $\sim$1 mm.

There are two points worth noting:

- Tightening the pin-vices (and therefore increasing the factor γ) should result in an increase in size of the amplitude below which 'stick-slip' damping is no longer significant.
- By expanding the wire/fibre diameter into thicker sections for insertion into the clamp we can reduce the effect of 'stick-slip' damping. This has the effect of moving the bending region of the wire/fibre downwards and out of the jaws of the clamp. Doing this helps to reduce the shear stress at the edge of the clamp and hence reduce the tendency for the wire/fibre to slip.

Returning to the results given in figure 5.6, the minimum value of the pendulum mode loss factor measured at 1 Hz can be compared to the level of expected pendulum mode loss factor calculated from equation 2.30 given the material loss factor, $\phi_{mat_{total}}(\omega_0)$. In section 3.2, results were reported for the measured material loss factors of two different thicknesses of carbon steel wires; 178 μm diameter wire (as used to suspend the

material loss	pendulum loss		
measured $\phi_{mat_{intrinsic}}(\omega)$	predicted $\phi_{pend_{total}}(\omega_0)$ at 1 Hz for 178 μm wire	best measured $\phi_{pend_{total}}(\omega_0)$ at 1 Hz for 178 μm wire	factor $\frac{measured}{predicted}$
$(4.54 \pm 0.40) \times 10^{-4}$ for 178 μm wire	$(2.88 \pm 0.32) \times 10^{-6}$	$(1.30 \pm 0.06) \times 10^{-5}$	~ 4.5
$(1.58 \pm 0.15) \times 10^{-4}$ for 127 μm wire	$(1.00 \pm 0.10) \times 10^{-6}$	$(1.30 \pm 0.06) \times 10^{-5}$	~ 13

Table 5.1: *Comparison of observed $\phi_{pend_{total}}(\omega_0)$ and predicted $\phi_{pend_{total}}(\omega_0)$. Predicted level of $\phi_{pend_{total}}(\omega_0)$ is calculated from the intrinsic material losses, $\phi_{mat_{intrinsic}}(\omega_0)$, reported in section 3.2. Column 4 gives the factor by which the observed pendulum loss is higher than the predicted value.*

test pendulum under discussion) and 127 μm diameter wire. The 127 μm diameter wire displayed the lower loss factor of the two samples and was believed at the time to be a more realistic level for $\phi_{mat_{intrinsic}}(\omega)$. It was postulated that there may have been an excess loss present in the measurements performed on the 178 μm diameter wire. For completeness in table 5.1, the lowest level of measured loss factor of the pendulum mode (i.e. $\phi_{pend_{total}}(\omega_0) = (1.30 \pm 0.06) \times 10^{-5}$), is compared with that predicted from the measured material loss factors of both diameter wires.

Comparison of the measured result with the predicted loss show that an excess loss was exhibited in the measured pendulum loss factor.

5.5 Cause of the Excess Loss Present in the Initial Measurement

Two possible sources of the excess loss are

- damping due to eddy currents induced in the pin-vices swinging in a magnetic field gradient
- hysteresis loss in the ferromagnetic pin-vices swinging in a magnetic field gradient.

An estimate of the level of loss attributable to each of these damping mechanisms was made (the calculation of the levels of loss associated with eddy current and hysteresis damping can be found in Appendix C). The expected loss in both instances was found to be too small to have caused any noticeable effect. They were both therefore dismissed as the cause of the excess loss. Some other loss mechanism was causing the observed effect. This topic is investigated in the discussion below.

In the period between measuring the pendulum mode loss factor (reported in section 5.3) and the following investigation, the pendulum was removed from the vacuum tank to allow a number of unrelated experiments to be performed. When it was time to return the pendulum to the test structure, it was noted that at some time in the intervening period one of the suspension wires had slipped through its pin-vice. The upper pin-vices were undone, the wire lengths adjusted and both of the pin-vices then retightened, this time using pliers. The pendulum was then re-hung in the tank. The only significant change to the experimental system was an increase in the clamping force at the upper pin-vices. The tank was evacuated and the pendulum re-swung. The pendulum mode loss factor was re-measured using the same method as was employed before. The results are shown in figure 5.10.

With reference to figure 5.10 the pendulum mode loss factor obtained in the first section of the amplitude decay was $\phi_{pend_{total}}(\omega_0) = (3.87 \pm 0.34) \times 10^{-6}$ decreasing to $\phi_{pend_{total}}(\omega_0) = (1.78 \pm 0.14) \times 10^{-6}$ in the second section of trace. A break in slope appears at a swing amplitude of 0.17 mm.

There are a number of observations worth noting in comparing the results presented in figure 5.6 ('experiment 1') and figure 5.10 ('experiment 2') which help us to understand what the source of additional damping present is in the initial pendulum mode loss measurement:

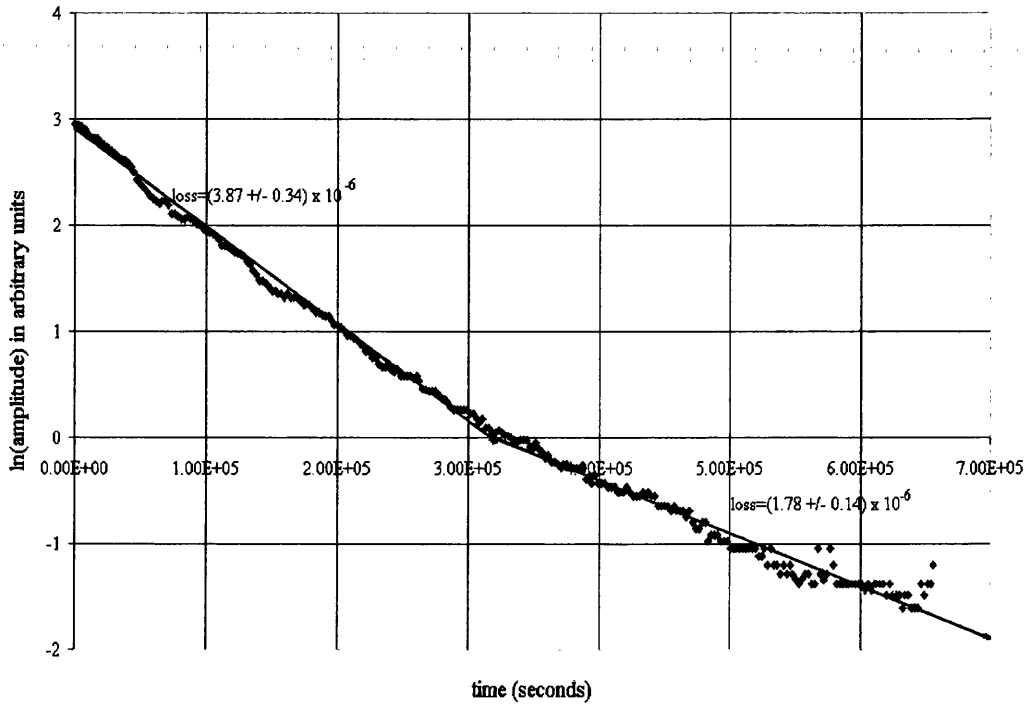

Figure 5.10: *Measurement of the amplitude decay of the pendulum after tightening of the pin-vices.*

1. If the only excess loss mechanism present in each of the two measurements was 'stick-slip' damping we would not expect to see any change in loss factor between the second sections of experimental results after having tightened the pin-vices; at amplitudes lower than that at which the 'knee' occurs, the loss due to 'stick-stip' damping is negligible. The loss factor obtained from the second sections however decreased from $\phi_{pend_{total}}(\omega_0) = (1.30 \pm 0.06) \times 10^{-5}$ in 'experiment 1', to $\phi_{pend_{total}}(\omega_0) = (1.78 \pm 0.14) \times 10^{-6}$ in 'experiment 2'. This decrease in loss factor confirms the presence of an excess loss in 'experiment 1'.

2. The lowest loss that the pendulum mode can exhibit is set by the total material loss of the suspension wires. The lowest measured pendulum mode loss factor ($\phi_{pend_{total}}(\omega_0) = (1.78 \pm 0.14) \times 10^{-6}$, obtained in 'experiment 2'), was lower than that predicted using the material loss factor of the 178 μm diameter wire (i.e. $\phi_{pend_{total}}(\omega_0) = (2.88 \pm 0.32) \times 10^{-6}$). This confirms that the material loss factor, $\phi_{mat_{intrinsic}}(\omega_0)$, obtained from the sample of 178 μm diameter wire was indeed too large, as was suspected at the time of its measurement. Comparing the best measured pendulum mode loss factor with that calculated from the material loss of the 127 μm diameter wire ($\phi_{pend_{total}}(\omega_0) = (1.00 \pm 0.10) \times 10^{-6}$), shows better agreement. This suggests that tightening the pin-vices

has reduced (but not entirely eliminated) the excess loss that was evident in 'experiment 1'.

3. The above statement suggests that poor clamping was the source of the excess loss in 'experiment 1'. We can postulate that the observed break in slope in figure 5.6 was the effect of 'stick-slip' damping ceasing to exist in one pin-vice only and that an excess loss was still present as a result of 'stick-slip' damping associated with the other pin-vice. This could occur should the tightening factor in this pin-vice be much smaller. If this was so the pendulum tested in 'experiment 1' never reached a swing amplitude small enough for the effect of 'stick-slip' in the loose pin-vice to become negligible. This introduces a constant loss factor throughout the entire duration of 'experiment 1'. The presence of weak clamping in one of the pin-vices is supported by the observation that one of the suspension wires slipped through its pin-vice.

4. We can test the theory of an excess loss factor caused by an under-tightened pin-vice by examining the levels of excess loss present between corresponding sections of the two sets of experimental results. Consider the second sections of experimental data shown in figure 5.6 and figure 5.10. The difference in loss factor between these two sections, $\phi_{pend_{excess}}(\omega_0)$, can be calculated by subtracting the loss factor obtained in the second section of 'experiment 2', $\phi_{exp\,2_{section\,2}}(\omega_0)$, from the loss factor obtained in the second section of 'experiment 1', $\phi_{exp\,1_{section\,2}}(\omega_0)$

$$\begin{aligned} \phi_{pend_{excess}}(\omega_0) &= \phi_{exp\,1_{section\,2}}(\omega_0) - \phi_{exp\,2_{section\,2}}(\omega_0) \\ &= (1.12 \pm 0.06) \times 10^{-5}. \end{aligned} \tag{5.15}$$

For the excess loss to be caused by an under-tightening of one pin-vice it should maintain a constant level throughout the entire experiment. To check if this occurred, the excess loss, $\phi_{pend_{excess}}(\omega_0)$, was added to the loss factor measured during the first section of 'experiment 2', $\phi_{exp\,2_{section\,1}}(\omega_0) = (3.87 \pm 0.34) \times 10^{-6}$, to give a total loss factor of $(1.51 \pm 0.07) \times 10^{-5}$. This loss factor is very similar to the level of pendulum mode loss factor observed during the first section of 'experiment 1', $\phi_{exp\,1_{section\,1}}(\omega_0) = (1.70 \pm 0.07) \times 10^{-5}$ within the accuracy of the measurement. The presence of a constant loss factor in the first experiment supports the theory that it was due to a clamping loss

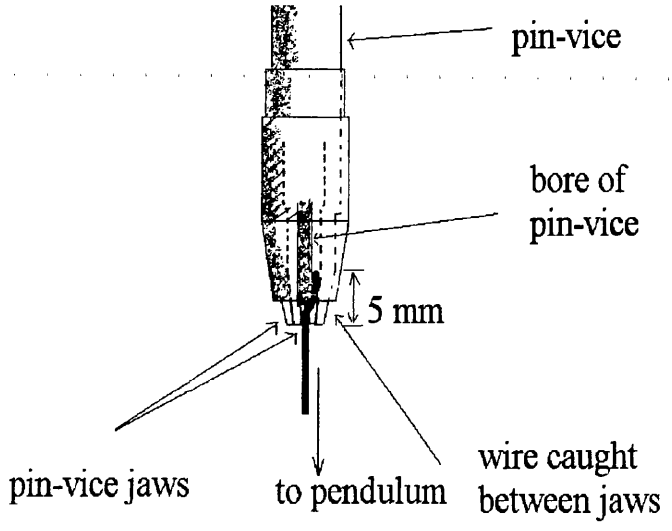

Figure 5.11: *Diagram showing the possible incorrect position of the wire inside the pin-vice.*

present in one pin-vice throughout the whole experimental run shown in figure 5.6.

5. The final point which can be made is an observation about the positions of the breaks in slope in figure 5.6 and figure 5.10. With reference to equation 5.14, the amplitude below which 'stick-slip' damping should become negligible can be seen to be proportional to the tightening factor, γ. We know that γ in 'experiment 2' has increased from the original value of $\gamma = 2.6$. However, the observed amplitude at which the break in slope occurs has decreased from 1 mm in 'experiment 1' to $\sim$0.17 mm in 'experiment 2'. The knee position has moved in the opposite direction to that which would have been expected.

It was postulated that when the pin-vices were undone and the wire lengths readjusted, the wire was re-inserted into the pin-vice differently. Although the wire emerged from the pin-vice through the bore of the clamp, it is believed that the wire moved over to one side inside the pin-vice, becoming clamped between the flat surfaces of two of the jaws in the pin-vice. The result being that the wire was clamped over a significantly longer length, and hence the force was applied to a much larger area, A_c, than that in 'experiment 1'. Figure 5.11 shows this effect.

This hypothesis was tested by taking the pin-vice apart and measuring the maximum length over which the wire could have been caught between two of the jaws of the

clamp. This was found to be ~5 mm. The maximum area, $A_{c_{max}}$, over which the force could act was then calculated from $A_{c_{max}} = 2\pi r l_{max}$ where $l_{max} = 5\,\text{mm}$ i.e. $A_{c_{max}} = (2.76 \pm 0.28) \times 10^{-6}\,\text{m}^2$. Substituting this area and the amplitude at which the effect of 'stick-slip' damping was effectively overcome, $x \approx 0.17\,\text{mm}$, into equation 5.14 allows calculation of the only unknown of the inequality; the tightening factor, γ. This was calculated as $\gamma > 5.3 \pm 0.1$.

The tightening factor was then measured directly a number of times by a method similar to that discussed in section 5.4. Each time we clamped the wire so that it was seen to exit from the bore of the pin-vice, yet became sandwiched between two of the jaws inside the pin-vice (as discussed above). The pin-vice was then tightened using pliers. The wire was found to slip through the pin-vice with a mass of between 1 kg and 4 kg added. γ had therefore increased from 2.6 to some value in the range 9.5 to 38. The range of measured tightening factors lie in the range of the number predicted for the tightening factor given the maximum clamping area discussed above and the observed amplitude at which the break in slope occurred. The variation in measured γ obtained from wires nominally clamped by the same force highlights the uncertainty involved in clamping a given wire in an identical manner on each trial.

In conclusion, the excess loss factor present throughout the duration of the first experimental run was due to an under-tightened pin-vice. Once the clamp had been tightened sufficiently, the constant excess loss was effectively eliminated. The pendulum mode loss factor measured in the region free of 'stick-slip' damping agreed with the pendulum mode loss factor predicted using the better of the two observed material losses.

5.6 Conclusions

The experiments reported in this chapter proved useful for a number of different reasons. The experiments to measure the pendulum mode loss factor of pendulums suspended from wire allowed us to verify that the lower material loss factor (measured on a 127 μm diameter sample and discussed in section 3.2) was the intrinsic loss factor of the carbon steel tested.

Although pendulums hung from carbon steel wires will not be employed to suspend the main optics in GEO 600, performing these experiments allowed a number of potential damping mechanisms to be explored. One of the most important lessons that was learnt during the course of these tests was the effect that 'stick-slip' damping had on the level of loss associated with the pendulum mode (at the pendulum mode frequency). This effect can be exhibited in any type of pendulum suspension. However, it can be seen from examination of equation 5.14 that clamping tightly and also by expanding the diameter of the wire or fibre up to a thicker diameter within the clamping region, that the effect of 'stick-slip' damping can be reduced to negligible levels. This works for two reasons. By clamping tightly the swing amplitude, x, below which the pendulum is unaffected by 'stick-slip' damping increases. By expanding the diameter of the fibre in the section to be clamped, the region of bending is moved out of the jaws of the clamp. This reduces the motion present in the clamp helping to reduce frictional losses.

Chapter 6

Loss Factor Measurements of Fused Quartz Pendulum Suspensions

6.1 Introduction

We intend to prevent the sensitivity of GEO 600 from being degraded by the thermal noise contribution associated with the longitudinal pendulum mode of the test mass suspension. This is achieved by specifying a maximum acceptable loss factor associated with the pendulum mode of $\phi_{pend_{total}}(\omega) = 3.7 \times 10^{-8}$ at 50 Hz (see section 2.8).

This chapter contains a discussion of experiments undertaken to construct pendulums of small mass, suspended by fused quartz fibres, which exhibit loss factors low enough to let us deduce that suspensions suitable for GEO 600 can be constructed.

6.2 Construction of the Initial Test Pendulums

The pendulum used in the initial loss experiments was constructed from a ~200 g ceramic (tradename MACOR) mass of dimensions of 4.5 cm height, 8.5 cm width and 2 cm

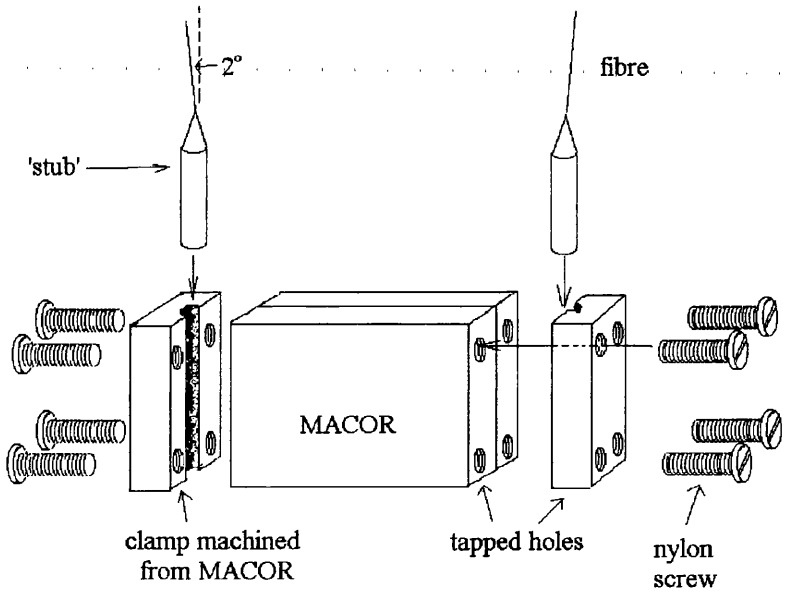

Figure 6.1: *Initial method of attaching the 'stub' ends of the fused quartz fibres to the pendulum mass.*

thickness. Two fused quartz fibres of $\sim 290\,\mu$m diameter at the point of bending and 26.4 cm long, were pulled from fused quartz rods of 3 mm diameter in the RF induction furnace (discussed in section 3.4.2). Sections of the 3 mm diameter rod left at both ends of the fibres ('stubs') were used for attachment at the point of suspension and at the pendulum mass to help minimise the excess loss known as 'stick-slip' damping (refer to section 5.4). Each upper stub was attached to the point of suspension by coating the stub with a thin layer of quick-setting epoxy and inserting it into a tightly fitting section of brass tube down the length of which a slot was cut. These brass sections were then pushed into clamps that were machined from a piece of aluminium – the 'suspension plate' (see figure 4.2). The clamps were tightened down onto the brass tubing and hence onto the fused quartz rods. The stubs at the other end of the fibres were attached to opposite sides of the pendulum mass by glueing and clamping (the clamps having been machined from the MACOR mass). The fibres were splayed by 2° to the vertical in order to separate the frequency of the main pendulum mode from its transverse mode (refer to figure 6.1). By this means, coupling of the two orthogonal modes induced by the Coriolis effect was eliminated. A small flag was also attached to the under-side of the pendulum during its construction.

6.3 Initial Pendulum Loss Experiments

The pendulum was lowered into the pendulum support structure described in section 4.2 until the aluminium suspension plate rested on the 'top-hat'. The suspension plate was then tightened into position by two aluminium cross-pieces. The vacuum tank was evacuated to a pressure of $\sim 5 \times 10^{-7}$ mbar to minimise the effect of external viscous damping on the pendulum mode.

The pendulum mode was excited by means of the coil and magnet 'pusher' previously discussed in section 5.3. A beam of white light was shone across the tank. The beam was partially obscured by the flag attached to the base of the pendulum allowing a shadow sensing technique to be employed to detect the amplitude decay of the pendulum swing (refer to section 5.3). The signal from the photodiode was filtered, amplified and recorded on a chart recorder (and in later experiments, also by a data acquisition program running under LabVIEW [1]).

A loss factor, $\phi_{pend_{total}}(\omega_0)$, was measured which varied over time. Its value started at a few $\times 10^{-7}$ and steadily deteriorated to $\sim 4 \times 10^{-5}$ over a period of $\sim$24 hours.

The following section contains a discussion of a series of experiments conducted to determine the cause of the change with time of the measured pendulum mode loss factor.

6.4 Investigations to Determine the Cause of Change in the Measured Loss Factor

Various candidates were considered for the source of apparently increasing loss recorded during the experiment. These included:

1. a loosening over time of the clamps at the point of suspension
2. a non-linearity present within the sensing or data recording equipment
3. an increasing level of recoil loss with time

[1] National Instruments Corp.

1. Tests were performed to check whether loosening of the clamps over the interval of the experiment was responsible for the observed increase in measured loss factor. First the pendulum was stopped (whilst under vacuum) when the loss factor was at the high value. The pendulum was then re-started. The loss factor was re-measured and was found to have the same value as that just before the pendulum was stopped. The tank was then backfilled with dry nitrogen to atmospheric pressure and opened, the clamps tightened, the tank evacuated and the experiment repeated. In this instance the measured loss factor started at a low value and increased over time. These two measurements are both consistent with a loosening of the clamps over time. However, when the tank was again backfilled with dry nitrogen to atmospheric pressure and then evacuated (with no further retightening of the clamps), the measured loss factor was found to have returned to its original low value which increased over time. This would not be expected if slackening of the clamps was responsible for the increase in loss.

2. Checks similar to those discussed in point 1 of section 5.4 were performed and proved that the chart recorder, amplifier and the photodiode were not responsible for the increased level of loss factor.

The shape of the light beam however could have caused a change in the gradient of the type observed during the experiment if the initial swing amplitude had been large enough (as was shown in point 1 of section 5.4). The initial swing amplitude was $\sim$3 mm. As can be seen with reference to figure 5.8, a 3 mm swing amplitude lies within the region of the light beam where the non-linearity is too small to cause the observed effect. We would therefore not expect the light beam to be the source of the non-linearity. However to be sure of this a check was carried out. The light beam was masked to give a rectangular shape as it entered the vacuum tank. This ensured that the light reaching the photodiode was linearly proportional to the amplitude of swing at *all* swing amplitudes. The loss factor measurement was repeated and the same change in its value was observed. In conclusion the shape of the light beam was disregarded as the source of increased loss displayed.

3. The next possibility to be considered was a change in the stiffness of the pendulum support structure (and therefore the level of recoil loss) due to the system being under vacuum. It should be noted that the recoil measurement discussed in Chapter 4 in

which the stiffness of the support structure was measured was undertaken at atmospheric pressure. It was postulated that during the course of a loss measurement, the large forces caused by the decrease in pressure inside the tank may have caused it to 'relax', thus slowly changing the shape of the tank by enough to alter the rigidity produced by bracing the pendulum support structure against the walls, and therefore changing the stiffness of the tank.

To test this hypothesis, a vacuum compatible accelerometer (Brüel & Kjær model 4379) was placed on the top-hat inside the vacuum tank and connected, via a vacuum feedthrough and amplifier, to a spectrum analyser. The signal from the accelerometer was found to correspond to a motion of the support structure of $x_{rms} = 1.67 \times 10^{-7}\,\mathrm{m}$ at 1 Hz (for a maximum pendulum displacement of 3 mm). The stiffness of the support structure was recalculated using this value and found to be $k_s \approx 1 \times 10^5\,\mathrm{N\,m^{-1}}$ which is a factor of 55 less than that reported for k_s in section 4.6. By assuming that the recoil phase shift, δ, is at best equal to the value reported in section 4.7, the minimum obtainable loss for the 200 g pendulum would then be expected to be $\phi_{recoil}(\omega_0) = 1.7 \times 10^{-6}$.

The loss factor measured during the same time interval as the accelerometer reading was taken was a few $\times 10^{-7}$ – approximately an order of magnitude lower than the loss suggested by the accelerometer reading. This is clearly not possible and implies that the signal from the accelerometer was not a true measure of the acceleration of the support structure. To check this the ground lead of the accelerometer was disconnected. A signal was still observed which would not have been expected had the accelerometer been measuring acceleration. However the observed signal might have resulted from coupling between the circuitry of the accelerometer and the amplified signal from the photodiode. This was checked by turning the shadow sensing equipment off. A signal was again observed at the pendulum frequency and was therefore inferred to be a genuine signal induced in the accelerometer cable. For simplicity the accelerometer was removed from the tank and replaced by a wire antenna (which was this time positioned lower down inside the tank beside the pendulum).

It was initially believed that the induced signal was caused by the swinging of the dielectric pendulum modulating the non-uniform electric field of the ion pump. This theory was tested by inserting an earthed metal gauze into the mouth of the ion pump to screen

its field. The gauze was found to have no effect on the level of the observed signal. Since the field of the ion pump was blocked by the mesh, the electrical signal must have resulted from a charge on the pendulum. As a result, the movement of the charged pendulum was inducing currents in its surroundings (for example the vacuum tank, the conducting foam pad of the pusher and the wire positioned inside the tank).

6.5 The Determination of Sign of Charge on the Pendulum

We wanted to determine the sign of charge on the pendulum so that the charging mechanism might be understood. The experimental apparatus used to measure the pendulum mode loss is represented schematically in figure 6.2. An electronic circuit equivalent to this apparatus is shown in figure 6.3. The swinging of the charged pendulum resulted in a sinusoidally varying capacitance, C_1, between the pendulum and the pusher pad. This in turn induced a fluctuating charge at the sensing capacitance, C_3, which was measured as a sinusoidally changing voltage at the output of the amplifier. The definition of the symbols marked on the diagram are as follows:

- C_1 is the sinusoidally varying capacitance between the pad of the pusher and the face of the pendulum
- C_T is the capacitance between the pendulum and the tank wall
- $C_{||}$ is the parallel combination of capacitances C_1 and C_T
- C_2 is the capacitance between the pendulum face and the wire
- C_3 is the combined capacitance of the wire positioned inside the tank and the capacitance across the input of the amplifier
- R is the input impedance of the amplifier
- V_{in} is the potential difference between the left hand face of the swinging pendulum and ground
- V_{out} is the voltage measured at the output of the amplifier.

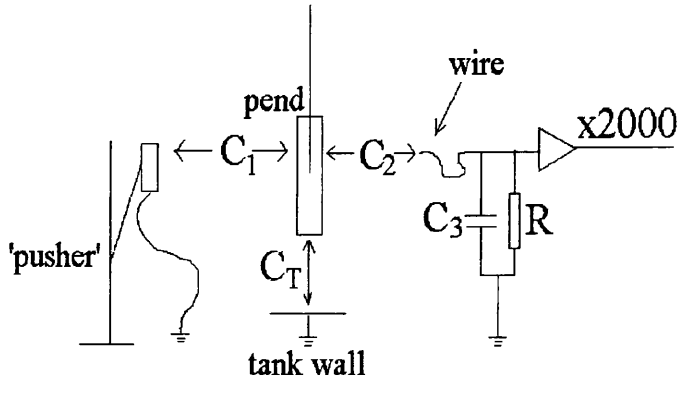

Figure 6.2: *Experimental apparatus used to measure* $\phi_{pend_{total}}(\omega_0)$ *with capacitances either measured directly or scaled.*

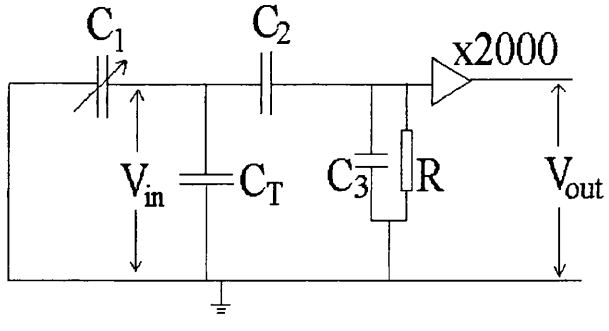

Figure 6.3: *Electronic circuit analogous to the apparatus.*

Consider the following. If the charge on the pendulum was positive, we would expect that the voltage on the pendulum would be at its most positive when the value of capacitance C_1 was at its smallest. This would occur when the pendulum was furthest away from the pendulum pusher. We wanted to perform an experiment which would allow us to determine the sign of the voltage out of the amplifier when the pendulum was at the position furthest away from the pusher. This measurement could be made with a lock-in amplifier. The lock-in amplifier would allow us to determine the phase at the output of the amplifier with respect to the position of the pendulum as sensed by the shadow sensor. If there were no inversions present in the detection scheme, and the charge on the pendulum was positive, we would expect that the phase at the output of the amplifier would lead the phase of the position signal by $\sim 90°$. This is because the circuit in figure 6.3 behaves as a high pass filter for the voltage generated by C_1 at the pendulum frequency.

On performing the experiment described above, the phase of the signal out of the amplifier was found to lead the phase of the position signal by $\sim 70°$ – which is approximately equal to 90°. However there was an inversion included in the signal representing the measurement of position. Working backwards through the argument given above, and taking into account the inversion present, we infer that the charge on the pendulum must have been negative.

It was concluded that ultra-violet radiation emitted from the ion pump liberated electrons from the pendulum support structure and wall of the vacuum tank. These electrons collected on the pendulum leaving it with an overall negative charge. This was supported by investigations which showed that it was possible to inhibit the rate of charging of the pendulum by placing a solid earthed plate in the mouth of the ion pump (thus preventing the radiation entering the vacuum tank). It should also be noted that the amount of charge present on the pendulum could be decreased by shining light from an ultra-violet bulb directly at the pendulum causing the excess electrons to be knocked off.

The currents induced in the tank, pusher pad and wire by the motion of the charged pendulum represent a source of energy dissipation that was responsible for the increase in pendulum mode loss factor observed. An increase in the level of charge on the pendulum over a period of time is consistent with this – as the charge on the pendulum increased,

the induced currents and consequently the energy dissipated also increased. As a result the loss factor increased as a function of time. A suitable model for this energy dissipation will be discussed in the following section.

6.6 Model of Energy Dissipation Consistent with the Level of Loss Factor Measured

The values of the capacitances marked on the figure 6.2 and figure 6.3 are given below and were either measured directly or scaled from other measured capacitances:

- $C_1 = 0.75\,\text{pF}$ to $1.50\,\text{pF}$
- $C_T = 40\,\text{pF}$
- $C_{||} = 40.75\,\text{pF}$ to $41.50\,\text{pF}$
- $C_2 = 0.01\,\text{pF}$
- $C_3 = 384\,\text{pF}$
- $R = 100 \times 10^6\,\Omega$.

The pendulum was re-swung once charge had accumulated. The maximum amplitude of swing was $x_0 \approx 3\,\text{mm}$ and the voltage measured at the output of the amplifier was $V_{out} = 400\,\text{mV}_{rms}$. This is equivalent to a signal $V'_{out} = 200\,\mu\text{V}_{rms}$ at a point in the equivalent circuit before the $\times 2000$ gain of the amplifier.

The potential difference, V_{in}, between the left hand face of the pendulum and ground can be calculated from the potential divider formed by capacitance C_2 and the parallel combination of R and C_3 as

$$V_{in} = 32.77\,\text{V}_{rms}. \tag{6.1}$$

The peak-to-peak potential difference that gives the rms voltage in equation 6.1 is

$$\Delta V_{in} = 92.68\,\mathrm{V}_{pk/pk} \tag{6.2}$$

which equals the change in the potential difference experienced between ground and the left face of the pendulum at the two extreme positions of the pendulum swing.

It is interesting to calculate the number of electrons present on the face of the pendulum that results in the potential difference between ground and the pendulum as the pendulum swings. This can be calculated from

$$\Delta V_{in} = q\left(\frac{1}{C_A} - \frac{1}{C_B}\right) \tag{6.3}$$

where q is the charge on the pendulum and C_A and C_B are the values of $C_{||}$ at the extremes of the pendulum swing. Rearranging equation 6.3 and substituting for ΔV_{in}, C_A, and C_B gives the charge on the pendulum as $2 \times 10^{-7}\,\mathrm{C}$ – equivalent to 1.3×10^{12} electrons.

The loss factor, when dominated by the loss associated with charging, was measured as $\phi_{pend_{total}}(\omega_0) = \phi_{pend_{charge}}(\omega_0) = 4 \times 10^{-5}$. It is possible to calculate the percentage of the maximum possible change in electrical energy that must be dissipated per cycle to correspond to this level of loss. Consider the definition of loss given in equation 2.27 i.e.

$$\phi_{pend_{charge}}(\omega_0) = \frac{E_{lost/cycle}}{2\pi E_{stored}}.$$

The energy stored in the swinging pendulum is

$$\begin{aligned} E_{stored} &= \frac{1}{2}m\omega_0^2 x^2 \\ &= 3.5 \times 10^{-5}\,\mathrm{J} \end{aligned} \tag{6.4}$$

where m is the mass of the pendulum, ω_0 is the resonant angular frequency and x is the maximum displacement of the pendulum.

The maximum change in electrical energy that may be dissipated per cycle is

$$\begin{aligned} E_{lost/cycle_{max}} &= \frac{q^2}{2}\left(\frac{1}{C_A} - \frac{1}{C_B}\right) \\ &= 8.9 \times 10^{-6}\,\mathrm{J}. \end{aligned} \tag{6.5}$$

It can be seen from substitution of the numbers calculated in equation 6.4 and equation 6.5 into equation 2.27 that if all of the energy that can be dissipated is dissipated per cycle, a loss factor of $\phi_{pend_{total}}(\omega_0) = 4 \times 10^{-2}$ would be measured. Since a loss factor of $\phi_{pend_{total}}(\omega_0) = 4 \times 10^{-5}$ was observed, we can conclude that ~0.1% of the maximum available change in electrical energy was in fact dissipated per cycle.

6.7 Investigations to Control the Charge on the Pendulum

The loss factor measured during the charging of the pendulum can be expressed as

$$\phi_{pend_{total}}(\omega_0) = \phi_{pend_{charge}}(\omega_0) + \phi_{pend_{other}}(\omega_0) \tag{6.6}$$

where $\phi_{pend_{charge}}(\omega_0)$ is the loss associated with the currents induced in the surroundings of the pendulum and $\phi_{pend_{other}}(\omega_0)$ is the sum of the remaining losses associated with the pendulum mode. It can be shown (from substitution of equation 6.5 into equation 2.27) that $\phi_{pend_{charge}}(\omega_0)$ equals a constant, K, multiplied by the charge squared i.e.

$$\phi_{pend_{total}}(\omega_0) = Kq^2 + \phi_{pend_{other}}(\omega_0). \tag{6.7}$$

The amplitude of the pendulum swing, $A(t)$, and the signal from the amplifier were recorded simultaneously. The effect of the swing amplitude on the size of the signal from the wire antenna inside the tank was removed by dividing the size of this signal at a time, t, by the swing amplitude at the same instant. The corrected value of the amplifier signal was subsequently squared – and is proportional to q^2. A plot was then generated of the loss factor (calculated from the amplitude decay) as a function of the normalised

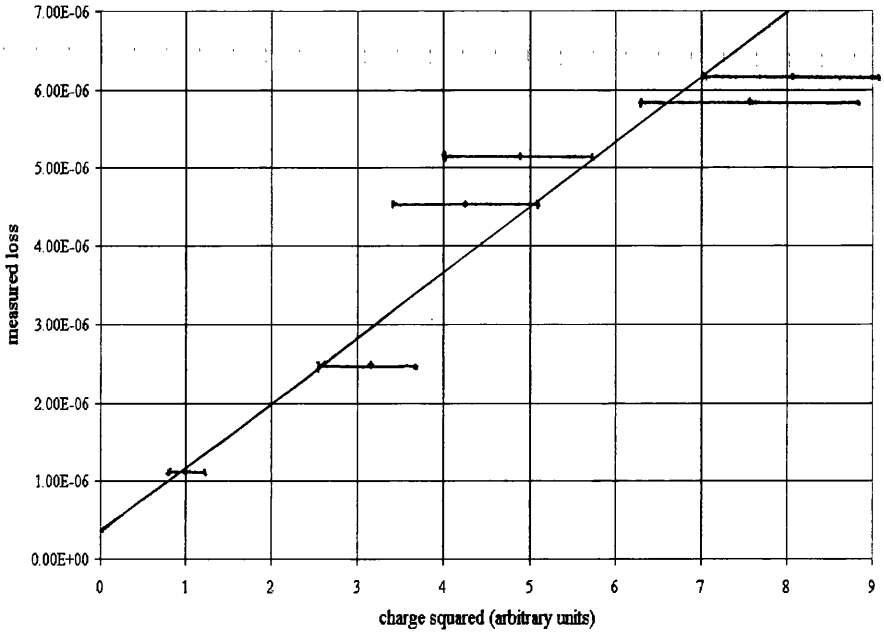

Figure 6.4: *Variation in loss for the pendulum mode of* $\sim 200\,g$ *pendulum suspended on fused quartz fibres as a function of the square of the electrostatic charge on the pendulum.*

value of q^2 (given in arbitrary units). This can be seen in figure 6.4. The equation of the line shown in figure 6.4 has the form of equation 6.7.

By extrapolating the straight line fit of this plot back to the y-axis, it is possible to obtain a value for the loss factor with the effect of charging removed (i.e. where $q^2 = 0$). This value is found to be $(3.3 \pm 1.0) \times 10^{-7}$.

With the earthed metal shield in position, the pendulum mode loss factor was remeasured. The resulting decay trace can be seen in figure 6.5. The measured loss factor calculated from this decay trace remained constant with a value of $\phi_{pend_{total}}(\omega_0) = (3.19 \pm 0.73) \times 10^{-7}$. We can conclude from this result that the effect of charging could be reduced to a level where it no longer affected the loss measured.

Once the loss associated with the charging of the pendulum was effectively removed, the remaining losses at the pendulum mode frequency could be expressed as

$$\phi_{pend_{total}}(\omega_0) = \phi_{pend_{expect}}(\omega_0) + \phi_{pend_{excess}}(\omega_0)$$

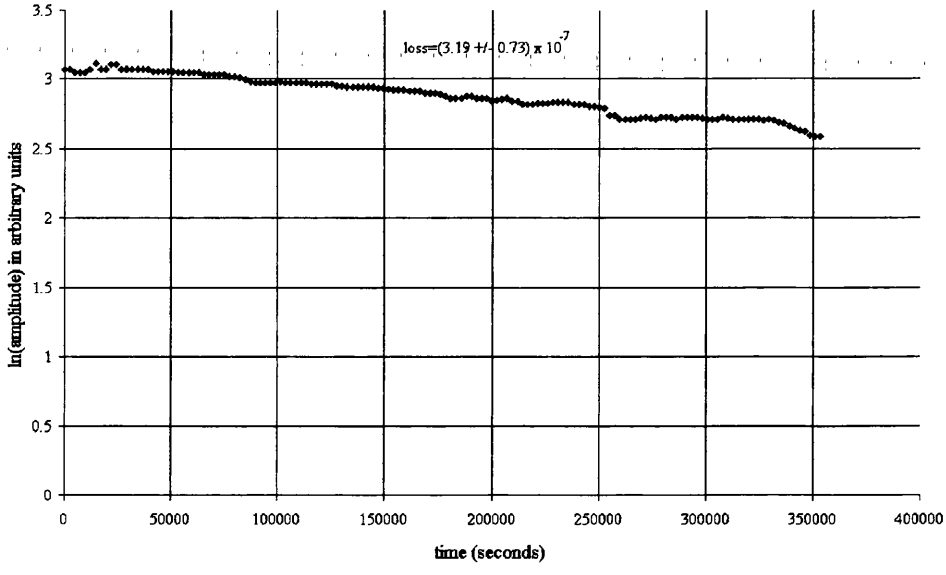

Figure 6.5: *ln(amplitude) versus time of pendulum decay with earthed metal shield in place.*

$$= (\phi_{recoil}(\omega_0) + \phi_{pend_{intrinsic}}(\omega_0) + \phi_{pend_{t.e.}}(\omega_0)) + \phi_{pend_{excess}}(\omega_0) \quad (6.8)$$

where the losses on the right hand side of equation 6.8 are as follows[2]:

- the recoil damping contribution, $\phi_{recoil}(\omega_0)$. For a pendulum of mass, $m \sim 0.2\,\mathrm{kg}$, and the values of the constants k_s and δ (reported in section 4.6 and section 4.7 respectively) this can be calculated (using equation B.12) to be $\sim 4 \times 10^{-8}$.

- the contribution, $\phi_{pend_{intrinsic}}(\omega_0)$, set by the material loss of the suspension fibres (where $\phi_{mat_{intrinsic}}(\omega) \sim (0.5 - 1) \times 10^{-6}$). This is calculated using equation 2.30 to be in the range $(4.79 - 9.58) \times 10^{-9}$.

- the contribution, $\phi_{pend_{t.e.}}(\omega_0)$, due to presence of thermoelastic damping in the suspension fibres. This is calculated from equation 2.30 (where $\phi_{mat_{t.e.}}(\omega_0) = 1.5 \times 10^{-7}$ at 1 Hz) to be 1.5×10^{-9}. Because this loss is $< 10\%$ of the recoil loss contribution, it is ignored.

- any excess loss contribution, $\phi_{pend_{excess}}(\omega_0)$.

[2]The contributing loss factors relate to suspension fibres of 290 μm diameters

The sum of the known losses in the system, $\phi_{pend_{expect}}(\omega_0) = \phi_{pend_{intrinsic}}(\omega_0) + \phi_{recoil}(\omega_0)$, has a value that is a factor of $\sim 7\times$ lower than the measured loss, $\phi_{pend_{total}}(\omega_0)$. Rearranging equation 6.8 and substituting for the known losses, we find that an excess loss factor of $\phi_{pend_{excess}}(\omega_0) = (2.69 - 3.19) \times 10^{-7}$ has yet to be accounted for.

6.8 Determining the Source of the Excess Loss Factor

Three possible causes of the excess loss factor were considered.

1. Since the measurements using the accelerometer (discussed in section 6.4) were found to be invalid, we again considered an increased level of recoil damping as the source of excess loss factor.

2. It is possible that the intrinsic loss factor of the suspension fibres, $\phi_{mat_{intrinsic}}(\omega)$, is in some way stress dependent and therefore larger than that measured for the unloaded fibres (discussed in Chapter 3).

3. Although we chose a clamping method which should minimise 'stick-slip' damping [45], we considered that the method might be inadequate.

Consequently a series of measurements of pendulum mode loss factors was performed on pendulums with different masses, fibre diameter and methods of fibre attachment. The results are given in table 6.1, where $\phi_{pend_{total}}(\omega_0)$ are the measured loss factors. It should be noted that the loss factor associated with the rotational mode, $\phi_{rot_{total}}(\omega_0)$, of the 96 g pendulum suspended on 60 μm diameter fibres was also measured. The significance of this is explained below. The term $\phi_{pend_{expect}}(\omega_0)$ is the sum of the expected losses in the system (assuming the values of k_s and δ given in section 4.6 and section 4.7 respectively for the constants needed to calculate the recoil limit). The excess loss factor, $\phi_{pend_{excess}}(\omega_0)$, (calculated from equation 6.8) is the loss yet to be explained. Using the results given in table 6.1 we consider each of the three possible causes of excess loss in turn.

1. In Appendix B.1 the limiting loss due to recoil damping is shown to be proportional to the mass of the pendulum. Correspondingly, if the excess loss was due to increased recoil

		pend. mass (g)	fibre diam. (μm)	$\phi_{pend_{total}}(\omega_0)$ (measured) $\times 10^{-8}$	$\phi_{rot_{total}}(\omega_{rot})$ (measured) $\times 10^{-8}$	$\phi_{pend_{expect}}(\omega_0)$ $\times 10^{-8}$	$\phi_{pend_{excess}}(\omega_0)$ $\times 10^{-8}$
Original	1	200	290	33 ± 4	-	4.7 ± 0.6	28 ± 4
Clamps	2	32	60	7.2 ± 0.7	-	0.72 ± 0.09	6.5 ± 1.0
	3	96	60	22 ± 1	-	1.9 ± 0.2	20 ± 1
	4	96	60	-	33 ± 10	-	-
New	5	12	290	6.9 ± 0.5	-	3.7 ± 1.0	3.3 ± 1.0
Clamps	6	28	290	6.0 ± 0.6	-	2.9 ± 0.7	3.1 ± 0.9
Tightened	7	28	290	3.0 ± 0.4	-	2.9 ± 0.7	0.1 ± 0.8
Clamps	8	96	290	2.8 ± 0.7	-	2.9 ± 0.4	-0.1 ± 0.8

Table 6.1: *A summary of the results of measurements made of loss factors for various pendulums suspended on fused quartz fibres.*

damping it should be greater for pendulums of greater mass. Comparing case 7 with case 5 (where there is a factor of ~ 2 increase in mass) it can be seen that, on the contrary, the excess loss has decreased. Also, consider cases 2 and 7 obtained from pendulums of approximately the same mass. The excess loss factors should remain approximately equal but were measured to be quite different.

In cases 3 and 4 the loss factors for the longitudinal mode and the rotational mode of the same pendulum are given. By comparing these we can obtain information about the level of recoil damping in the system. The loss of the longitudinal pendulum mode, $\phi_{pend_{total}}(\omega_0)$, measured in a rigid system (i.e. one with a small contribution to the measured loss factor from recoil damping) should yield a loss of the same order of magnitude as that measured for the rotational mode of the pendulum, $\phi_{rot_{total}}(\omega_{rot})$. This is because the loss factor for both of these modes results from the same mechanism – the loss associated with the bending of the fibres. However, if the level of recoil damping was much higher than had been anticipated (perhaps due to the pendulum rocking the tank on its mountings), it would seem likely that the support structure would be stiffer in rotation and that the loss factor measured for the longitudinal mode should therefore be higher.

In fact it is not significantly different from that measured for the rotational mode. We conclude that the excess loss in the system was not due to the effects of increased recoil damping.

2. The simplest form of stress dependent damping would be where $\phi_{mat_{intrinsic}}(\omega)$ is proportional to $\frac{m}{r^2}$, where m is the pendulum mass and r the radius of the fibres. Substitution of $\phi_{mat_{intrinsic}}(\omega) \propto \frac{m}{r^2}$ into equation 2.30 shows that the excess loss factor should be $\propto \sqrt{m}$ and independent of the fibre radius. In cases 5 and 7, the pendulums have equal fibre radii and different masses. Instead of observing the excess loss factor increasing by a factor $\sqrt{m}$ between case 5 and 7, the excess loss decreases. In cases 3 and 8 the pendulums have the same mass but different fibre radii. The excess loss factor however is significantly different between the two cases and is not independent of radii. Both of these cases suggest that the excess loss does not result from a stress dependence in the material of the suspension fibres of the form discussed above.

3. When a pendulum suspended by two fibres swings, bending occurs in the necked region of the fibre below the stubs. However a bending moment is applied to these stubs, which in cases 1-4 were encased in brass tubes with a layer of non-rigid glue. Motion between the stubs and the brass tubes will transfer energy to the glue causing a source of excess loss. Accordingly the method of attachment of the upper stubs was changed to involve direct clamping in the form of precision engineered pin-vices (whilst the stubs at the bottom were welded onto a fused quartz mass). Cases 5-8 are obtained from pendulums clamped in this manner. Comparing case 7 with case 2 and case 8 with case 3 shows the decrease in excess loss factor due to the use of glueless attachment. Between case 6 and case 7 (conducted on the same pendulum) the clamps were tightened and a further reduction in the excess loss factor was observed. In case 8 the excess loss is effectively eliminated.

We thus conclude that the method used to attach the fibres to the point of suspension in the original loss experiments was the source of the excess loss observed.

6.9 The Effect of Seismic Noise on the Level of Measured Loss Factor

When making measurements of the pendulum mode loss factor, care must be taken to ensure that any coupling of ground motion into the pendulum mode has a negligible effect – if the effect is too large, this coupling can result in driven motion of the pendulum mode and lead to an artificially low loss factor, $\phi_{pend_{total}}(\omega_0)$, being measured.

We have seen during previous experiments that background noise can be corrected for if its level is known (refer to section 2.5). To do this however requires that the oscillator decays to the amplitude resulting from the external noise source. In the case of a 1 Hz oscillator of very low loss factor this would require us to leave the experiment running for an extremely long time (of the order of a year). It is however possible to estimate the effect of seismic excitation on the level of pendulum motion, thus allowing us to decide if it is an effect that should be accounted for in the calculation of the loss factor. This estimation can be made using equation D.18 (derived in Appendix D) i.e.

$$\frac{x_p}{x_g} = \sqrt{\frac{\pi f_p}{2\phi_{pend}}}$$

where x_p is the rms displacement of the pendulum induced by seismic motion at the point of suspension of amplitude spectral density, x_g. Here f_p is the resonant frequency of the pendulum and ϕ_{pend} is the true loss factor of the pendulum mode (and not that resulting from the effects of ground noise).

An accelerometer was used to measure the magnitude of horizontal seismic motion (in the direction of the pendulum swing) of the laboratory floor close to the vacuum tank in which our pendulum was suspended. This motion was found to be $x_g \approx 1 \times 10^{-8}\,\mathrm{m}/\sqrt{\mathrm{Hz}}$ at 1 Hz. We assume also a true loss factor of $\phi_{pend} \sim 3 \times 10^{-8}$ (refer to the measured loss given as result number 8 in table 6.1). A maximum rms motion resulting from seismic excitation of the pendulum of $x_p \sim 68\,\mu$m is calculated from substitution of the values given above into equation D.15. This is equivalent to a peak motion of $\sim 96\,\mu$m – a factor of approximately 30 times smaller than the 3 mm peak displacement of the initial pendulum swing. This suggests that our measurements of the pendulum mode loss factor

are not affected significantly by seismic excitation.

6.10 Loss Factor Measurements Performed on an All-Welded Pendulum

The results given in table 6.1 highlight the importance of the method used to attach the fibres to the point of suspension. To further investigate this, an all-welded fused quartz pendulum was constructed. This was made by dispensing with the pin-vices and instead welding the 3 mm stubs onto a fused quartz plate (7.5 cm wide, 12 cm long and 0.5 cm thick) which acted as a substitute for the aluminium suspension plate. The stubs at the lower ends of the suspension fibres were welded onto a fused quartz mass weighing 96 g. This fused quartz plate was carefully clamped into position inside the vacuum tank using the aluminium cross-pieces used in all previous measurements of the pendulum mode loss factor.

The logarithmic fit of a typical amplitude decay obtained from this pendulum can be seen in figure 6.6. The pendulum mode loss factor was calculated from figure 6.6 (by the method described in section 2.5) and found to be $\phi_{pend_{total}}(\omega_0) = (3.0 \pm 0.3) \times 10^{-8}$.

Using equation B.12 and the values for k_s and δ given in section 4.6 and section 4.7 respectively, we can calculate the level of recoil damping affecting the 96 g pendulum to be $\phi_{recoil}(\omega_0) = (1.9 \pm 0.2) \times 10^{-8}$. Subtracting this from the measured loss, we are left with a loss of $(1.1 \pm 0.4) \times 10^{-8}$. If all excess losses have been eliminated from the system, this loss should equal the contribution to the pendulum mode loss resulting from the fibre material at 1 Hz. The theoretical contribution from the fibre material is calculated to be $\phi_{pend_{intrinsic}}(\omega_0) + \phi_{pend_{t.e.}}(\omega_0) = (1.3 \pm 0.4) \times 10^{-8}$. The two values for the pendulum mode loss factor agree within the accuracy of the experiment and thus the excess loss has been reduced to negligible levels. In comparing these two loss factors we see that, with care, it is possible to reduce the excess losses in the system to a level that allows us to observe pendulum mode loss factors predicted by the limiting source of loss – that set by the material of the suspension fibres itself.

Using the material limited value for the pendulum mode loss obtained from the measured

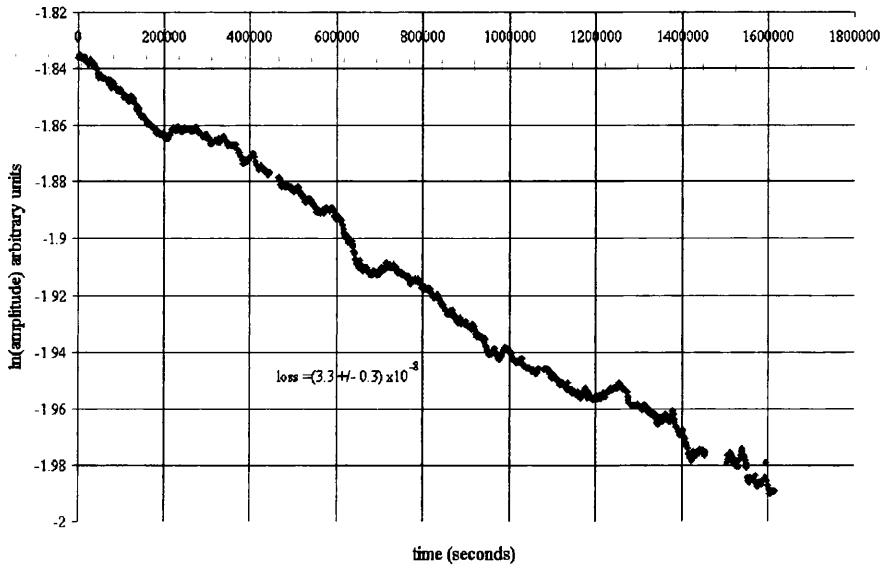

Figure 6.6: *Logarithmic fit to a typical amplitude decay of the all-welded fused quartz pendulum of mass 96 g.*

loss factor (i.e. $(1.1 \pm 0.4) \times 10^{-8}$), we can predict the level of loss associated with the pendulum mode at 50 Hz of a GEO 600 test mass hung from fused quartz fibres. This was achieved using the following:

- The level of loss associated with the material of the suspension fibres was calculated using the pendulum mode loss factor given above, the parameters of the 96 g suspension and equation 2.30. This was found to be $\phi_{mat_{total}}(\omega_0) = (7.6 \pm 2.1) \times 10^{-7}$.
- The thermoelastic damping contribution for the 290 μm fibres at 1 Hz was then calculated (i.e. $\phi_{mat_{t.e.}}(\omega_0) = 1.5 \times 10^{-7}$) and subtracted from $\phi_{mat_{total}}(\omega_0)$. The loss remaining is the intrinsic loss factor of the fused quartz fibres[3], $\phi_{mat_{intrinsic}}(\omega) = (6.1 \pm 1.7) \times 10^{-7}$).
- As a property of the material, this loss factor is independent of fibre diameter. Because fused quartz is structurally damped, this loss factor is also independent of frequency. The loss associated with a fibre suitable for suspending the GEO 600 test mass (i.e. 220 μm radius) is therefore also $\phi_{mat_{intrinsic}}(\omega) = (6.1 \pm 1.7) \times 10^{-7}$ at 50 Hz.

[3]This value of $\phi_{mat_{intrinsic}}(\omega)$ lies in the range measured directly on samples of fused quartz ribbons – refer to Chapter 3.

- Add to this the thermoelastic damping contribution at 50 Hz for the fibre of radius 220 μm (i.e. $\phi_{mat_{t.e.}}(\omega) = 5.6 \times 10^{-7}$) to give a total loss of $\phi_{mat_{total}}(\omega) = (1.2 \pm 0.3) \times 10^{-6}$.

- This loss factor is combined with the parameters of a GEO 600 suspension using equation 2.30. Thus the loss factor associated with the pendulum mode at 50 Hz is calculated to be $\phi_{pend_{total}}(\omega) = (8.5 \pm 1.6) \times 10^{-9}$.

This level of loss factor is considerably lower than the GEO 600 specification of $\phi_{pend_{total}}(\omega) = 3.7 \times 10^{-8}$ at 50 Hz.

6.11 Conclusions

In this chapter it has been shown that care must be taken not to introduce an additional loss into the measurement of the pendulum mode loss factor by electrostatically charging the pendulum from UV light emitted by an ion-pump used on the system. Ion-pumps will not be employed in GEO 600.

The experiments reported highlight the importance of choosing a low loss method of attaching the fibres to the point of suspension. In doing this we demonstrated that the level of the pendulum mode loss factor could be reduced to levels predicted by the known losses present in the system (i.e. that due to the sum of the recoil loss and the loss associated with the fibre material). Removing the effect of recoil predicted for an all-welded pendulum of 96 g from the measured loss gave a pendulum loss of $(1.1 \pm 0.4) \times 10^{-8}$ at 1 Hz. This loss can be used to calculate an equivalent loss factor for a 16 kg GEO 600 test mass of $\phi_{pend_{total}}(\omega) \sim 8.5 \times 10^{-9}$ at 50 Hz which is considerably lower than the GEO 600 thermal noise specification (refer to section 2.8). We can conclude from this that fibres pulled from 'standard grade' fused quartz, when attached with care to the point of suspension, are ideal for use as the suspension fibres of the main test masses in GEO 600.

Chapter 7

The Losses Associated with the Bonding of Fused Quartz Suspension Fibres to Fused Quartz Test Masses

7.1 Introduction

There are a number of factors that must be considered when choosing a material for the main test masses in an interferometer. Fused silica will be used for the test masses in GEO 600 for the following reasons:

- It is transparent, non-birefringent and can be polished to a 'super' smooth finish making it optically suitable for use in an interferometric gravitational wave detector.
- It has a low value of optical absorbtion, A, and low coefficient of thermal expansion, α, which helps to minimise distortion of the test mass when laser light heats it.
- Being non-magnetic and non-conducting, it is not susceptible to eddy current damping.

The sensitivity of GEO 600 at the low end of the detection band will be set by the level of thermal noise that is associated with the internal modes of the test masses. This level is determined by the properties of the material of the test masses. Fused silica exhibits low levels of thermal noise within the frequency band of interest because:

- the relatively high speed of sound, c, (and the choice of test mass dimensions) ensures that the resonant frequencies of the test mass can be set well above the detection band of the interferometer
- this material is of low intrinsic loss; typically values of $\phi_{internal}(\omega) = 2 \times 10^{-7}$ have been measured on bulk samples of fused quartz [30, 51, 63].

Fused quartz has also been chosen as the material from which the suspension fibres will be formed. In Chapter 3 experimental results are given which show that samples of fused quartz fibres have an intrinsic loss factor, $\phi_{mat_{intrinsic}}(\omega)$, that is potentially ten times lower than the minimum requirements set for GEO 600. These measurements are of particular interest because they were made over a frequency range that is within the detection band of GEO 600. Measurements made of the longitudinal pendulum mode of an all fused quartz pendulum were reported in Chapter 6. These measurements show that pendulum mode losses of the order specified for GEO 600 are obtainable. Although all fused quartz/silica suspensions appear extremely promising for the lower stage of the double pendulum suspension, one important question remains; how to form a pendulum by jointing fused quartz suspension fibres to the fused silica test mass without degrading the level of internal thermal noise at 50 Hz.

We first consider the level of thermal noise (at 50 Hz) resulting from the different choices of the number of fibres and the position of the points of attachment of the fibres to the test masses. Following this, various methods of bonding the fibres to the test mass will be discussed and a conclusion will be drawn about which bonding method should be used for attaching the fibres to the test masses in GEO 600.

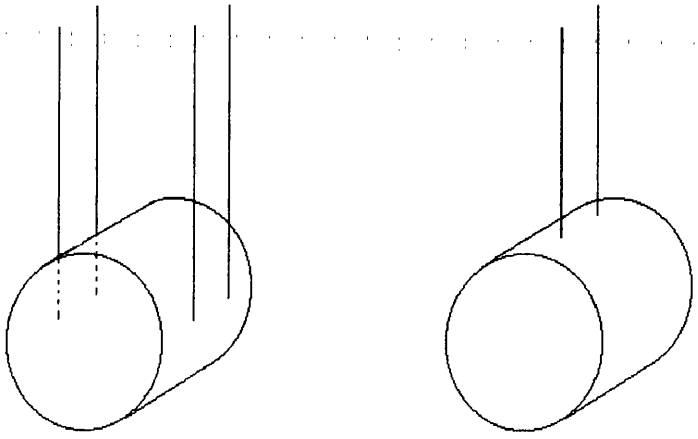

Figure 7.1: *Two configurations for the attachment of suspension fibres to the test mass.*

7.2 Two Fibres or Four?

The positions of attachment of the suspension fibres to the final pendulum stage has to be such that they allow the orientation of the test mass to be controlled by forces applied at the intermediate mass from which the final stage pendulum is suspended. Two configurations are considered. The first involves the attachment of four fibres, two along each side of the test mass, on a horizontal plane close to that passing through the centre of mass. The second employs two suspension fibres positioned on the upper surface of the test mass along the direction of the longitudinal pendulum mode. These configurations are represented schematically in figure 7.1.

There are a number of advantages and disadvantages which have to be considered for each arrangement. The first to be discussed will be a comparison of the pendulum thermal noise in the two cases.

The level of loss factor associated with the pendulum mode of a pendulum of mass, m, suspended from fused quartz fibres of total loss factor, $\phi_{mat_{total}}(\omega)$, can be calculated using equation 2.30 which is repeated below,

$$\begin{aligned}\phi_{pend_{total}}(\omega) &= \phi_{mat_{total}}(\omega)\frac{\xi n\sqrt{TEI}}{2mgl} \\ &= (\phi_{mat_{intrinsic}}(\omega) + \phi_{mat_{t.e.}}(\omega))\frac{\xi n\sqrt{TEI}}{2mgl}\end{aligned}$$

where the terms of the equation are as defined in section 2.6.1. If the fibres are tensioned to one third of the breaking stress of fused quartz in both the 2 and the 4 fibre case, the sum of the cross-sectional areas of the fibres will remain constant. The radius of each fibre in the two fibre suspension is $\sqrt{2}\times$ thicker than in the four fibre suspension ($r_2^2 = 2r_4^2$). For a full size GEO 600 test mass, the radii are $r_4 \sim 220\,\mu$m and $r_2 \sim 310\,\mu$m. The vertical separation of the point of suspension and the plane through the centre of mass (and hence the approximate length of the fibres in the four wire case, l_4,) is chosen to give a 1 Hz pendulum frequency. This distance (and therefore the length l_4) is ~ 0.25 m. This separation is fixed. The length of the fibres in the 2 fibre case, l_2, is the fixed separation minus the radius of the GEO 600 test mass ($r_{t.m.} = 0.125\,$m). From this information $l_4 = 2l_2$.

Consider the ratio, $\frac{\phi_{pend_{total4}}(\omega)}{\phi_{pend_{total2}}(\omega)}$, of the pendulum mode loss factor for a four fibre suspension to that for a two fibre suspension. Substitution of equation 2.30 into this ratio for the four and the two fibre case gives

$$\frac{\phi_{pend_{total4}}(\omega)}{\phi_{pend_{total2}}(\omega)} = \frac{(\phi_{mat_{intrinsic}}(\omega) + \phi_{mat_{t.e.4}}(\omega))}{(\phi_{mat_{intrinsic}}(\omega) + \phi_{mat_{t.e.2}}(\omega))} \frac{\sqrt{2} l_2 r_4^2}{l_4 r_2^2}. \tag{7.1}$$

We also know that $r_2^2 = 2r_4^2$ and $l_4 = 2l_2$ which, on substitution into equation 7.1 allows further simplification [1],

$$\frac{\phi_{pend_{total4}}(\omega)}{\phi_{pend_{total2}}(\omega)} = \frac{(\phi_{mat_{intrinsic}}(\omega) + \phi_{mat_{t.e.4}}(\omega))}{(\phi_{mat_{intrinsic}}(\omega) + \phi_{mat_{t.e.2}}(\omega))} \frac{1}{2\sqrt{2}}. \tag{7.2}$$

In Chapter 3, experiments to measure the intrinsic loss factor of fused quartz were reported. The loss factor was found to be $\phi_{mat_{intrinsic}}(\omega) \sim 5 \times 10^{-7}$ and is independent of frequency. The thermal noise requirement for GEO 600 is specified at 50 Hz. Knowing the radius required for the suspension fibres of the two and four fibre suspension, one can calculate the level of thermoelastic damping at 50 Hz. Using the material constants for fused quartz given in section 3.7.1, the thermoelastic loss at 50 Hz for the fibre of radius $r_4 = 220\,\mu$m can be calculated as $\phi_{mat_{t.e.4}}(\omega) = 5.6 \times 10^{-7}$ i.e. $\sim \phi_{mat_{intrinsic}}(\omega)$. The thermoelastic loss at 50 Hz for the fibre of radius $r_2 = 310\,\mu$m is $\phi_{mat_{t.e.2}}(\omega) = 3 \times 10^{-7}$

[1] A similar calculation up to this point can be found in S.D. Killbourn's Ph.D. thesis, University of Glasgow, 1997.

i.e. $\sim \frac{2}{3}\phi_{mat_{intrinsic}}(\omega)$. These two contributions can be substituted into equation 7.2 to give

$$\begin{aligned} \frac{\phi_{pend_{total4}}(\omega)}{\phi_{pend_{total2}}(\omega)} &= \frac{3}{5\sqrt{2}} \\ &= 0.42. \end{aligned} \tag{7.3}$$

Since the power spectral density of thermal motion associated with the pendulum mode, $\tilde{x}^2_{therm}(\omega)$, at frequencies above that of the pendulum mode is proportional to the pendulum mode loss factor (refer to equation 2.24), the thermal noise power expected from the pendulum mode of the four fibre suspension is a factor of $\frac{3}{5\sqrt{2}}$ times that of a two fibre suspension (i.e. the total loss associated with the pendulum mode for the four fibre suspension is $\sim 40\%$ of that of the two fibre suspension).

If the laser beam is not perfectly centred on the face of the test mass, the thermal noise associated with the tilt mode should also be considered. An advantage of using four fibre suspensions is that the resonant frequency of the tilt mode may be lower than that of the two fibre suspension. If this is the case, the thermal noise contribution at 50 Hz resulting from the tail of the tilt mode resonance in the two fibre case would be slightly worse than that of the four fibre case. In addition, it is easier to design the control electronics used to orientate the mass in a four wire suspension so that any residual noise from the electronics is of an acceptable level at 50 Hz.

Although the four fibre suspension is better in terms of the level of pendulum thermal noise present, there is some advantage in using a two fibre suspension. By suspending the mass from two fibres instead of four, the number of violin modes is halved. Also the series of violin modes in the two fibre case starts at a higher frequency than the series in the four fibre case. As a consequence the number of violin modes present within the detection band in the two fibre suspension is less. Both of these points mean that the number of notch filters required in the signal detection system is smaller for the two fibre suspension. Because the suspension is designed to be low loss, each violin mode has a very narrow bandwidth and the amount of bandwidth lost through notching out these signals is small in both cases.

Since the series of violin modes start at a higher frequency for the two fibre suspension, the thermal noise contribution from the tails of the violin modes at 50 Hz will be lower. The thermal noise contribution from the violin modes of both the two and four fibre suspensions are negligible however when compared with the dominant thermal noise contribution at 50 Hz – that associated with the internal modes of the test mass.

On weighing the advantages and disadvantages of both types of suspensions, it has been decided that a four fibre suspension is the more desirable. However there does exist the problem of *how* to bond the fibres to the test mass. The bonding method should be suitably strong in tension and/or shear and the bond should be such that it does not increase the intrinsic loss factor associated with the internal modes of the test mass. The following section contains a discussion of various methods of bonding fibres to the test mass.

7.3 Bonding Techniques

The use of two loops of wire as slings is a common method of suspending the masses, and is used because of its simplicity. To ensure that additional loss is not introduced into the system sharp 'break-aways' are required on the sides of the mass to define the points at which the wires leave the mass. When planning to suspend the mass from fused quartz fibres, sharp break-aways were considered a potential problem due to the brittle nature of the fused quartz. Sitting the mass in slings made from two loops of fused quartz fibres was not considered as a method of suspending the test masses.

Another method of attaching the fibres to the test mass might be to glue the 'stubs' (i.e. the 3 mm diameter rods left attached to the ends of the fused quartz fibres) directly onto the test mass. This however appeared undesirable due to the observed adverse effect of glueing – it was reported in section 6.8 that a glue joint increases the level of loss factor associated with the pendulum mode. For this reason glueing the fibres onto the test mass was not considered as a method of attachment.

Four possible methods of bonding the fused quartz fibres onto the mass were considered. These were welding, indium bonding, optical contacting and hydroxide catalysis bond-

bond type	bond strength in tension	bond strength in shear	source
welding.	bulk strength of material expected ($\sim 800\,\mathrm{MPa}$).	bulk strength of material expected ($\sim 800\,\mathrm{MPa}$).	–
indium.	$6 \times 10^6\,\mathrm{Pa}$.	expected to be $< 6 \times 10^6\,\mathrm{Pa}$.	Indium Corp. of America
optical contact.	$\sim 1.4 \times 10^6\,\mathrm{Pa}$.	$\sim 9 \times 10^5\,\mathrm{Pa}$.	D.-H. Gwo
hydroxide catalysis.	–	$3 \times 10^7\,\mathrm{Pa}$.	D.-H. Gwo

Table 7.1: *Comparison of bond strengths.*

ing [2]. Bonds of three of these methods were successfully formed and tested. A discussion follows in which the strengths of the various bonds are comparred and the bonding of the fibres to 500 g test masses is described.

7.3.1 Comparison of Bond Strengths

We intend to suspend the GEO 600 test mass from a bond tensioned to some fraction of its bond strength (typically $\frac{1}{3}$ of the bond strength in the case of a 16 kg mass). The strength of the bond will therefore determine a suitable bond area. In terms of minimising the effect of the bond on the levels of thermal noise present, it would be an advantage to keep the bond area to a minimium. With this criterion in mind, it is desirable to find a method of bonding that is as strong as possible. In table 7.1 the bond strengths of the different bond types are listed.

[2]Hydroxide catalysis bonding is being developed by D.-H. Gwo at Stanford University as a robust method of bonding together parts of the Gravity Probe-B space telescope. Stanford University has filed a patent application for the process of hydroxide catalysis bonding. Further information on its commercial application can be obtained from Mr. Jon Sandelin, Office of Technology Licensing, Stanford University, 900 Welch Road, Suite 350, Palo Alto, CA 94304-1850. e-mail: sandelin@leland.stanford.edu

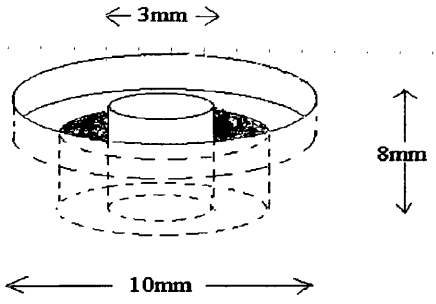

Figure 7.2: *Diagram of the recessed post ultrasonically milled in the fused quartz test mass.*

7.3.2 Formation of the Weld

The 500 g fused quartz masses used in the following tests were cylinders of HOQ 310 grade fused quartz of diameter 64 mm by 70 mm long. The cylinder was prepared for welding by ultrasonically milling a recessed post in the cylindrical surface of the mass, half way along its length. The post dimensions were approximately 3 mm in diameter, by ~8 mm deep and positioned centrally within a 10 mm diameter stepped hole as shown in figure 7.2. The post was formed to isolate the rest of the mass from the heat of the welding torch.

A 'T-piece' was formed by welding (with an oxy-hydrogen burner) a 30 mm section of 1 mm diameter fused quartz rod to the centre of a 16 mm section of 3 mm diameter rod. The T-piece was attached to a jig that allowed accurate positioning of the T-piece onto the milled post. The two pieces were welded into position using the oxy-hydrogen burner. Water was allowed to flow over the mass throughout the welding process to help minimise the effect of localised heating.

Two matching fused quartz fibres, 16 cm in length, were pulled from 3 mm diameter rods in an oxy-hydrogen flame. 3 mm stubs were left attached to both ends of the fibres. One of the stubs from each fibre was welded to each end of the cross-bar of the T-piece as can be seen in figure 7.3. The stubs at the other ends of the two fibres were glued into tightly fitting sections of brass tubing ready for hanging in the test structure as explained in section 7.4.3. The dimensions of the T-piece and fibres were chosen so that integer multiples of the frequencies of the lowest order modes of these pieces did not coincide

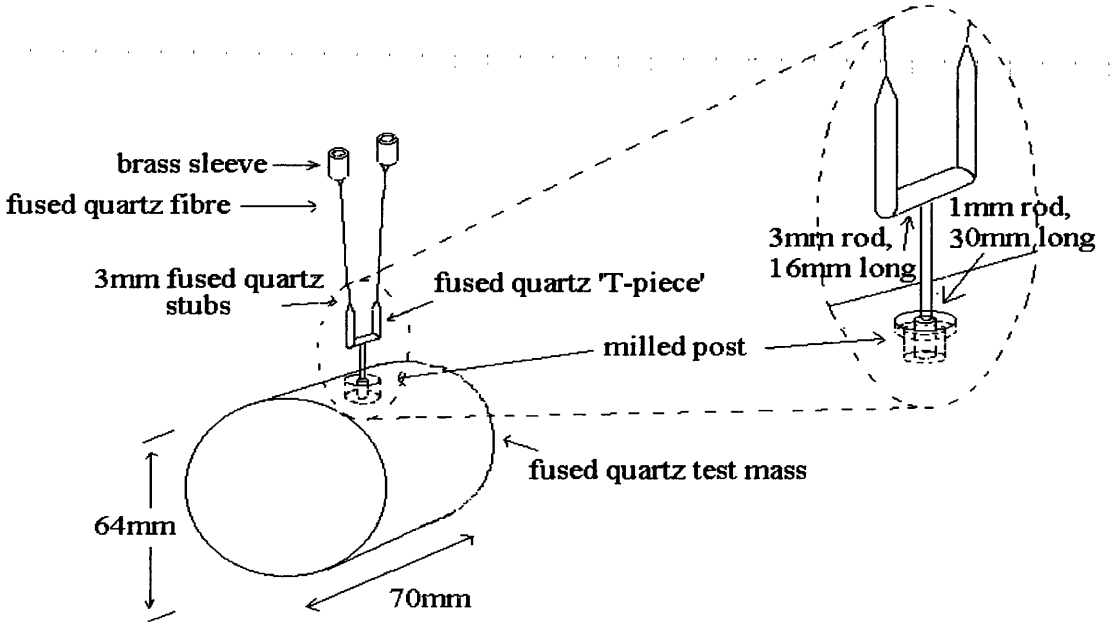

Figure 7.3: *Construction of test mass with welded attachment.*

Figure 7.4: *Cylinder used in the construction of the indium and hydroxide catalysis bonded test mass (diameter 1 cm, length 2 cm).*

exactly with the predicted frequencies of the first few vibrational modes of the test mass.

7.3.3 Formation of the Indium Bond

Indium is peculiar in that it 'wets' fused quartz and this behaviour allows it to act like a solder when joining two pieces together. To form an indium bond, a 15 mm wide flat was polished along the length of another 500 g fused quartz mass. A 10 mm diameter by 20 mm long fused quartz cylinder was also polished at one of its ends, and its other end was ground to a 3 mm diameter post. This 'bonding cylinder' can be seen in figure 7.4.

The test mass and bonding cylinder were thoroughly degreased and cleaned and heated to a temperature of $\sim 140°C$, just below the melting temperature of indium. The use of an ultrasonic soldering iron allowed thin layers of indium to be deposited in the centre of the flat polished on the test mass and also to cover completely the 10 mm diameter polished surface of the bonding cylinder [3]. An ultrasonic soldering iron was required to break the thin oxide layer that forms on the surface of the indium, thus allowing it to flow evenly across the surface of the fused quartz. The two indium coated flats were brought quickly into contact with one another. Heating of the mass was continued for a period of approximately three hours after which it was allowed to cool naturally. The mass of indium used in the bond was later measured [4] as 30.7×10^{-6} kg. This allowed the thickness of the bond to be calculated as $\sim 50\,\mu$m (using the density of indium, $\rho = 7.3 \times 10^3\,\mathrm{kg\,m^{-3}}$).

A pendulum was constructed by welding the 3 mm post of the bonding cylinder to the T-piece and suspension fibres from the welded system discussed in the previous section. To keep the bond cool during the welding process a small reservoir was built up around the bonded area and filled with water. The resulting pendulum is shown in figure 7.5. The welding process was performed with the T-piece and fibres in situ within the experimental apparatus; thus any changes in the loss measured between the two bonded masses should be attributable directly to the method of bonding.

7.3.4 Formation of the Optical Contacted Bond

The process of forming an optical contact must be carried out in a clean room environment, between two grease-free pieces polished to be optically flat (i.e. the pieces should be polished to better than $\frac{\lambda}{10}$ distortion in the interference pattern formed between the bonding piece and a reference flat). Water present on the surface of two optically flat pieces causes silanol (Si-OH) to form on the surface of the fused quartz. Silanol then attracts further water molecules. When the two pieces are brought into contact bonding occurs. The dominant bond formed is the hydrogen bond which occurs between the water molecules present on the adjacent surfaces. Chemical bonds between silanol groups

[3] The initial test bond was formed by Hans Rohner of JILA, Boulder, USA.

[4] Courtesy of the Department of Chemistry, University of Glasgow.

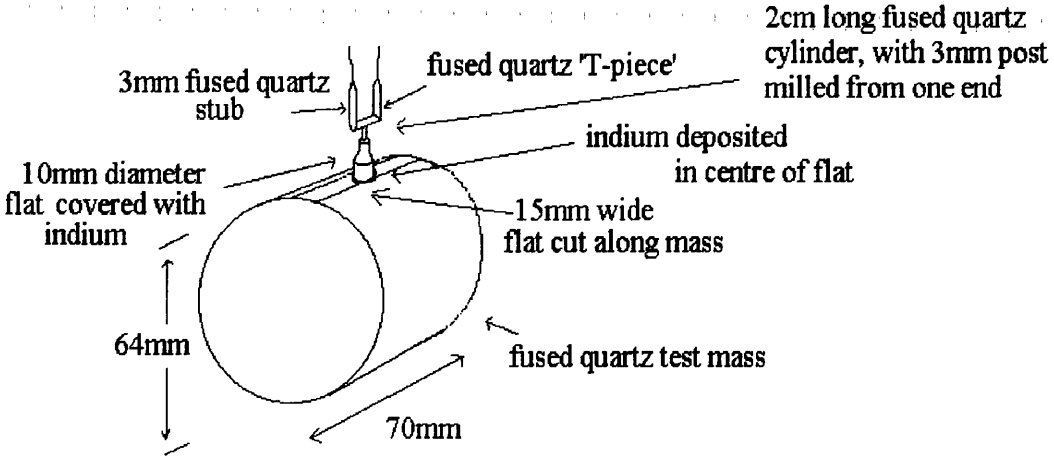

Figure 7.5: *Pendulum constructed with an indium bonded attachment.*

present on the adjacent surfaces is energetically unfavourable although it can occur in the sub-100 μm scale.

Small chamfers were polished around the edges of all of the optical flats. This was to prevent the smaller flat scratching the larger flat when the two pieces were brought together. With a small piece (i.e. the the 1 cm bonding cylinder), the chamfer has the effect of bevelling the flat. In addition, optical contacting is usually performed with a bonding piece of height that is smaller than the diameter of the optical flat. This configuration helps by allowing the flat to be slightly deformed when pressure is applied (when trying to form the optical contact) thus encouraging even bond formation. Our bonding cylinder however was twice the length of the diameter making it more difficult for the surface deformation to occur. These factors meant that we had difficulty forming a bond of the quality that was required. This and the lower bond strength of the optical contact made us decide not to pursue optical contacting as a method of bonding.

7.3.5 Formation of the Hydroxide Catalysis Bond

Hydroxide catalysis bonding (or hydroxide catalysed hydration/dehydration) takes place between two flats in clean room conditions. Although the flatness of the bonding pieces required for hydroxide catalysis bonding is not as stringent as in optical contacting, it is desirable to use pieces that are as flat as possible. A $\frac{\lambda}{10}$ optical flat, 15 mm wide

was polished along the length of a 500 g test mass. A bonding cylinder, with one of the ends ground to a 3 mm post (as described previously) had its 10 mm diameter end polished nominally to $\frac{\lambda}{10}$ flatness. Both of the optical flats were cleaned thoroughly using trichloroethylene, rinsed with water and then in isopropanol to remove any trace of grease or dust particles. A weak aqueous solution of potassium hydroxide was made and filtered (1:500 molecular number ratio of KOH in H_20). This solution is used as a catalyst in the jointing process. 0.2 μl of the solution introduced between the two surfaces was found to be more than adequate to bond the 10 mm diameter flat to the test mass.

A model of the bonding process follows. A number of siloxane bridges (Si-O-Si) are exposed on the polished surfaces of the fused quartz. The presence of water in the atmosphere forms a small number of silanol groups (Si-OH) from these siloxane bridges (as has been discussed previously in the context of optical contacting). Hydration of the bonding surfaces by the introduction of the KOH solution increases the number of silanol groups present, forming 2 per exposed siloxane bridge (refer to figure 7.6(i)). The KOH also reacts with the surface of the fused quartz (SiO_2). This reaction can take many forms, the simplest of which is

$$SiO_2 + 2KOH \rightarrow K_2Si0_3 + H_2O \tag{7.4}$$

i.e. the KOH etches SiO_3^{2-} ions from the bonding surface, depositing them into the solution along with K^+ ions. The KOH also strips the H^+ ion from each of the silanol groups. These then bond with hydroxyl ions (OH^-) present in the solution to form H_20 – i.e. dehydration takes place (refer to figure 7.6(ii)). A silicate ion is then attracted to the O^- remainder of each silanol group. Further silicate ions then bond to the free O^- present on each subsequent silicate ion to form an extended silicate chain. The K^+ ion is not involved in the bond formation and potassium hydroxide is therefore returned to the solution at the end of the reaction (refer to figure 7.6(iii)). A similar process happens on the other bonding surface. The activated pieces are brought into contact and a complicated interlocking structure is formed.

The bonding process was carried out in a laminar flow cabinet to prevent contamination of the pieces. Minor adjustments of the pieces could be made within the first forty

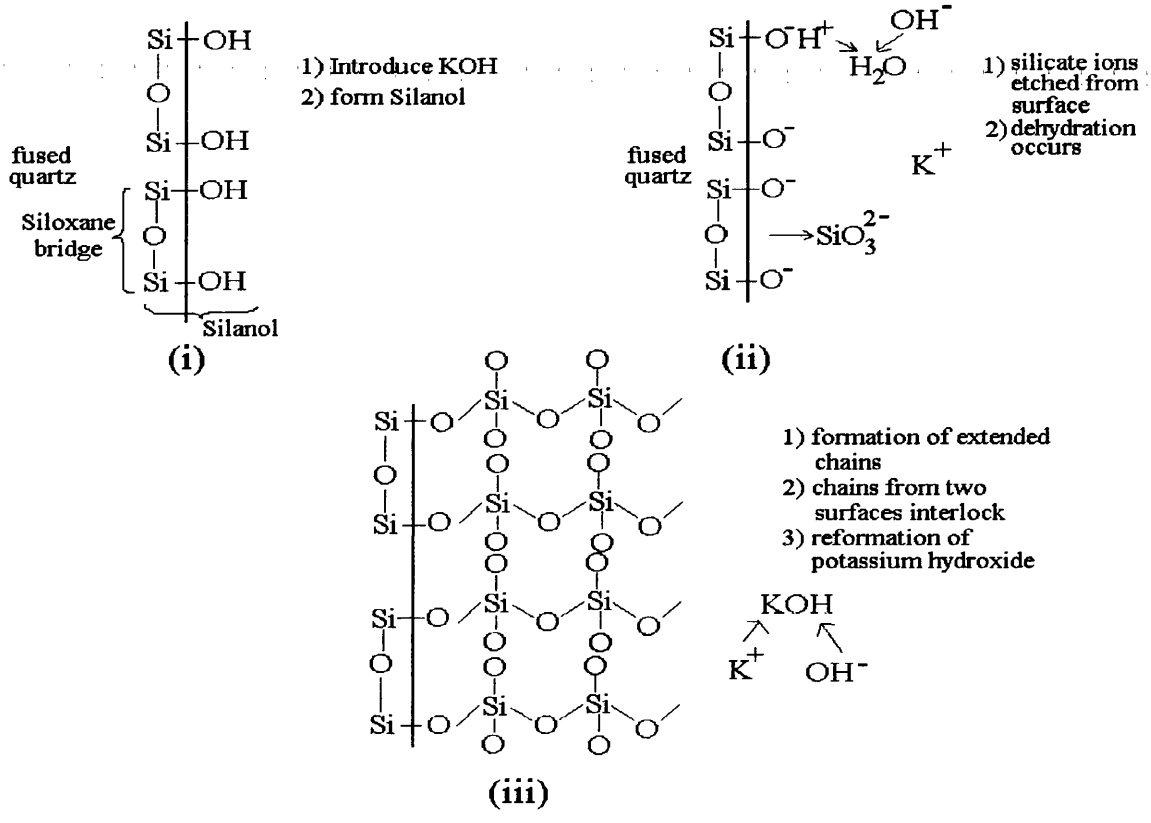

Figure 7.6: *Model of chemistry involved in hydroxide catalysis bond.*

minutes after the bond was formed. This type of bond reaches its maximum strength after several weeks but sets sufficiently to handle after only a few hours. The bond formed and used in the subsequent tests was later examined closely and found to have some small imperfections (i.e. small sections which had not bonded successfully).

Again, the pendulum was formed by welding the 3 mm post of the milled cylinder to the original T-piece and fibres in position within the vacuum tank. The bond area was irrigated with water throughout the welding process to minimise the effect of heat on the hydroxide catalysis bond (see figure 7.7).

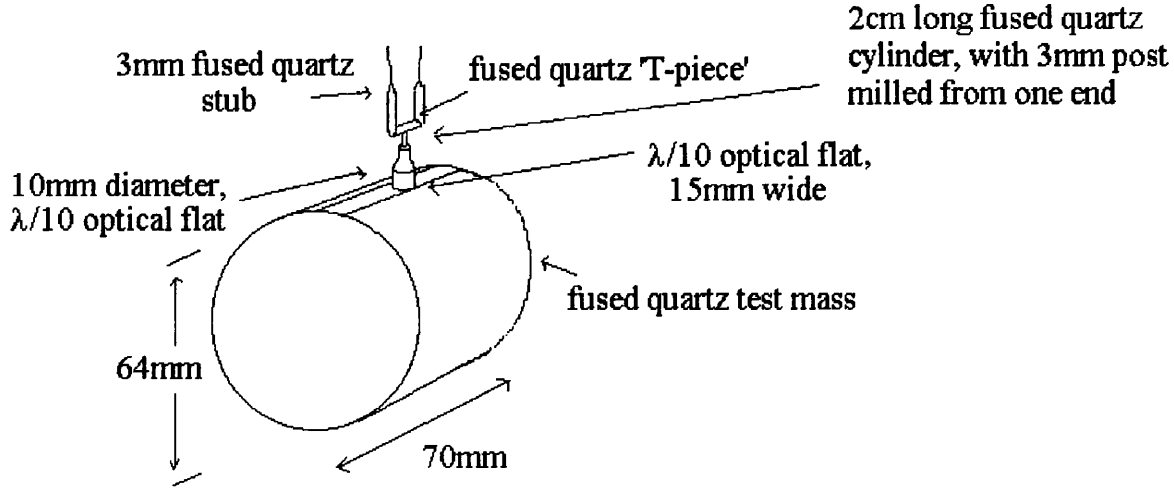

Figure 7.7: *Pendulum constructed using an attachment made by hydroxide catalysis bonding.*

7.4 Investigation of the Effect of Bonding Technique on the level of Internal Loss

7.4.1 Determination of the Mode Frequencies

An approximate value for the frequency of the fundamental longitudinal mode of a cylindrical mass is given by substitution of the dimensions and material constants of the test mass into equation 7.5 [64, 65] i.e.

$$\omega_0 = \frac{\pi c}{L}\left[1 - \left(\frac{\sigma \pi r}{2L}\right)^2\right] \tag{7.5}$$

where c is the speed of sound [5], L and r are the length and radius of the test mass respectively and σ is Poisson's ratio [6]. The value of ω_0 was calculated to be $\sim 40.2\,\mathrm{kHz}$. The fundamental longitudinal mode and higher order mode frequencies can be determined by examination of the plots in McMahon's paper on vibrational modes of aluminium

[5] the speed of sound in fused quartz is $5720\,\mathrm{m\,s^{-1}}$.

[6] Poisson's ratio in fused quartz is 0.17.

and steel cylinders [66]. Firstly, using the aspect ratio of our test mass ($\frac{L}{r} = 2.2$), the dimensionless frequency parameter of a mode, $\frac{\omega r}{c}$, (in either aluminium or steel) was extrapolated from the appropriate curve on one of the plots. If the mode in question was 'symmetric', a correction was made to the dimensionless frequency parameter to account for the difference in Poisson's ratio of the two materials. A definition of 'symmetric' and 'anti-symmetric' modes can be found in the following section. The dimensionless frequency parameter (either with or without the correction) is then multiplied by the speed of sound in fused quartz and divided by the radius of the mass. The result is an estimate of the equivalent mode frequency in the fused quartz test mass.

7.4.2 Classification of Modes

The internal modes of the test mass are classified according to McMahon's [66] scheme. In his paper McMahon named modes according to the order of circumferential and longitudinal symmetry of the mode of vibration.

- The circumferential order (n) of a mode informs us of the order of symmetry with respect to rotation about the longitudinal axis of the test mass.
- A mode is longitudinally symmetric if the radial and tangential displacements are symmetric about the mid-plane of the cylinder (i.e. $u_r(z) = u_r(-z)$ where u_r is the radial displacement). Symmetric modes are denoted by even numbers. Antisymmetric modes, denoted by odd numbers, are modes with motion $u_r(z) = -u_r(-z)$.

A demonstration of this classification for the internal modes observed in the tests can be seen in figure 7.8. End and side views of the test mass are given for each mode together with the McMahon mode classification and a descriptive name for the mode. The lines shown on the end view of the masses represent nodes.

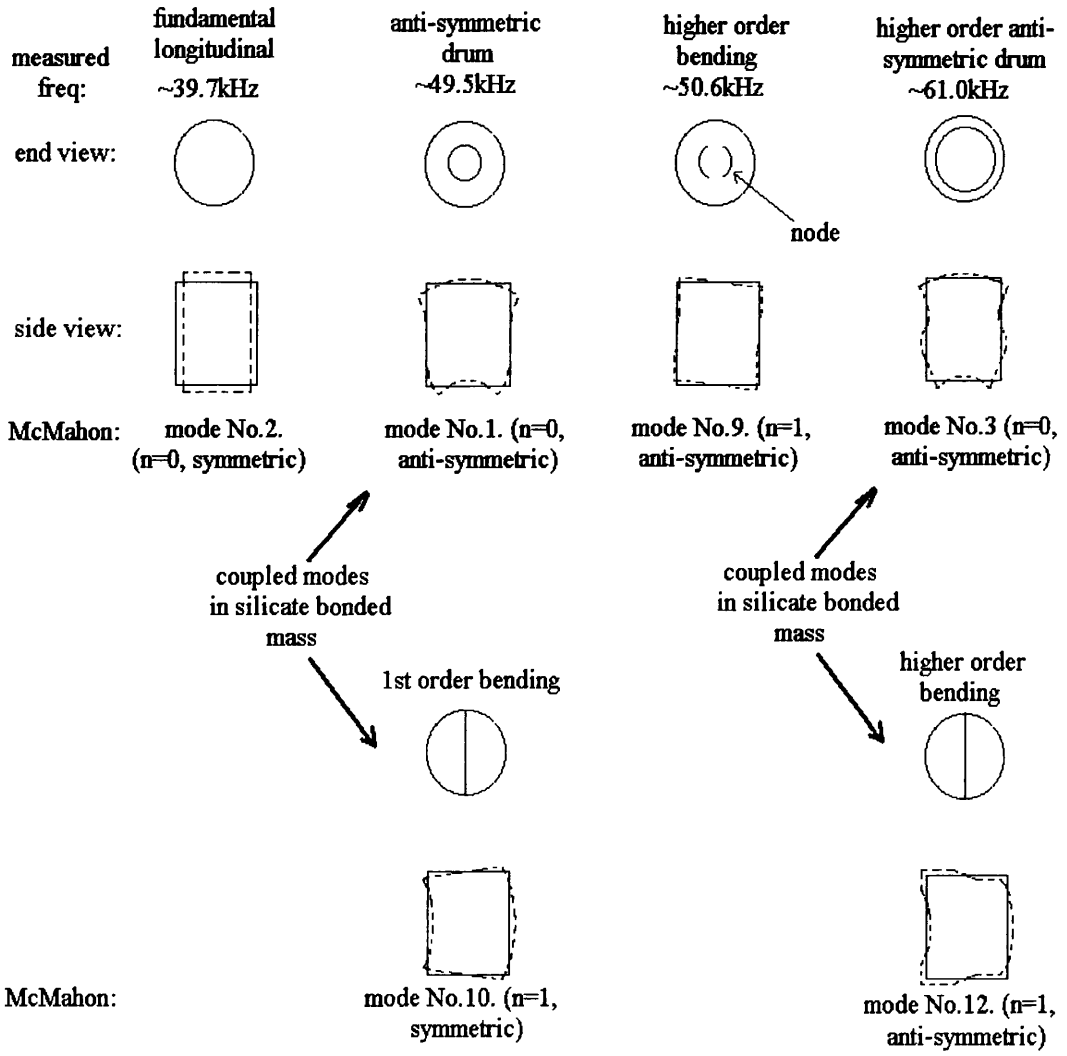

Figure 7.8: *Example of end and side views of the observed internal modes together with the associated mode numbers.*

7.4.3 Experimental Technique

A three legged aluminium table was placed on three pads of RTV rubber on a rigid platform inside a vacuum tank. The brass encased stubs at the free ends of the fibres were fed up through a slot cut in the top of this table and clamped into an aluminium suspension plate (refer to figure 4.2). Two suspension fibres were used to inhibit excitation of the rotational mode of the pendulum. The separation between the upper ends of these were made slightly larger than the separation of the lower ends to prevent coupling of the two orthogonal pendulum modes from the Coriolis effect. The suspension plate was then lowered down on to three RTV rubber pads which rested on the upper surface of the three legged table. Finally, a large aluminium block was placed on top of the suspension plate. The pendulum was therefore isolated from external vibrations by two sets of rubber/aluminium layers. The tank was evacuated to a level of $\sim 10^{-7}$ mbar to minimise gas damping of the internal modes.

The internal modes of each bonded mass were excited by means of an electrostatic drive plate situated parallel to one end of the mass. The drive plate consisted of two series of interlocking metal fingers that were etched onto a fibreglass board (the fingers being separated by $\sim$ 1 mm). One series of fingers was grounded and the other was biased to $\sim$+750 V. The separation between the mass and plate was $<$ 1 mm. A large resistor was inserted in series between the high voltage amplifier and the drive plate to protect the high voltage amplifier in the event that the drive plate should short circuit. A spectrum analyser was used to apply a slowly varying swept sine wave (in a frequency band around the calculated resonant frequencies) to a high voltage amplifier connected to the d.c. biased drive plate. The alternating electric field between the two sets of fingers coupled to the dielectric material of the mass. This produces an oscillating force and hence causing the mass it to oscillate. The frequency spectrum that resulted (as detected by the interferometer arrangement discussd below) was used to determine the exact mode frequencies. When a resonant frequency had been found, a signal generator set to that frequency was used to send a 1500 $V_{pk/pk}$ drive signal to the plate. Once the resonance had been excited sufficiently the a.c. drive signal was switched off and the resonant motion allowed to decay freely. The levels of damping caused by the mass moving in the d.c. field and inducing currents to flow in the resistor discussed above have been shown in calculations to be negligible [64].

The motion of the test mass surface was sensed using a Michelson interferometer. One arm of this was formed between the beamsplitter and a mirror evaporated onto the front face of the test mass. The other arm was formed between the beamsplitter and three mirrors positioned in a folded arrangement (to ensure that the second arm was approximately the same length as the first). Two of the three mirrors were mounted on loudspeakers and the third was attached to a piezoelectric transducer (PZT). The loudspeakers, PZT and beamsplitter were mounted on a table outside the vacuum tank. The interferometer was illuminated by light from a Helium-Neon laser. A photodiode was positioned at the output and used to detect the changing interference pattern. This pattern contained information about the motion of the front face of the test mass at both high frequencies (resulting from the internal resonant modes of the test mass) and dominantly, at low frequency (resulting from the pendulum mode of the system). By feeding back a fraction of the low frequency signal (i.e. $<100\,\mathrm{Hz}$) to the loudspeakers and PZT, the mirrors mounted on them were forced to follow the pendulum motion of the test mass. This allowed the much smaller signals resulting from the motion of the internal modes to be observed.

The high frequency signals from the internal modes of the test mass were filtered, amplified and sent to the input channel of a lock-in amplifier. Each of the resulting signals was then mixed with a signal of constant amplitude supplied by the internal reference source of the lock-in amplifier. In each case, the reference signal was adjusted to be $\sim 10\,\mathrm{Hz}$ away from the mode frequency. The resulting $\sim 10\,\mathrm{Hz}$ beat signal was of low enough frequency to be recorded with a chart recorder. The amplitude of the beat signal decayed at the same rate as the high frequency internal mode. The rate of amplitude decay and the internal mode frequency were used to calculate the mechanical loss factor associated with the mode as was described in section 2.5. The experimental equipment is shown schematically in figure 7.9.

7.4.4 Experimental Results

The loss factors associated with four internal mode frequencies were measured for each type of bonded test mass. The loss factor of each mode was measured several times and the average result for each mode is shown in table 7.2. Sketches of the measured modes

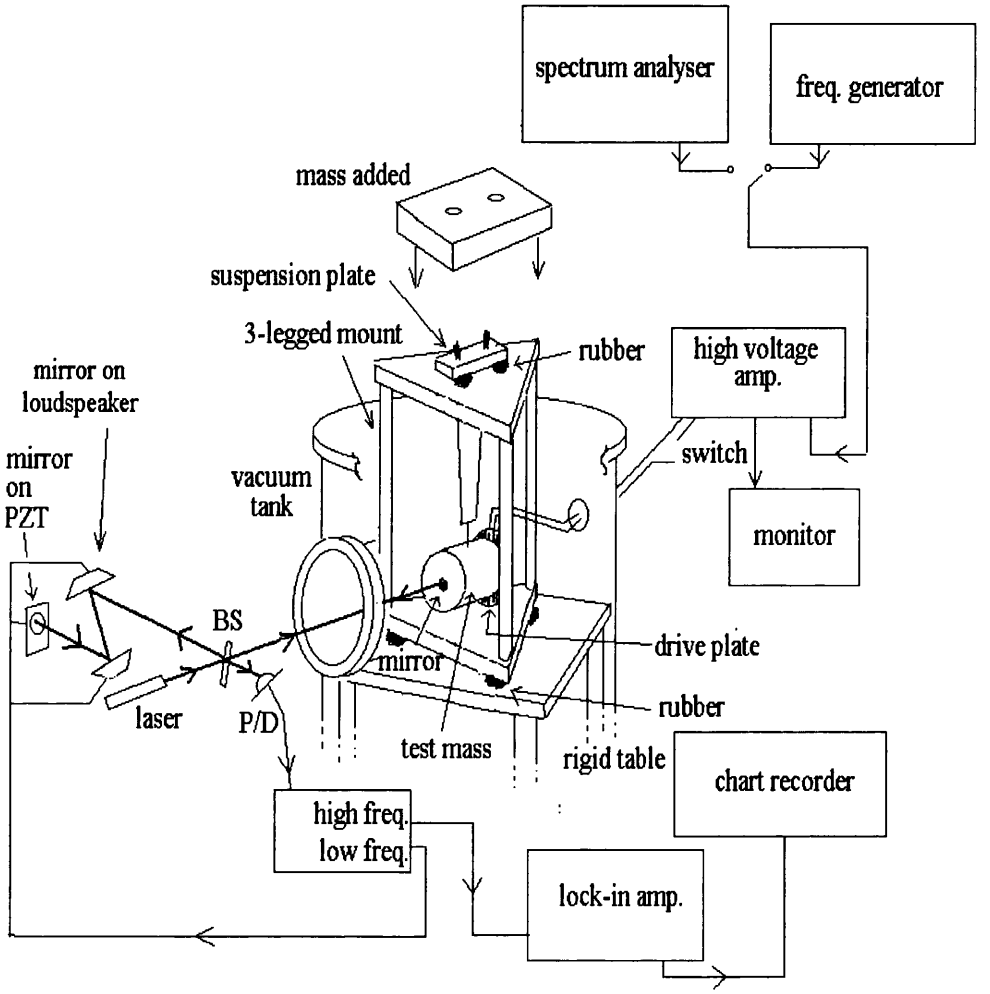

Figure 7.9: *Experimental apparatus used to measure the losses asociated with the internal modes of the bonded test masses.*

bond type	measured loss factor			
	fund. (Mode No.2) ~ 39.7 kHz	anti-symm. drum (Mode No.1) ~ 49.5 kHz	high-order bend. (Mode No.9) ~ 50.6 kHz	high-order anti-symm. drum (Mode No.3) ~ 61.0 kHz
Weld.	$(5.5 \pm 0.2) \times 10^{-7}$	$(6.2 \pm 0.1) \times 10^{-7}$	$(1.9 \pm 0.1) \times 10^{-6}$	$(7.1 \pm 1.1) \times 10^{-7}$
Indium.	$(1.4 \pm 0.1) \times 10^{-5}$	$(2.1 \pm 0.2) \times 10^{-6}$	$(4.3 \pm 0.3) \times 10^{-5}$	$(3.0 \pm 0.2) \times 10^{-5}$
hydroxide catalysis.	$(1.8 \pm 0.1) \times 10^{-5}$	$(7.7 \pm 1.8) \times 10^{-7}$ predominantly Mode No.1	$(2.9 \pm 1.2) \times 10^{-5}$	$(4.8 \pm 0.6) \times 10^{-6}$ predominantly Mode No.3
	-	$(8.3 \pm 0.8) \times 10^{-6}$ predominantly Mode No.10	-	$(1.7 \pm 0.2) \times 10^{-6}$ predominantly Mode No.12
wire-slung	7.3×10^{-7}	-	-	-

Table 7.2: *Losses obtained for the various bond types.*

are shown in figure 7.8. The modes were identified by studying the relative positions in frequency space of each mode with respect to one another and then comparing these positions to those in McMahon's plots [66].

To give a reference point, the loss factors obtained were also compared with the loss factor measured on a mass of the same grade of fused quartz suspended by a single wire loop [63]. Assuming that fused quartz is structurally damped, the level of loss factor expected for higher order modes would be the same as that observed at the fundamental longitudinal frequency.

In an interferometric gravitational wave detector only modes which involve motion of the centre of the test mass face will contribute to the level of displacement noise. These same modes were the only ones expected to be detectable with this measurement scheme. It should however be noted that some modes which do not exhibit motion of the centre of the mass face were in fact detected in the experiment. These modes were mode No. 10 and mode No. 12 observed in the hydroxide catalysis bonded mass. Diagrams of these modes

are shown in figure 7.8. Care had been taken to ensure that the laser was accurately positioned on the centre of the mass face. It was therefore thought that the reason for observing these modes was that the bonded attachment altered both the frequency of a detectable mode and that of a second mode (closely positioned to the detectable mode in frequency space but previously undetected). This brought the frequencies close enough to allow the two modes to couple and form two new modes.

The difference in frequency between the two modes measured at $\sim 49.5\,\mathrm{kHz}$ was 102 Hz. Using the plots in McMahon [66] and searching for a previously undetected mode close in frequency to the detected mode in question, it was concluded that the two observed modes were formed from the coupling of the anti-symmetric drum mode (mode No.1) and the first order bending mode (mode No. 10). The lowest loss was measured for the lower frequency mode. It is believed that this mode was composed primarily of mode No. 1. We infer this because the amount of flexing of the mass in the region of the bond is smaller for this mode. The smaller motion in this region reduces the possibility of inducing frictional losses in the bond (which, as stated before, had some small imperfections). The upper frequency mode was thought to consist mainly of mode No. 10. This mode has increased flexing in the bonded region of the mass and a correspondingly higher loss.

Consider now the modes measured at $\sim 61.0\,\mathrm{kHz}$. The difference between the two mode frequencies was measured to be 75 Hz and it is believed that they were formed by the coupling of a higher order anti-symmetric mode (mode No. 3) and a higher order symmetric mode (mode No. 12). The measured amplitude of the lower frequency mode was observed to be very dependent on the position of the laser beam on the mass face. It was therefore concluded that the dominant mode at this frequency was that of mode No. 12 – the mode with the greatest amount of motion near the centre of the mass face. Consequently, the higher frequency mode was believed to be composed mainly of mode No. 3.

7.5 Comparison of the Suitability of the Various Bonding Techniques

We will now discuss the relative merits of each type of bond, considering the measured losses associated with each bond type (refer to table 7.2) in conjunction with the practicalities involved in forming each bond.

7.5.1 Welding

The loss factors obtained for the mass with the welded attachment are low and are approximately the same as that measured for the mass suspended by a wire loop (i.e. a few $\times 10^{-7}$) for all but the higher-order bending mode. However the process of welding can induce stress in the mass. This was observed when we viewed the mass during welding through crossed polarisers – a region of induced stress was seen to form in the mass despite the use of water cooling. Over a period of time most of this stress relaxed out of the mass, leaving only a small region at the edge of the milled hole at the point where the heat of the welding torch was concentrated. This region can be seen as the small bright spot near the top of the mass in figure 7.10. This remaining area of induced stress eventually caused a small crack to form in the region of the mass around the drilled hole. Cracking is clearly undesirable in the optics of an interferometric gravitational wave detector. The problem of induced stress and the subsequent cracking could in principle be alleviated by drilling a larger hole around the milled post and using a smaller welding flame

Welding has the advantage of forming a bond as strong as the material itself. The disadvantages of welding are however as follows. A permanent hole had to be milled into the mass thus leaving no scope for alteration in the bond position. Also, care needs to be taken to try and form a perfect joint on the first attempt. Taking too many attempts to weld can melt and deform the post beyond use and the fused quartz mass may be wasted – an expensive process.

Figure 7.10: *Photograph showing the region of stress caused by the welding torch during the formation of the welded bond.*

7.5.2 Indium Bonding

The loss factors measured for the indium bonded mass appear to be somewhat worse than those measured for either the wire-slung or welded pendulums – ranging between $\sim 4 \times 10^{-5}$ and $\sim 2 \times 10^{-6}$. As a result, this loss factor is assumed to be primarily associated with the bond itself. However it is instructive to scale the highest measured loss factor to find the level of loss that might be expected for a full sized GEO 600 test mass suspended on bonds tensioned to $\frac{1}{3}$ of their bond strength.

In scaling from 500 g to a GEO 600 test mass, there is an increase in mass of a factor of 32. It is believed that the increase in mass will lead to a decrease in loss by at least the same factor for a bond of identical size. From the bond strength it can be shown that a bond area the same as the 1 cm diameter bond used in the reported tests would be suitable for suspending the 16 kg mass at $\frac{1}{3}$ of the bond strength. Because the bond area does not require to be scaled, there is no corresponding change in loss. However, the bond, at 50 μm thick could be reduced to $\sim \frac{1}{10}$ of the original thickness. This might be expected to reduce the loss by at least a corresponding factor of 10. Combination of these two scaling factors decreases the highest measured loss factor of the indium bonded mass to $\phi_{bond_{scaled}}(\omega_0) = (1.3 \pm 0.1) \times 10^{-7}$ which, being approximately the same level as that expected from the fused quartz, suggests that indium bonding should not have too severe an effect on the loss associated with the material of the test mass.

The process of indium bonding proved rather difficult to perform successfully. Although the use of the ultrasonic soldering iron helps to alleviate the problem of build up of the oxide layer, oxidisation of the exposed surfaces can re-occur rapidly thus requiring the bond to be formed quickly. Depositing layers of indium on each of the bonding surfaces with the soldering iron led to the formation of a relatively thick and, therefore lossy bond. In order to avoid this we attempted to evaporate thin layers of indium onto the two surfaces. However oxidisation of the two layers set in immediately and appeared to prevent the bond from being formed.

The main advantage of indium bonding is that the bond can be separated without damaging either bonding pieces. Indium bonding is the weakest of the methods tested and results in the need for a correspondingly larger bond area. Because of the low melting point of indium (147°C), creep of the bond during bake-out of the vacuum system prior to operation of the detector may be of some concern. Vacuum bakes will be performed at 80°C.

7.5.3 Hydroxide Catalysis Bonding

The results obtained from the pendulum formed using the hydroxide catalysis bond (i.e. ranging between $\sim 8 \times 10^{-7}$ and $\sim 3 \times 10^{-5}$) appear to be on average worse than the results from either the wire-hung or welded pendulum [7]. Once again this loss is therefore assumed to be primarily associated with the bond itself. However it is once more instructive to scale the worst measured result to find the level of loss factor that might be expected from a bond area of a size that can suspend the 16 kg GEO 600 test mass at $\frac{1}{3}$ of the bond strength. A mass increase of a factor of 32 is obtained in moving from the 500 g mass to a full sized test mass. This is believed to cause a decrease in loss of at least a corresponding factor for a bond of the same size and quality as that used in the experiment. From the bond strength it can be shown that a bond area which is a factor of 5 times smaller than the 1 cm diameter bond used would be suitable for suspending the GEO 600 test mass at $\frac{1}{3}$ of the accepted bond strength. This should reduce the loss by the same factor. Combining these two factors with the worst measured loss from the

[7] The results presented in table 7.2 for the pendulum formed using hydroxide catalysis bonding were measured 12 days after the bond was formed. Further loss measurements made after 26 days and 101 days did not differ significantly.

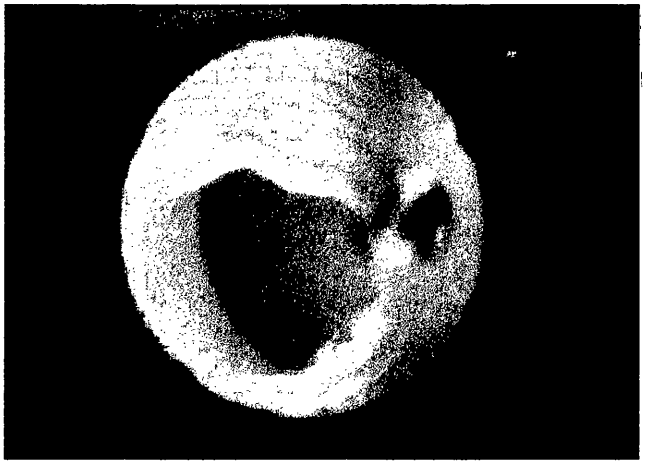

Figure 7.11: *Photograph showing the interference fringes present between the two bonding surfaces of an imperfectly formed hydroxide catalysis bond.*

mass bonded by hydroxide catalysis, scales the loss to $\phi_{bond_{scaled}}(\omega_0) = (1.8 \pm 0.7) \times 10^{-7}$ for a bond of the same quality as the tested bond. Therefore hydroxide catalysis bonding is not expected to have too severe an effect on the level of internal loss associated with the test masses of GEO 600.

Close examination of the hydroxide catalysis bonded interface showed some small imperfections. It seems possible that as the mass oscillates, particles of dried KOH may 'grind' in the area where bonding was unsuccessful and therefore cause additional loss. It is believed that the formation of a more complete bond may decrease the measured losses further. A picture of an earlier and less complete attempt at hydroxide catalysis bonding can be seen in figure 7.11. The interference fringes show the region over which the bond did not form.

Hydroxide catalysis bonding has many further advantages. It is an inexpensive and reasonably straightforward method of bonding in which there is a period of time to make adjustments of the position of the bond. It is reported that the bonding pieces can usually be separated with minimal damage within the weeks before the bond has completely taken [67]. This can be achieved by placing the pieces in an ultrasonic bath. Hydroxide catalysis bonding is a strong bonding method. Strength tests reported by D.-H. Gwo [67] performed on fully formed bonds ultimately result in tearing of the bulk material at the bond strength quoted.

7.6 Recent Results

Care had been taken in designing the pendulums to reduce the effect of coupling between higher order violin modes and internal modes of the mass. The presence of coupling can result in a transfer of energy into a violin mode with a corresponding increase in the measured loss factor of the internal mode [64]. Further experiments were conducted by Dr. S. Rowan [68] to check if this effect had been significant in any of the above measurements.

In this test, a bonding cylinder was attached to a 500 g test mass using hydroxide catalysis bonding and a T-piece welded onto the post of the cylinder. The cross-bar of this T-piece was however formed from a section of fused quartz capilliary tubing. A length of carbon steel wire was passed through this tube. The ends of the wire were attached to a system that allowed the length of the wire to be adjusted.

The fundamental longitudinal mode of the mass was excited using the method described in section 7.4.3 and the loss factor measured at a series of different wire lengths. The best measured loss factor was $\phi_{internal_{bond}}(\omega_0) = (7.14 \pm 0.10) \times 10^{-7}$.

A control experiment was also performed. This involved sitting a 500 g mass in a loop of carbon steel wire and measuring the loss factor of the fundamental longitudinal mode at various different wire lengths. The best loss factor measured in this experiment was $(6.80 \pm 0.09) \times 10^{-7}$.

If we assume that any difference between the loss factors measured for the masses with and without the hydroxide catalysis bond is due to the bond itself, we can estimate the level of excess loss, $\phi_{internal_{excess}}(\omega_0)$, associated with this size of bond. This can be achieved with the following equation:

$$\begin{aligned} \phi_{internal_{excess}}(\omega_0) &= \phi_{internal_{bond}}(\omega_0) - \phi_{internal_{control}}(\omega_0) \\ &= (3.4 \pm 1.3) \times 10^{-8}. \end{aligned} \tag{7.6}$$

The excess loss can in turn be scaled (following the same argument as that em-

ployed in section 7.5.3) to give a figure for the excess loss expected from a hydroxide catalysis bond suitable for suspending a GEO 600 sized test mass. This figure is $\phi_{internal_{excess}}(\omega_0) =\sim 2 \times 10^{-10}$ – substantially lower than the intrinsic loss factor of the material itself (i.e. $\phi_{internal_{control}}(\omega_0) \sim 7 \times 10^{-7}$). It can therefore be concluded that the excess loss introduced by hydroxide catalysis bonding will give a negligible contribution to the intrinsic loss associated with the material of the test mass.

7.7 Conclusions

A four fibre suspension will be employed in GEO 600 to minimise the thermal noise associated with the pendulum mode of the test mass suspension.

Various methods of attaching the fused quartz fibres to small test masses were considered. The strength of each bond type and their ease of formation were compared. The effect on the measured loss factor associated with four internal mode frequencies were measured. Consideration of all the facts suggest that hydroxide catalysis bonding would be ideal for use in the construction of the test mass suspensions in GEO 600.

Chapter 8

Conclusions

This thesis is a study of various loss mechanisms present within the test mass suspensions for GEO 600, and the implications of these losses in terms of the resulting thermal noise levels.

Measurements have shown that suspension fibres pulled from 'standard grade' fused quartz exhibit an intrinsic loss factor of $\phi_{mat_{intrinsic}}(\omega) = (0.5-1)\times 10^{-6}$ in the frequency range 6 Hz to 160 Hz – potentially a factor of 10 better than the maximum acceptable material loss factor as set by the GEO 600 design specification.

These fibres were subsequently used in the construction of small mass pendulums. When the fibres were attached to the point of suspension using either a mechanical clamping method or by welding, the pendulum mode loss factor was measured to equal that determined by known losses in the system. On subtraction of the recoil damping contribution from the measured loss, the remaining loss could be used to predict that achievable by a full size GEO 600 suspension. The projected loss was $\phi_{pend_{total}}(\omega) \sim 8.5 \times 10^{-9}$ at 50 Hz – approximately a factor of four better than the design specification for GEO 600. 'Standard grade' fused quartz has been shown to be an ideal material for the suspension fibres the test masses in GEO 600.

The investigation of hydroxide catalysis bonding to attach fused quartz fibres to fused silica test masses has shown that it can be used without introducing significant excess loss. It also has advantages in the process of assembly and the strength of the bond formed.

Therefore it has been proposed that hydroxide catalysis bonding will be employed in the construction of GEO 600.

Both the use of fused quartz fibres and hydroxide catalysis bonding are novel approaches to test mass suspension that have yet to be implemented by the other major interferometer projects. However we have shown that by adopting these techniques it should be possible to achieve (and with care improve upon) the GEO 600 design specification and therefore ensure that the detector remains limited by the thermal noise associated with the losses intrinsic to the mirror material itself.

Building on the techniques developed and lessons learned and reported in this thesis, the development of full-scale suspensions are being continued by Dr. S. Rowan and Mr. S. McIntosh and are advancing rapidly towards the final goal of installation in GEO 600 within the next year.

Appendix A

External Gas Damping

It is imperative that we know the extent of gas damping present within our vacuum chamber. The following proof allows us to determine the minimum level of pendulum mode loss factor achievable in a system for a given pressure or, alternatively, the level of vacuum pressure required for the pendulum to experience a negligible effect from external gas friction.

Consider the case of a gas damped pendulum. We can derive the fluctuation-dissipation theorem for this example using the following procedure. The equation of motion of the system is

$$F = m_p\ddot{x} + b\dot{x} + kx \tag{A.1}$$

where F is the driving force (in this instance the fluctuating thermal force of gas atoms randomly hitting the pendulum), m_p is the mass of the pendulum, the term $b\dot{x}$ is the frictional force the pendulum experiences as it moves through the gas and kx is the restoring force of the suspension wires. This equation can be rewritten in terms of velocity, v, (where $\ddot{x} = i\omega v$ and $x = \frac{v}{i\omega}$) to give

$$F = i\omega m_p v + bv - i\frac{k}{\omega}v. \tag{A.2}$$

Dividing F by v allows us to determine the mechanical impedance

$$Z(f) = b + i\left(\omega m_p - \frac{k}{\omega}\right). \tag{A.3}$$

Taking the real part of the impedance, $\Re(Z(\omega))$, and substituting into the fluctuation-dissipation theorem (equation 2.1) gives

$$\tilde{F^2}(f) = 4k_B T b \text{ per Hz.} \tag{A.4}$$

We can also derive the fluctuation-dissipation theorem for a viscously damped pendulum in an alternative form in terms of known quantities of the surrounding gas. We shall assume that the pressure within the tank, P, is small enough so that the mean free path of the gas molecules is large compared to the dimensions of the pendulum (of surface area, A). In this situation only collisions between the molecules and pendulum mass need be considered. Let the vacuum tank contain n molecules per unit volume each travelling with an rms speed, $\frac{v}{\sqrt{3}}$, in each dimension. On average $\frac{n}{2}$ of the molecules will approach with a component normal to one surface of the pendulum and $\frac{n}{2}$ the other. The number of molecules that hit one surface of the mass with a component in the normal direction in a time interval, t, is

$$N = \frac{nAvt}{2\sqrt{3}}. \tag{A.5}$$

The total number of molecules hitting the pendulum (in a normal direction) in a time interval, t, is twice this i.e. $2N$. Because we are counting individual molecular impacts, we expect that this number will fluctuate. The fluctuation, ΔN_{total}, should obey Poisson statistics and so

$$\begin{aligned} \Delta N_{total} &= \sqrt{2N} \\ &= \sqrt{\frac{nAvt}{\sqrt{3}}}. \end{aligned} \tag{A.6}$$

Each molecule has a momentum equal to $\frac{mv}{\sqrt{3}}$ in the normal direction. If this molecule was to undergo an elastic collision with the pendulum, twice this momentum would be transferred to the mass. In the time interval, t, this would result in a force of $F = \frac{2mv}{\sqrt{3}t}$ per molecule being applied to the mass.

The total force applied to the mass (in a time, t,) will fluctuate, ΔF, due to the variation in the number of molecules hitting the mass:

$$\Delta\tilde{F} = \frac{2mv}{\sqrt{3}t}\sqrt{\frac{nvAt}{\sqrt{3}}}. \tag{A.7}$$

The above equation is then squared to give

$$\Delta\tilde{F}^2 = \frac{4nvA}{3\sqrt{3}}\frac{m^2v^2}{t}. \tag{A.8}$$

The kinetic energy of each gas molecule is $\frac{1}{2}mv^2 = \frac{3}{2}k_BT$ (according to the Equipartition theorem). The gas density can be expressed as $\rho = mn$ and the gas pressure as $P = \frac{1}{3}\rho v^2$. Substituting for n, mv^2 and then $\frac{v}{\sqrt{3}}$ into equation A.8 leads to the square of the fluctuating force being

$$\Delta\tilde{F}^2 = 4k_BT\frac{A\sqrt{P\rho}}{t} \tag{A.9}$$

which can be expressed in terms of frequency by substituting for $\frac{1}{t} = \Delta f$

$$\Delta\tilde{F}^2 = 4k_BT\left(A\sqrt{P\rho}\Delta f\right). \tag{A.10}$$

The square of the fluctuating force per unit bandwidth ($\Delta f = 1\,\mathrm{Hz}$) is

$$\Delta\tilde{F}^2(f) = 4k_BT\left(A\sqrt{P\rho}\right) \quad \text{per Hz.} \tag{A.11}$$

The ideal gas law states that $PV = \eta\mathcal{R}T$ where η is the number of moles of gas present and $\mathcal{R}$ is the gas constant. Substituting for η (where $\eta M = m_{total}$, M is the mass of

one mole of the gas and m_{total} is the total mass of the gas present) gives $PM = \rho \mathcal{R} T$. Substitution for ρ into equation A.11 leads to

$$\Delta \tilde{F}^2 = 4 k_B T \left(AP \sqrt{\frac{M}{\mathcal{R} T}} \right) \quad \text{per Hz} \tag{A.12}$$

where, on comparison with equation A.4, $AP\sqrt{\frac{M}{\mathcal{R}T}}$ is equivalent to b.

The quality factor, Q, of a viscously damped pendulum is related to the damping coefficient, b, by the expression given in equation 2.11. The quality factor is equal to the inverse of the loss factor on resonance (equation 2.12). Combining these two pieces of information gives $\phi(\omega_0) = \frac{b}{m\omega_0}$. Substituting for b into this expression leads to

$$\phi_{gas}(\omega_0) = \frac{AP}{m_p \omega_0} \sqrt{\frac{M}{\mathcal{R} T}}. \tag{A.13}$$

This equation can be rearranged to allow the calculation of a suitable working pressure, P, that ensures the level of loss due to gas damping, $\phi_{gas}(\omega)$, is significantly below the pendulum mode loss factor desired (i.e. that of the GEO 600 specification) and therefore not the limiting source of loss present.

The use of equation A.13 can be extended to allow an approximate calculation of a suitable working pressure that should allow measurement of a loss factor free of the significant effects of gas-damping for any oscillator. An example might be a vibrational mode of a ribbon fibre clamped at one of its ends (refer to Chapter 3). The calculation is approximate in this case because the effective mass, $m_{effective}$, and effective area, $A_{effective}$, involved in the oscillation (and therefore the parameters which should be substituted into equation A.13) may not have the same values as the actual mass, m and surface area, A.

Appendix B

Proofs Relating to Chapter 4

B.1 Determination of the Recoil Limit

It is useful to derive an expression for the limit to the measurable pendulum mode loss factor, $\phi_{recoil}(\omega_0)$, due to recoil damping (from the support structure) in terms of measurable quantities of the experimental system. The loss factor at the resonant frequency, ω_0, is given by equation 2.27 as

$$\phi_{recoil}(\omega_0) = \frac{E_{lost/cycle}}{2\pi E_{stored}}$$

where $E_{lost/cycle}$ is the energy lost in the top structure per cycle of the pendulum swing and E_{stored} is the energy stored in the pendulum. Expressions must be found for both the numerator and the denominator. The numerator can be expressed as

$$E_{lost/cycle} = P_{average} . \frac{2\pi}{\omega_0} \tag{B.1}$$

and

$$P_{average} = \overline{F.\dot{x}_s} \tag{B.2}$$

with $\dot{x}_s$, the recoil velocity of the support structure, and F, the force applied to the support structure by the swinging pendulum. The force is given in Appendix B.3 as

$$\begin{aligned} F &= -T sin\theta \\ &= -m_p \left(\omega_0^2 + \frac{\gamma_p^2}{4}\right) x_p \end{aligned} \tag{B.3}$$

(where T is the tension in the suspension wire, θ is the angular displacement, $x_p = x_0 e^{-\frac{\gamma_p}{2}t} sin\omega_0 t$, the horizontal displacement of the pendulum and γ_p is the decay constant of the energy of the pendulum). Given that the pendulum is viscously damped, the force can also be expressed as

$$F = F_0 e^{-\frac{\gamma_p}{2}t} sin\omega_0 t \tag{B.4}$$

where $F_0 = -m_p \left(\omega_0^2 + \frac{\gamma_p^2}{4}\right) x_0$ is the maximum applied force.

Due to the presence of loss in the structure, it is known that there is a phase angle, δ, by which the displacement of the structure, x_s, lags the applied force, F. With reference to equation 4.1 we see that the displacement, x_s, can therefore be expressed as

$$x_s = \frac{F_0}{k_s} e^{-\frac{\gamma_p t}{2}} sin(\omega_0 t + \delta). \tag{B.5}$$

Differentiating x_s gives the recoil velocity of the support structure, $\dot{x}_s$, as

$$\dot{x}_s = \frac{F_0}{k_s} e^{-\frac{\gamma_p t}{2}} \left(-\frac{\gamma}{2} sin(\omega_0 t + \delta) + \omega_0 cos(\omega_0 t + \delta)\right). \tag{B.6}$$

Substituting equation B.4 and equation B.6 into equation B.2 and taking the small angle approximation (i.e. $cos\delta = 1$ and $sin\delta = \delta$) and the time averages over 1 cycle, $(sin\omega_0 t cos\omega_0 t)_{average} = 0$ and $(sin^2\omega_0 t)_{average} = \frac{1}{2}$, leads to

$$P_{average} = -\frac{F_0^2 e^{-\gamma_p t}}{2k_s} \left(\omega_0 \delta + \frac{\gamma_p}{2}\right). \tag{B.7}$$

The term $\frac{\gamma_p}{2}$ is assumed to be very small and thus

$$P_{average} = -\frac{F_0^2 \omega_0 \delta e^{-\gamma_p t}}{2k_s}. \tag{B.8}$$

The energy lost/cycle into the support structure, $E_{lost/cycle}$, can be found by substituting equation B.8 into equation B.1,

$$\begin{aligned} E_{lost/cycle} &= -\frac{F_0^2 e^{-\gamma_p t} \pi \delta}{k_s} \\ &= -\frac{m_p^2(\omega_0^2 + \frac{\gamma_p^2}{4})^2 x_0^2 e^{-\gamma_p t} \pi \delta}{k_s} \end{aligned} \tag{B.9}$$

and since $\frac{\gamma_p^2}{4} \ll \omega_0^2$, $E_{lost/cycle}$ aproximates to

$$E_{lost/cycle} = -\frac{m_p^2 \omega_0^4 x_0^2 e^{-\gamma_p t} \pi \delta}{k_s}. \tag{B.10}$$

An expression for the numerator (i.e. the energy stored in the pendulum, E_{stored}) can be obtained from the maximum kinetic energy of the pendulum during the same cycle and is expressed as

$$E_{stored} = \frac{1}{2} m_p \omega_0^2 (x_0 e^{-\frac{\gamma_p t}{2}})^2. \tag{B.11}$$

Substituting equation B.10 and equation B.11 into equation 2.27 gives an expression for $\phi_{recoil}(\omega_0)$ as

$$\phi_{recoil}(\omega_0) = -\frac{m_p \omega_0^2 \delta}{k_s} \tag{B.12}$$

in terms of measurable quantities. This is the limit of measurable pendulum loss factor due to losses in the support structure.

Substituting for the variables in equation B.12 will show whether recoil damping of

the pendulum by a lossy suspension structure was responsible for the original value of pendulum loss obtained.

Equation B.12 also shows that the effect of recoil loss, $\phi_{recoil}(\omega_0)$, can be minimised by designing a pendulum suspension structure with a large value for the stiffness, k_s, and a small value of loss angle, δ.

B.2 The Inverted Pendulum Accelerometer and it's Calibration

The accelerometer can be considered in two distinct parts; the inverted pendulum and its associated circuitry. The inverted pendulum consists of a mass mounted on a hinge made from parallel plates so that it is constrained to move in one plane only above a rigid base plate. The recoil acceleration, $\ddot{x}_s$, of the pendulum support structure causes a relative displacement of the base plate with respect to the mass. This displacement, x_r, is sensed by measuring the capacitance between the moving pendulum and a vertical strut rigidly attached to the base plate. The relative displacement is directly proportional to the acceleration of the structure up to the resonant angular frequency, $\omega_{0_{accel}}$, of the inverted pendulum. The transfer function of the relative displacement with respect to the acceleration is given by

$$\begin{aligned} G &= \frac{x_r}{\ddot{x}_s} \\ &= \frac{1}{s^2 + \frac{\omega_{0_{accel}}}{Q} s + \omega_{0_{accel}}^2} \end{aligned} \tag{B.13}$$

where $s = i\omega$ and Q is the quality factor of the inverted pendulum.

If negative feedback is included, the relative displacement signal is amplified, filtered and fedback as a force to the mass. In principle, the transfer function of the accelerometer feedback is of the form

$$H = H_0(1 + s\tau) \tag{B.14}$$

where H_0 can be thought of as a d.c. gain contribution and the $(1+s\tau)$ term provides a phase lead for the purpose of damping of the mass. The closed loop transfer function of the relative displacement, x_r, with respect to the acceleration, $\ddot{x}_s$ is

$$\begin{aligned}\left(\frac{x_r}{\ddot{x}_s}\right)_f &= \frac{G}{1+GH} \\ &= \frac{1}{s^2 + s\left(\frac{\omega_{0_{accel}}}{Q_0} + H_0\tau\right) + \omega_{0_{accel}}^2 + H_0} \\ &= \frac{1}{s^2 + \frac{\omega_{f_{accel}}}{Q_f}s + \omega_{f_{accel}}^2}\end{aligned} \tag{B.15}$$

where $\frac{\omega_{f_{accel}}}{Q_f} = \frac{\omega_{0_{accel}}}{Q_0} + H_0\tau$, $\omega_{f_{accel}}^2 = \omega_{0_{accel}}^2 + H_0$ and Q_f is the quality factor of the inverted pendulum when feedback is applied. The use of feedback can be seen to increase the working range of the accelerometer by raising the natural angular frequency to $\omega_{f_{accel}}$. It should be noted that in practice the form of the gain, H, is more complicated than that given in equation B.14 and more typically takes the form

$$H = H_{dc}\frac{(1+s\tau)}{s\tau_2 + 1} \tag{B.16}$$

where $\tau_2 < \tau$. This is necessary as the gain cannot tend to infinity as ω increases.

Figure B.1 shows a simplified block diagram of the main elements of a feedback system of the type used by an inverted pendulum accelerometer.

Note that the transfer function of feedback acceleration, $\ddot{x}_f$, with respect to the acceleration of the structure, $\ddot{x}_s$, is given by

$$\left(\frac{\ddot{x}_f}{\ddot{x}_s}\right)_f = \frac{GH}{1+GH}. \tag{B.17}$$

It can be seen from equation B.17 that in the case of high loop gain (ie. $GH \gg 1$), that $\frac{\ddot{x}_f}{\ddot{x}_s}$ tends to 1 and that direct measurements of the structure's acceleration can be made from the feedback acceleration.

Figure B.2 shows the main components of the inverted pendulum accelerometer.

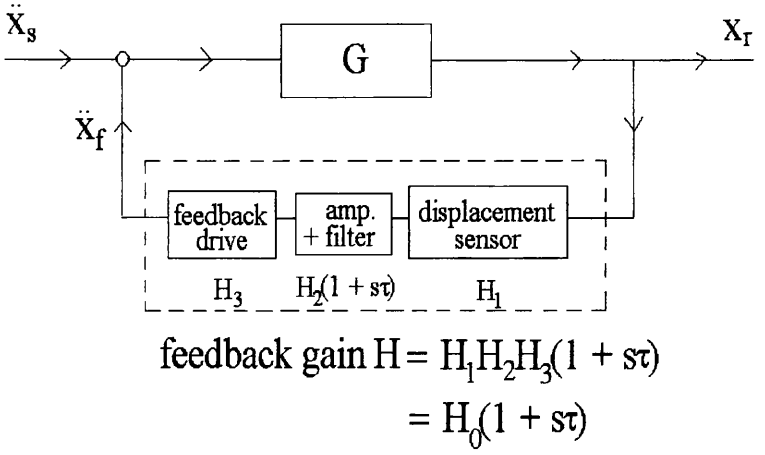

Figure B.1: *Simplified block diagram of a feedback system.*

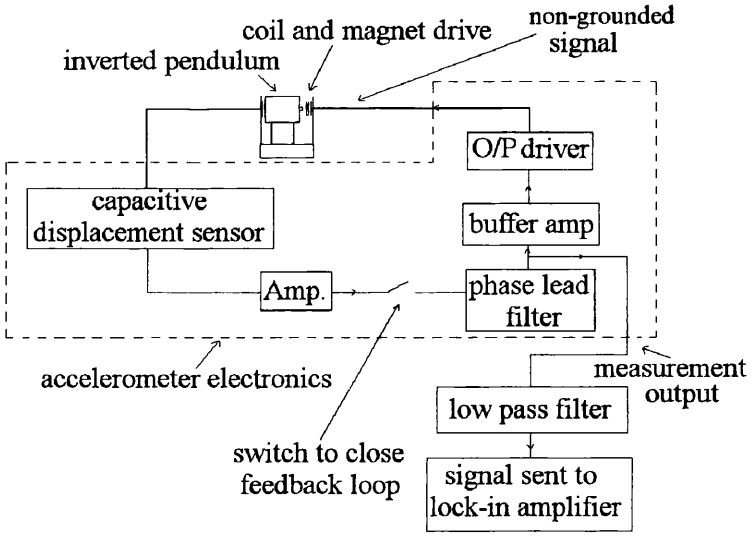

Figure B.2: *Simplified diagram of the inverted pendulum accelerometer.*

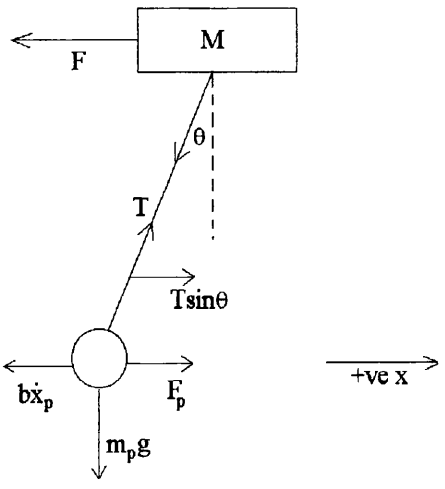

Figure B.3: *Diagram showing the forces acting on both a swinging pendulum and the pendulum support structure.*

The accelerometer was calibrated by applying a known acceleration and measuring its corresponding voltage applied by the coil of the coil and magnet drive. The calibration constant was found to be $68\,\mathrm{V/ms^{-2}}$.

B.3 The Phase Relationship Between the Shadow Sensed Motion of the Pendulum and the Applied Force

Consider the force, F_p, acting on a swinging mass, m_p, which is hung as a pendulum from a support structure

$$\begin{aligned} F_p &= m_p\ddot{x}_p \\ &= Tsin\theta - b\dot{x}_p \end{aligned} \tag{B.18}$$

where T is the tension in the suspension wire, θ is the angular displacement of the mass, b is the viscous damping coefficient and $\dot{x}_p$, the relative velocity of the mass as shown in figure B.3.

The reaction force, F, acting on the top-plate is due to the tension in the suspension

wire and

$$\begin{aligned} F &= -T sin\theta \\ &= b\dot{x}_p + m_p\ddot{x}_p. \end{aligned} \tag{B.19}$$

The pendulum displacement takes the form of a decaying exponential

$$x_p = x_0 e^{(i\omega_0 - \frac{\gamma_p}{2})t} \tag{B.20}$$

where x_0 is the maximum pendulum displacement, ω_0 is the resonant angular frequency of the pendulum, and $\frac{\gamma_p}{2}$ is the decay constant of the pendulum amplitude, where $\gamma_p = \frac{b}{m_p}$ [49].

Differentiating equation B.20 and substituting into equation B.19 gives an equation in which the imaginary term vanishes leaving only real terms in the expression for $\frac{F}{x_p}$ and thus showing that F and x_p are in phase. This equation is

$$F = -m_p(\omega_0^2 + \frac{\gamma_p^2}{4})x_p \tag{B.21}$$

This implies that shadow sensing the motion of the swinging pendulum gives the same phase information as sensing the applied force directly.

Appendix C

Eddy Current and Hysteresis Damping

C.1 Eddy Current Damping

The 'pusher' used to excite the pendulum mode of the suspension had a permanent magnet as an integral part of it. When the pendulum swung in the field of the magnet, it encountered a field gradient. The stronger, vertical field gradient was measured over the region of the pendulum swing as $\left(\frac{dB}{dx}\right)_{air} = 1.5 \times 10^{-3}\,\mathrm{Tm}^{-1}$ (the field being approximately 0 at the rest position of the pendulum) [1]. As a result of this varying field, eddy currents are induced in the tool steel pin-vices. Energy from the swinging pendulum can be dissipated, via the electrical resistance of the pin-vices, as heat.

We can make an estimate of this loss with the following: Recall that the pendulum mode loss factor, $\phi_{pend}(\omega_0)$, can be expressed (using equation 2.27) as

$$\begin{aligned} \phi_{pend}(\omega_0) &= \frac{1}{Q} \\ &= \frac{E_{lost/cycle}}{2\pi E_{stored}} \end{aligned}$$

Consider the denominator first. The energy stored in the swinging pendulum is

[1] For the purpose of this proof the pin-vices are modelled as hollow cylinders of radius, $r = 3 \times 10^{-3}$ m, wall thickness, $t = 1 \times 10^{-3}$ m and height, $h = 7.5 \times 10^{-2}$ m.

$$E_{stored} = \frac{1}{2}mv^2 \tag{C.1}$$

where m is the mass and v is the peak velocity of the pendulum.

Now consider the numerator in equation C.1. The energy lost per cycle can be expressed as

$$E_{lost/cycle} = P\frac{2\pi}{\omega_0} \tag{C.2}$$

where P is the total power dissipated in both pin-vices (and is equal to twice that dissipated in one pin-vice, i.e. $P = 2\frac{V^2}{R}$, where V is the induced EMF in one pin-vice and R is the resistance around the circumference of a pin-vice) and ω_0 is the resonant angular frequency of the pendulum.

The EMF can be calculated from Faraday's law as

$$V = -A_0\left(\frac{dB}{dt}\right)_{pin-vice} - A_{hole}\left(\frac{dB}{dt}\right)_{air} \tag{C.3}$$

where $A_0 = \pi t(2r - t)$ is the cross-sectional area of the pin-vice (t is the thickness of the pin-vice wall and r is the radius of the pin-vice), $A_{hole} = \pi(r - t)^2$ is the cross-sectional area of the air-gap in the centre of the pin-vice and $\left(\frac{dB}{dt}\right)_{pin-vice}$ and $\left(\frac{dB}{dt}\right)_{air}$ are the rate of change of magnetic flux density inside the pin-vice and air-gap respectively. By using the following equations

$$\begin{aligned}\left(\frac{dB}{dt}\right)_{pin-vice} &= \left(\frac{dB}{dx}\right)_{pin-vice} \cdot \left(\frac{dx}{dt}\right) \\ &= \left(\frac{dB}{dx}\right)_{pin-vice} .v\end{aligned} \tag{C.4}$$

and

$$B_{pin-vice} = \mu_r B_{air}, \tag{C.5}$$

the rate of change of flux density can be expressed alternatively as

$$\left(\frac{dB}{dt}\right)_{pin-vice} = \mu_r \left(\frac{dB}{dx}\right)_{air} v \tag{C.6}$$

where $\left(\frac{dB}{dx}\right)_{air}$ is the measured field gradient and μ_r is the relative permeability of the tool steel [2].

The expression for the cross-sectional area, A_0, and equation C.6 can be substituted into equation C.3 to give the EMF as

$$V = -\pi t(2r - t)\left(\frac{dB}{dx}\right)_{air} \mu_r v - \pi(r - t)^2 \left(\frac{dB}{dx}\right)_{air} v. \tag{C.7}$$

The second term of equation C.7 is approximately 5% of the first term and is therefore ignored i.e.

$$V = -\pi t(2r - t)\left(\frac{dB}{dx}\right)_{air} \mu_r v. \tag{C.8}$$

To calculate the power dissipated we also need to know the resistance, R. This is calculated from $R = \frac{\rho l}{A_1} = \frac{\rho 2\pi r}{th}$ (where ρ is the resistivity, l is the circumference of the pin-vice and is equal to $2\pi r$, and A_1 is the cross-sectional area through the wall of the pin-vice, th, where h is the height of the pin-vice).

Squaring equation C.8 and substituting it, together with the expression for R, into the equation for the total dissipated power leads to a power of

$$P = \frac{\pi t^2(2r - t)^2 \left(\frac{dB}{dx}\right)^2_{air} \mu_r^2 v^2 th}{\rho r}. \tag{C.9}$$

Substitution of equation C.9 into equation C.2 gives an expression for $E_{lost/cycle}$. The resulting expression can then be substituted together with equation C.1 into equation 2.27.

[2] A value for the relative permeability of $\mu_r = 14.5$ was measured for the pin-vice under weak field conditions using a Vibrating Sample Magnetometer by Dr. P.I. Williams, Wolfson Centre for Magnetic Technology, University of Wales Cardiff.

This allows an equation to be generated for the contribution to the pendulum mode loss factor due to eddy current damping, namely

$$\phi_{eddy}(\omega_0) = \frac{2\pi(2r-t)^2 t^2 \left(\frac{dB}{dx}\right)^2_{air} \mu_r^2 th}{m\rho r\omega_0}. \tag{C.10}$$

The values of the parameters are $m = 0.2\,\mathrm{kg}$

$$r = 3 \times 10^{-3}\,\mathrm{m}$$
$$\rho = 15 \times 10^{-8}\,\Omega\mathrm{m}$$
$$\omega_0 = 2\pi \times 1\,\mathrm{rad\,s^{-1}}$$
$$t = 1 \times 10^{-3}\ \mathrm{m}$$
$$h = 7.5 \times 10^{-2}\ \mathrm{m}$$
$$\left(\frac{dB}{dx}\right)_{air} = 1.5 \times 10^{-3}\,\mathrm{T\,m^{-1}}$$

and $\mu_r = 14.5$

which on substitution into equation C.10 gives a loss due to eddy current damping of $\phi_{pend}(\omega_0) \approx 1 \times 10^{-8}$. This loss is 3 orders of magnitude lower that the observed loss (refer to figure 5.6) and is therefore not considered to be the source of the excess loss.

C.2 Hysteresis Damping

The magnetisation of the pin-vices will increase and subsequently decrease as the pendulum swings in the varying magnetic field. The pin-vices are made of tool-steel, a material which is ferromagnetic. As a result, a fraction of the energy associated with the pendulum mode will be dissipated as heat by hysteresis in the pin-vices. We can estimate the level of hysteresis damping present in the pin-vices as follows. We will start by using a general definition of loss (refer to equation 2.27) in the form:

$$\begin{aligned} \phi_{pend}(\omega_0) &= \frac{1}{Q} \\ &= \frac{E_{lost/cycle}}{2\pi E_{stored}}. \end{aligned}$$

The energy stored in the swinging pendulum is

$$E_{stored} = \frac{1}{2} m\omega_0^2 x^2 \tag{C.11}$$

where m is the mass and ω_0 and x are the resonant angular frequency and the maximum displacement of the swinging pendulum respectively.

Now consider the numerator of equation 2.27. The maximum energy that may be lost in one cycle of a pendulum swing occurs when all of the energy stored in the magnetic field is dissipated. This is

$$dU = \frac{1}{2} dB_{pin-vice}.dH_{pin-vice} \text{ per unit volume} \tag{C.12}$$

where dU is the energy stored in the magnetic field, $dB_{pin-vice}$, is the magnetic flux density through the pin-vice (of the stronger, vertical field component) and $dH_{pin-vice}$ is the magnetic field strength. By using $dB_{pin-vice} = \mu_0 \mu_r dH_{pin-vice}$ (where μ_0 is the permeability of free space and μ_r is the relative permeability of the tool steel in the weak field) and equation C.5, dU can be expressed as

$$dU = \frac{\mu_r dB_{air}^2}{2\mu_0} \text{ per unit volume.} \tag{C.13}$$

An expression for dB_{air} can be obtained from the measured field gradient

$$dB_{air} = 1.5 \times 10^{-3} x. \tag{C.14}$$

Substituting dB_{air} into equation C.13 gives

$$dU = \frac{\mu_r (1.5 \times 10^{-3})^2 x^2}{2\mu_0} \text{ per unit volume.} \tag{C.15}$$

By multiplying dU by the volume of the two pin-vices we can calculate the maximum possible energy dissipated per cycle due to hysteresis in both pin-vices. The volume

of one pin-vice is $\pi\left(r^2-(r-t)^2\right)h = 1.13\times10^{-6}\,\mathrm{m}^{-3}$ (using the dimensions of the pin-vices as given in section C.1).

The maximum possible energy lost per cycle is therefore

$$E_{lost/cycle_{max}} = 3\times10^{-5}x^2. \tag{C.16}$$

However, not all of the available energy is in fact dissipated per cycle. Measurements of the magnetisation cycle of our pin-vices were provided by P.I. Williams [3]. From these measurements it appears that a maximum of 2% of the available energy is in fact lost per cycle in the weak magnetic field and thus

$$E_{lost/cycle} = \frac{2}{100}(3\times10^{-5})x^2. \tag{C.17}$$

Substitution of equation C.17 and equation C.11 into equation 2.27 gives the maximum hysteresis loss attributable to the two pin-vices of

$$\begin{aligned}\phi_{hysteresis_{max}}(\omega_0) &= \frac{\frac{2}{100}(3\times10^{-5})}{\pi m\omega_0^2}\\ &= 2\times10^{-8}\end{aligned} \tag{C.18}$$

(on substitution of the relevant values for m and ω_0). Because this loss is approximately three orders of magnitude lower than the best loss reported in figure 5.6, hysteresis damping is not considered to be the source of excess loss in this experiment.

[3] P.I. Williams, Wolfson Centre for Magnetics Technology, University of Cardiff Wales.

Appendix D

Derivation of an Expression for the Level of Pendulum Motion Resulting from Ground Excitation

It is important to know what effect ground motion has on the level of loss factor associated with the pendulum mode of our test pendulums. We shall therefore derive an expression for the level of rms pendulum displacement, $x_p(f)$, resulting from seismic motion at the point of suspension of amplitude spectral density, $x_g(f)$.

Consider the equation of motion of a pendulum subject to structural internal damping,

$$m\ddot{x}_p(f) = -k(1 + i\phi_{pend})\,[x_p(f) - x_g(f)] \tag{D.1}$$

where m is the mass of the pendulum, k is the stiffness of the wire, ϕ_{pend} is the true loss factor of the pendulum mode and represents the phase lag existing between the applied force and the response of the mass (and is independent of frequency for the case of structural damping).

Substitute for $\ddot{x}_p(f) = -(2\pi f)^2 x_p(f)$ into equation D.1 and solve for $\frac{x_p(f)}{x_g(f)}$. Dividing the resulting expression top and bottom by m and then substitiuting for $\frac{k}{m} = (2\pi f_p)^2$ (where f_p is the resonant frequency of the pendulum) leads to

$$\frac{x_p(f)}{x_g(f)} = \frac{f_p^2(1+i\phi_{pend})}{(f_p^2 - f^2) + if_p^2\phi_{pend}}. \tag{D.2}$$

The magnitude squared of equation D.2, $\left|\frac{x_p(f)}{x_g(f)}\right|^2$, can be calculated by multiplying by the complex conjugate of equation D.2. After suitable cancellation of terms, this reduces to

$$\left|\frac{x_p(f)}{x_g(f)}\right|^2 = \frac{1+\phi_{pend}^2}{(1+\phi_{pend}^2) - 2\frac{f^2}{f_p^2} + \frac{f^4}{f_p^4}}. \tag{D.3}$$

The total power spectrum of motion can be obtained by integrating equation D.3 over all frequencies i.e.

$$\left|\frac{x_p(f)}{x_g(f)}\right|^2 = (1+\phi_{pend}^2)\int_0^\infty \frac{df}{(1+\phi_{pend}^2) - 2\frac{f^2}{f_p^2} + \frac{f^4}{f_p^4}}. \tag{D.4}$$

The integral takes the form

$$W = \int_0^\infty \frac{dx}{a + bx^2 + cx^4} \tag{D.5}$$

where $a = (1+\phi_{pend}^2)$ (and $\phi_{pend} \approx 10^{-8}$ - refer to case 8, table 6.1), $b = -\frac{2}{f_p^2}$ (where $f_p = 1\,\text{Hz}$) and $c = \frac{1}{f_p^4}$. There are two solutions to the integral given in equation D.5. Which solution is used depends on the sign of $h^2 = b^2 - 4ac$. h^2 is negative and so the solution of the integral is [69]

$$W = \frac{1}{4cq^3 sin\alpha}[Y+Z]_0^\infty \tag{D.6}$$

where

$$Y = \left[sin\frac{\alpha}{2} ln\left(\frac{x^2 + 2qxcos\frac{\alpha}{2} + q^2}{x^2 - 2qxcos\frac{\alpha}{2} + q^2}\right)\right] \tag{D.7}$$

and

$$Z = \left[2cos\frac{\alpha}{2}arctg\left(\frac{x^2-q^2}{2qxsin\frac{\alpha}{2}}\right)\right]. \tag{D.8}$$

Also $q = \left(\frac{a}{c}\right)^{\frac{1}{4}}$ which reduces to $q = f_p\left(1+\frac{1}{4}\phi_{pend}^2\right)$ (on using the binomial expansion) and $cos\alpha = -\frac{b}{2\sqrt{ac}} = \frac{1}{\sqrt{1+\phi_{pend}^2}}$. Using $cos\alpha = \frac{1}{\sqrt{1+\phi_{pend}^2}}$, and knowing that $\phi_{pend}^2 \ll 1$, we can also show that $\alpha = \phi_{pend}$.

For ease we shall consider the terms Y and Z separately. With reference to equation D.8, consider first the term Z.

$$\begin{aligned} Z &= \left[2cos\frac{\alpha}{2}arctg\left(\frac{x^2-q^2}{2qxsin\frac{\alpha}{2}}\right)\right]_0^\infty \\ &= 2\pi cos\frac{\alpha}{2}. \end{aligned} \tag{D.9}$$

Now let us examine term Y (equation D.7). Consider the two limits in turn. When $x = 0$, Y reduces to

$$Y(0) = sin\frac{\alpha}{2}ln(1). \tag{D.10}$$

Next we look at what happens when $x \to \infty$. For ease we remove a common factor of x^2 so that

$$Y = \left[sin\frac{\alpha}{2}ln\left(\frac{1+\frac{2q}{x}cos\frac{\alpha}{2}+\frac{q^2}{x^2}}{1-\frac{2q}{x}cos\frac{\alpha}{2}+\frac{q^2}{x^2}}\right)\right]. \tag{D.11}$$

When $x \to \infty$ we can see that $\frac{q^2}{x^2} \to 0$, which leads to

$$Y(\infty) = sin\frac{\alpha}{2}ln(1). \tag{D.12}$$

On combining the two limiting cases, Y becomes

$$\begin{aligned} Y &= sin\frac{\alpha}{2}[ln(1) - ln(1)] \\ &= 0. \end{aligned} \tag{D.13}$$

Substitution of Z and Y into equation D.6 leads to

$$W = \frac{\pi cos\frac{\alpha}{2}}{2cq^3 sin\alpha}. \tag{D.14}$$

Substituting for c, q, α and $cos\frac{\alpha}{2} \sim 1$ gives

$$W = \frac{\pi f_p}{2(1 + \frac{1}{4}\phi_{pend}^2)^3 \phi_{pend}}. \tag{D.15}$$

and since $\phi_{pend} \ll 1$, we can reduce equation D.15 to

$$W = \frac{\pi f_p}{2\phi_{pend}}. \tag{D.16}$$

On substitution of equation D.16 into equation D.4 we see that

$$\left|\frac{x_p(f)}{x_g(f)}\right|^2 = (1 + \phi_{pend}^2)\frac{\pi f_p}{2\phi_{pend}} \tag{D.17}$$

and, again, using $\phi_{pend}^2 \ll 1$, it can be seen that

$$x_p(f) = x_g(f)\sqrt{\frac{\pi f_p}{2\phi_{pend}}}. \tag{D.18}$$

where it is assumed that the drive noise spectrum is approximately white in the frequency range about 1 Hz, i.e. that $x_g(f)$ is a constant.

Appendix E

Revised Mirror Sizes for GEO 600

During the period that the author was writing this thesis, the mass of a full sized mirror for GEO 600 was reduced from 16 kg to 5.6 kg. This change was proposed primarily because of the technical difficulties involved in coating the 16 kg masses. Decreasing the masses however also eased the construction of the final, triple pendulum. Analysis shows that the original thermal noise specification of $\tilde{x}_{internal}(\omega) = 7 \times 10^{-20}\,\mathrm{m}/\sqrt{\mathrm{Hz}}$ at 50 Hz can be reached using a 5.6 kg test mass of 18 cm diameter and 10 cm long [1].

As with the original suspension, we aim to reach a power spectral density of thermal motion associated with the pendulum mode a factor of ten lower than that associated with the internal modes. This is equivalent to a rms thermal displacement of $\tilde{x}_{pend}(\omega) = 2.2 \times 10^{-20}\mathrm{m}/\sqrt{\mathrm{Hz}}$ at 50 Hz. By substituting the desired thermal displacement and value of the pendulum mass into equation 2.24, the noise can be expressed as a total loss factor due to the pendulum mode of $\phi_{pend_{total}}(\omega) = 1.27 \times 10^{-8}$ at 50 Hz.

Recall from Chapter 2 that the theoretical limit set to the level of loss that is obtainable for the pendulum mode of a given suspension is given by equation 2.30 i.e.

$$\phi_{pend_{total}}(\omega_0) = \phi_{mat_{total}}(\omega_0)\frac{\xi n\sqrt{TEI}}{2mgl}$$

[1] The level of thermal noise achievable is not determined by the mass of the mirror but by the aspect ratio.

where the parameters are defined in section 2.6.1. The unknowns in equation 2.30 are

- the fibre radius, r
- the loss factor, $\phi_{mat_{total}}(\omega)$ at 50 Hz

which are determined as follows:

Using the mass of the mirror and the breaking stress of fused quartz we can calculate the radius of each of the four quartz fibres: to suspend a 5.6 kg mass on fibres tensioned to $\frac{1}{3}$ of their breaking stress would require 128 μm radius fibres.

Let us assume the best 'measured' intrinsic loss factor of $\phi_{mat_{intrinsic}}(\omega) = 0.5 \times 10^{-6}$ (refer to section 3.8). In addition the thermoelastic damping contribution of a 128 μm radius fibre can be calculated to be $\phi_{mat_{t.e.}}(\omega) = 1.3 \times 10^{-6}$ at 50 Hz. Adding the two loss factors gives a total loss factor associated with the suspension fibres of $\phi_{mat_{total}}(\omega) = 1.8 \times 10^{-6}$ at 50 Hz.

By substituting the relevant parameters into equation 2.30, we can calculate that a loss factor associated with the pendulum mode of $\phi_{pend_{total}}(\omega) = 0.75 \times 10^{-8}$ should be obtainable at 50 Hz. This value is approximately a factor of two better than the new, maximum loss factor (calculated from the GEO 600 thermal noise specification). Thus indications are that we can achieve the minimum thermal noise requirements using the new 5.6 kg mirrors.

Bibliography

[1] K. Danzmann et. al., *GEO 600: Proposal for a 600 m laser interferometric gravitational wave antenna*, Max-Planck-Institut für Quantenoptik Report 190, Garching, Germany (1994).

[2] A. Einstein, *Die Grundlage der Algemeinen Relativitätstheorie*, Annalen der Physik, **49**, (1916) 769.

[3] R.A. Hulse, J.H. Taylor, Astrophys. J., **195**, (1975), L51.

[4] J.H. Taylor, Rev. of Mod. Phys., **66**, (1994), 711.

[5] S. Bonnanzola, J.A. Marck, Annual Review of Nuclear and Particle Science, **45**, (1994), 655.

[6] B.F. Schutz, *The Detection of Gravitational Waves*, Proceed. 1995 Houches School on Astrophysical Sources of Gravitational Radiation, Ed. J.A. Marck, J.P. Lasota (Springer Berlin), 1996.

[7] B.F. Schutz, Nature, **323**, (1986), 310.

[8] S. Phinney, Private Communication.

[9] K.S. Thorne, *Gravititional Waves*, Proceed. Snowmass 95 Study on Particle and Nuclear Astrophysics and Cosmology, Ed. E.W. Kolb, R. Peccei (World Scientific, Singapore).

[10] R.V. Wagoner, Astrophys. J., **278**, (1984), 345.

[11] L. Bildsten, Astrophys. J., **501**, (1998), L89.

[12] R.A. Battye, E.P.S. Shellard, Class. Quant. Grav., **13**, (1996), A239.

[13] J. Weber, Phys. Review, **117**, (1960), 306.

[14] Solomonson et. al., Proceed. of 6^{th} Marcel Grossmann Meeting, Ed. H. Sato, A. Nakamura, (World Scientific, Singapore).

[15] Astone et. al., Phys. Rev. D., **47**, (1993), 2.

[16] A. Abramovici, P. Bender, R. Drever, et.al., *Gravitational Wave Astrophysics*, Proceed. Snowmass 94 Summer Study on Particle and Nuclear Astrophysics and Cosmology in the Next Millenium, Ed. E.W. Kolb, R. Peccei (World Scientific, Singapore), 1995.

[17] C.M. Caves, Phys. Rev. D., **26**, (1982), 1817.

[18] K.S. Thorne, C.M. Caves, V.D. Sandberg, M. Zimmermann, *The Quantum Limit for Gravitational-Wave Detectors and Methods of Circumventing it* in *Sources of Gravitational Radiation*, Ed. L. Smarr, (Cambridge, 1979).

[19] R.L. Forward, Phys. Rev. D, **17**, (1978), 379.

[20] R. Weiss, M.I.T. Quarterly Progress Report No. 105, 1972.

[21] W. Winkler, *A Michelson Interferometer Using Delay Lines* in *The Detection of Gravitiational Waves*, Ed. D.G. Blair, (Cambridge University Press, Cambridge 1991).

[22] D. Shoemaker, R. Schilling, L. Schnupp, W. Winkler, K. Maischberger, A. Rüdiger, Phys. Rev. D., **38**, (1988), 423.

[23] R.W.P. Drever, G.M. Ford, J. Hough, I.M. Kerr, A.J. Munley, J.R. Pugh, N.A. Robertson, H. Ward, *A Gravity-Wave Detector Using Optical Cavity Sensing*, Proceed. 9^{th} International Conference on General Relativity and Gravitation, Jena 1980, Ed. E. Schmutzer (VEB Deutscher Verlag der Wissenschaften, Berlin 1983).

[24] D. Sigg, N. Mavalvala, J. Giaime, P. Fritschel, D. Shoemaker, Applied Optics, **37**, (1998), 5687.

[25] D.I. Robertson, E. Morrison, J. Hough, S. Killbourn, B.J. Meers, G.P. Newton, K.A. Strain, H. Ward, Rev. Sci. Instrum., **66**, (1195).

[26] C.M. Caves, Phys. Rev. Lett., **45**, (1980), 75.

[27] J. Hough, H. Walther, B.F. Schutz, J. Ehlers, H. Welling, I.F. Corbett, V. Kose, et. al., *Proposal for a Joint German-British Interferometric Gravitational Wave Detector*, Max-Planck-Institut für Quantenoptik Report 147 and GWD/137/JH(89) (1989).

[28] P.R. Saulson, *Fundamentals of Interferometric Gravitational Wave Detectors*, 1994, (World Scientific, Singapore).

[29] W.A. Edelstein, J. Hough, J.R. Pugh, W. Martin, J. Phys. E: Scientific Instruments, **11**, (1978), 710.

[30] A. Gillespie, *Thermal Noise in the Initial LIGO Interferometers*, Ph.D. Thesis, California Institute of Technology, 1995.

[31] M.V. Plissi, K.A. Strain, C.I. Torrie, N.A. Robertson, S. Killbourn, S. Rowan, S.M. Twyford, H. Ward, K.D. Skeldon, J. Hough, Rev. Sci. Inst., In press.

[32] P.R. Saulson, Phys. Rev. D, **30**, (1984), 732.

[33] R. Spero, *Science Underground*, Proceed. Los Alamos Conf. 1982, Ed. M.M. Nieto et al., (AIP, New York, 1983).

[34] R.E. Vogt, R.W.P. Drever, K.S. Thorne, F.J. Raab, R. Weiss, *A laser interferometer gravitational-wave observatory (LIGO)*, Proposal to the National Science Foundation, (1989).

[35] A. Brillet, VIRGO final conceptual design, (1992).

[36] K. Tsubono and the TAMA collaboration, TAMA Project, *Gravitational Wave Detection*, Ed. K. Tsubono, M.K. Fujimoto and K. Kurodo, Universal Academy Press, Inc. (Tokyo, 1997), 183.

[37] K.D. Skeldon, K.A. Strain, A.I. Grant, J. Hough, Rev. Sci. Instrum., **67**, (1996), 2443.

[38] B.J. Meers, Phys. Rev. D., **38**, (1988), 2317.

[39] R.W.P. Drever, *Gravitational Radiation*, Ed. N. Dereulle, T. Piran, (North Holland Publishing Co., 1983).

[40] K. Danzmann, A. Rüdiger, R. Schilling, W. Winkler, J. Hough, et. al., Max-Planck-Institut für Quatenoptik Report MPQ 177, 1993.

[41] R. Brown, Ann. Phys. Chem., **14**, (1828), 294.

[42] A. Einstein, *Investigations on the Theory of Brownain Movement*, (Dover, New York), 1956.

[43] H.B. Callen, T.A. Walton, Phys. Rev. **83**, (1951), 34.

[44] H.B. Callen, R.F. Greene, Phys. Rev. **86**, (1952), 702.

[45] T.J. Quinn, C.C. Speake, R.S. Davis, W. Tew, Phys. Lett., **197A**, (1995), 197.

[46] A.S. Nowick, B.S. Berry, *Anelastic Relaxations in Crystalline Solids*, (Academic, New York), 1972.

[47] A.L. Kimball, D.E. Lovell, Phys. Rev. **30**, (1927), 948.

[48] C. Zener, *Elasticity and Anelasticity of Metals*, (University of Chicago Press, Chicago), 1948.

[49] A.P. French, *Vibrations and Waves*, M.I.T. Introductory Physics Series, (Van Nostrand International), 1965.

[50] V.B. Braginsky, V.P. Mitrofanov, O.A. Okhrimenko, JEPT Lett., **55**, (1992), 432 and references therein.

[51] S. Traeger, B. Willke, K. Danzmann, Phys. Lett. A., **225**, (1997), 39.

[52] A. Gillespie, F. Raab, Presented at a Workshop on Thermal Noise in Laser Interferometers, Caltech 1994.

[53] P.R. Saulson, Phys. Rev. D., **42**, (1990), 2437.

[54] V.B. Braginsky, V.P. Mitrofanov, V.I. Panov, *Systems of Small Dissipation*, (The University of Chicago Press, Chicago), 1985.

[55] J.E. Logan, J. Hough, N.A. Robertson, Phys. Lett. A, **183**, (1993), 145.

[56] G.I. Gonzalez, P.R. Saulson, J. Acoust. Soc. Am., **96**, (1994), 207.

[57] A. Gillespie, A. Raab, Phys. Lett. A., **178**, (1993), 357.

[58] V.B. Braginsky, V.P. Mitrofanov, S.P. Vyatchanin, Rev. Sci. Instrum., **65**, (1994), 3771.

[59] A.C. McLaren, Ph.D. Thesis, University of Glasgow, 1996.

[60] Edwards High Vacuum International, Instruction Manual, Active Inverted Magnetron Gauge.

[61] W.J. Startin, M.A. Beilby, P.R. Saulson, to be submitted to Rev. Sci. Inst.

[62] J.E. Logan, Private Communication.

[63] J.E. Logan, Private Communication.

[64] J.E. Logan, Ph.D Thesis, University of Glasgow, 1993.

[65] C. Chree, Quart. Jour. Math., **21**, (1886), 287.

[66] G.W. McMahon, Journ. Acoustical Soc. Am., **36**, (1964), 85.

[67] D.-H. Gwo, Private Communication.

[68] S. Rowan, S.M. Twyford, J. Hough, D.-H. Gwo, R. Route, Phys. Lett. A, In press.

[69] I.S. Gradshteyn, I.M. Ryzhik, *Tables of Integrals, Series, and Products*, (Academic Press Incorporated. (London) Ltd.), 1963.